Development of Solution Processable Materials for Use as Hosts in OLED Devices

A thesis submitted in partial fulfilment of the requirements for the degree
of Doctor of Philosophy
By

Abdulelah Alsulami

Department of Chemistry
June 2022

Declaration

I hereby declare that this thesis is completely my original work, unless referenced. This thesis is submitted for the degree of Doctor of Philosophy (PhD) at the University of Sheffield, having been submitted for no other degree. It records the research carried out at the University of Sheffield from January 2018 to June 2022.

Signature Abdulelah Alsulami

Date 27/06/2022

Acknowledgements

First of all, I would like to thank to Allah almighty, who enabled me to undertake this research study. Without his blessings, this achievement would not have been possible.

To my love and my heart, my mother, I realise your missing me in my absence for all past years, but I have achieved what you desired. I really appreciate your moral support.

Furthermore, I would like to thank Dr Ahmed Iraqi for his advice, effort, support, and encouragement throughout my PhD study and completing my research. I can frankly state that I would never have completed my PhD thesis without the motivation of Dr Ahmed. I acquired skills from him, not only in academia, but also in terms of personal growth and development. I thank Dr Ahmed Iraqi for his kindness.

I would also like to thank all my laboratory colleagues for their crucial role in conducting my research, especially Osama and Yazeed. I will never forget them.

Lastly, but most of all, I thank my beloved wife, Seham Abdullah, for her continuous encouragement and support through stressful and difficult times. I will not forget the most difficult time that we passed throughout our son's complex operations. Our son, Malek, is our blessing. To my son Omar, I express my thanks for being such a good boy. Omar if you read this in the future, I would like you to memorise in full the holy Quran and thank Allah for everything.

Abstract

The current advances in cutting-edge OLED technologies based on TADF materials are significant. The new generation of TADF-based materials has the ability to upconvert triplet excitons into singlet excitons, providing theoretically 100% exciton utilisation efficiency (EUE) without incorporating any heavy-metal phosphorescent components. In spite of efficiency improvements, the evaporated deposition technique for making OLEDs requires sophisticated structures, high costs, and difficult control, making them impractical for large-scale device production. Compared to other manufacturing techniques, a solution process is a simpler, less expensive and more readily controlled choice for enabling large-scale production. However, the majority of published TADF dopants are essentially small molecules, which are incompatible with solution processing. Consequently, there is a commercial interest in developing solution-processable organic emissive materials with TADF characteristics. It has been established that the efficiency of solution-processed devices can be enhanced and that polymeric materials comprise excellent emissive materials.

We proposed applying a sidechain engineering method to introduce a TADF channel in a single-polymer system. This polymeric design strategy involved grafting the TADF emitter onto the polymer sidechain. Using this approach, two types of distinct functional units were entered into a single-polymer system, which is comprised of a polymer backbone and grafted moieties on polymeric sidechains. The target TADF polymers (**PmCP-DPOXH-PxzTrz-X**, and **PDPEPO-DPOXH-PxzTrz-X**) were designed to enable the use of the molecules, **mCP** and **DPEPO**, as hosts because they have high triplet energy levels (E_T) = 2.9 and 3.0 eV, respectively. These are higher than the E_T of potential TADF guests, thereby avoiding the undesired triplet energy back-transfer (TEBT) from the guest to the host. Additionally, the addition of the **mCP** molecule into the polymer backbone enhances the hole transport performance, while the **DPEPO** molecule boosts electron transport performance. Furthermore, **PXZ-TRZ** was employed as a green TADF emitter, generating excellent TADF properties, such as a low ΔE_{ST}. **PXZ-TRZ** was thus exploited in generating the target TADF polymers (**PmCP-DPOXH-PxzTrz-X**, and **PDPEPO-DPOXH-PxzTrz-X**).

The CV analysis of TADF polymers (**PmCP-DPOXH-PxzTrz-X** and **PDPEPO-DPOXH-PxzTrz-X**) revealed an increasing trend of the HOMO levels with rising

loading ratios of TADF moiety in the polymers. Dual emission peaks in the PL profiles of TADF polymers (**PmCP-DPOXH-PxzTrz-X** and **PDPEPO-DPOXH-PxzTrz-X**) in toluene solution were observed in the ranges of 340-460 nm and 460-700 nm, which can be attributable to the emissions of both the polymeric backbone and the TADF moiety, respectively.

Table of Contents

Chapter 3: DPEPO-Based Polymers with Pendant TADF Emitters for use in Solution Processable OLEDs 121

Chapter 4: Conclusions and Future Work 156

Chapter 5: Experimental Section 164

Chapter 6: Supplementary Information 190

List of Figures

List of Schemes

List of Tables

List of Abbreviations

Ar	Argon gas
bs	Broad singlet (NMR)
$CDCl_3$	Deuterated Chloroform
CI	Chemical Ionisation
CV	Cyclic Voltammetry
d	Doublet (NMR)
dd	Doublet of doublet (NMR)
DCM	Dichloromethane
DF	Delayed Fluorescence
DMF	*N*,*N*-Dimethylformamide
DMSO	Dimethylsulfoxide
DP	Degree of Polymersition
DPEphos	Bis[(2-diphenylphosphino)phenyl] ether
DPEPO	Bis[2-(diphenylphosphino)phenyl] ether oxide
EA	Elemental Analysis
EBL	Electron Blocking Layer
$Eg_{(opt)}$	Optical gap
EI	Electron Ionisation
EL	Electroluminescence
EML	Emissive Layer
ETL	Electron Transport Layer
eV	Electronvolt
FWHM	Full Width Half Maximum
GPC	Gel Permeation Chromatography
HIL	Hole Injection Layer
HOMO	Highest Occupied Molecular Orbitals
HTL	Hole Transport Layer
IC	Internal Conversion
ICT	Intramolecular charge transfer

IQE	Internal quantum efficiency
ISC	Intersystem Crossing
ITO	Indium Tin Oxide
J	Coupling constant (NMR)
LED	Light-Emitting Diode
LUMO	Lowest Unoccupied Molecular Orbitals
Mn	Number-average molecular weight
MS	Mass Spectrometry
m/z	Mass-to-charge ratio (MS)
NBS	*N*-Bromosuccinimide
OLED	Organic Light Emitting Diode
PDI	Polydispersity Index
PF	Promote Fluorescence
PL	Photoluminescence
PLQY	Photoluminescence Quantum Yields
ppm	Part per million
PPV	Poly(p-phenylene vinylene)
RISC	Reverse Intersystem Crossing
S_0	Singlet Ground State
S_1	Singlet Excited State
T_1	Triplet Excited State
TADF	Thermally Activated Delayed Fluorescence
TGA	Thermogravimetric analysis
TTA	Triplet-Triplet Annihilation
UV-vis	Ultra-Violet-visible spectroscopy
V	Volt
VR	Vibrational Relaxation
ΔE_{ST}	Energy level difference between T_1 and S_1

Chapter 1: Introduction

1. Introduction

1.1 Organic Light Emitting Diodes (OLEDs)

1.1.1 A Brief History of OLEDs

In 1953, Bernanose *et al.* first discovered the electroluminescence (EL) phenomenon in organic molecules utilising a cellulose film doped with acridine orange.[1] Following that, Pope *et al.* improved the EL phenomenon in organic materials using single-crystal anthracene in 1963.[2] In 1982, Vincett *et al.* generated a visible EL in typical lighting conditions using anthracene films produced by *vacuum* deposition at an operating voltage of approximately 30 V. Furthermore, the thickness of films amounted to around 0.6 µm.[3] Five years later, Tang and Van Slyke facilitated significant advancements in EL characteristics. They utilised the EL cell comprising an organic double layer of thin films, including an emissive tris(8-hydroxyquinoline) aluminium (Alq_3) film on the top of a diamine film using a mixture of Mg: Ag electrode as a cathode and indium tin oxide (ITO) as an anode.[4] In 1990, researchers employed poly(p-phenylene vinylene) (PPV) as a solution-processed conjugated polymer, applied as an active semiconductor layer between two metallic electrodes and Burroughes *et al.* went on to report the first discovery of the EL from conjugated polymers.[5,6]

1.1.2 The Structure of OLED

Figure 1.1 presents the structure of various OLEDs. The design of the simplest OLED structure consists of a single organic layer sandwiched between an anode and a cathode which is known as a single-layer OLED. This organic layer requires the performance of three essential functions: light emission, hole and electron transport. Ideally, the efficiency of injection of both holes and electrons as well as their transport should be similar to one another. This organic layer must exhibit high quantum efficiency for photoluminescence (PL). In addition, it must possess excellent properties of hole transport and electron transport. In a two-layer OLED, two individual layers separately transport the hole and electron, with one acting as an electron transport layer (ETL) and the other acting as a hole transport layer (HTL).[7] In addition, applying these two layers aims to solve the issue of low efficiency that the single-layer OLED may encounter. The hole-electron recombination, which produces electroluminescence, occurs at the interface between the two layers. Coupling the thin organic layers raises both the transport efficiency and the injection of charge because of the prompt connection of the OLEDs' light emission with the current density via the electroluminescent medium. This approach results in the light emission of OLEDs providing a low voltage. A further luminescent layer is added between the hole and electron layers in order to create a triple-layer OLED which shows its suitability for emissive materials that do not contain elevated carrier transporting features.[8] Therefore, the emitting layer is primarily a recombination of hole-electron to generate electroluminescence. The addition of an electron injection layer results in a structure identified as a multi-layer OLED. The leaking charge carrier and exciton quenching are removed by introducing the multi-layer OLED structure. These structures contain different layers, such as an anode, ETL, emissive layer (EML), hole blocking layer (HBL), electron blocking layer (EBL), HTL, hole injection layer (HIL) and electron injection layer (EIL).[9]

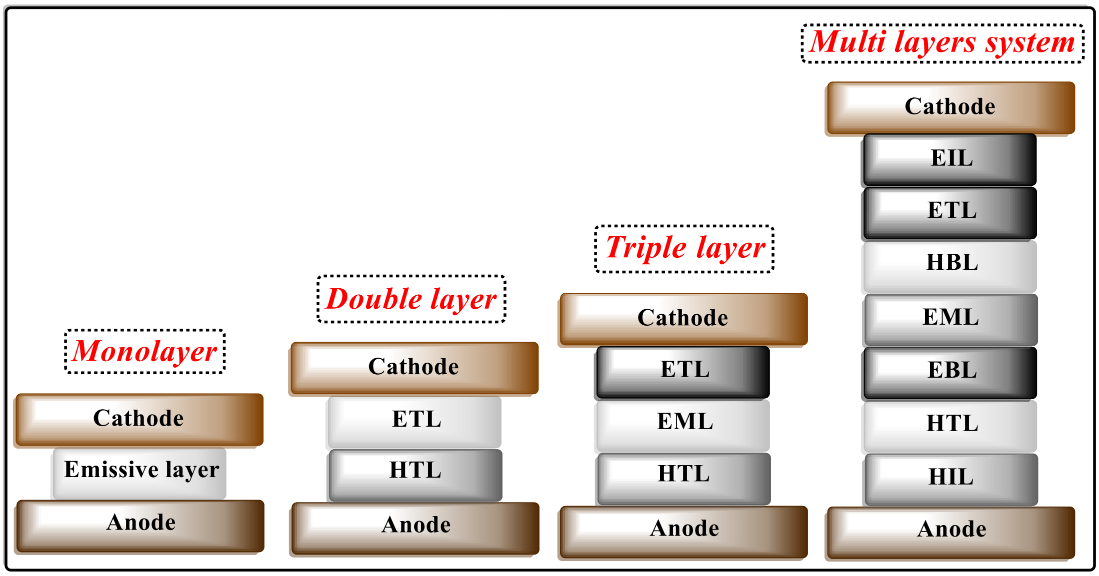

Figure 1.1: Different structures of OLEDs: Monolayer OLED, Double layer OLED, Triple layer OLED, and Multilayers OLED.

1.1.3 The Working Principle of OLED

The principle of electroluminescence plays a crucial role in OLEDs. The performance of an OLED relies on an organic luminophore. Manufacturing an OLED device can prove to be challenging in terms of adjusting the device to equally balance the number of holes and electrons to meet in the emissive layer. However, this equal number of holes and electrons also creates difficulties making adequate organic molecules due to the fact that mobility of electrons is generally significantly lower than hole mobility. Once a voltage is applied to an OLED, movement of an electrical current from the cathode to the anode takes place across the organic layers. In organic compounds, a cathode injects the emissive layer with electrons while the anode takes away electrons from the conductive layer. Merging of the positive and negative charges results in the creation of exciton pairs followed by light emission. In addition, the difference in light colour relies upon the type of organic material in the emissive layer. **Figure 1.2** displays the working principle of an OLED device. The amount of electrical current applied plays an integral role in the intensity or brightness of the light.[10]

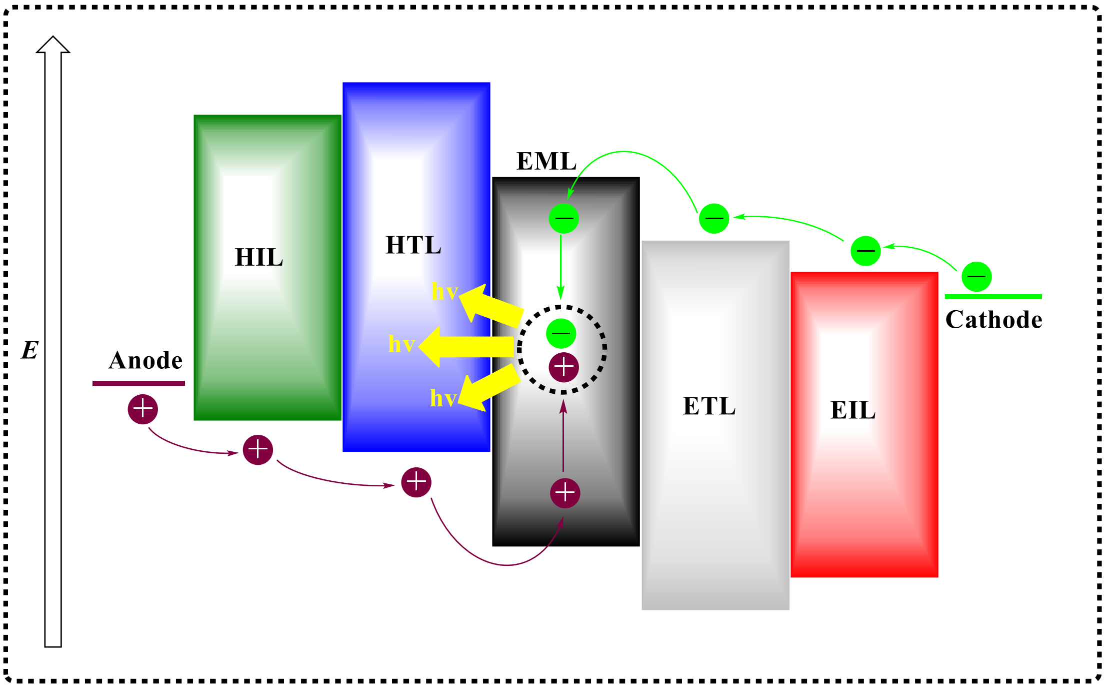

Figure 1.2: The working principle of an OLED device.

1.2 Thermally Activated Delayed Fluorescence (TADF)

1.2.1 Fundamental Understanding of the TADF Phenomenon

In 1929, Perrin first streamlined the utilisation of TADF, otherwise identified as E-type delayed fluorescence (DF).[11] Lewis[12] then applied TADF in fluorescein solutions in 1941 and after twenty years, Parker and Hatchard recorded the E-type DF in eosin and benzyl.[13,14] However, the device efficiency was extremely unsatisfactory as a result of short lifetime of the luminance.[15,16] In 1968, Wilkinson and Horrocks proposed the form of TADF to recognise delayed luminescence.[17] In 2012, Adachi went on to refresh and develop this familiar mechanism and suggested a method to harvest non-emissive triplet-excited levels in OLEDs using TADF materials. Materials containing TADF can be employed in the temperature and oxygen sensor as the TADF process shows its elevated sensitivity to these two factors.[18] A contrast of energy between the first singlet-excited state (S_1) and the first triplet-excited state (T_1) is considerable in traditional fluorescent materials; the possibility of transitioning from S_1 to T_1 is extremely limited. Hence, only singlet excitons can make a clear contribution to the fluorescence. However, much research has recently shown that a major contribution to the fluorescence can be provided by triplet excitons during TADF. In TADF materials, a specific process, namely, a reverse intersystem crossing (RISC) process, efficiently harvests the triplet excitons from T_1 to S_1. Stimulation or activation of this type of RISC process has to occur because the S_1 state is always higher than the T_1 state based on Hund's rule. The endothermic RISC process is controllable by the thermal process once the energy difference between the two levels of T_1 and S_1 is minimised. In TADF molecules, the non-radiative triplet excitons, because of a spin-forbidden transition of T_1 to the ground singlet state (S_0), are converted to singlet excitons by the RISC process, resulting in enhanced luminescence from S_1 to S_0 via delayed fluorescence. The discovery of TADF has led to the development of the exciton statistical limit of 25% in fluorescence to the maximum quantum efficiency of 100% in fluorescence for a significant value of rare metal-free organic molecules. The prompt fluorescence (PF) and the delayed fluorescence (DF) are considered as two apparent unimolecular mechanisms for TADF.[19,20] After the excitation from the S_0 to S_1 state followed by a rapid decay from the S_1 to S_0 level, the emission happens directly within a few nanoseconds with respect to concerning the PF mechanism of singlet excitons. In respect of the DF process, triplet excitons are required to turn into singlet excitons through the RISC mechanism, giving rise to a remarkable increase of fluorescent lifetime reaching several microseconds due to delay of luminescent process by the additional step that occurs prior to fluorescence emission. The formation of triplet excitons is generated after an efficient intersystem crossing (ISC) process once TADF materials are optically excited. In spite of two PF and DF processes for TADF materials possess the same spectral distribution as traditional fluorescence, it is clear that they have two diverse fluorescent lifetimes. In addition, four vital stages must occur for TADF emission in OLED devices which require emphasis as illustrated in **Figure 1.3**. The recombination of charges (electrons and holes) in a singlet-to-triplet ratio of 1:3, in accordance with spin statistics, produces singlet and triplet excitons, which are considered to be the first process. Next, the second process involves shifting the high exciton states to the lowest exciton levels, which are either S_1 or T_1, by means of rapid vibrational relaxation (VR), internal conversion (IC), and ISC. Moreover, thermal activation assists the amassed triplet excitons at T_1 in order to convey back to S_1 during RISC process; this step constitutes the third essential TADF process. Furthermore, the fourth process is that the radiative deactivation of singlet excitons at S_1, which are produced either by back-transitioning from T_1 or after exciting electronically, to S_0 is performed for PF and long-lived DF, respectively. In these processes, the efficient RISC plays a crucial role in harvesting the triplet excitons to boost the fluorescent luminescence. The efficient transitioning from T_1 to S_1 stimulated through the thermal activities of molecular atoms requires a low singlet-triplet energy splitting (ΔE_{ST}) to aid the RISC process. Therefore, the ISC is efficient if maintaining such an efficient RISC because of the higher S_1 energy level related to T_1 in TADF molecules. As a consequence, balanced distribution of excitons is obtained between S_1 and T_1 in TADF materials and most of the excitons are distributed on T_1 since it has a comparatively low energy level compared to S_1. As a result, T_1 ought to be sufficiently stable for the RISC mechanism for the emission of fluorescence in TADF molecules.[21]

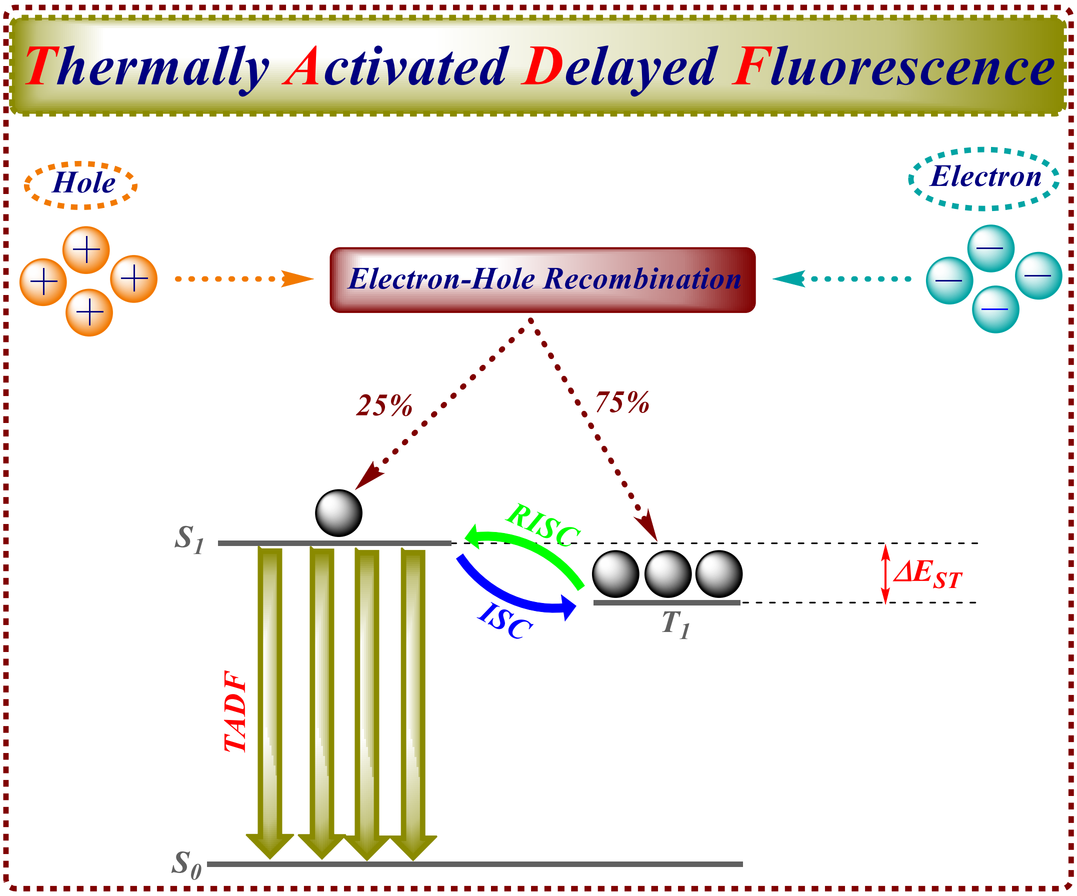

Figure 1.3: Schematic energy diagram of TADF emitters in OLED.

1.2.2 Design Principles of Organic TADF Molecules

The production of TADF emitters meets the essential key prerequisites of small ΔE_{ST} and high photoluminescence quantum yields (PLQY), which bear a strong connection to light-emitting features. Furthermore, full width at half-maximum (FWHM) of the emission spectrum and molecules' stability may play crucial roles in driving the process forward. Since the parameters have an association with one another, the TADF materials were designed with a view to enhancing the parameters, although this design can lead to a small loss of some factors. Numerous reports have found that the design of the donor-acceptor represents the most viable strategy to produce TADF molecules, and recent emitters are built on the basis of the donor-acceptor molecular style with a large separation of the HOMO and LUMO.[22–24] Despite the benefits of straightforward molecular design based on the donor-acceptor, the shortcomings of this design are evident in a broad light emission spectrum. Such a situation occurs because of the charge transfer (CT) emissive state, and, in some cases, the lifetime (τ) of the device is short because of the molecular structure’s instability. A broad emission spectrum correlates to the device’s colour purity, whereas the chemical structure’s instability corresponds to the lifetime of the devices. Thus, modifying the construction of the straightforward donor-acceptor design has sought to remove these concerns. The aforementioned product parameters correlate with the device's properties. These properties include its lifetime, which depends upon material stability, colour purity as determined by FWHM, external quantum efficiency (EQE) as controlled by PLQY and efficiency roll-off, which signifies the efficiency of OLED decreases as the brightness increases, relies upon the lifetime of delayed fluorescence administered by ΔE_{ST}. The principal characteristics, including the long lifetime of the device, low-efficiency roll-off, excellent colour purity and high EQE, must be met in the TADF devices to facilitate the use of TADF emitters in display applications. Despite that, the lighting applications do not necessitate good colour purity. Consequently, the description of the molecular structural design strategy will encompass the properties of the emitter and the device. **Figure 1.4** shows a schematic diagram illustrating the devices’ performances, the material parameters, and the material design strategies.[23]

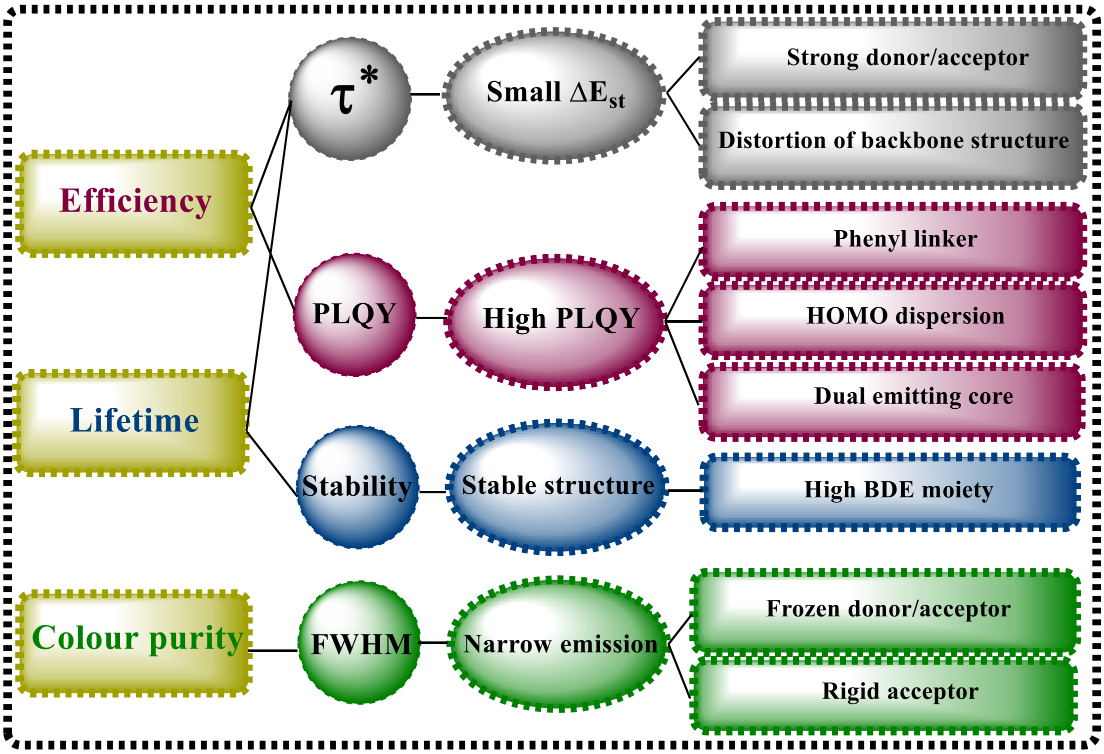

Figure 1.4: General diagram showing the TADF parameters, TADF design approaches, and device performances.

1.2.2.1 Donor and Acceptor Moieties of TADF Emitters

The donor and acceptor units require careful selection in order to control the photophysical properties. For strong donors and acceptors, the HOMO and the LUMO will be localised on the donor and acceptor units, respectively. Such an approach lowers the TADF emitters' singlet energy by spatial separation between the HOMO and the LUMO orbitals with a slight impact on the triplet energy. Whereas weak donor and acceptor moieties cause less considerable localisation of the HOMO and LUMO energies and thereby giving rise to a slight decrease in the singlet energy levels relative to strong donors and acceptors. Thus, strong donor and acceptor units have a greater capacity to lower the TADF materials’ energy transitions than their weak equivalents. Numerous donor and acceptor units have recently been employed in the molecular design of TADF emitters which have distinct donor/acceptor strengths. Noteworthily, each of the emitter's HOMO and LUMO levels could well determine the strengths of the donor and acceptor. In terms of donor moieties, deep and shallow HOMO indicates weak and strong electron donor strength, respectively, while deep and shallow LUMO indicates strong and weak electron acceptor strength, respectively, with respect to acceptor moieties. The selection of donor units tends to come from specific structures, including amine, diamine, phenazine, phenothiazine, phenoxazine, acridine, carbazole, bicarbazole, thienocarbaozle, benzofurocarbazole and indolocarbazole, as illustrated in **Figure 1.5**. On the other hand, aromatic ketone, triazole, benzothiazole, oxadiazole, benzoxazole, thiadiazole, triazine, heptazine, phthalonitrile, benzonitrile, diphenyl sulfone, anthraquinone and quinoxaline are typically applied to acceptor units, as depicted in **Figure 1.6**. Examples of strong donor moieties include phenoxazine, acridine and phenothiazine, whereas carbonitrile derivatives represent strong acceptor moieties.[23]

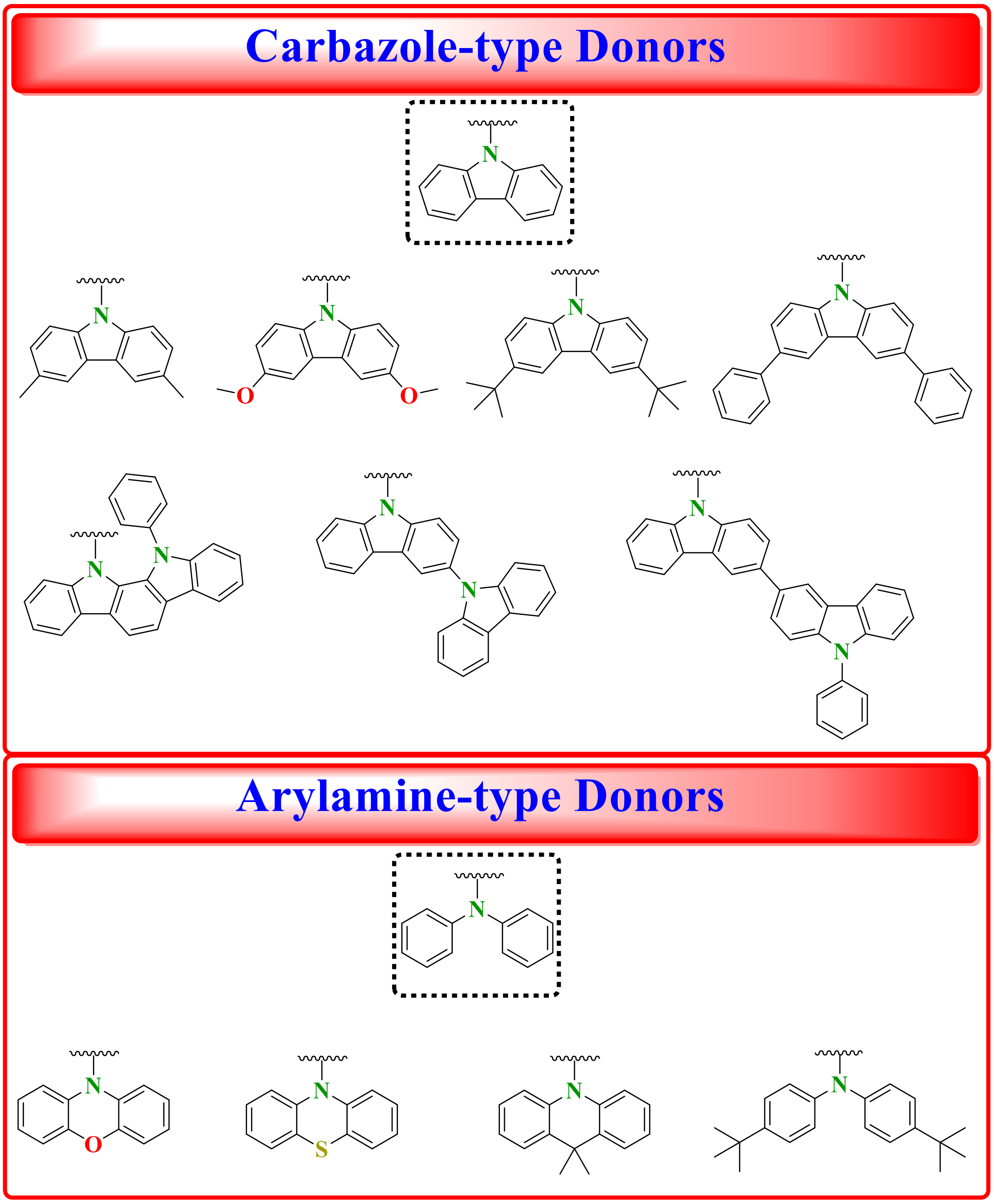

Figure 1.5: Schematic structures of different donor moieties.

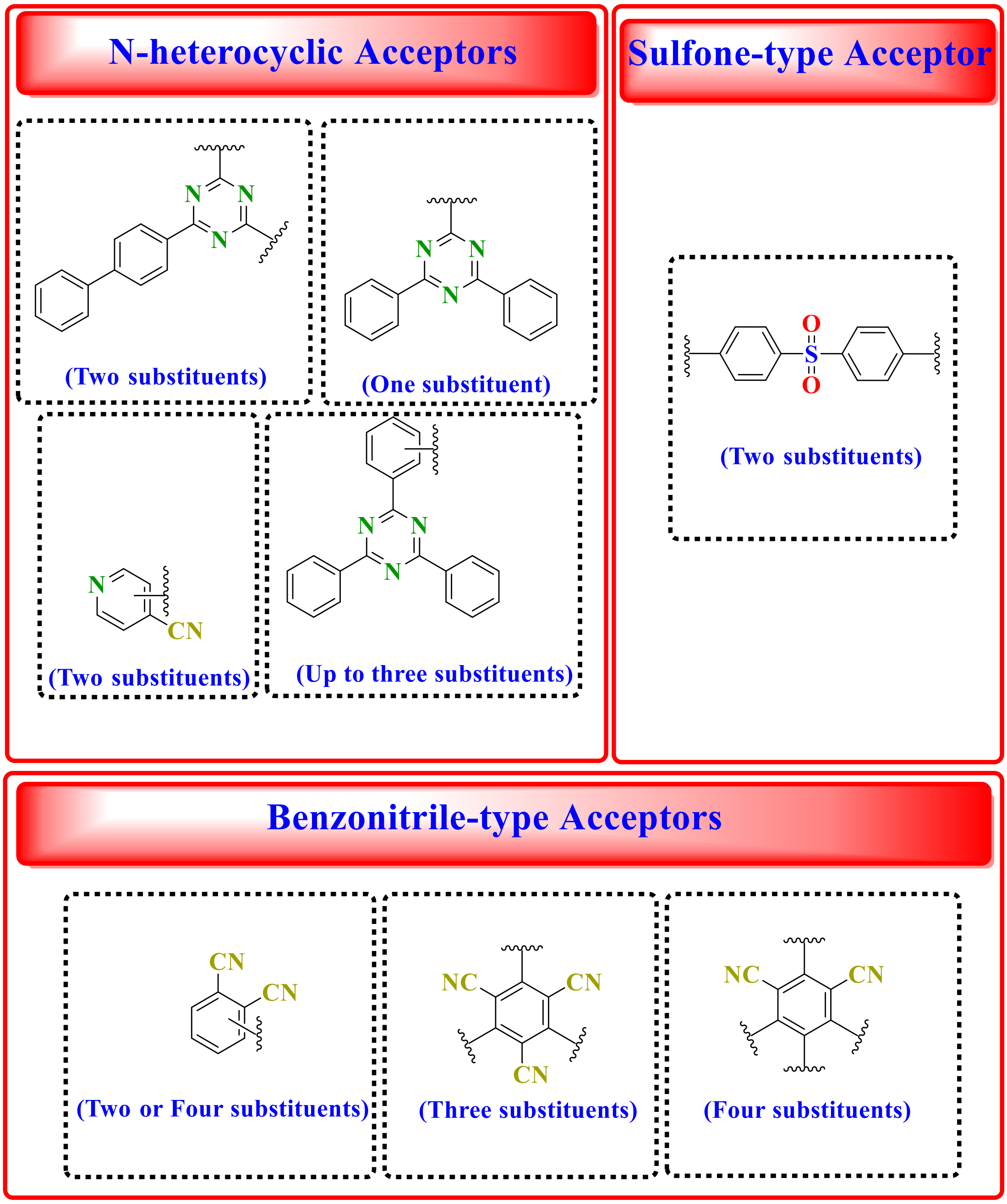

Figure 1.6: Schematic structures of different acceptor moieties.

1.2.2.2 Molecular Design for Short Delayed Fluorescence Lifetime

In the TADF emitters' light emission phase, fluorescence and delayed fluorescence arise over a period of nanosecond and microsecond ranges, respectively. According to reports, the non-radiative loss mechanism does not result from the fast-decaying fluorescence. However, the slow-decaying delayed fluorescence entails a level of efficiency that decreases non-radiation processes like triplet-triplet annihilation (TTA), since electrons will remain in the T_1 level in microsecond ranges for a prolonged period on microsecond scales. Consequently, TADF emitters require a design that minimises the τ parameter for delayed fluorescence, which is caused by slow transition originating from $T_1 \rightarrow S_1 \rightarrow S_0$ in the microsecond range. Once the molecular design method reduces the delayed fluorescence lifetime, ΔE_{ST} is lowered due to the increased rate of reverse intersystem crossing (k_{RISC}) that regulates the lifetime with lowering ΔE_{ST}. Dealing with the ΔE_{ST} of TADF emitters requires the employment of two principal strategies: raising donor-acceptor strength and distorting a linker between the donor and acceptor. Both approaches showed their effectiveness when dealing with minimised lifetime for delayed fluorescence and lower ΔE_{ST}.[23]

1.2.2.2.1 Donor and Acceptor Strengths

1.2.2.2.1.1 Management of Donor and Acceptor Units

One effective strategy in designing TADF emitters for lower ΔE_{ST} involves the utilisation of strong donor and acceptor moieties as they strengthen the CT character of the materials, thereby stabilising the singlet energy. The prominent donors used as strong donor moieties are acridan, phenothiazine, phenazine and phenoxazine, whereas the most popular acceptor moieties utilised as strong acceptors are CN substituted heteroaromatics, heptazine and CN. The findings indicated that in the TADF materials utilising the strong donors and acceptors, a short lifetime was evident for the delayed fluorescence to last less than five microseconds. Various TADF emitters, which exploited acridan as a strong donor, can achieve a short lifetime reaching to a few microseconds due to a strong donor strength of acridan. In addition, 10,10′-(sulfonylbis(4,1-phenylene))bis(9,9-dimethyl-9,10-dihydroacridine) (**DMAC-DPS**), which is popular as a blue TADF emitter, has a minimised lifetime of 3.1 microseconds.[25] Despite the weak electron-accepting diphenyl sulfone utilised as an acceptor of **DMAC-DPS**, the existence of acridan, which is considered as the strong electron donor character, serves to effectively minimise the lifetime. There are several related compounds, including 2,7-bis (9, 9-dimethylacridin-10 (9H)- yl)-9,9- dimethyl-9H-thioxanthene 10,10 -dioxide (**DMTDAc**) and 10-(4-((4-(9H-carbazol-9-yl)phenyl)-sulfonyl)phenyl)-9,9-dimethyl-9,10-dihydroacridine (**CzAcSF**), which have a short lifetime of 1.2 microseconds and 5.6 microseconds, respectively.[26–28] Acridan is one of the most commonly recognised donor units with a short lifetime, but it is not a stronger electron donor than a set of donor units including phenoxazine, phenazine and phenothiazine. The order of donor strengths was determined to be phenazine > phenothiazine >> phenoxazine >> acridan because of the electron-donating abilities of nitrogen, sulphur, oxygen and carbon in the donor units. The findings show that as the donor strength rose, the singlet energy level decreased, which, in turn, lowered ΔE_{ST} and shortened the lifetime. Moreover, the use of strong acceptors have the same effect on TADF emitters in terms of reducing ΔE_{ST} and lifetime. It was proven that applying strong acceptors with weak donors leads to minimising ΔE_{ST} and lifetime such as 5, 5-bis(4-(9H-carbazol-9-yl) phenyl)-1, 3-bis- (trifluoromethyl) - 5H - pyrrolo [1′, 2′:3, 4] [1, 3, 2] diazaborolo[1,5-a]pyridin- 6- ium-5-uide (PrFPCz).[23]

1.2.2.2.1.2 Multiple Donor Approach

In TADF emitters, donor and acceptor nature could be handled by the strengths of donor and acceptor as aforementioned. Furthermore, the character of the donor and acceptor could be regulated by the number of donors and acceptors. The addition of donors or acceptors, or the strong donor and acceptor moieties in the molecular design for TADF materials, serves to increase the molecules’ donor and acceptor character. Consequently, multiple donor-based TADF emitters were produced with diverse optimisations in order to decrease both ΔE_{ST} and lifetime in the TADF emitters.[23,29–34]

1.2.2.2.2 A Twist Between Donor and Acceptor Moieties

A powerful CT character reduces the lifetime and ΔE_{ST} and are induced by the backbone distortion between acceptor and donor units in the molecular structure. Linking the donor and acceptor units through the *ortho*-position of a phenyl linker represents one of the most effective molecular design methods for the twisted molecular structure due to the occurrence of steric hindrance between the donor and acceptor moieties, which raises the dihedral angle. Three molecules, 5-(2-(4,6-diphenyl-1,3,5-triazin-2-yl)-phenyl)-5H-benzofuro [3,2-c] carbazole (**oBFCzTrz**), 5-(3-(4,6-diphenyl-1, 3,5-triazin-2-yl)-phenyl)-5H-benzofuro[3,2-c]carbazole (mBFCzTrz), and 5-(4-(4, 6-diphenyl-1, 3,5-triazin-2-yl)-phenyl)-5H-benzofuro [3,2-c] carbazole (pBFCzTrz), were introduced as ideal models in order to show the viability of the *ortho*-linking concept for twisting molecular structure.[35] Comparisons of three materials, namely,

oBFCzTrz, mBFCzTrz and pBFCzTrz, found that **oBFCzTrz** showed its superiority over mBFCzTrz and pBFCzTrz in minimising lifetime and ΔE_{ST}. The ΔE_{ST} value of **oBFCzTrz** was considerably lowered from 0.19 eV of mBFCzTrz to 0.002 eV and 0.30 eV of pBFCzTrz to 0.002 eV. Moreover, the τ value of **oBFCzTrz** significantly shortened from approximately 30 μs of mBFCzTrz and pBFCzTrz to 5.4 μs. Therefore, the enhancement of the efficiency roll-off in the TADF devices was supported by the short τ of **oBFCzTrz**, which resulted in a remarkable decrease of the EQE by approximately 15%. The effect of steric hindrance causing the rise of the CT character was also proved in the TADF emitters as in molecule 1, 3, 6, 8-tetramethyl-9-(10-(2, 4, 6-triisopropylphenyl)-10H-dibenzo [b, e][1 ,4]-oxaborinin-3-yl)-9H-carbazole (**7**) with a 1,3,6,8-tetramethylcarbazole donor.[36] In the (**7**) emitter, the two methyl groups at positions 1 and 8 of carbazole were sterically hindered between a phenyl linker and the carbazole donor. This situation resulted in the donor's vertical alignment to the phenyl linker and an increased CT character. Consequently, very small ΔE_{ST} (0.01 eV) and short τ (3.49 μs) values were recorded in the (**7**) emitter. The majority of TADF emitters which contain phenoxazine, acridan, and phenothiazine-derived donor units have small ΔE_{ST} and τ due to the donor distortion and the perpendicular arrangement of donor moieties to the phenyl linker. **Figure 1.7** presents a summary of molecular design approaches for short τ and emitters in each design method classification.[23]

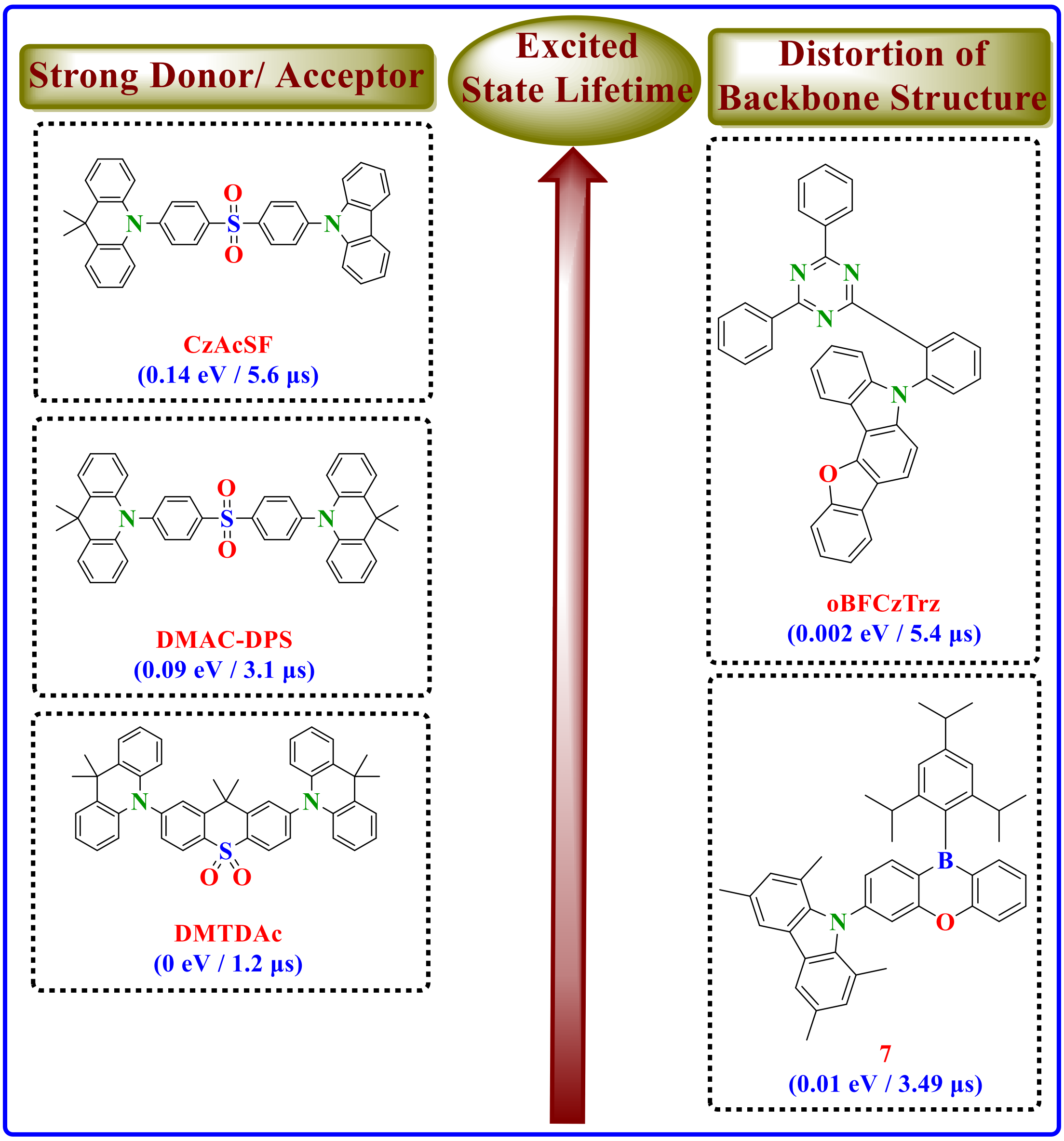

Figure 1.7: Chemical structures of emitters related to short lifetimes for delayed fluorescence.

1.2.2.3 Molecular Design for High PLQY

Various molecular structures have been produced to improve the PLQY of the TADF materials, and numerous materials were confirmed as high PLQY emitters. Despite the variety of these molecular designs, it is possible to divide the TADF emitters with high PLQY into three classes based on the design approach, including phenyl linker design, the HOMO dispersion design and dual emitting core design.[23]

1.2.2.3.1 Phenyl Linker Design

Earlier research documenting the TADF materials tended to focus on the phenyl linker free design when there was no need to reference the phenyl linker concept. Yet, the ground-breaking work of the Adachi group also proposed the usage of a phenyl linker to modify the molecular design for high PLQY via an overlap of the HOMO and LUMO. Furthermore, it was noted in the early TADF emitters, such as 9-(4,6-diphenyl-1,3,5-triazin-2-yl)-9′-phenyl- 9H, 9′H-3,3′-bicarbazole (CzT), 9,9″ -(6-phenyl-1,3,5-triazine-2,4-diyl) bis- ((9H-3,9′-bicarbazole)) (CC2TA), 12,12′-(6-([1,1′-biphenyl]-4-yl)-1,3,5-triazine-2, 4-diyl)bis(11-phenyl-11,12-dihydroindolo[2,3-a]carbazole) (PIC-TRZ) and 12-(4,6- diphenyl-1,3,5-triazin -2-yl)-5-phenyl -5,12- dihydroindolo [3,2-a] carbazole (PIC-TRZ2), that the PLQY of these emitters amounted to lower than 70% due to the large separation of the HOMO and LUMO, which caused a hindrance to light absorption and emission processes.[37–41] Thus, research has suggested high PLQY could be acquired through utilising the phenyl linker design and controlling the separation between the HOMO and LUMO. According to the fundamental concept of the phenyl linker design, the separation between the HOMO and LUMO is reduced by the phenyl linker due to the HOMO and LUMO extension to the aromatic phenyl linker. Noteworthily, the extension of the HOMO and LUMO to the phenyl linker in the TADF emitter plays an integral role in achieving large oscillator strength. This development enhances the light absorption of the emitter and ultimately causes a higher PLQY. The use of the first phenyl linker-based TADF emitter, known as 2,4,5,6-tetra(9H-carbazol-9-yl) isophthalonitrile (**4CzIPN**), proved significantly beneficial in increasing the PLQY to over 90% in both solution and film. Concerning **4CzIPN**, two electron-accepting CN moieties and four electron-donating carbazole moieties were connected to the phenyl linker. This attachment in the **4CzIPN** structure plays a significant role in increasing the PLQY to above 90% and prompting the EQE to rise to over 20%. These characteristic results in the increase of the PLQY and EQE were generated by the overlap between the HOMO and LUMO at the phenyl linker by means of the molecular orbital calculation.[42–45] Consequently, numerous TADF materials were designed by joining donor and acceptor units to the phenyl linker due to the proof that the phenyl linker design concept improves PLQY. These designs applying the phenyl linker in TADF emitters have successfully demonstrated the superior performance of the phenyl linker design in TADF emitters concerning the rising PLQY. Research shows that 4, 4′, 4″-(1, 3, 3a-1, 4, 6,7, 9-heptaazaphenalene-2, 5, 8-triyl) tris(N, N-bis(4-(tert-butyl)-phenyl) aniline) (HAP-3TPA) is one of the most significant operating red TADF emitters because of the efficient attachment of heptazine as an acceptor and t-butyl adjusted aromatic amine acting as a strong donor with the phenyl linker. This development results in PLQY hitting a high level of 95% and the EQE reaching 17.5%.[46] Moreover, the fact that PLQY exceeds 90% and has a high EQE value that reaches 26.5% signifies DMAC-Trz as one of the most efficient performing green TADF materials.[47] The TADF emitter of DMAC-Trz was successfully formed by connecting 9,9-dimethyl-9,10-dihydroacridine (DMAC) as a strong donor with 2,4,6-triphenyl-1,3,5-triazine (TRZ) as an acceptor to the phenyl linker at the *para* position. A similar design approach was applied on blue TADF emitters, such as spiroacridan-triazine hybrid, spiroAc-Trz[48] and 9,9′,9″-(5-(4,6-diphenyl-1,3,5-triazin-2-yl)-benzene-1,2,3-triyl)tris(9H-carbazole) (**TCzTrz**) compounds, by the phenyl linker concept, which is based on attaching donors and acceptors to the phenyl linker design.[23,49–52] **Figure 1.8** summarises the molecular design strategies based on high PLQY and the representative emitters in respect to phenyl linker design.

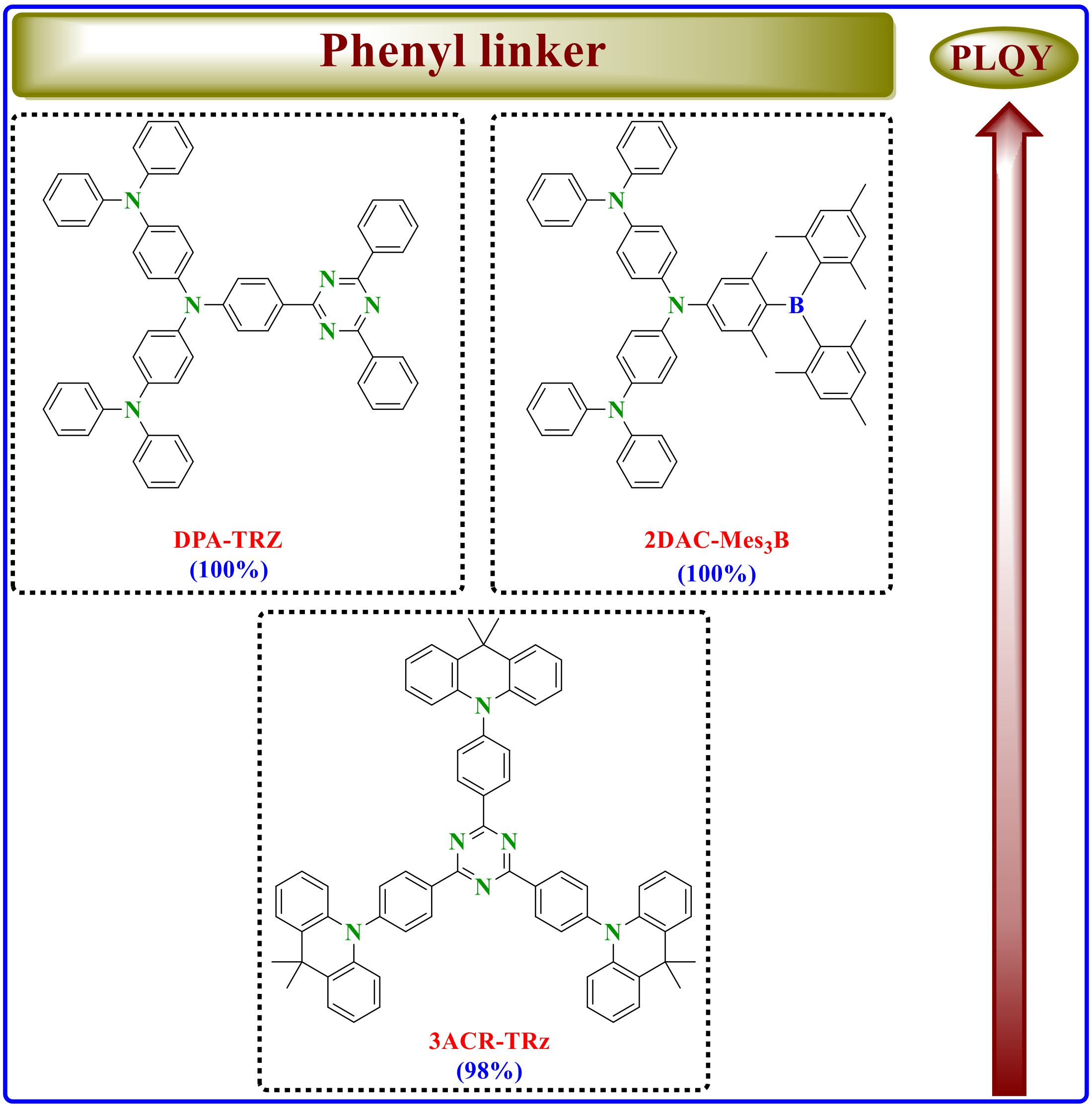

Figure 1.8: Chemical structures of TADF emitters for high PLQY in respect to phenyl linker design.

1.2.2.3.2 The HOMO Dispersion Design

Introducing the HOMO-dispersing molecular design in order to facilitate high PLQY performance levels in the TADF emitters proved to be successful and saw this design being used with the phenyl linker concept in the molecular structure. The purpose of the HOMO-dispersing molecular design concept is that a significant overlap of the HOMO and LUMO in the backbone structure between donors and acceptors is generated by the uniform distribution of the HOMO. Consequently, increasing the overlap of the HOMO and LUMO enhances the TADF emitters' oscillator strength and

PLQY. The HOMO dispersion approach was successfully incorporated in the design of **4CzIPN** utilising four HOMO-handling carbazole donor units.[5] In comparison of 4,6-di(9H-carbazol-9-yl)isophthalonitrile (DCzIPN), which has two carbazole moieties, **4CzIPN** obtained a much higher PLQY of 94% due to the HOMO-dispersing performance of the four carbazole donor moieties.[53] The PLQY increase initially prompted the EQE to exceed 20% in the TADF device, and the additional TADF device operation enhanced the EQE to more than 30%. Based on the same concept, 9, 9′, 9″-(5- (4, 6- diphenyl-1, 3, 5- triazin-2-yl) - benzene -1, 2, 3-triyl) tris (3, 6-dimethyl-9Hcarbazole) (**TmCzTrz**) and (**TCzTrz**), which contain three carbazoles as donor moieties, were confirmed as high PLQY emitters progressed from 9,9′-(5-(4,6-diphenyl-1,3,5-triazin-2-yl)-1,3-phenylene)bis(9H-carbazole)(DCzTrz), which has two carbazole donor units. Comparing both emitters with DCzTrz indicated that 100% PLQY of both emitters was achieved whereas 43% of DCzTrz was produced due to the number of additional carbazole units. This situation indicates that the additional carbazole moiety increases PLQY by means of the HOMO delocalisation. Noteworthily, **TCzTrz** was recorded as one of the highest EQE of blue TADF device reaching to 25% with the elevated PLQY. Additionally, five donor moieties, which were based on carbazoles such as 3-(3-(tert- butyl)-9H- carbazole -9-yl)-2, 4, 5, 6- tetra (9H- carbazol -9- yl) benzonitrile (**5CzBN**(**5CzCN**)), proved that the five donor units' ability to improve PLQY occurs as a result of uniform HOMO distribution.[54] **5CzBN**(**5CzCN**) emitter offered an excellent EQE value of 16.7%. Besides delocalising the HOMO by multi-donors, wide HOMO dispersion provided another method of achieving high PLQY. Such a development is attributed to a bulky donor structure in the TADF emitters. More importantly, 9′-(4-(4,6-diphenyl-1,3,5- triazin-2-yl)- phenyl)-3, 3″,6 ,6″- tetraphenyl- 9′H-9, 3′:6′,9″- terbenzo [b] indole (**2a**) compound acted as the TADF emitter which contained the HOMO dispersion of donor moieties in place of carbazoles.[30] Two 3,6-diphenylcarbazole substituted carbazole were utilised as donor moieties in the TADF emitter of **2a**. Research has found that PLQY of the **2a** molecule delivered 100%. Consequently, the EQE of the **2a** emitter reached 20.6%, correspond with the increase of both PLQY and the HOMO-dispersing ability. Furthermore, in 9-(4-(4, 6- diphenyl-1,3, 5-triazin-2-yl)- phenyl)-N^3,N^3,N^6,N^6-tetraphenyl-9H-carbazole-3,6-diamine (**DACT-II**) derived from the diphenyltriazine acceptor that the HOMO of two diphenylamine-substituted carbazoles at positions 3 and 6 distributed over the large donor unit, which contributed to high PLQY levels of 100% as well as EQE of 29%.[23,55–58] **Figure 1.9** summarises the molecular design strategies based on high PLQY and the representative emitters in respect to HOMO dispersion design.

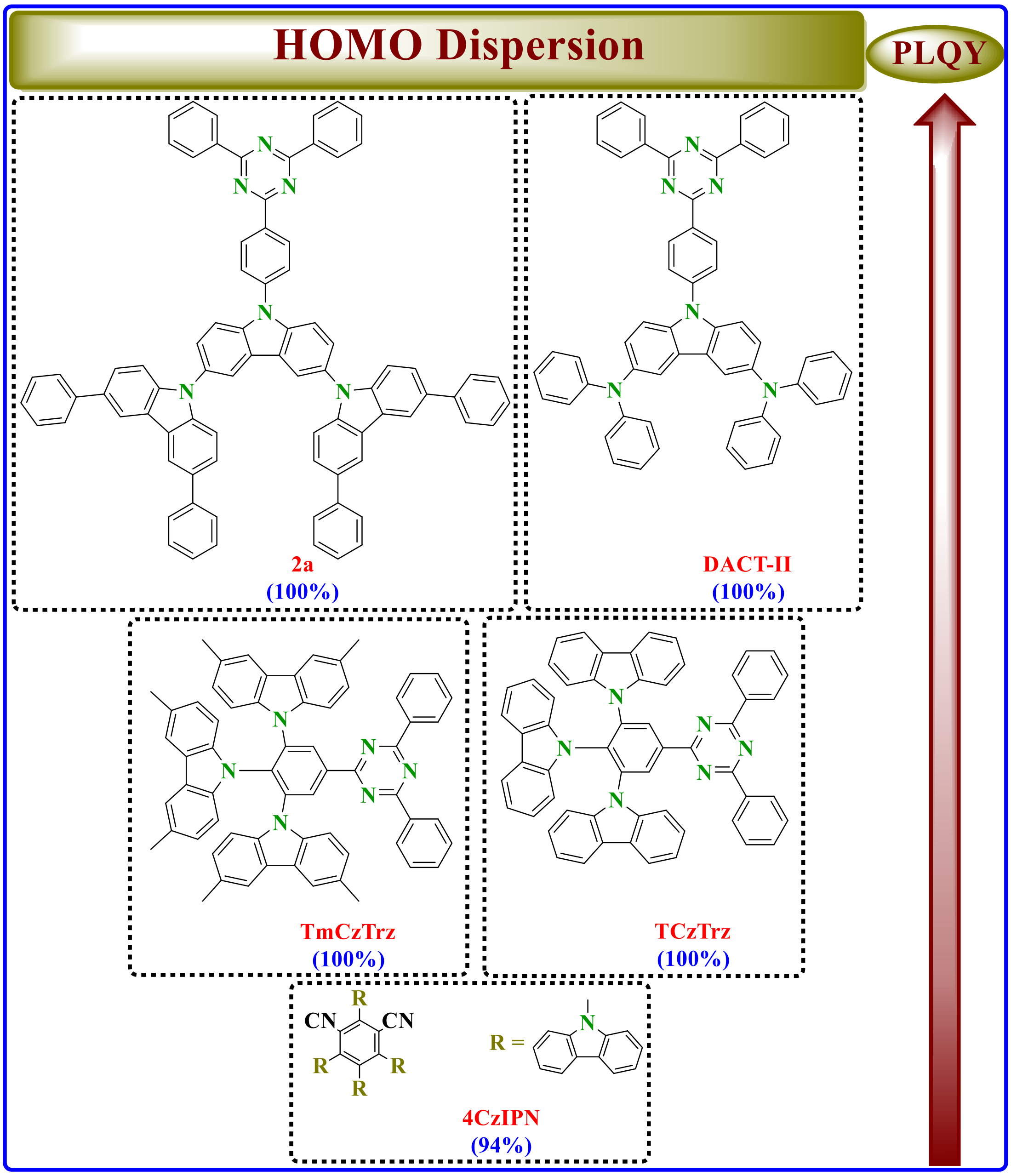

Figure 1.9: Chemical structures of TADF emitters for high PLQY in respect to HOMO dispersion design.

1.2.2.3.3 Dual Emitting Core Design

Recent developments have seen the introduction of an additional molecular design to create high PLQY, which is called dual emitting core design. This design comprises two joint TADF emitter moieties in one molecular structure. The fundamental idea of the dual emitting core design holds that coupling two emitter moieties together would significantly contribute to improved light absorption and emission of the TADF emitters compared with the single emitting core design. Moreover, 3,3′,5,5′-tetra(9H-carbazol-9-yl)-[1,1′-biphenyl]-2,2′,6,6′-tetracarbonitrile (**DDCzIPN**), successfully produced by the direct coupling reaction of two DCzIPN emitters, represented the first unique TADF emitter design using the dual emitting core approach.[59] Comparing DCzIPN and **DDCzIPN** indicated that the absorption coefficient of **DDCzIPN** was raised. Consequently, **DDCzIPN**'s PLQY and EQE increased from 67% to 91.3% and from 16.4% to 18.9%, respectively. Besides, a shift in the emission spectrum to the long wavelength of the dual emitting core TADF emitters, such as **DDCzIPN**, was observed. Such a shift occurred because of the increased extent of conjugation, which originated by direct phenyl-phenyl coupling. A possible approach could involve coupling two TADF emitter units by a donor moiety in the molecular structure in order to manage the colour shift issue of the dual emitting core design. Consequently, the emission spectrum of the dual emitting core TADF emitters could be effectively administered. The findings from studies involving two sets of molecules, based on diphenyltriazine and dicyanobenzene acceptor moieties, have shown this concept's validity in efficiently managing the emission spectrum regarding the dual emitting core emitters. In the case of dicyanobenzene compounds, which included various interlinked positions of carbazole moieties, such as 6,6′-(9H,9′H-[3,3′-bicarbazole]-9,9′-diyl)-bis(4-(9H-carbazol-9-yl)isophthalonitrile) (**33TCzPN**), 6,6′-(9H, 9′H- [3, 4′- bicarbazole]-9, 9′-diyl)- bis(4-(9H -carbazol- 9-yl) isophthalonitrile) (34TCzPN) and 6, 6′ -(9H, 9′H-[4, 4′- bicarbazole]-9, 9′-diyl)- bis(4-(9H-carbazol-9-yl) isophthalonitrile) (44TCzPN), different emission spectra were disparately displayed relying upon the interlinked position.[60] More specifically, the **33TCzPN** compound, which contains two carbazole moieties joined through the 3-position of each carbazole, showed a red-shifted emission spectrum. Therefore, such a development can be attributed to the small dihedral angle of **33TCzPN** between two carbazole moieties. A particularly noteworthy development saw significant increases in the dual emitting core TADF emitters' PLQY because of improved light absorption that brought about the elevated EQE in the TADF devices. **Figure 1.10** summarises the molecular design strategies based on high PLQY and the representative emitters in respect to dual emitting core design.[23]

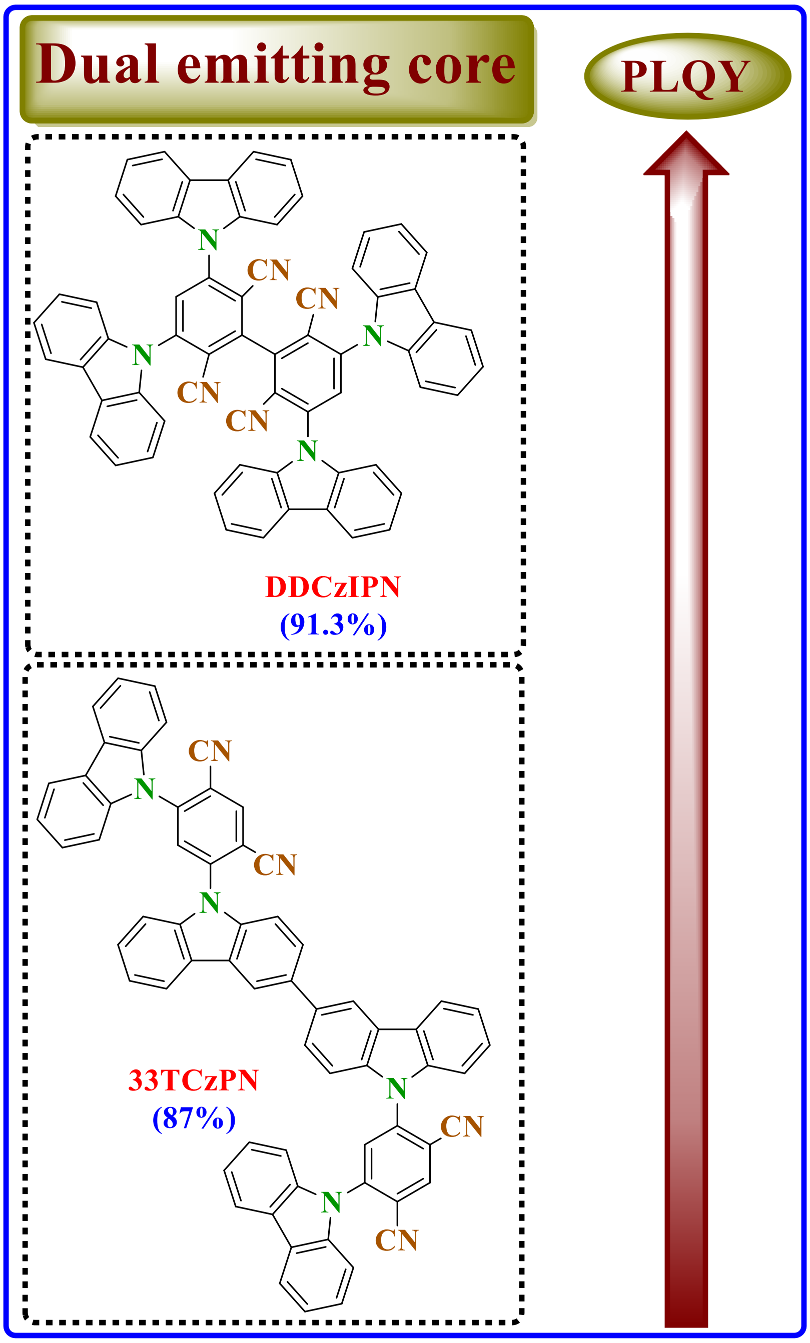

Figure 1.10: Chemical structures of TADF emitters for high PLQY in respect to dual emitting core design.

1.2.2.4 Molecular Design for Narrow Emission

Fluorescent emission for TADF emitters originates from the intramolecular CT singlet-excited state, while fluorescent emission for traditional fluorescent emitters arises from the local singlet-excited state. Therefore, the origin of fluorescent emission distinguishes TADF emitters from conventional fluorescent emitters. Generating the CT-excited state can take place in several forms with distinct energies, and, therefore, the CT-based TADF emitters could contain various CT-excited states. Consequently, the CT-based TADF emitters exhibit extremely broad emission spectra, which arises from the CT singlet-excited state. Although the character of the broad emission spectra is applicable in lighting devices, it should be averted in display devices that demand high purity of colour. Nowadays, OLEDs are being exploited in manufacturing display productions instead of lighting applications, demonstrating that TADF emitters have an improved narrow emission spectrum requirement.[23]

Molecular design strategies for narrow emission spectra can be categorised in two ways according to their chemical structure. One approach involves maintaining the donor-acceptor-based core structure without any change by means of the structure containing steric hindrance or the fused structure. The second approach is to opt a structure in possession of a rigid acceptor in order to decrease the TADF emitters' vibrational movement. Consequently, the first method is preferable to the second one since the overall molecular structure can be modified in the first method, whilst local rigidity of the molecular structure in the second method creates difficulties adjusting the molecule. Representative TADF emitters with a narrow emission spectrum are summarised in **Figure 1.11**.[23,61–68]

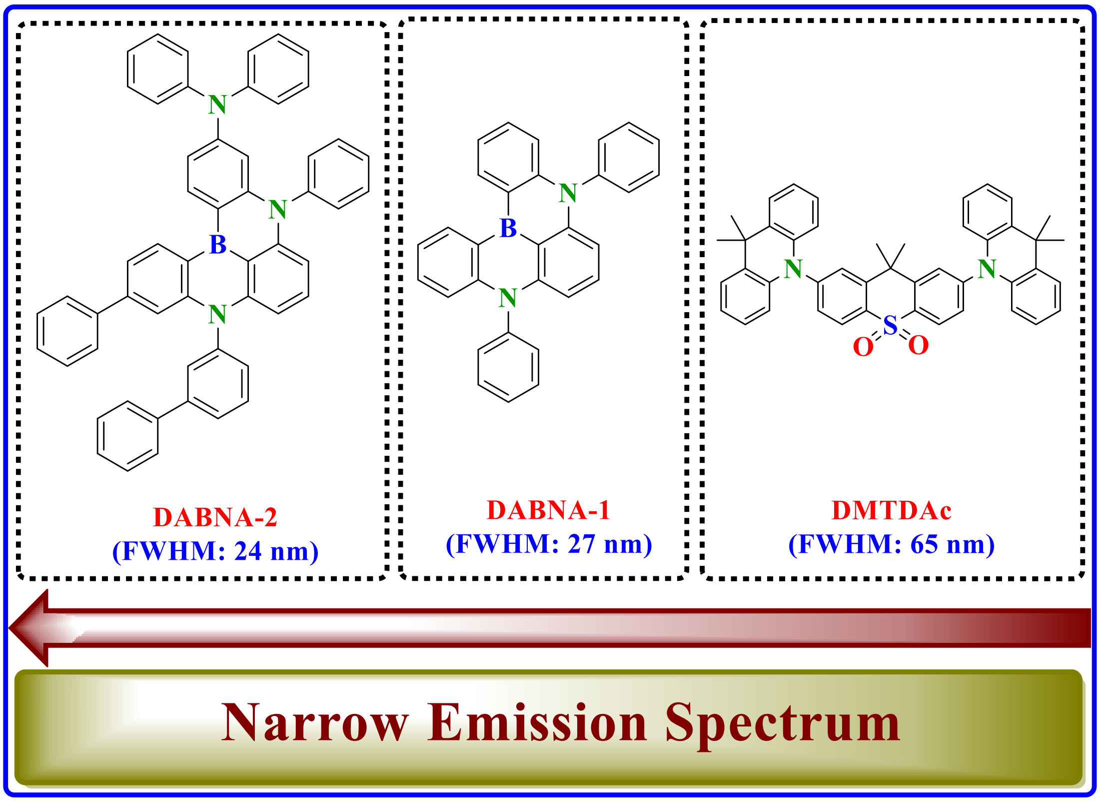

Figure 1.11: Chemical structures of TADF emitters in respect to narrow emission spectrum.

1.2.2.5 Molecular Design for Stability

Short lifetime OLED devices are not exploitable in practical approaches. Thus, lifetime plays an integral role in the performance of OLED devices. Consequently, the design of TADF materials should ensure that they have the capacity to withstand and resist degradation through operating OLED devices. Although several investigations have documented the lifetime of TADF devices, a few research reports have focused on the molecular design standards of TADF emitters with long lifetimes.[23]

In terms of chemical structure regarding operational stability, only stable units are permitted in the design of TADF emitters: this is the chemical structure perspective. Operating the OLED device means the TADF emitters acquire positive polarons, negative polarons and excitons, which also indicates the necessity of having stable molecules during charged conditions. More specifically, bond dissociation energy (BDE) can determine the stability of the molecules under positive polarons or negative polarons. In the donor units, donors containing acridan-derived or aromatic amine have relatively small BDE values at negative polarons, whilst donors containing carbazole-derived chemical moieties possess comparatively large BDE values. In the acceptor moieties, acceptors containing diphenylphosphine oxide or diphenylsulfone type have relatively low BDE values, while acceptors containing benzonitrile or diphenyltriazine type possess high BDE. To meet the above considerations, the TADF emitter design for long-term stability was aimed at preparing stable emitters, including donor and acceptor units with high BDE, such as carbazole-derived chemical moieties, diphenyltriazine, benzonitrile and triazine-derived chemical moieties. Examples of stable materials are summarised in **Figure 1.12**. [23,69–72]

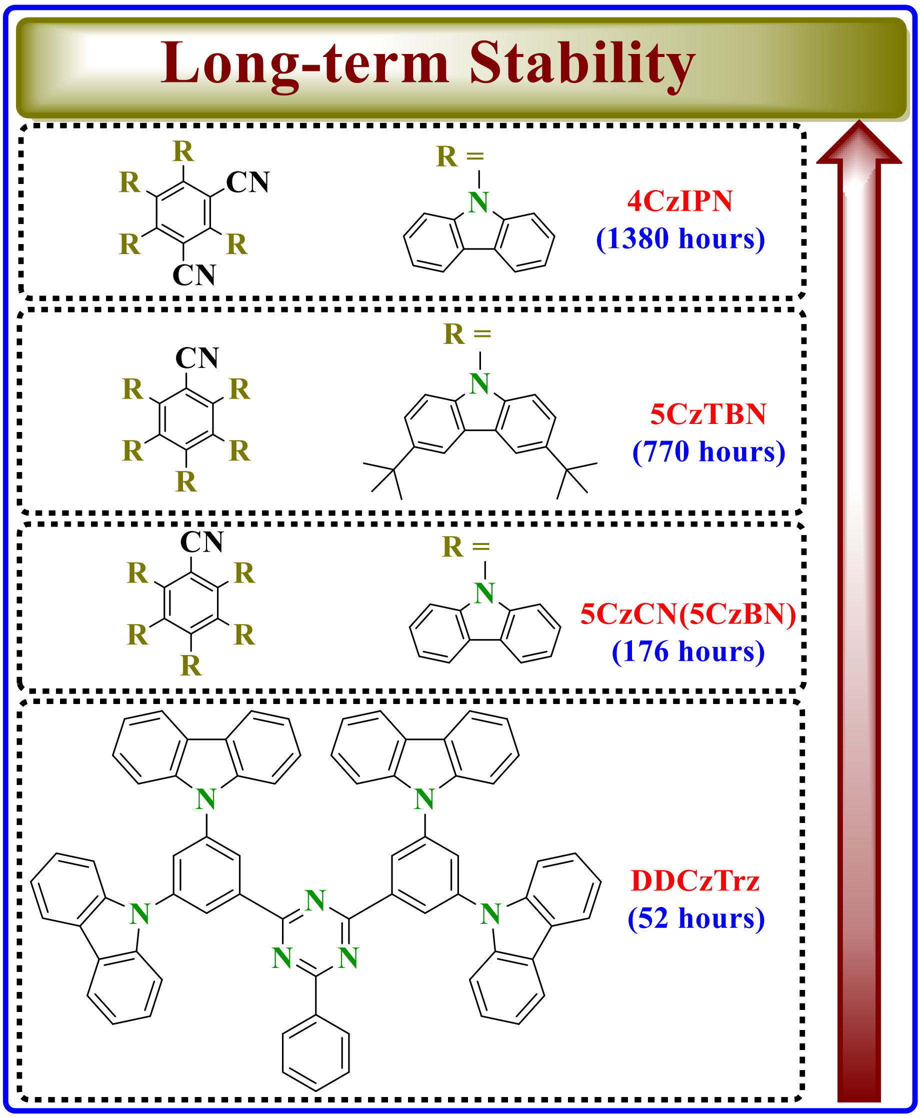

Figure 1.12: Chemical structures of TADF emitters in respect to the stability.

1.2.3 Molecular Design Strategy for Solution-Processing TADF Emitters

1.2.3.1 TADF Small Molecules

Small TADF molecules represent the most widely researched and produced materials for *vacuum*-processed OLEDs. In light of the above reasoning, manufacturing solution-processed EL devices utilising soluble TADF small molecules as emitters is a perfectly obvious and acceptable endeavour. Furthermore, like the TADF character, which is fundamental for triplet harvesting to achieve 100% internal quantum efficiency (IQE), many other aspects require consideration when developing solution-processing TADF small molecules. In the first place, the material should contain adequate solution processability in a common organic solvent to allow manufacturing through a solution process. The second crucial aspect involves ensuring the devices' capacity to employ a solution-processed film that shows sufficient morphology and stability at different temperatures and when connected to an electric current. Thirdly, in order to ensure the high efficiency of the device, the small molecules should possess high PLQYs in thin film. Furthermore, it is strongly recommended that the TADF materials have a balanced charge injection and transport capability to simplify device configuration. To date, only a few groups of effective solution-processing TADF small molecules have fulfilled these criteria.[73]

1.2.3.2 TADF Polymers

The majority of TADF materials tend to be small organic molecules because of simplicity of the formation. However, the solution processable small TADF molecules can incur significant expenses, and small TADF molecules cannot be applied for large-scale device manufacture. In comparison of small molecules, polymers exhibit tremendous promise in low-cost processing and are employed in large-scale industrial applications. Considering the above reasoning, polymers are more convenient than small molecules in solution processing.[74,75] The current primary design strategy constructs TADF polymers using an indirect approach that employs small molecules with identified TADF-active properties in the various positions of the polymer structure via the central TADF core, pendant TADF groups or main chain components. Self-emission TADF polymers constitute another type of polymer that exists in addition to these. In such cases, small molecules that lack TADF properties minimise ΔE_{ST} after polymerisation on account of the growth of the conjugated structure. Such a development proves to be sufficient in decreasing ΔE_{ST} so that heat can overcome it. Consequently, the polymer offers noteworthy TADF properties.[76] Accordingly, TADF polymers are categorised into the five types based on where TADF active moieties are situated in the polymer structure, as outlined in **Figure 1.13**.[77]

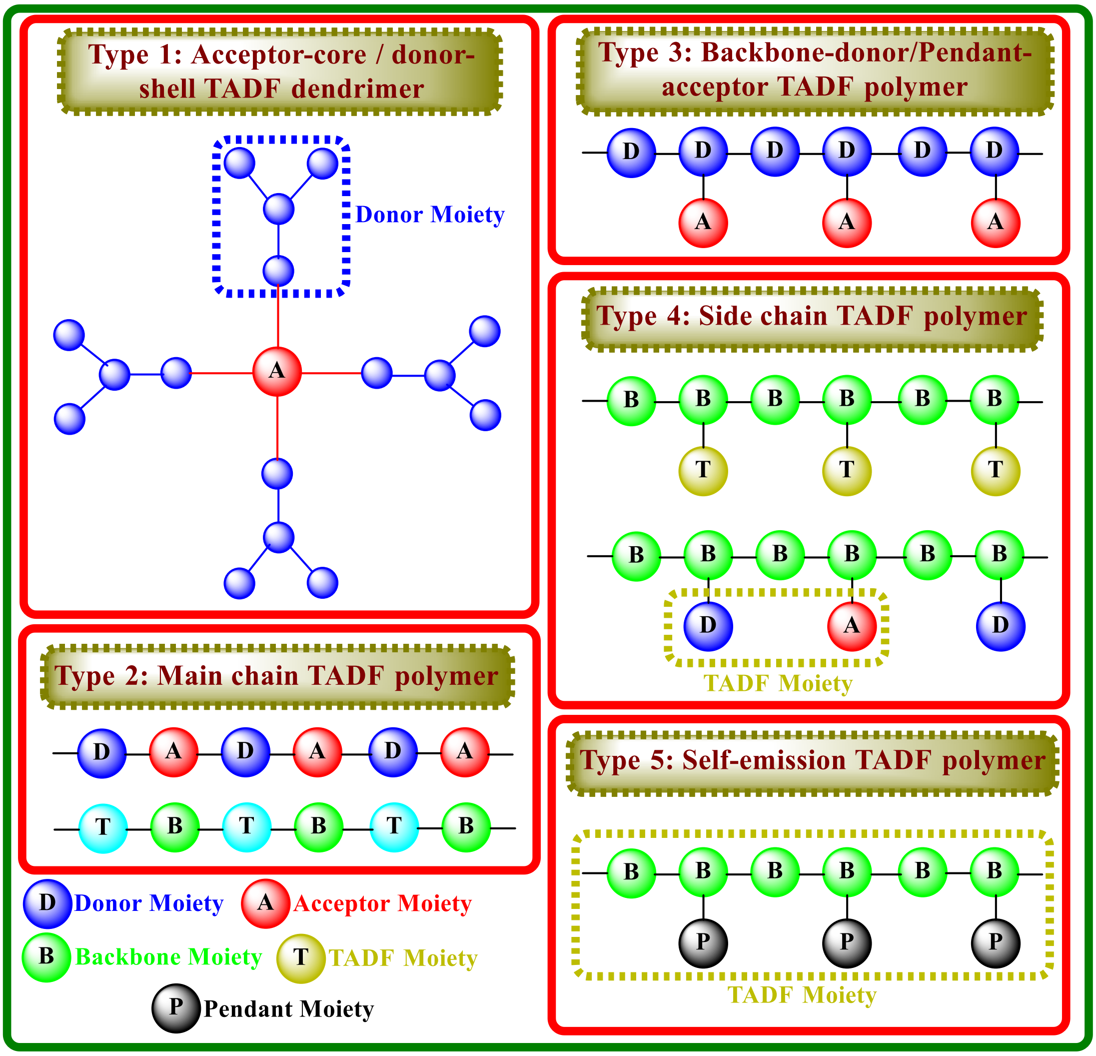

Figure 1.13: TADF polymer design strategy.

1.2.3.2.1 Side Chain Type TADF Polymers

Formulating a considerable conjugated structure involves a straightforward process in the main chain type TADF polymer, whereas the high steric hindrance effect creates complications synthesising this type of polymer. Moreover, due to the poor solubility and meltability of the main chain type TADF polymer, such polymers include fewer benefits during the processing and preparing the device.

A conventional side chain type TADF polymer comprises two components: a series of side chains with applicable properties, such as TADF, efficient charge injection, and charge transport characteristics, and a backbone that acts as a host and a charge transporting channel. Compared to the main chain type TADF polymer, the side chain type TADF polymer has an active TADF unit, meaning it is incorporated by chemical linking in the conjugated or non-conjugated backbone structure of polymers as a pendant group, as depicted in **Figure 1.14**. Furthermore, the side chain type TADF polymers use non-conjugated aliphatic chains to connect the backbone with side chains. Such an approach ensures that the presence of side chains does not impact the electronic properties of the polymer backbone. Moreover, this type of TADF polymer provides a simple and efficient strategy for attaining the blue emission because of the low conjugation on the polymer backbone.[77–84]

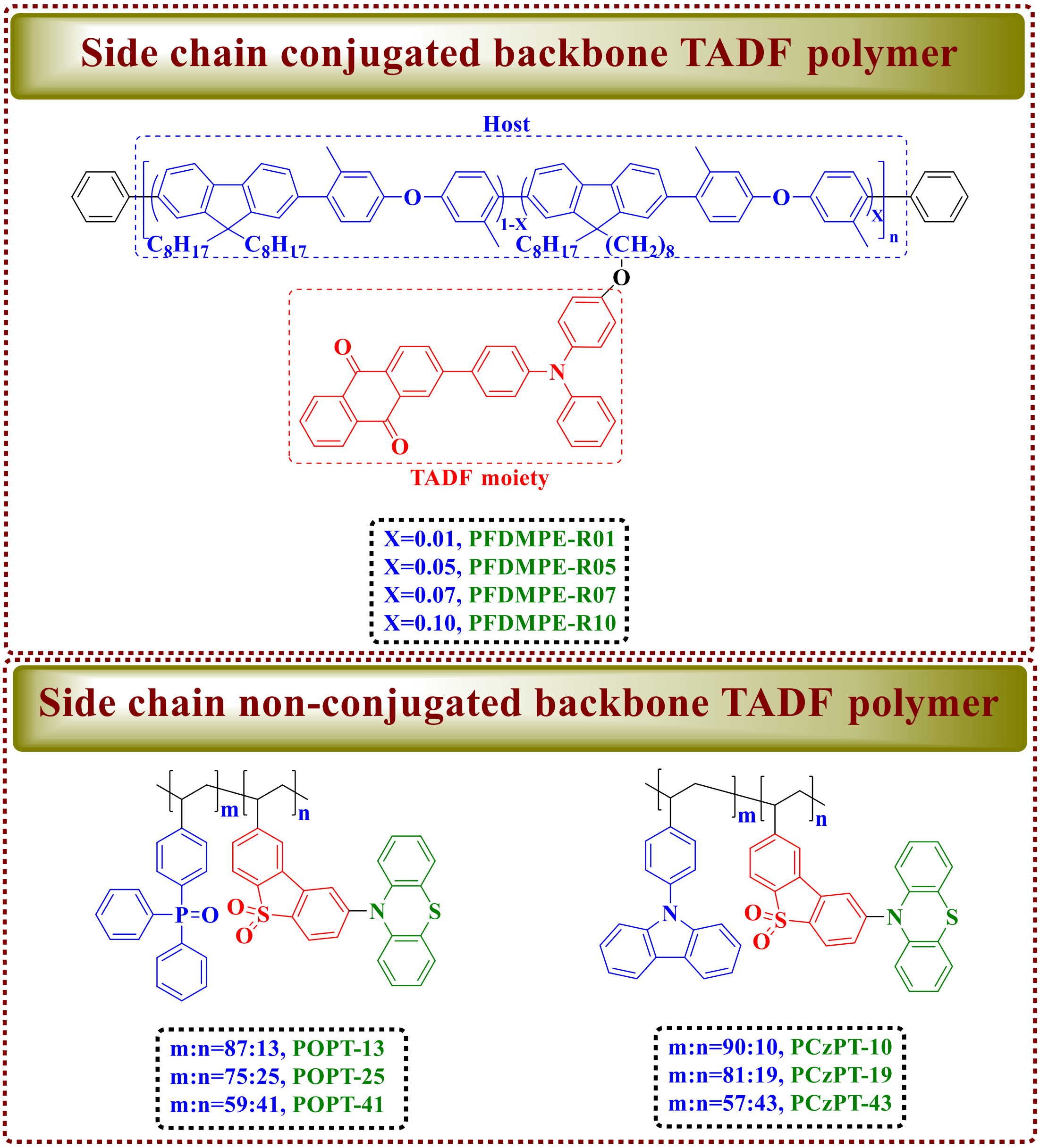

Figure 1.14: Two types of side chain TADF polymers.

1.2.4 Solution-Processed TADF OLEDs

Solution-processable OLEDs have garnered considerable interest for large-sized OLED displays due to their ease of manufacture, simple scaling and lower equipment costs. However, reliability concerns, reproducibility and lower EQEs mean these OLEDs have also encountered significantly slower commercialisation. Consequently, the performances of solution-processing OLED devices remain lower than the *vacuum* deposition of OLEDs. Therefore, additional development of solution-processable OLEDs is required.[85,86]

A small number of solution-processable TADF-based OLEDs have been generated and display promising device performances for polymers, dendrimers and small molecules, which make solution-processable TADF-based OLEDs attractive for research. Furthermore, it is strongly recommended that the TADF materials have balanced charge injection and transport capability to simplify device configuration. More specifically, the blue TADF emitter 4CzFCN showed that the highest EQE reached 20%, whilst the dithienylbenzothiadiazole-based red TADF emitter red-1b displayed lower EQE in a solution-processable OLED device to reach 1.75%. Such an event occurred due to the presence of fluorine atoms in the 4CzFCN molecular configuration, resulting in the high EQE. On the other hand, polymers and dendrimers displayed relatively elevated EQEs to reach 10% and 3.4%, respectively.[85,87,88]

1.3 Requirements for Host Materials

Research indicates that TADF emitters function unsatisfactorily in neat emitter films due to a variety of reasons, such as aggregation, concentration quenching and so forth. Consequently, the emitters require dilution with host materials at lower emitter concentrations of between 10% and 30% to enhance their photophysical properties. Furthermore, this dilution of the emitter molecules improves the efficiency of the devices.[89] It is essential for TADF host materials to possess an adequately high triplet state energy. More specifically, an undesired Dexter energy transfer process between T_1 states from the TADF emitter to the host material must be avoided, which indicates a significant loss mechanism in TADF-based OLED devices. Thus, the T_1 energy levels in the host materials should be perfectly higher than the T_1 energy states in the TADF emitter.[90]

It is also necessary to properly adjust the differences in the HOMO and LUMO energy levels between the host and emitter materials in the design. Significant differences in energy levels between the host and emitter can have undesired results, such as exciplex formation or charge trapping on the emitter. The energy levels of the molecules require precise adjustment in order to achieve charge carrier transfer between the two species and/or attain the required energy levels, which aids in enhancing light-emitting performance.[90]

Along with the previously mentioned vital features, TADF hosts should possess the additional characteristics listed below:[91–93]

Thermal and morphological stability: determined by the high glass transition temperature (T_g) for suppressing crystallisation and stabilising the film morphology.

High material stability: using the BDEs of single bonds in a molecule measured under three distinct conditions primarily assesses the stability of the material (cationic, anionic and neutral state).

Low polarity: in order to minimise the effect of local dipole interactions between the emitter and the host, which results in shifting the emission peak towards bathochromic shift (longer wavelengths).

Additionally, the following factors significantly affect the triplet energy T_1:[94–96]

Expanded π-conjugation: the triplet energy significantly reduces with increased π-conjugation (biphenyl lower than benzene). Additionally, the triplet energy is reduced with fused ring systems (naphthalene lower than biphenyl).

Torsion angles and linkage type: extremely twisted molecular structures minimise conjugation, which, in turn, raises the triplet energy; the *meta* position connection in the compound reduces the conjugation and is, therefore, more advantageous for achieving elevated triplet levels than *para*-linkage.

Aggregation: bulky substituents notably weaken the intermolecular reactions of π-conjugated host molecules, which, in turn, decrease the red-shift of phosphorescence spectra and increase the triplet level. Since the strength of interactions affects the triplet level, the T_1 value obtained from the solution could prove to be greater than that obtained from neat films.[97]

Blue TADF emitters require stable hosts with triplet energies that exceed 3.0 eV in order to ensure efficient confinement of the excitons. These stable hosts remain extremely scarce. Due to their highly effective triplet energies of 2.8-3.0 eV, the most versatile molecular building blocks, such as carbazole, benzofuran or thiophene, are frequently employed as host and emitter molecules for deep blue applications.

Owing to its high triplet energy of 3.00 eV, which makes it a particularly attractive host, bis[2-(diphenylphosphino)phenyl]ether oxide (**DPEPO**) represents one of the most popular choices as a host material for blue TADF.[98] Unfortunately, owing to the poor stability of **DPEPO**, **DPEPO**-based OLED devices typically experience severe efficiency roll-off.[99] **Figure 1.15** presents additional examples of common hosts sorted according to their potential charge transport properties:[90,100,101]

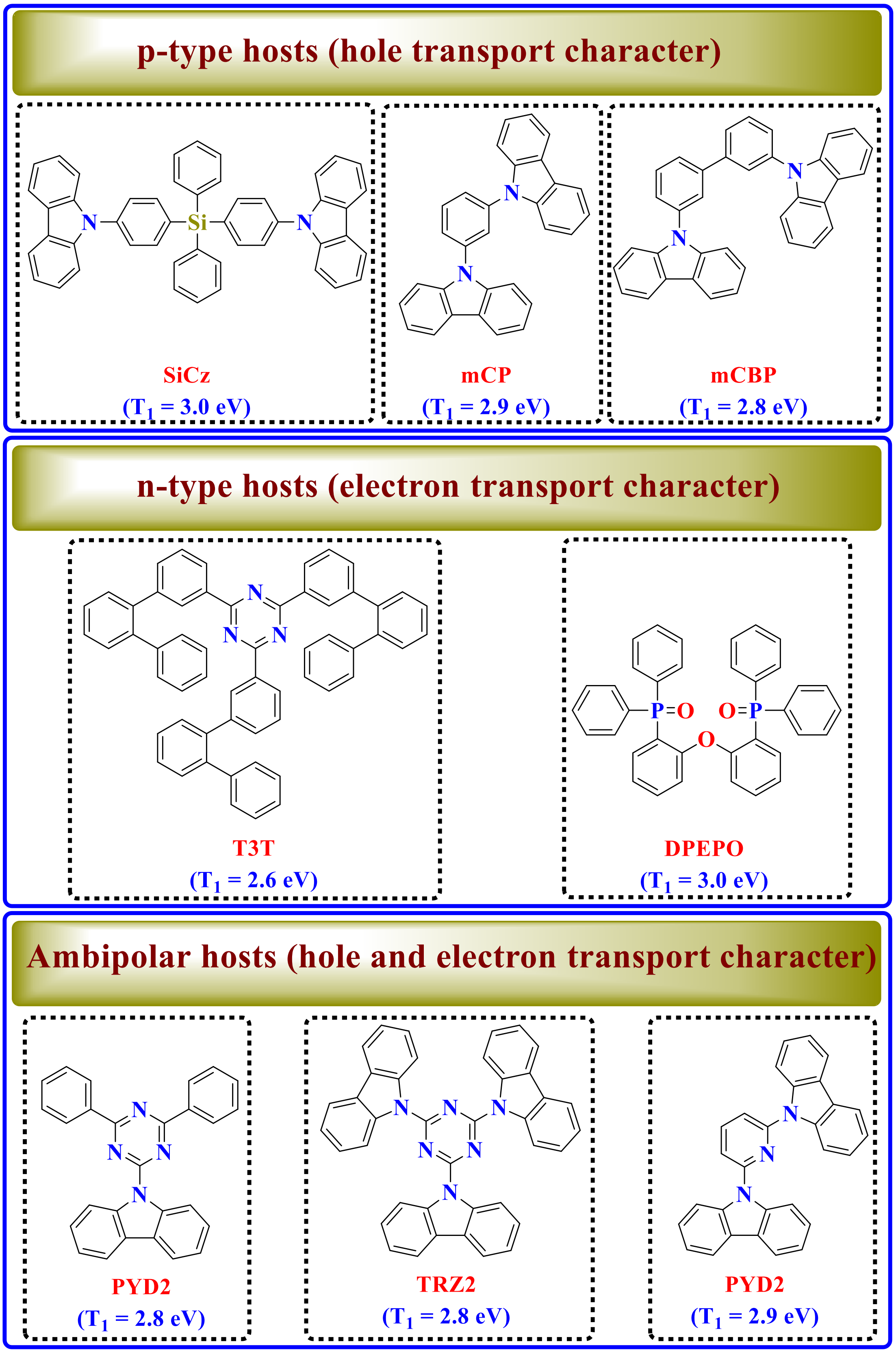

Figure 1.15: Typess of host materials for TADF.

1.4 Preparation Method of TADF Polymers

1.4.1 Suzuki Cross-Coupling

The Suzuki-Miyaura reaction constitutes one of the most vital approaches in the construction of carbon bonds.[102] This methodology relies upon the palladium-catalysed cross-coupling between various types of organic electrophilic portions, such as halides and organoboronic acids or esters, in any type of mild base, including potassium carbonate and palladium complexes like palladium acetate, as depicted below in **scheme 1.1**.[103]

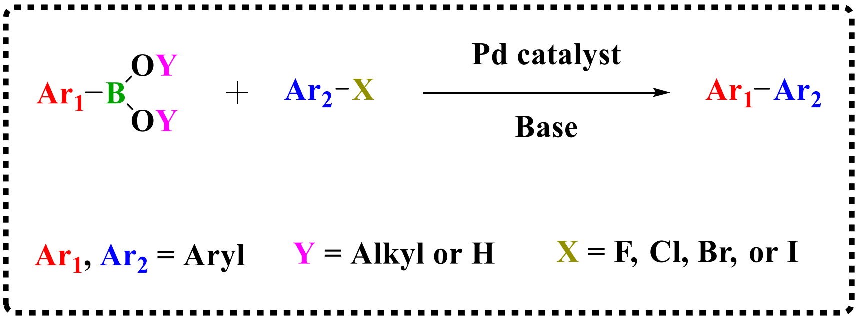

Scheme 1.1: Suzuki cross-coupling reaction.

This synthesis requires mild reaction conditions under refluxing, which proves to have several advantages for the Suzuki-Miyaura reaction. Furthermore, organoboron materials are often considered completely inert toward air and moisture as well as being thermally stable.[104] Moreover, they provide toleration with a diverse set of functional groups. Additionally, the treatment and separation of organoboron compounds are simple processes as these compounds are non-toxic so that the boron-carbon bond is significantly inert to ionic reactions.[105] Subsequently, the aforementioned benefits make this reaction suitable for large-scale synthesis.

The Suzuki cross-coupling reaction comprises four principal stages, as illustrated in **scheme 1.2**. The first stage involves the generation of an aryl palladium (II) halide complex by means of aryl halide, which is oxidatively added to the palladium (0) catalyst. The second stage involves the replacement of the halide group in the aryl palladium (II) halide complex by the KCO_3 group from potassium carbonate, giving rise to the generation of a second complex. The transmetallation stage activates the boron atom by generating a reaction between an organoboronic acid or ester and potassium carbonate. Such an approach raises the nucleophilic nature of the aryl group in the second complex, thereby facilitating the transmetallation process. Therefore, the second complex faces an attack by the activated organoboronic acid or ester activated by the base, resulting in the formation of an intermediate. The final stage involves the reductive elimination of the intermediate in order to generate the target coupling product with the palladium(0) catalyst, which, along with other aryl halides, can be exploited to form the target products.[106]

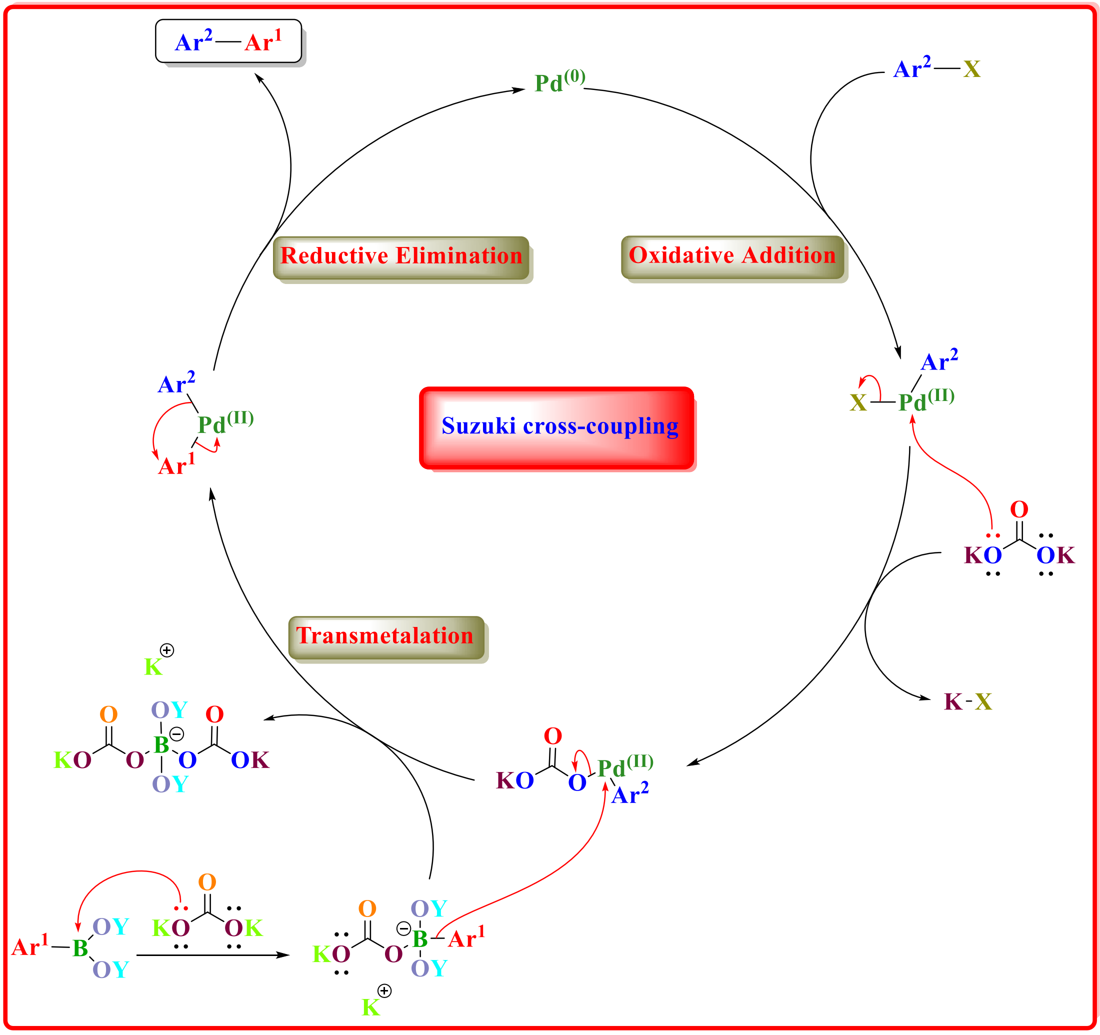

Scheme 1.2: The Suzuki cross-coupling mechanism.

1.5 Project Aims

In recent years, increasingly rapid advances have taken place in the field of OLEDs following their invention in 1987. TADF has been considered the most promising method of exciton harvesting in OLED devices. Moreover, the usage of an organic TADF emitter in OLEDs in 2011 fostered intense attention in improving the performance of OLED devices. TADF depends on a sufficiently low ΔE_{ST}, which is usually smaller than 0.1 eV. Therefore, TADF materials should have enough HOMO and LUMO separation on the molecule. Hence, the spatial separation of the HOMO and LUMO results in CT emission from the HOMO energy level to the LUMO energy level.

According to spin-statistics, the formation of excitons during hole-electron recombination in OLED devices leads to 25% singlets and 75% triplets. Therefore, the process of electroluminescence has the capacity to be totally efficient when harvesting both singlet and triplet states in emitting molecules. The molecules exhibiting TADF have demonstrably generated high-performance OLED devices. However, most fabrications of these OLED devices involve laborious processes during the thermal evaporation of multi-layers on substrates. Consequently, the application of solution processing methods can produce cheaper OLED devices due to their economical cost and ease of use.

This study aims to prepare a range of polymers grafted by TADF units into the polymer side chains. The polymers will be made through Suzuki cross-coupling polymerisations. The grafted TADF moieties to the sidechains of polymers will be exploited as guest molecules, while the backbone of the polymers will act as host materials to convert the produced triplet excitons into the emissive singlet excitons by means of RISC from T_1 to S_1. The proportions of TADF sidechains attached to the host polymers will be varied in order to investigate their photophysical and electronic properties and ultimately develop highly efficient TADF polymers that could be applied in solution-processable OLED devices.

mCP (**Figure 1.16**) has been used extensively as a small molecule host for the preparation of efficient TADF OLED devices prepared through the evaporation method. The preparation of polymers which could be used as emissive materials in OLED devices, and which use **mCP** as a repeat unit is therefore an attractive method to prepare TADF polymers. **PmCP-DPOXH-PxzTrz-5**, **PmCP-DPOXH-PxzTrz-10**, and **PmCP-DPOXH-PxzTrz-20**, (**Figure 1.16**) were therefore targeted in this work.

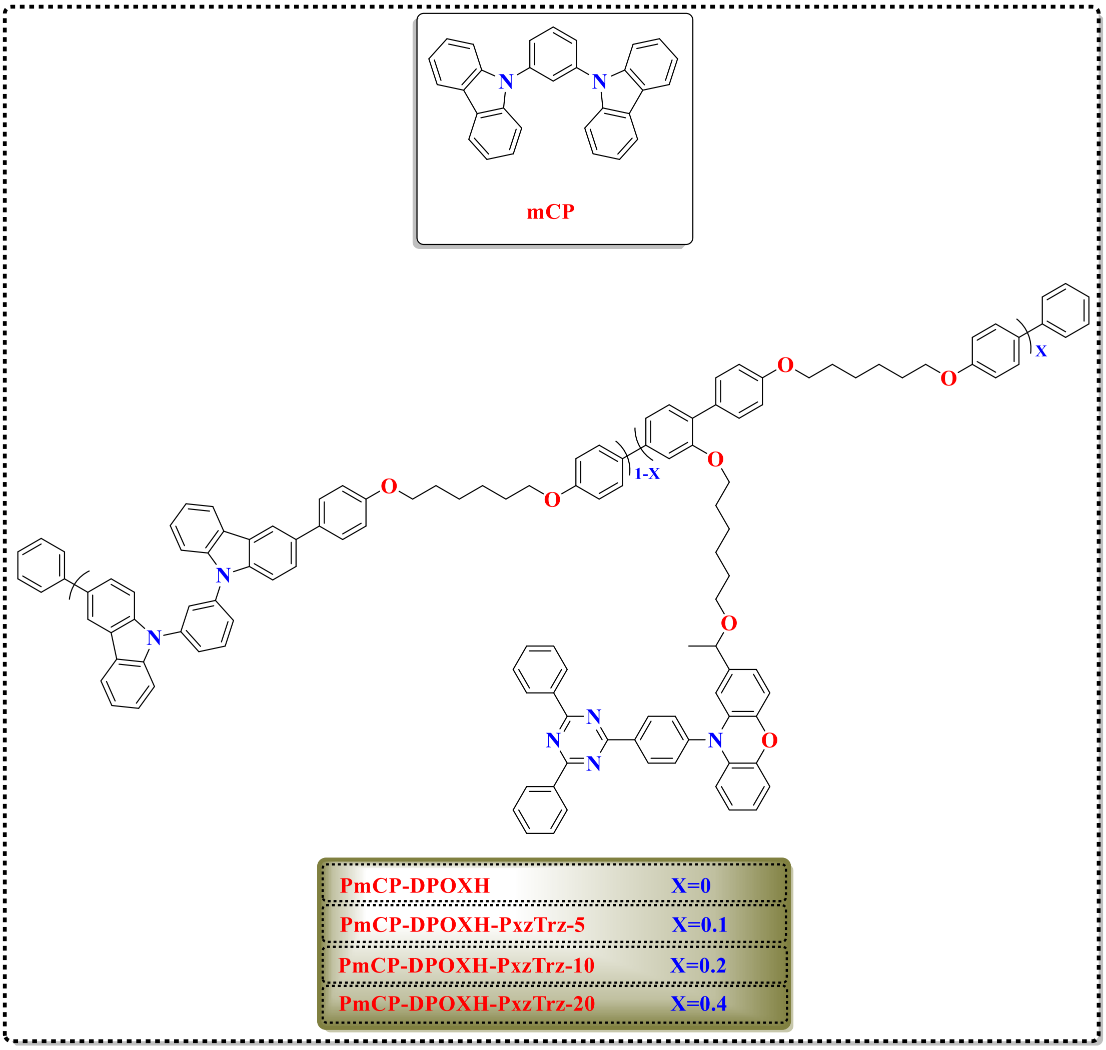

Figure 1.16: mCP polymers targeted in this work.

These polymers have restricted electronic delocalisation along their polymeric backbone through introduction of methylene chain repeat units, in order to keep the triplet state of the polymer chain as high as possible and with a value similar to that of **mCP**. The sidechains of the polymer act as guest molecules tethered on the polymer backbone with the phenoxazine-triazine **PXZ-TRZ** TADF units. All polymers are designed here as side chain type TADF polymers containing both partially conjugated and non-conjugated system in the main chain backbone. Additionally, the addition of the **mCP** molecule enhances the hole transport performance. Furthermore, the **mCP**-containing main chain functions as the charge transport channel to the side chain of the polymer as well as suppress the TADF moieties from concentration quenching. The target polymers are expected to be ideal candidates for solution processable OLEDs.

DPEPO (**Figure 1.17**) is another high triplet energy host material used in a wide variety of OLED devices deposited through evaporation of small molecules. Incorporation of **DPEPO** units into polymer chains was therefore also targeted in this work.

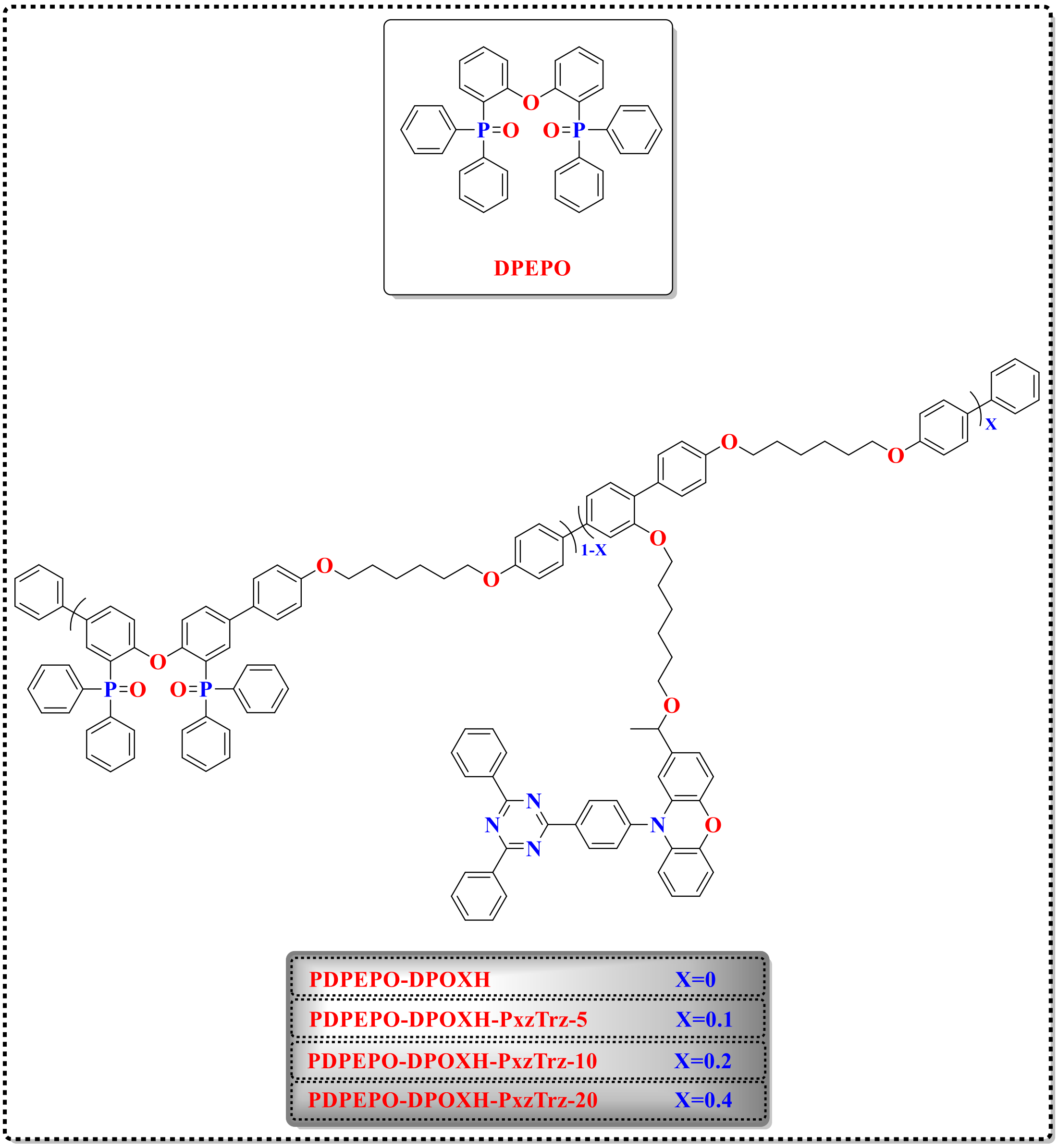

PDPEPO-DPOXH	X=0
PDPEPO-DPOXH-PxzTrz-5	X=0.1
PDPEPO-DPOXH-PxzTrz-10	X=0.2
PDPEPO-DPOXH-PxzTrz-20	X=0.4

Figure 1.17: **DPEPO** polymers targeted in this work.

Polymers **PDPEPO-DPOXH-PxzTrz-5**, **PDPEPO-DPOXH-PxzTrz-10**, and **PDPEPO-DPOXH-PxzTrz-20** comprise a polymer backbone, acting as a polymer host and the charge transporting channel, and a side chain connected to the polymer chain, which works as a guest molecule. The polymer chains are grafted by TADF sidechains, incorporated in different ratios to investigate the effects of their concentration on the photophysical properties of the resulting polymers. Preventing the undesired TEBT from the TADF emitter to the host molecule requires the use of **DPEPO** molecule as a host molecule of the polymeric backbone in designing TADF polymers since the **DPEPO** molecule possesses the requisite high triplet energy level (E_T)= 3.0 eV , which is considered sufficiently higher than the triplet energy level (E_T) of the TADF guest.[81] Additionally, adding the **DPEPO** molecule to the polymer backbone helps improve the electron transport character's performance levels. The TADF polymers exploit **PXZ-TRZ** as a green TADF guest while the convenient side chain unit of polymers has the requisite TADF features, such as a low ΔE_{ST}. More importantly, **PXZ-TRZ** comprises two units, namely, **PXZ** as a donor and **TRZ** as an acceptor, to form a charge-transfer structure. These target TADF polymers were selected as ideal candidates for solution-processing OLEDs.

1.6 References

(1) Uoyama, H.; Goushi, K.; Shizu, K.; Nomura, H.; Adachi, C. Highly Efficient Organic Light-Emitting Diodes from Delayed Fluorescence. *Nature* **2012**, *492* (7428), 234–238.

(2) Pope, M.; Kallmann, H. P.; Magnante, P. J. Electroluminescence in Organic Crystals. *The Journal of Chemical Physics* **1963**, *38* (8), 2042–2043.

(3) Vincett, P. S.; Barlow, W. A.; Hann, R. A.; Roberts, G. G. Electrical Conduction and Low Voltage Blue Electroluminescence in Vacuum-Deposited Organic Films. *Thin Solid Films* **1982**, *94* (2), 171–183.

(4) Tang, C. W.; VanSlyke, S. A. Organic Electroluminescent Diodes. *Applied Physics Letters* **1987**, *51* (12), 913–915.

(5) Burroughes, J. H.; Bradley, D. D. C.; Brown, A. R.; Marks, R. N.; Mackay, K.; Friend, R. H.; Burns, P. L.; Holmes, A. B. Light-Emitting Diodes Based on Conjugated Polymers. *Nature* **1990**, *347* (6293), 539–541.

(6) Friend, R. H. Conjugated Polymers. New Materials for Optoelectronic Devices. *Pure and Applied Chemistry* **2001**, *73* (3), 425–430.

(7) Kido, J.; Nagai, K.; Ohashi, Y. Electroluminescence in a Terbium Complex. *Chemistry Letters* **1990**, *19* (4), 657–660.

(8) Segura, J. L. The Chemistry of Electroluminescent Organic Materials. *Acta Polymerica* **1998**, *49* (7), 319–344.

(9) Kalyani, N. T.; Dhoble, S. J. Organic Light Emitting Diodes: Energy Saving Lighting Technology—A Review. *Renewable and Sustainable Energy Reviews* **2012**, *16* (5), 2696–2723.

(10) Thejokalyani, N.; Dhoble, S. J. Novel Approaches for Energy Efficient Solid State Lighting by RGB Organic Light Emitting Diodes–A Review. *Renewable and Sustainable Energy Reviews* **2014**, *32*, 448–467.

(11) Perrin, F. La Fluorescence Des Solutions-Induction Moléculaire.–Polarisation et Durée d’émission.–Photochimie. In *Annales De Physique*; EDP Sciences, **1929**, *10*, 169–275.

(12) Lewis, G. N.; Lipkin, D.; Magel, T. T. Reversible Photochemical Processes in Rigid Media. A Study of the Phosphorescent State. *Journal of the American Chemical Society* **1941**, *63* (11), 3005–3018.

(13) Parker, C. A.; Hatchard, C. G. Triplet-Singlet Emission in Fluid Solutions. Phosphorescence of Eosin. *Transactions of the Faraday Society* **1961**, *57*, 1894–1904.

(14) Parker, C. A.; Joyce, T. A. Activation-Controlled Delayed Fluorescence of Benzil. *Chemical Communications (London)* **1968**, No. 22, 1421–1422.

(15) Adachi, C.; Tsutsui, T.; Saito, S. Blue Light-emitting Organic Electroluminescent Devices. *Applied Physics Letters* **1990**, *56* (9), 799–801.

(16) Gebler, D. D.; Wang, Y. Z.; Blatchford, J. W.; Jessen, S. W.; Fu, D.-K.; Swager, T. M.; MacDiarmid, A. G.; Epstein, A. J. Exciplex Emission in Bilayer Polymer Light-Emitting Devices. *Applied Physics Letters* **1997**, *70* (13), 1644–1646.

(17) Wilkinson, F.; Horrocks, A. R. Phosphorescence and Delayed Fluorescence of Organic Substances Luminescence in Chemistry Ed EJ Bowen et al. Van Nostrand: London **1968**, 116–153.

(18) BALEIZao, C.; Berberan-Santos, M. N. Thermally Activated Delayed Fluorescence in Fullerenes. *Annals of the New York Academy of Sciences* **2008**, *1130* (1), 224–234.

(19) Wallikewitz, B. H.; Kabra, D.; Gelinas, S.; Friend, R. H. Triplet Dynamics in Fluorescent Polymer Light-Emitting Diodes. *Physical Review B* **2012**, *85* (4), 045209.

(20) Valeur, B.; Berberan-Santos, M. N. Autofluorescence and Fluorescence Labeling in Biology and Medicine. *Molecular Fluorescence: Principles and Applications, 479* **2012**, *505*.

(21) Tao, Y.; Yuan, K.; Chen, T.; Xu, P.; Li, H.; Chen, R.; Zheng, C.; Zhang, L.; Huang, W. Thermally Activated Delayed Fluorescence Materials towards the Breakthrough of Organoelectronics. *Advanced Materials* **2014**, *26* (47), 7931–7958.

(22) Hirata, S.; Sakai, Y.; Masui, K.; Tanaka, H.; Lee, S. Y.; Nomura, H.; Nakamura, N.; Yasumatsu, M.; Nakanotani, H.; Zhang, Q. Highly Efficient Blue Electroluminescence Based on Thermally Activated Delayed Fluorescence. *Nature Materials* **2015**, *14* (3), 330–336.

(23) Im, Y.; Kim, M.; Cho, Y. J.; Seo, J.-A.; Yook, K. S.; Lee, J. Y. Molecular Design Strategy of Organic Thermally Activated Delayed Fluorescence Emitters. *Chemistry of Materials* **2017**, *29* (5), 1946–1963.

(24) Zhang, Q.; Li, B.; Huang, S.; Nomura, H.; Tanaka, H.; Adachi, C. Efficient Blue Organic Light-Emitting Diodes Employing Thermally Activated Delayed Fluorescence. *Nature Photonics* **2014**, *8* (4), 326–332.

(25) Lee, I.; Lee, J. Y. Molecular Design of Deep Blue Fluorescent Emitters with 20% External Quantum Efficiency and Narrow Emission Spectrum. *Organic Electronics* **2016**, *29*, 160–164.

(26) Song, W.; Lee, I.; Lee, J. Y. Host Engineering for High Quantum Efficiency Blue and White Fluorescent Organic Light-Emitting Diodes. *Advanced Materials* **2015**, *27* (29), 4358–4363.

(27) HoáLee, I.; YeobáLee, J. High Efficiency Blue Fluorescent Organic Light-Emitting Diodes Using a Conventional Blue Fluorescent Emitter. *Journal of Materials Chemistry C* **2015**, *3* (34), 8834–8838.

(28) Zhang, Q.; Tsang, D.; Kuwabara, H.; Hatae, Y.; Li, B.; Takahashi, T.; Lee, S. Y.; Yasuda, T.; Adachi, C. Nearly 100% Internal Quantum Efficiency in Undoped Electroluminescent Devices Employing Pure Organic Emitters. *Advanced Materials* **2015**, *27* (12), 2096–2100.

(29) Lee, D. R.; Kim, M.; Jeon, S. K.; Hwang, S.; Lee, C. W.; Lee, J. Y. Design Strategy for 25% External Quantum Efficiency in Green and Blue Thermally Activated Delayed Fluorescent Devices. *Advanced Materials* **2015**, *27* (39), 5861–5867.

(30) Hwang, S.-H. Stable Blue Thermally Activated Delayed Fluorescent Organic Light-Emitting Diodes with Three Times Longer Lifetime than Phosphorescent Organic Light-Emitting Diodes. *Advanced Materials* **2015**, *27* (15), 2515–2520.

(31) Zhang, D.; Cai, M.; Zhang, Y.; Zhang, D.; Duan, L. Sterically Shielded Blue Thermally Activated Delayed Fluorescence Emitters with Improved Efficiency and Stability. *Materials Horizons* **2016**, *3* (2), 145–151.

(32) Cho, Y. J.; Yook, K. S.; Lee, J. Y. High Efficiency in a Solution-processed Thermally Activated Delayed-fluorescence Device Using a Delayed-fluorescence Emitting Material with Improved Solubility. *Advanced Materials* **2014**, *26* (38), 6642–6646.

(33) Nishide, J.; Nakanotani, H.; Hiraga, Y.; Adachi, C. High-Efficiency White Organic Light-Emitting Diodes Using Thermally Activated Delayed Fluorescence. *Applied Physics Letters* **2014**, *104* (23), 87_1.

(34) Masui, K.; Nakanotani, H.; Adachi, C. Analysis of Exciton Annihilation in High-Efficiency Sky-Blue Organic Light-Emitting Diodes with Thermally Activated Delayed Fluorescence. *Organic Electronics* **2013**, *14* (11), 2721–2726.

(35) Lee, D. R.; Choi, J. M.; Lee, C. W.; Lee, J. Y. Ideal Molecular Design of Blue Thermally Activated Delayed Fluorescent Emitter for High Efficiency, Small Singlet–Triplet Energy Splitting, Low Efficiency Roll-off, and Long Lifetime. *ACS Applied Materials & Interfaces* **2016**, *8* (35), 23190–23196.

(36) Numata, M.; Yasuda, T.; Adachi, C. High Efficiency Pure Blue Thermally Activated Delayed Fluorescence Molecules Having 10 H-Phenoxaborin and Acridan Units. *Chemical Communications* **2015**, *51* (46), 9443–9446.

(37) Serevičius, T.; Nakagawa, T.; Kuo, M.-C.; Cheng, S.-H.; Wong, K.-T.; Chang, C.-H.; Kwong, R. C.; Xia, S.; Adachi, C. Enhanced Electroluminescence Based on Thermally Activated Delayed Fluorescence from a Carbazole–Triazine Derivative. *Physical Chemistry Chemical Physics* **2013**, *15* (38), 15850–15855.

(38) Mayr, C.; Lee, S. Y.; Schmidt, T. D.; Yasuda, T.; Adachi, C.; Brütting, W. Efficiency Enhancement of Organic Light-emitting Diodes Incorporating a Highly Oriented Thermally Activated Delayed Fluorescence Emitter. *Advanced Functional Materials* **2014**, *24* (33), 5232–5239.

(39) Youn Lee, S.; Yasuda, T.; Nomura, H.; Adachi, C. High-Efficiency Organic Light-Emitting Diodes Utilizing Thermally Activated Delayed Fluorescence from Triazine-Based Donor–Acceptor Hybrid Molecules. *Applied Physics Letters* **2012**, *101* (9), 093306.

(40) Sato, K.; Shizu, K.; Yoshimura, K.; Kawada, A.; Miyazaki, H.; Adachi, C. Organic Luminescent Molecule with Energetically Equivalent Singlet and Triplet Excited States for Organic Light-Emitting Diodes. *Physical Review Letters* **2013**, *110* (24), 247401.

(41) Endo, A.; Sato, K.; Yoshimura, K.; Kai, T.; Kawada, A.; Miyazaki, H.; Adachi, C. Efficient Up-Conversion of Triplet Excitons into a Singlet State and Its Application for Organic Light Emitting Diodes. *Applied Physics Letters* **2011**, *98* (8), 42.

(42) Kim, O. Y.; Kim, B. S.; Lee, J. Y. High Efficiency Thermally Activated Delayed Fluorescent Devices Using a Mixed Host of Carbazole and Phosphine Oxide Derived Host Materials. *Synthetic Metals* **2015**, *201*, 49–53.

(43) Sun, J. W.; Lee, J.; Moon, C.; Kim, K.; Shin, H.; Kim, J. A Fluorescent Organic Light-emitting Diode with 30% External Quantum Efficiency. *Advanced Materials* **2014**, *26* (32), 5684–5688.

(44) Kim, B. S.; Lee, J. Y. Engineering of Mixed Host for High External Quantum Efficiency above 25% in Green Thermally Activated Delayed Fluorescence Device. *Advanced Functional Materials* **2014**, *24* (25), 3970–3977.

(45) Lee, D. R.; Kim, B. S.; Lee, C. W.; Im, Y.; Yook, K. S.; Hwang, S.-H.; Lee, J. Y. Above 30% External Quantum Efficiency in Green Delayed Fluorescent Organic Light-Emitting Diodes. *ACS Applied Materials & Interfaces* **2015**, *7* (18), 9625–9629.

(46) Li, J.; Nakagawa, T.; MacDonald, J.; Zhang, Q.; Nomura, H.; Miyazaki, H.; Adachi, C. Highly Efficient Organic Light-emitting Diode Based on a Hidden Thermally Activated Delayed Fluorescence Channel in a Heptazine Derivative. *Advanced Materials* **2013**, *25* (24), 3319–3323.

(47) Tsai, W.-L.; Huang, M.-H.; Lee, W.-K.; Hsu, Y.-J.; Pan, K.-C.; Huang, Y.-H.; Ting, H.-C.; Sarma, M.; Ho, Y.-Y.; Hu, H.-C. A Versatile Thermally Activated Delayed Fluorescence Emitter for Both Highly Efficient Doped and Non-Doped Organic Light Emitting Devices. *Chemical Communications* **2015**, *51* (71), 13662–13665.

(48) Lin, T.; Chatterjee, T.; Tsai, W.; Lee, W.; Wu, M.; Jiao, M.; Pan, K.; Yi, C.; Chung, C.; Wong, K. Sky-blue Organic Light Emitting Diode with 37% External Quantum Efficiency Using Thermally Activated Delayed Fluorescence from Spiroacridine-triazine Hybrid. *Advanced Materials* **2016**, *28* (32), 6976–6983.

(49) Wada, Y.; Shizu, K.; Kubo, S.; Suzuki, K.; Tanaka, H.; Adachi, C.; Kaji, H. Highly Efficient Electroluminescence from a Solution-Processable Thermally Activated Delayed Fluorescence Emitter. *Applied Physics Letters* **2015**, *107* (18), 105_1.

(50) Shizu, K.; Tanaka, H.; Uejima, M.; Sato, T.; Tanaka, K.; Kaji, H.; Adachi, C. Strategy for Designing Electron Donors for Thermally Activated Delayed Fluorescence Emitters. *The Journal of Physical Chemistry C* **2015**, *119* (3), 1291–1297.

(51) Lee, D. R.; Hwang, S.-H.; Jeon, S. K.; Lee, C. W.; Lee, J. Y. Benzofurocarbazole and Benzothienocarbazole as Donors for Improved Quantum Efficiency in Blue Thermally Activated Delayed Fluorescent Devices. *Chemical Communications* **2015**, *51* (38), 8105–8107.

(52) Shizu, K.; Uejima, M.; Nomura, H.; Sato, T.; Tanaka, K.; Kaji, H.; Adachi, C. Enhanced Electroluminescence from a Thermally Activated Delayed-Fluorescence Emitter by Suppressing Nonradiative Decay. *Physical Review Applied* **2015**, *3* (1), 014001.

(53) Cho, Y. J.; Yook, K. S.; Lee, J. Y. Cool and Warm Hybrid White Organic Light-Emitting Diode with Blue Delayed Fluorescent Emitter Both as Blue Emitter and Triplet Host. *Scientific Reports* **2015**, *5* (1), 1–7.

(54) Cho, Y. J.; Jeon, S. K.; Lee, J. Y. Molecular Engineering of High Efficiency and Long Lifetime Blue Thermally Activated Delayed Fluorescent Emitters for Vacuum and Solution Processed Organic Light-Emitting Diodes. *Advanced Optical Materials* **2016**, *4* (5), 688–693.

(55) Kim, M.; Jeon, S. K.; Hwang, S.-H.; Lee, S.-S.; Yu, E.; Lee, J. Y. Correlation of Molecular Structure with Photophysical Properties and Device Performances of Thermally Activated Delayed Fluorescent Emitters. *The Journal of Physical Chemistry C* **2016**, *120* (5), 2485–2493.

(56) Kim, H. M.; Choi, J. M.; Lee, J. Y. Blue Thermally Activated Delayed Fluorescent Emitters Having a Bicarbazole Donor Moiety. *RSC Advances* **2016**, *6* (68), 64133–64139.

(57) Li, B.; Nomura, H.; Miyazaki, H.; Zhang, Q.; Yoshida, K.; Suzuma, Y.; Orita, A.; Otera, J.; Adachi, C. Dicarbazolyldicyanobenzenes as Thermally Activated Delayed

Fluorescence Emitters: Effect of Substitution Position on Photoluminescent and Electroluminescent Properties. *Chemistry Letters* **2014**, *43* (3), 319–321.

(58) Kaji, H.; Suzuki, H.; Fukushima, T.; Shizu, K.; Suzuki, K.; Kubo, S.; Komino, T.; Oiwa, H.; Suzuki, F.; Wakamiya, A. Purely Organic Electroluminescent Material Realizing 100% Conversion from Electricity to Light. *Nature Communications* **2015**, *6* (1), 1–8.

(59) Cho, Y. J.; Jeon, S. K.; Chin, B. D.; Yu, E.; Lee, J. Y. The Design of Dual Emitting Cores for Green Thermally Activated Delayed Fluorescent Materials. *Angewandte Chemie International Edition* **2015**, *54* (17), 5201–5204.

(60) Kim, M.; Jeon, S. K.; Hwang, S.-H.; Lee, S.; Yu, E.; Lee, J. Y. Highly Efficient and Color Tunable Thermally Activated Delayed Fluorescent Emitters Using a “Twin Emitter” Molecular Design. *Chemical Communications* **2016**, *52* (2), 339–342.

(61) Hatakeyama, T.; Shiren, K.; Nakajima, K.; Nomura, S.; Nakatsuka, S.; Kinoshita, K.; Ni, J.; Ono, Y.; Ikuta, T. Ultrapure Blue Thermally Activated Delayed Fluorescence Molecules: Efficient HOMO–LUMO Separation by the Multiple Resonance Effect. *Advanced Materials* **2016**, *28* (14), 2777–2781.

(62) Zhang, J.; Ding, D.; Wei, Y.; Xu, H. Extremely Condensing Triplet States of DPEPO-Type Hosts through Constitutional Isomerization for High-Efficiency Deep-Blue Thermally Activated Delayed Fluorescence Diodes. *Chemical Science* **2016**, *7* (4), 2870–2882.

(63) Li, J.; Ding, D.; Wei, Y.; Zhang, J.; Xu, H. A “Si-Locked” Phosphine Oxide Host with Suppressed Structural Relaxation for Highly Efficient Deep-Blue TADF Diodes. *Advanced Optical Materials* **2016**, *4* (4), 522–528.

(64) Zhang, J.; Ding, D.; Wei, Y.; Han, F.; Xu, H.; Huang, W. Multiphosphine-Oxide Hosts for Ultralow-Voltage-Driven True-Blue Thermally Activated Delayed Fluorescence Diodes with External Quantum Efficiency beyond 20%. *Advanced Materials* **2016**, *28* (3), 479–485.

(65) Duan, C.; Fan, C.; Wei, Y.; Han, F.; Huang, W.; Xu, H. Optimizing the Intralayer and Interlayer Compatibility for High-Efficiency Blue Thermally Activated Delayed Fluorescence Diodes. *Scientific Reports* **2016**, *6* (1), 1–13.

(66) Lee, S. Y.; Yasuda, T.; Yang, Y. S.; Zhang, Q.; Adachi, C. Luminous Butterflies: Efficient Exciton Harvesting by Benzophenone Derivatives for Full-color Delayed Fluorescence OLEDs. *Angewandte Chemie International Edition* **2014**, *53* (25), 6402–6406.

(67) Zhang, Q.; Kuwabara, H.; Potscavage Jr, W. J.; Huang, S.; Hatae, Y.; Shibata, T.; Adachi, C. Anthraquinone-Based Intramolecular Charge-Transfer Compounds: Computational Molecular Design, Thermally Activated Delayed Fluorescence, and Highly Efficient Red Electroluminescence. *Journal of the American Chemical Society* **2014**, *136* (52), 18070–18081.

(68) Cho, Y. J.; Jeon, S. K.; Lee, S.-S.; Yu, E.; Lee, J. Y. Donor Interlocked Molecular Design for Fluorescence-like Narrow Emission in Deep Blue Thermally Activated Delayed Fluorescent Emitters. *Chemistry of Materials* **2016**, *28* (15), 5400–5405.

(69) Song, W.; Lee, W.; Kim, K. K.; Lee, J. Y. Correlation of Doping Concentration, Charge Transport of Host, and Lifetime of Thermally Activated Delayed Fluorescent Devices. *Organic Electronics* **2016**, *37*, 252–256.

(70) Cho, Y. J.; Yook, K. S.; Lee, J. Y. A Universal Host Material for High External Quantum Efficiency Close to 25% and Long Lifetime in Green Fluorescent and Phosphorescent OLEDs. *Advanced Materials* **2014**, *26* (24), 4050–4055.

(71) Nakanotani, H.; Masui, K.; Nishide, J.; Shibata, T.; Adachi, C. Promising Operational Stability of High-Efficiency Organic Light-Emitting Diodes Based on Thermally Activated Delayed Fluorescence. *Scientific Reports* **2013**, *3* (1), 1–6.

(72) Tsang, D. P.-K.; Matsushima, T.; Adachi, C. Operational Stability Enhancement in Organic Light-Emitting Diodes with Ultrathin Liq Interlayers. *Scientific Reports* **2016**, *6* (1), 1–10.

(73) Zou, Y.; Gong, S.; Xie, G.; Yang, C. Design Strategy for Solution-Processable Thermally Activated Delayed Fluorescence Emitters and Their Applications in Organic Light-Emitting Diodes. *Advanced Optical Materials* **2018**, *6* (23), 1800568.

(74) Gustafsson, G.; Cao, Y.; Treacy, G. M.; Klavetter, F.; Colaneri, N.; Heeger, A. J. Flexible Light-Emitting Diodes Made from Soluble Conducting Polymers. *Nature* **1992**, *357* (6378), 477–479.

(75) Wu, H.; Zhou, G.; Zou, J.; Ho, C.; Wong, W.; Yang, W.; Peng, J.; Cao, Y. Efficient Polymer White-Light-Emitting Devices for Solid-State Lighting. *Advanced Materials* **2009**, *21* (41), 4181–4184.

(76) Wei, Q.; Kleine, P.; Karpov, Y.; Qiu, X.; Komber, H.; Sahre, K.; Kiriy, A.; Lygaitis, R.; Lenk, S.; Reineke, S. Conjugation-Induced Thermally Activated Delayed Fluorescence (TADF): From Conventional Non-TADF Units to TADF-Active Polymers. *Advanced Functional Materials* **2017**, *27* (7), 1605051.

(77) Yin, X.; He, Y.; Wang, X.; Wu, Z.; Pang, E.; Xu, J.; Wang, J. Recent Advances in Thermally Activated Delayed Fluorescent Polymer—Molecular Designing Strategies. *Frontiers in Chemistry* **2020**, 725.

(78) Nobuyasu, R. S.; Ren, Z.; Griffiths, G. C.; Batsanov, A. S.; Data, P.; Yan, S.; Monkman, A. P.; Bryce, M. R.; Dias, F. B. Rational Design of TADF Polymers Using a Donor–Acceptor Monomer with Enhanced TADF Efficiency Induced by the Energy Alignment of Charge Transfer and Local Triplet Excited States. *Advanced Optical Materials* **2016**, *4* (4), 597–607.

(79) Zhou, X.; Huang, M.; Zeng, X.; Chen, T.; Xie, G.; Yin, X.; Yang, C. Combining the Qualities of Carbazole and Tetraphenyl Silane in a Desirable Main Chain for Thermally Activated Delayed Fluorescence Polymers. *Polymer Chemistry* **2019**, *10* (30), 4201–4208.

(80) Yang, Y.; Zhao, L.; Wang, S.; Ding, J.; Wang, L. Synthesis and Characterization of Red-Emitting Thermally Activated Delayed Fluorescent Polymers Based on Poly (2, 7-Carbazole-Co-3, 3′-Dimethyldiphenyl Ether) as the Main Chain. *Acta Polym. Sin* **2019**, *50*, 685–694.

(81) Yang, Y.; Zhao, L.; Wang, S.; Ding, J.; Wang, L. Red-Emitting Thermally Activated Delayed Fluorescence Polymers with Poly (Fluorene-Co-3, 3′-Dimethyl Diphenyl Ether) as the Backbone. *Macromolecules* **2018**, *51* (23), 9933–9942.

(82) Xie, Y.; Li, Z. Thermally Activated Delayed Fluorescent Polymers. *Journal of Polymer Science Part A: Polymer Chemistry* **2017**, *55* (4), 575–584.

(83) Xie, G.; Luo, J.; Huang, M.; Chen, T.; Wu, K.; Gong, S.; Yang, C. Inheriting the Characteristics of Tadf Small Molecule by Side-chain Engineering Strategy to Enable

Bluish-green Polymers with High PLQYs up to 74% and External Quantum Efficiency over 16% in Light-emitting Diodes. *Advanced Materials* **2017**, *29* (11), 1604223.

(84) Luo, J.; Xie, G.; Gong, S.; Chen, T.; Yang, C. Creating a Thermally Activated Delayed Fluorescence Channel in a Single Polymer System to Enhance Exciton Utilization Efficiency for Bluish-Green Electroluminescence. *Chemical Communications* **2016**, *52* (11), 2292–2295.

(85) Yang, Z.; Mao, Z.; Xie, Z.; Zhang, Y.; Liu, S.; Zhao, J.; Xu, J.; Chi, Z.; Aldred, M. P. Recent Advances in Organic Thermally Activated Delayed Fluorescence Materials. *Chemical Society Reviews* **2017**, *46* (3), 915–1016.

(86) Duan, L.; Hou, L.; Lee, T.-W.; Qiao, J.; Zhang, D.; Dong, G.; Wang, L.; Qiu, Y. Solution Processable Small Molecules for Organic Light-Emitting Diodes. *Journal of Materials Chemistry* **2010**, *20* (31), 6392–6407.

(87) Albrecht, K.; Matsuoka, K.; Fujita, K.; Yamamoto, K. Carbazole Dendrimers as Solution-Processable Thermally Activated Delayed-Fluorescence Materials. *Angewandte Chemie International Edition* **2015**, *54* (19), 5677–5682.

(88) Nikolaenko, A. E.; Cass, M.; Bourcet, F.; Mohamad, D.; Roberts, M. Thermally Activated Delayed Fluorescence in Polymers: A New Route toward Highly Efficient Solution Processable OLEDs. *Advanced Materials* **2015**, *27* (44), 7236–7240.

(89) Méhes, G.; Goushi, K.; Potscavage Jr, W. J.; Adachi, C. Influence of Host Matrix on Thermally-Activated Delayed Fluorescence: Effects on Emission Lifetime, Photoluminescence Quantum Yield, and Device Performance. *Organic Electronics* **2014**, *15* (9), 2027–2037.

(90) Arjona-Esteban, A.; Szafranowska, B.; Ochsmann, J. TADF Technology for Efficient Blue OLEDs: Status and Challenges from an Industrial Point of View. In *Luminescence-OLED Technology and Applications*; IntechOpen London, **2019**, 1–18.

(91) Song, W.; Lee, J. Y. Degradation Mechanism and Lifetime Improvement Strategy for Blue Phosphorescent Organic Light-emitting Diodes. *Advanced Optical Materials* **2017**, *5* (9), 1600901.

(92) Tao, Y.; Yang, C.; Qin, J. Organic Host Materials for Phosphorescent Organic Light-Emitting Diodes. *Chemical Society Reviews* **2011**, *40* (5), 2943–2970.

(93) Zhang, D.; Cai, M.; Bin, Z.; Zhang, Y.; Zhang, D.; Duan, L. Highly Efficient Blue Thermally Activated Delayed Fluorescent OLEDs with Record-Low Driving Voltages Utilizing High Triplet Energy Hosts with Small Singlet–Triplet Splittings. *Chemical Science* **2016**, *7* (5), 3355–3363.

(94) Strohriegl, P.; Wagner, D.; Schrögel, P.; Hoffmann, S. T.; Köhler, A.; Heinemeyer, U.; Münster, I. Novel Host Materials for Blue Phosphorescent OLEDs. In *Organic Light Emitting Materials and Devices XVII*; SPIE, **2013**, *8829*, 9–20.

(95) Oshiyama, T.; Yasukawa, N.; Kita, H.; Matsui, T.; Sumita, M.; Morihashi, K. A Theoretical Guideline for Designing Effective Host Materials Based on 4, 4′-Bis (9-Carbazolyl)-1, 1′-Biphenyl Derivatives for Blue Phosphorescent Devices. *Bulletin of the Chemical Society of Japan* **2017**, *90* (2), 195–204.

(96) Varathan, E.; Vijay, D.; Kumar, P. S. V.; Subramanian, V. Computational Design of High Triplet Energy Host Materials for Phosphorescent Blue Emitters. *Journal of Materials Chemistry C* **2013**, *1* (27), 4261–4274.

(97) Woon, K. L.; Hasan, Z. A.; Ong, B. K.; Ariffin, A.; Griniene, R.; Grigalevicius, S.; Chen, S.-A. Triplet States and Energy Back Transfer of Carbazole Derivatives. *RSC Advances* **2015**, *5* (74), 59960–59969.

(98) Han, C.; Zhao, Y.; Xu, H.; Chen, J.; Deng, Z.; Ma, D.; Li, Q.; Yan, P. A Simple Phosphine–Oxide Host with a Multi-insulating Structure: High Triplet Energy Level for Efficient Blue Electrophosphorescence. *Chemistry–A European Journal* **2011**, *17* (21), 5800–5803.

(99) Ihn, S.; Lee, N.; Jeon, S. O.; Sim, M.; Kang, H.; Jung, Y.; Huh, D. H.; Son, Y. M.; Lee, S. Y.; Numata, M. An Alternative Host Material for Long-Lifespan Blue Organic Light-Emitting Diodes Using Thermally Activated Delayed Fluorescence. *Advanced Science* **2017**, *4* (8), 1600502.

(100) Wong, M. Y.; Zysman-Colman, E. Purely Organic Thermally Activated Delayed Fluorescence Materials for Organic Light-emitting Diodes. *Advanced Materials* **2017**, *29* (22), 1605444.

(101) Chen, D.; Su, S.-J.; Cao, Y. Nitrogen Heterocycle-Containing Materials for Highly Efficient Phosphorescent OLEDs with Low Operating Voltage. *Journal of Materials Chemistry C* **2014**, *2* (45), 9565–9578.

(102) Suzuki, A. Recent Advances in the Cross-Coupling Reactions of Organoboron Derivatives with Organic Electrophiles, 1995–1998. *Journal of Organometallic Chemistry* **1999**, *576* (1–2), 147–168.

(103) Suzuki, A. Cross-coupling Reactions of Organoboranes: An Easy Way to Construct C–C Bonds (Nobel Lecture). *Angewandte Chemie International Edition* **2011**, *50* (30), 6722–6737.

(104) Miyaura, N. Cross-Coupling Reaction of Organoboron Compounds via Base-Assisted Transmetalation to Palladium (II) Complexes. *Journal of Organometallic Chemistry* **2002**, *653* (1–2), 54–57.

(105) Miyaura, N.; Suzuki, A. Palladium-Catalyzed Cross-Coupling Reactions of Organoboron Compounds. *Chemical Reviews* **1995**, *95* (7), 2457–2483.

(106) Suzuki, A. Organoboron Compounds in New Synthetic Reactions. *Pure and Applied Chemistry* **1985**, *57* (12), 1749–1758.

Chapter 2: mCP-Based Polymers with Pendant TADF Emitters for use in Solution Processable OLEDs

Abstract

The application of polymers with TADF properties is favourable for solution-processable OLEDs. Nevertheless, to date, few reports of efficient solution processable TADF polymers have been published, severely restricting their commercial utility in display and lighting products. A number of green emitting TADF polymers were synthesised in this work. These polymers exhibited suitably excellent solubility and good thermal stability. The results of UV-vis studies as well as PL studies are presented along with cyclic voltammetry (CV) studies and TGA analyses. Interestingly, using PL spectroscopy, an almost entire interchain and intrachain energy transfer from the polymeric backbone to the sidechain TADF moiety was observed, giving rise to only a TADF emission peak, with scarcely any residual emission from the main chain backbone for **PmCP-DPOXH-PxzTrz-10** and **PmCP-DPOXH-PxzTrz-20**. Moreover, the HOMO levels of the TADF polymers, e.g., **PmCP-DPOXH-PxzTrz-X,** vary from -5.09 eV to -4.99 eV, demonstrating a rising trend of HOMO levels with increasing proportions of the TADF moiety in the polymers. It is worth noting that the HOMO-LUMO gaps of the TADF polymers, i.e., **PmCP-DPOXH-PxzTrz-X**, decrease clearly with a rise in the loading of the TADF unit, i.e., from 1.56 eV (**PmCP-DPOXH-PxzTrz-5**) to 1.47 eV (**PmCP-DPOXH-PxzTrz-20**). Also, all polymers displayed excellent thermal stability with thermal decomposition temperatures above 280 °C, indicating that these target polymers could be applied in solution processable OLED devices with long-term stability.

2.1 Introduction

A surge of commercial interest in the application of OLEDs as next-generation sources of display and lighting has fuelled an accelerated expansion of organic emissive materials. In recent years, primary organic emissive materials in OLEDs have quickly evolved from fluorescent materials to phosphorescent heavy-metal complexes and finally, to TADF materials.[1–4] This ability to convert triplet excitons into singlet excitons provides approximately 100% exciton utilisation efficiency (EUE) without incorporating any heavy-metal components in the new generation of materials containing TADF features.[5–7]

Significant current advances in cutting-edge OLED technologies based on TADF materials have been made. For instance, the **D-Ph-A-Ph-D**-type molecule as a red emitter, **DMAC-DPS** as a blue emitter and **4CzIPN** as a green emitter in OLED devices have each attained 12.5%, 19% and 28.6%, respectively, of their external quantum efficiencies (EQEs).[8–10] In spite of efficiency improvements, their evaporated deposition technique requires sophisticated structures, elevated costs and fine control. Compared to other manufacturing techniques, a solution process is a simpler, less expensive and more readily controlled choice for enabling large-scale production. However, the majority of published TADF dopants are essentially small molecules which are incompatible with solution processing. Consequently, the development of solution-processable organic emissive materials with TADF characteristics is of critical relevance.[11–15]

It has been established that the efficiency of solution-processing devices can be enhanced by using polymeric materials as excellent emissive materials.[16,17] However, the minimised EUE in the EL process restricts the performance of these polymer-based devices to some degree owing to the fact that deactivation of 50–75% of triplet excitons is induced by the non-radiative decay mechanism. This results in a reduction in device performance; the singlet and triplet ratios for devices based on these polymers vary from 1:1 to 1:3.[18–21] Thus, employing a TADF mechanism, which is composed of metal-free organic emissive materials, may represent a feasible approach for increasing polymeric material EUE.

Yang *et al.* initially proposed the application of a sidechain engineering method in relation to the polymeric design in order to configure a TADF channel in a single-polymer system.[15] This method involved grafting the TADF emitter onto the polymer sidechain (**Figure 2.1**). Using this design approach, two types of distinct functional units were provided in a single-polymer system, which included the polymer backbone and the grafted moieties on the polymer sidechain. The polymer backbone served as both the charge-carrying channel and the host, whereas the grafted moieties on the sidechain provided additional capabilities without compromising the backbone's electronic characteristics.

3,6-Linked polycarbazole was selected as the polymer backbone for two reasons, firstly, its excellent hole-transporting capacity and secondly, its high triplet energy of approximately 2.6 eV. 10- (4- (5- Phenyl-1, 3, 4-oxadiazol-2-yl) phenyl)- 10H-phenoxazine (**PXZ-OXD**) was chosen as a grafted moiety on the polymer sidechain owing to its evident TADF properties and molecular modification potential (**Figure 2.1**).[22,23] In order to promote hole injection, triphenylamine (TPA) and carbazole (Cz) moieties were inserted into the polymer sidechains. The resultant light-emitting copolymers, which have been grafted with various proportions of **PXZ-OXD** components, exhibited distinct TADF characteristics. Amongst these copolymers, PLQY was observed to be the highest within polymer **P12**, i.e., 33.7%. When this copolymer was utilised as emissive layers, a peak EL wavelength of 506 nm was observed, together with a maximum external quantum efficiency of 4.3%, which surpasses the theoretical limit of traditional fluorescent organic/polymer LEDs, achieving an elevated EUE of 63.7%.[15,24–27]

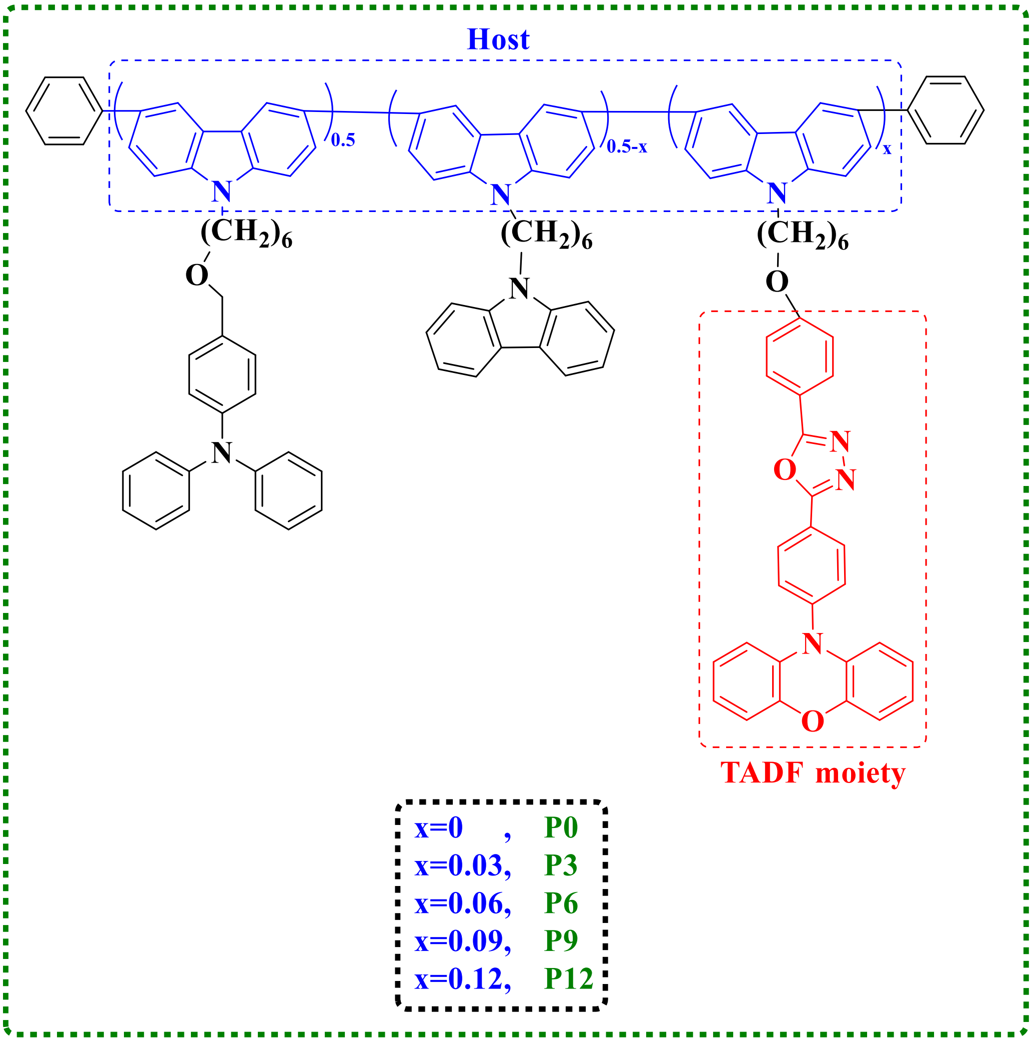

Figure 2.1: TADF polymers synthesised by Yang *et al.*[15]

2.2 Results and Discussion

In this chapter, the design approach for green-emitting TADF polymers relies upon the presence of two main factors, including the main chain backbone and the polymer sidechain. The former consists of a mixture of partially conjugated and non-conjugated systems; using only a non-conjugated main chain backbone may lead to poor device performance and an unfavourable effect on the charge transfer characteristics. Thus, a combination was employed in order to achieve equilibrium. In addition, the **mCP**-containing main chain units serve as the charge transport channel to the polymer sidechain as well as suppressing the TADF moieties from concentration quenching.

The **mCP** moiety in **M1** was applied as a host since **mCP** includes an excellent high triplet energy state, i.e., (E_T) = 2.9 eV, which is sufficiently higher than the E_T of the TADF emitter **PXZ-TRZ**. This is in order to preclude the undesirable TEBT from the TADF emitter to the host compound, as well as its capacity for optimum hole transport performance. Additionally, the **mCP** host in **M1** experiences a large steric hindrance, leading to increasing the polymer's triplet energy. Thus, 1,6-diphenoxyhexane (**DPOXH**) in **M2** was included into the polymeric backbone so as to interrupt the polymeric backbone's conjugation system and to tune the triplet energy of the polymer host.

The polymer's sidechain comprises the grafted TADF emitter, which functions as a guest compound tethered onto the polymeric backbone; this facilitates the presence of TADF properties in a single-polymer system. Furthermore, **PXZ-TRZ** in **M3** was utilised in these polymers as a green TADF emitter in order to generate excellent TADF properties, such as the low ΔE_{ST}. **PXZ-TRZ** in **M3** was employed for the synthesis of green-emitting TADF polymers since this TADF emitter contains two sufficiently robust moieties, i.e., phenoxazine as a donor, and triphenyltriazine as an acceptor. These have the ability to transport the intramolecular charge transfer (ICT) between them.

The preparation of the target green-emitting TADF polymers uses dibrominated **mCP** in **M1**, and the π-interrupted structure of 1,6-diphenoxyhexane (**DPOXH**) in **M2**. Interestingly, these desired green-emitting TADF polymers were considered suitable candidates for solution-processable OLEDs. **Scheme 2.1** illustrates a polymer, **PmCP-DPOXH**, generated successfully utilising two monomers, **M1** and **M2**, with a molar ratio of 50:50. As shown in **scheme 2.1**, the green-emitting TADF polymers were successfully manufactured using typical Suzuki polycondensation of the monomers, **M1**, **M2** and **M3**, at concentrations of 45:50:5, 40:50:10 and 30:50:20, respectively. These green-emitting TADF polymers were termed **PmCP-DPOXH-PxzTrz-5**, **PmCP-DPOXH-PxzTrz-10**, and **PmCP-DPOXH-PxzTrz-20**, according to their respective feed ratios to **M3**. Additionally, the polymer, **PmCP-DPOXH**, which lacks the TADF moiety, was conveniently produced for comparison with **PmCP-DPOXH-PxzTrz-5**, **PmCP-DPOXH-PxzTrz-10**, and **PmCP-DPOXH-PxzTrz-20**.

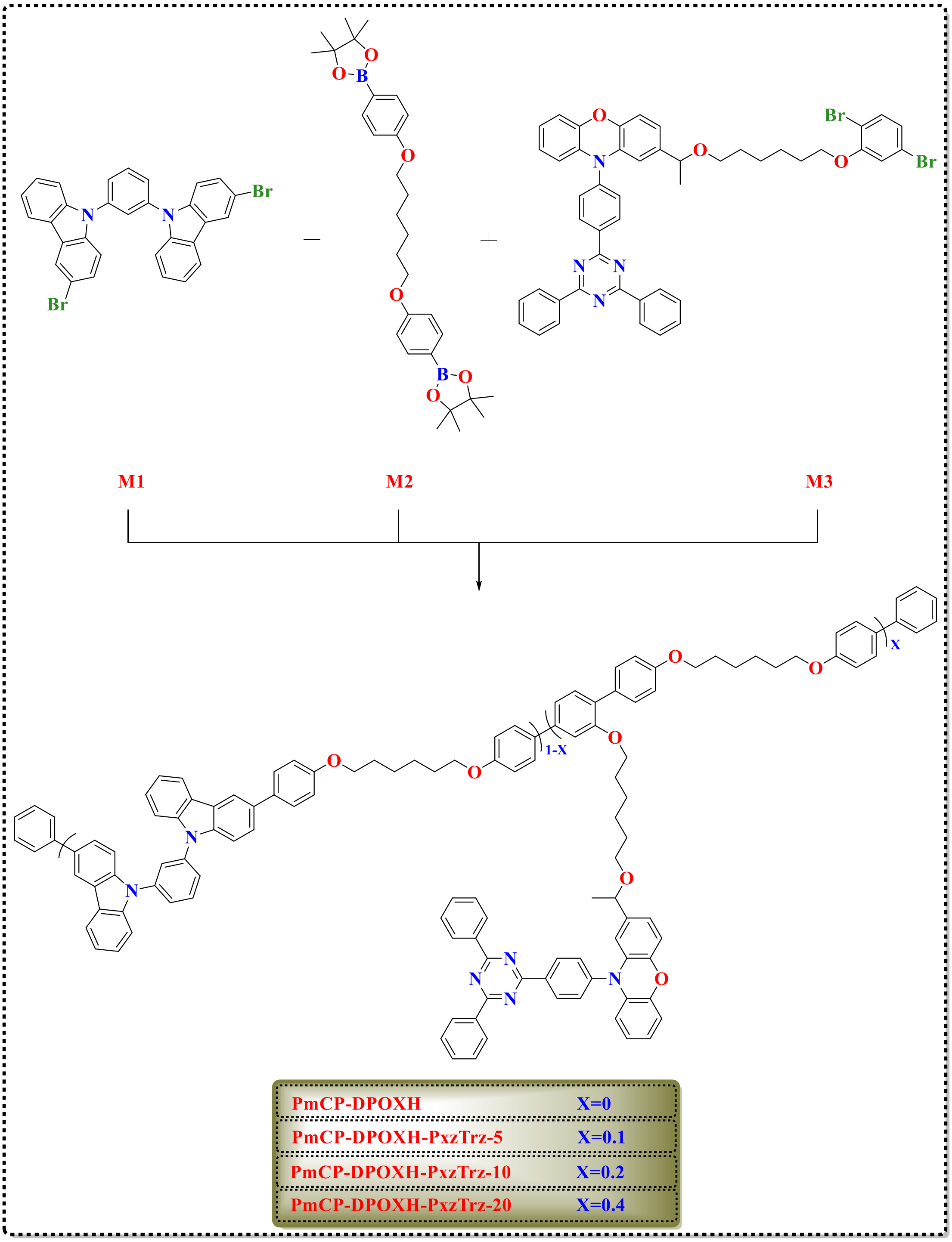

Scheme 2.1: Synthetic route of **PmCP-DPOXH**, **PmCP-DPOXH-PxzTrz-5**, **PmCP-DPOXH-PxzTrz-10**, and **PmCP-DPOXH-PxzTrz-20**. Reagents and conditions: anhydrous toluene, K_2CO_3, $Pd(OAc)_2$, $P(o\text{-}tol)_3$, 100 °C.

2.2.1 Synthesis of Host Monomer M1

2.2.1.1 Synthesis of 3-bromo-9*H*-carbazole (1)

9*H*-Carbazole was selectively brominated at the 3-position using equimolar amounts of *N*-bromosuccinimide (NBS) in dimethylformamide (DMF) and 9*H*-carbazole, in order to form **(1)**, as reported by Sun *et al*. and illustrated in **scheme 2.2**.[28] The bromination was sensitively performed in dark conditions; equivalent quantities of starting materials were utilised in order to avoid the formation of a multi-brominated product. The process resulted in the production of molecule **(1)**, as a colourless solid, in a high yield (92%).

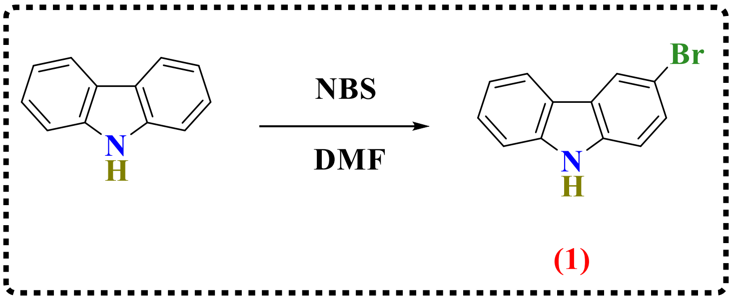

Scheme 2.2: Synthesis of **(1)**.

The reaction mechanism of carbazole bromination is an electrophilic aromatic substitution (EAS) (**scheme 2.3**). This mechanism comprises three crucial steps in order to obtain product **(1)**, which uses a stoichiometry of NBS as a source of a bromine atom at a cooling temperature and a specific time in order to control the bromination of 9*H*-carbazole in dark conditions. Firstly, the amino group donates electron density into the ring through resonance, and then a lone pair of electrons on the nitrogen atom of 9*H*-carbazole is delocalised into the ring, rendering the *ortho* and *para* positions to the amino group more electron rich. The *para* position is here favoured to be more reactive due to the lesser steric hindrance effect compared to the *ortho* position, which is affected by highly steric hindrance. Thus, as the more electron rich position is a good nucleophile, an EAS reaction will be carried out on this position more rapidly. The second step is a carbon of the *para* position to the amino group on 9*H*-carbazole, which works as a nucleophilic component, attacks the bromine atom of NBS, which acts as an electrophilic part in the reaction, resulting in the formation of an intermediate **(A)** with a succinimide anion. The positive charge is put on a nitrogen atom of the intermediate

(A) in order to achieve a complete octet for all atoms. The final step involves deprotonation of the intermediate **(A)**, which is facilitated by the nitrogen atom of the succinimide anion in order to afford compound **(1)**.

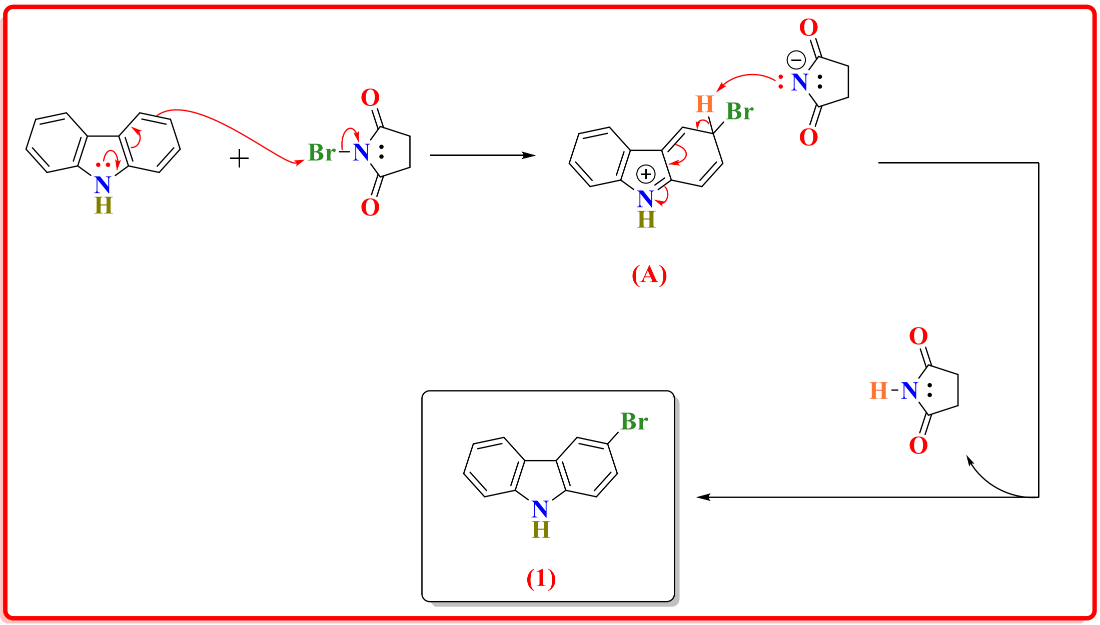

Scheme 2.3: The proposed mechanism of bromination of **(1)**.

Compound **(1)** was fully identified by means of ^{1}H NMR spectroscopy, ^{13}C NMR spectroscopy, TLC, mass spectrometry and elemental analysis. After purifying product **(1)** by column chromatography, the TLC plate was employed in order to check the presence of one spot only for the product **(1)**. The structure of the product **(1)** was identified by ^{1}H NMR and ^{13}C NMR spectra. Specifically, the ^{1}H NMR spectrum of compound **(1)** displayed a broad singlet peak at 8.08 ppm, which can be attributed to the proton of the amino group, due to rapid intermolecular exchange of amine proton. Furthermore, the ^{1}H NMR spectrum of **(1)** evidenced some peak shifts and appearance of new signals because of breaking a plane of symmetry for compound **(1)** relative to the starting material. Additionally, it was noted that the total integrated proton number in the ^{1}H NMR spectrum of **(1)** decreased to eight owing to the hydrogen atom substitution at the *para* position to the amino group on 9*H*-carbazole for the bromine atom. In addition, the ^{13}C NMR spectrum of compound **(1)** exhibited twelve different environments of carbons owing to disturbance of product symmetry, whilst the starting material, 9*H*-carbazole, showed six environmentally different carbon signals. More specifically, the ^{13}C NMR spectrum of the molecule **(1)** showed a new negative peak at 112.3 ppm, which can be ascribed to the *ipso* carbon to the bromine atom, and the reason for this position to be more shielded is the heavy atom effect of bromine. Besides, the mass spectrometry of compound **(1)** exhibited two main integer masses at 245 and 247 in 1:1 ratio as anticipated owing to the presence of two bromine isotopes ^{79}Br and ^{81}Br. Moreover, the elemental analysis of **(1)** was in line with what was expected in order to prove the purity of **(1)**. Therefore, all these abovementioned results of ^{1}H NMR spectroscopy, ^{13}C NMR spectroscopy, elemental analysis and mass spectrometry demonstrated the formation of **(1)**.

2.2.1.2 Synthesis of 1,3-bis(3-bromo-9*H*-carbazole-9-yl)benzene M1

The reaction between **(1)** and 1,3-diiodobenzene was successfully performed to produce **M1** via an Ullmann reaction as described by Jeon *et al*. (**scheme 2.4**).[29] Potassium carbonate, copper powder and orthodichlorobenzene (ODCB) as a base, catalyst and solvent, respectively, were combined in a reaction performed at 180 °C in order to give rise to the required product **M1** in a yield of greater than 90%.

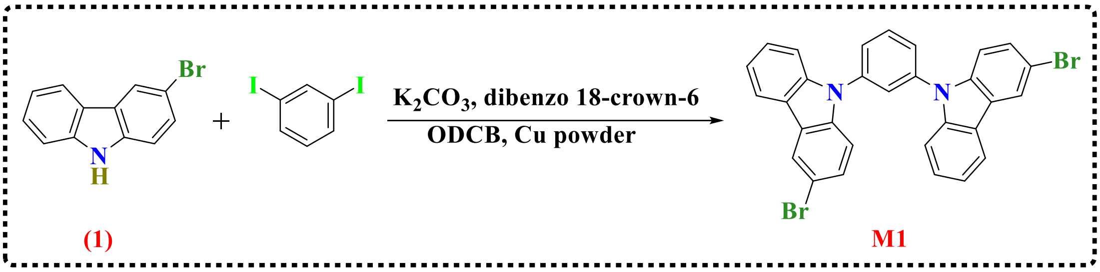

Scheme 2.4: Synthetic route of **M1**.

Ullmann coupling reaction is the mechanism underlying the synthesis of **M1**. This includes four stages and utilises stoichiometric amounts of copper metal at a high temperature in order to obtain **M1** in high yield. In the first stage, oxidative addition of copper metal to 1,3-diiodobenzene occurs to form copper iodide complex **(A)**, where the copper possesses the (II) oxidation state. The second stage involves transmetalation between copper iodide complex **(A)** and compound **(1)** in order to afford a second copper complex **(B)**. During the transmetalation stage, a deprotonation process of product **(1)** is carried out by a potassium carbonate base so as to generate potassium hydrogen carbonate with potassium iodide as side products. Thirdly, copper complex

(B) proceeds through reductive elimination to obtain 3-bromo-9-(3-iodophenyl)-9H-carbazole **(C)**. At last, the whole process is repeated for another equivalent of compound **(1)** with 3-bromo-9-(3-iodophenyl)-9H-carbazole **(C)** in order to form the desired molecule **M1** as outlined in **scheme 2.5**.

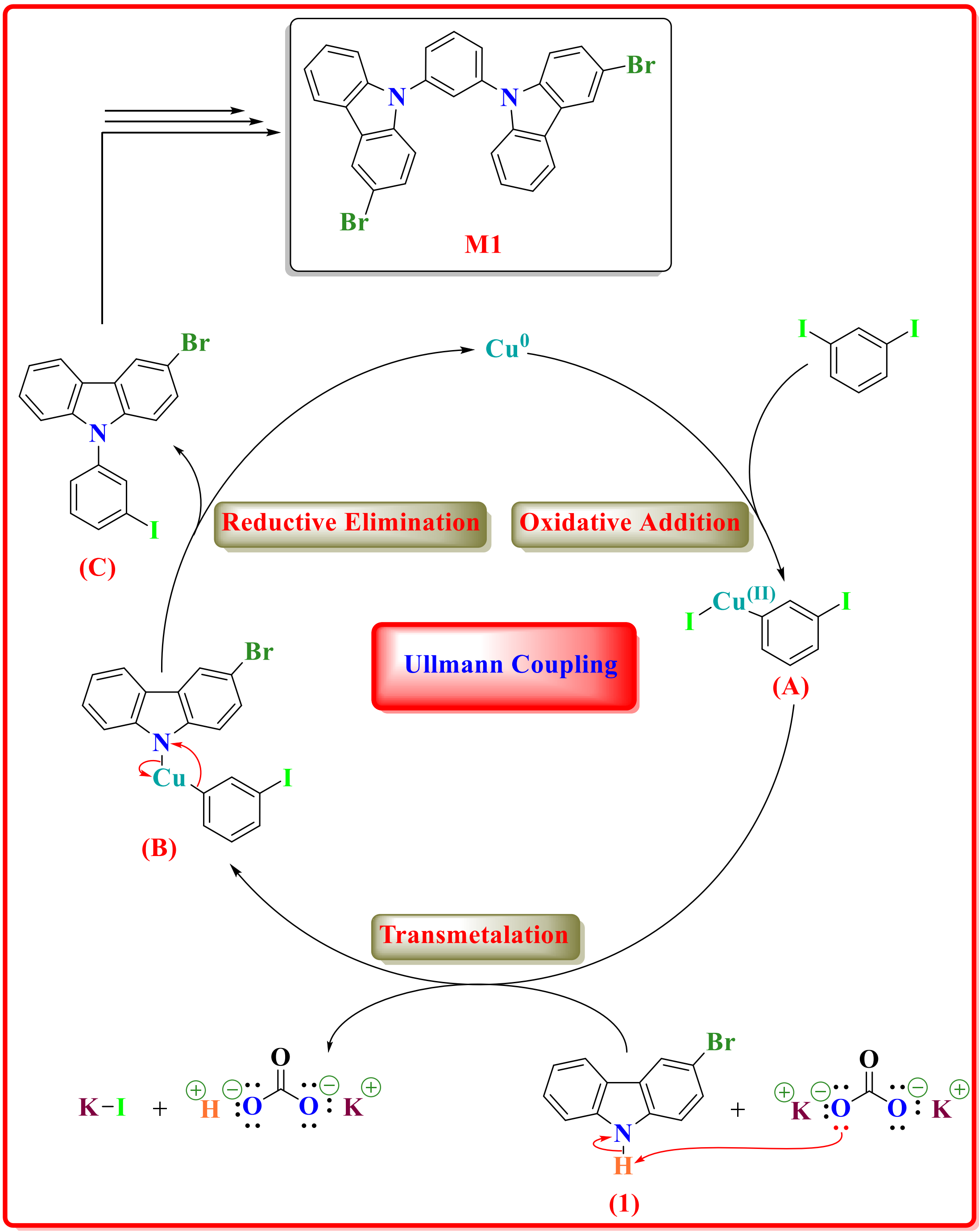

Scheme 2.5: The proposed mechanism of the formation of **M1** utilising Ullmann coupling reaction.

The purity and chemical structure of **M1** was sufficiently analysed using different characterisations, including ^{1}H NMR spectroscopy, ^{13}C NMR spectroscopy, TLC, mass spectrometry and elemental analysis. Based on the ^{1}H NMR spectrum of **M1**, a significant increase in proton number, with the integration of eighteen protons, is observed, which is the first indication of the formation of **M1** (**Figure 2.2**). Secondly, the ^{1}H NMR spectrum of **M1** demonstrated that the broad singlet peak at 8.08 ppm disappeared, representing the amino proton in the product **(1)**. This was the most vital evidence relating to the production of **M1**. By comparing the ^{1}H NMR spectrum of both **M1** and 1,3-diiodobenzene, the ^{1}H NMR spectrum of **M1** displays two triplets and a doublet of doublet peaks at 7.85, 7.73 and 7.67 ppm, respectively, which can be related to four protons of *m*-phenylene in the product **M1**, while their chemical shifts are different in 1,3-diiodobenzene. More specifically, two triplet signals at 7.85 and 7.73 ppm in the ^{1}H NMR spectrum of **M1** can be assigned to two sites of **3** and **4** on *m*-phenylene, respectively, according to their coupling constants. While the doublet of doublet peak at 7.67 ppm corresponds to the position at **5** on the *m*-phenylene due to its spin-spin coupling with the *ortho* proton of position **3** and the *meta* proton of the position **4**. Comparing both ^{1}H NMR spectrum for **(1)** and **M1**, two doublet peaks at 8.25 and 8.09 ppm in the product **M1** pertained to two positions of **1** and **2** on 3-bromo-9*H*-carbazole in the product **M1**, respectively, based on their coupling constants as shown in **Figure 2.2**. Furthermore, the doublet peak of 8.25 ppm at position **1** is more deshielded than the doublet peak of 8.09 ppm at position **2** due to the electronegativity of the adjacent bromine atom. Additionally, the doublet peak at 7.37 ppm in the molecule **M1** can be related to the position **7**, which is considered the proton of the *ortho* position to the amino group and the *meta* position to the bromine group on the 3-bromo-9*H*-carbazole, as there is the adjacent *ortho* proton only, bringing about its spin-spin coupling with the adjacent *ortho* proton to obtain the doublet peak. Moreover, the triplet of doublet peak at 7.32 ppm in the ^{1}H NMR spectrum of **M1**, attributing to the *para* proton to the amino group on the 3-bromo-9*H*-carbazole at the site of **8**, as shown in **Figure 2.2**, is more shielded than other peaks due to the impact of the electron-donating amino group on the *para* location. Also, the total integrated proton number in the ^{1}H NMR spectrum of **M1** increased to eighteen protons, which was one of the factors to prove the successful formation of **M1**. In general, these factors offered obvious evidence for product **(1)** association with 1,3-diiodobenzene to create **M1**.

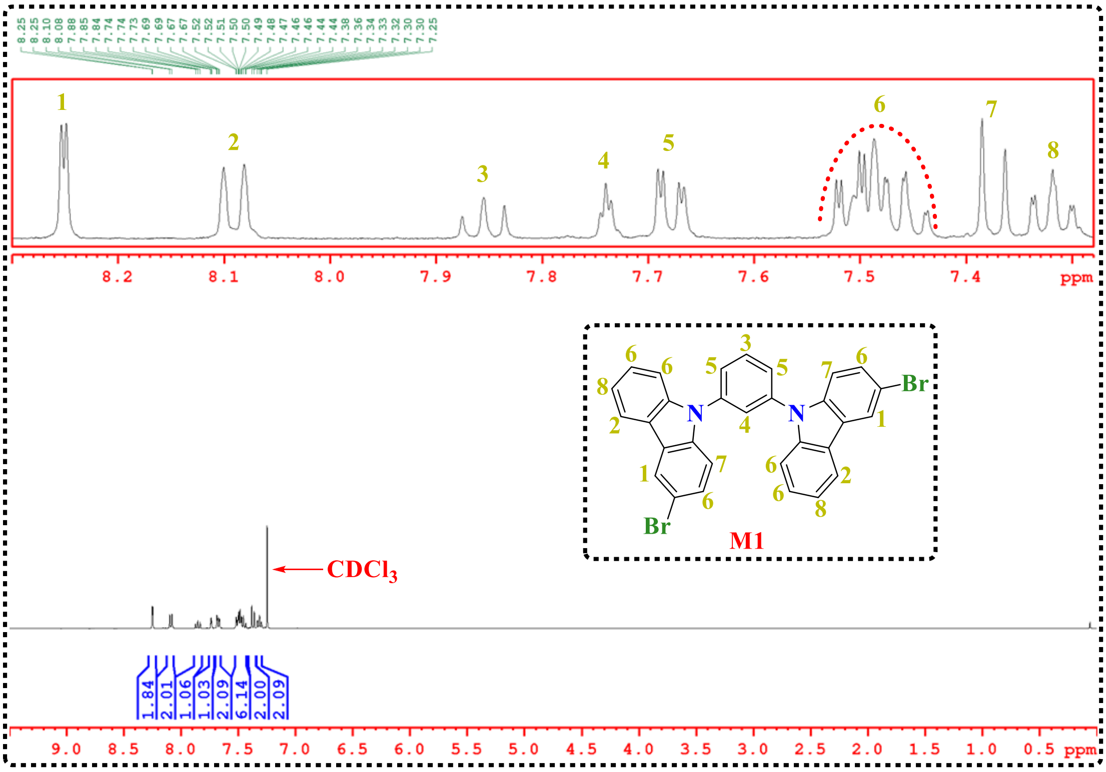

Figure 2.2: ^{1}H NMR spectrum of **M1** in CDCl$_3$.

Significantly, the ^{13}C NMR spectrum of **M1** shows a variety of carbon environments with a rise in these concerning **M1**, offering excellent evidence for the formation of **M1** (**Figure 2.3**). More importantly, a signal at 94.9 ppm in the ^{13}C NMR spectrum of 1,3-diiodobenzene, which can be assigned to *ipso* carbons bound to two iodine atoms, is shifted towards a deshielded region at the position of 139.1 ppm in the ^{13}C NMR spectrum of **M1** owing to the strong inductive effect of a nitrogen atom attached to the *ipso* carbon on the *m*-phenylene of **M1**. In addition, negative peaks of **1** and **2** in the ^{13}C NMR spectrum of **M1** can be attributed to *ipso* carbons directly bonded to nitrogen atoms on 3-bromo-9*H*-carbazole moiety due to the inductive effect of nitrogen atom on *ipso* carbons to be downfield. Additionally, a negative peak of **14** in the ^{13}C NMR spectrum of **M1** can be ascribed to the *ipso* carbon directly attached to the bromine atom due to the heavy atom effect of bromine. Moreover, positive peaks of **15** and **16** in the ^{13}C NMR spectrum of **M1** are shifted to the shielded area, meaning that these carbons can be *ortho* to the nitrogen atom due to the impact of an electron-donating amino group. More precisely, the electron-donating amino group with a small effect of the electron-withdrawing bromine group affect the peak **15**. In contrast, peak **16** is influenced by the electron-releasing amino group only and peak **16** thereby is more shielded than peak **15**. These signals mentioned above in the ^{13}C NMR spectrum of **M1** prove the formation of product **M1**. In addition, the mass spectrometry of **M1** displayed the main integer signals at 564.8, 566.8, and 568.8 in a 1:2:1 ratio as expected due to the presence of two bromine isotopes ^{79}Br and ^{81}Br. Moreover, the elemental analysis determined the following result for $C_{30}H_{18}Br_2N_2$: C, 63.75; H, 3.33; Br, 28.01; N, 4.79, which concurs with its proposed formula. Therefore, all these abovementioned results of ^{1}H NMR spectroscopy, ^{13}C NMR spectroscopy, elemental analysis and mass spectrometry proved the formation of **M1**.

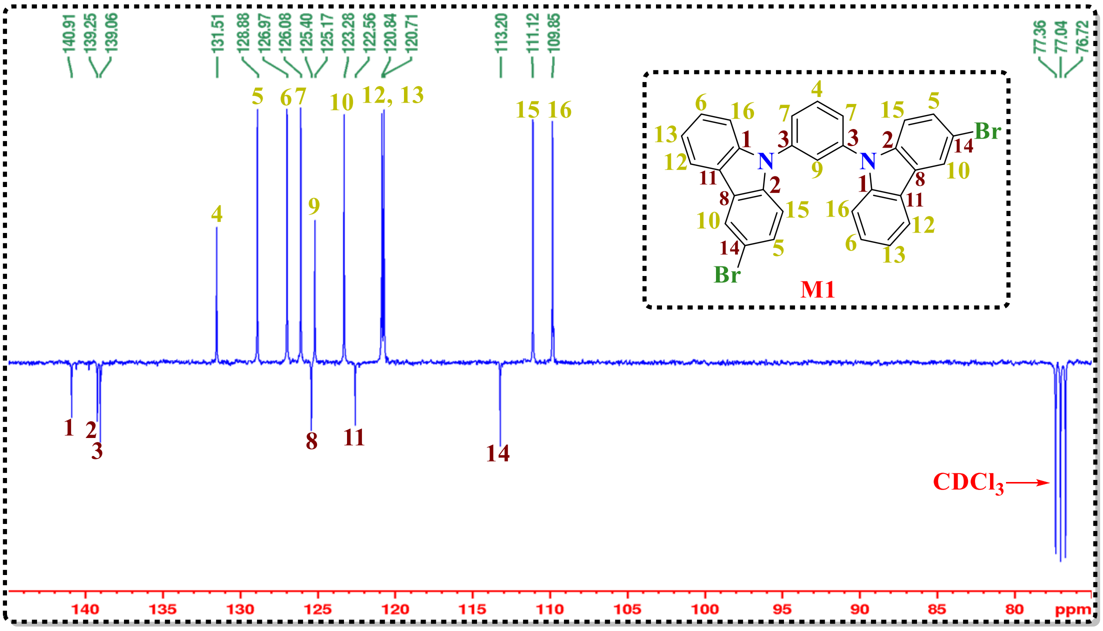

Figure 2.3: ^{13}C NMR spectrum of **M1** in $CDCl_3$.

2.2.2 Synthesis of Host Monomer M2

2.2.2.1 Synthesis of 1,6-bis(4-bromophenoxy)hexane (2)

Scheme 2.6 shows the dietherification reaction that was appropriately carried out to generate **(2)** according to Zhang *et al.*[30] The preparation of product **(2)** was conducted by reacting 4-bromophenol with 1,6-dibromohexane in the presence of potassium carbonate and anhydrous acetone as a base and solvent, respectively. Recrystallisation was conducted for the crude of **(2)** in order to obtain the desired pure product **(2)**, which was a white solid, in an acceptable yield (77%).

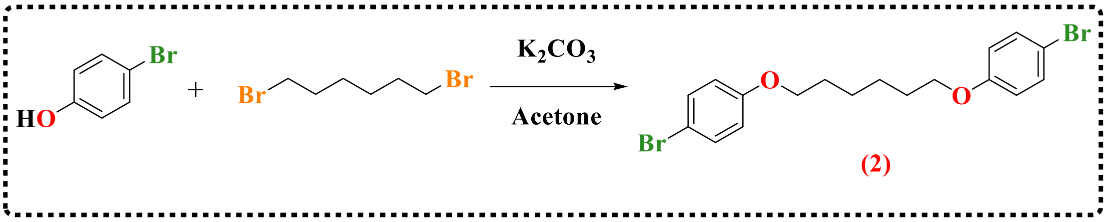

Scheme 2.6: Synthetic route of **(2)**.

The synthesising compound **(2)** reaction follows the Williamson reaction mechanism of a bimolecular nucleophilic substitution (S_N2) and includes three steps, as depicted in **scheme 2.7**. In the first phase, deprotonation of the hydroxyl group in 4-bromophenol is carried out to afford 4-bromophenolate as an intermediate of a phenoxide anion, which functions as a nucleophile, using potassium carbonate as a base. The weaker base is utilised in the reaction as the phenoxide anion is a resonance stabilised conjugate base, and thereby 4-bromophenol is a relatively more acidic. In the subsequent step, one of the terminal carbon atoms bound directly to the bromine atom on 1,6-dibromohexane is attacked by the formed phenoxide anion to form 1-bromo-4-((6-bromohexyl)oxy)benzene **(A)** and potassium bromide as a salt. Finally, a further deprotonation process is carried out for another equivalent of 4-bromophenol to obtain a phenoxide anion, thereby attacking the α carbon to the bromine atom on the aliphatic area of **(A)**. Thus, this gives rise to the generation of the desired molecule **(2)** as a bisether product.

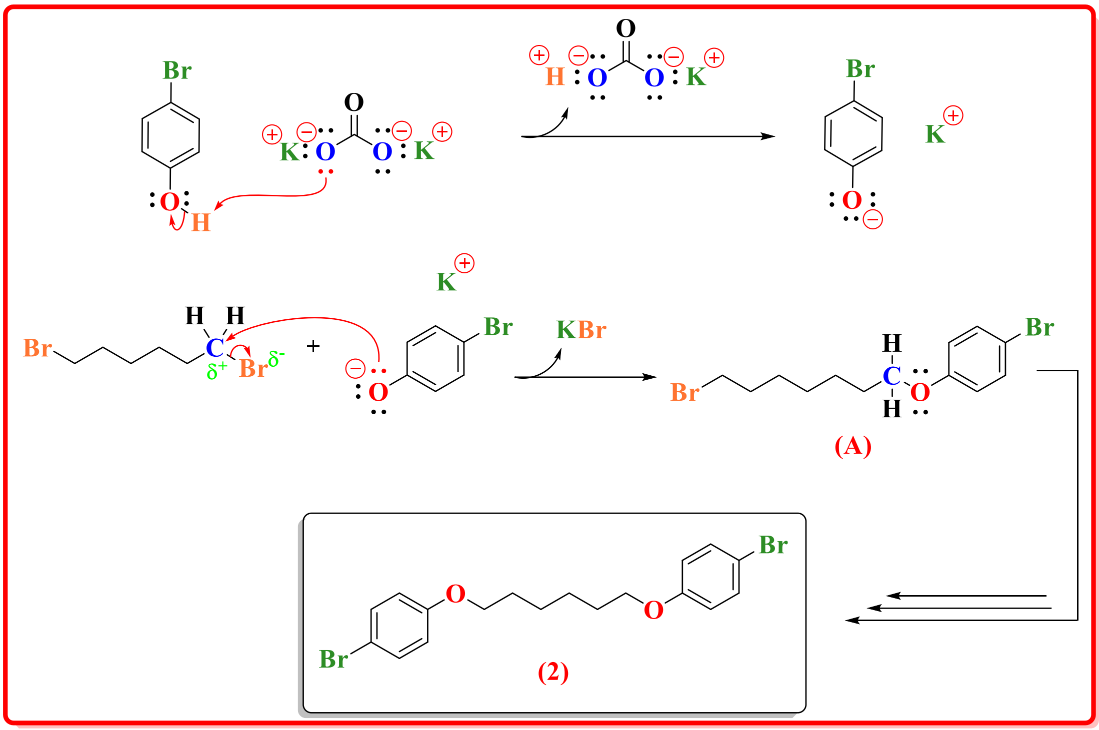

Scheme 2.7: The proposed mechanism of the formation of **(2)** using the dietherification reaction.

Compound **(2)** was adequately characterised using different techniques, including ^{1}H NMR spectroscopy, ^{13}C NMR spectroscopy, TLC, mass spectrometry and elemental analysis. The critical analysis of **(2)** was conducted by ^{1}H NMR spectroscopy in order to check that the hydroxyl group had disappeared from 4-bromophenol and that peaks attributed to 1,6-dibromohexane had appeared in an aliphatic area. Using the ^{1}H NMR spectrum for **(2)**, the broad singlet signal at 4.96 ppm, attributed to the 4-bromophenol hydroxyl group, was no longer visible, indicating the successful dietherification reaction. In addition, the ^{1}H NMR spectrum of **(2)** exhibited two doublet peaks at 7.35 and 6.75 ppm in the aromatic area with the integration of eight protons, which can be related to protons of *p*-phenylene, whilst a triplet peak and two multiples at 3.92, 1.83-1.76 and 1.55-1.44 ppm, respectively, were observed in the aliphatic area with the integration of twelve protons. The total number of integrated protons in the ^{1}H NMR spectrum of the product **(2)** in aromatic and aliphatic regions of twenty protons with the disappearance of broad signal for proton of the hydroxyl group proved a successful formation of the product **(2)**. Particularly, the doublet peak of 6.75 ppm in the ^{1}H NMR spectrum of **(2)** can be assigned to *ortho* protons to the ether group because of an increase of electron density in the *ortho* position affected by the electron-donating group of the ether group, resulting in a lower chemical shift. Additionally, the doublet peak of 7.35 ppm in the ^{1}H NMR spectrum of **(2)** can be attributable to *ortho* protons to the bromine atom due to the bromine atom's induction that causes a lowering of electron density in the *ortho* position, giving rise to a slightly deshielding of a specified signal. Furthermore, the triplet peak at 3.92 ppm, with the integration of four protons, can be assigned to protons of the methylene group bound to the oxygen atom. This triplet peak is more deshielded than the other peaks in the aliphatic area because of the inductive effect of the oxygen atom. Compared to 1,6-dibromohexane, the triplet peak at 3.40 ppm in the ^{1}H NMR spectrum of 1,6-dibromohexane, which belongs to protons of the methylene group bound to the bromine atom, was deshielded to the position of 3.92 ppm in the product **(2)** owing to the change of the adjacent atom from the bromine atom to the more electronegative oxygen atom that led to deshielding the peak. Thus, all of these mentioned peaks of the ^{1}H NMR spectroscopy of the product **(2)** provided apparent evidence for the reaction's success.

Seven carbon environments in the ^{13}C NMR spectrum of **(2)** were observed, agreeing with the expected structure of **(2)**. In particular, the ^{13}C NMR spectrum of **(2)** exhibited negative signals at 158.3 and 112.7 ppm, which can be ascribed to *ipso* carbons bonded to oxygen and bromine atoms, respectively. More interestingly, the peak at 158.3 ppm was more downfield than the peak at 112.7 ppm on account of the strong inductive effect of the oxygen atom, while the peak at 112.7 ppm was more upfield because of heavy atom effect of bromine. Compared to 4-bromophenol, a negative signal at 154.5 ppm in the ^{13}C NMR spectrum of 4-bromophenol, which can be attributed to the *ipso* carbon bound to the hydroxyl group, was deshielded in the ^{13}C NMR spectrum of **(2)** to the position of 158.3 ppm owing to the conversion of the hydroxyl moiety to the ether group. Furthermore, the ^{13}C NMR spectrum of **(2)** showed positive peaks at resonances of 116.3 and 132.3 ppm, which can be related to *ortho* and *meta* carbons to the ether group on *p*-phenylene, respectively. More specifically, the signal at 116.3 ppm is ascribed to *ortho* carbons to the ether group on *p*-phenylene due to the strongly electron-donating effect of ether group on the specified signal, whereas the peak at 132.3 ppm is assigned to *ortho* carbons to the bromine atom on *p*-phenylene because of the inductive effect of bromine atom on the determined peak. Moreover, the ^{13}C NMR spectrum of **(2)** exhibited negative signals at 68.2, 29.1 and 25.8 ppm, which can be assigned to aliphatic carbons of compound **(2)**. Significantly, the signal at 68.2 ppm can be attributed to carbon of the methylene group attached directly to the oxygen atom due to a high electronegativity of oxygen atom. The ^{13}C NMR spectral analysis of **(2)** demonstrated the successful formation of product **(2)**. In addition, the mass spectrometry of **(2)** determined the main integer signals to be at 426, 428, and 430 in a 1:2:1 ratio as predicted because of the presence of two bromine isotopes ^{79}Br and ^{81}Br. Hence, all these abovementioned results of ^{1}H NMR spectroscopy, ^{13}C NMR spectroscopy, and mass spectrometry proved the formation of **(2)**.

2.2.2.2 Synthesis of 1,6-bis(4-(4,4,5,5-tetramethyl-1,3,2-dioxaborolan-2-yl)phenoxy)hexane M2

Generation of **M2** was successfully performed through the synthesis of borylated bisether according to Hermann *et al*.[31] The preparation of **M2** was conducted perfectly by reacting product **(2)** with 2-isopropoxy-4,4,5,5-tetramethyl-1,3,2-dioxaborolane (*i*-PrOBpin) using two equivalents of *n*-butyllithium (*n*-BuLi), as illustrated in **scheme 2.8**. Column chromatography was utilised in order to purify **M2**; the final product was a colourless solid, produced with an 89% yield.

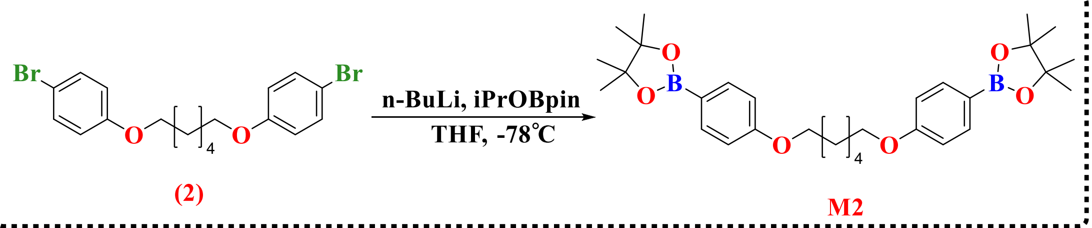

Scheme 2.8: Synthetic route of **M2**.

Numerous analytical methods, including ^{1}H NMR spectroscopy, ^{13}C NMR spectroscopy, TLC, mass spectrometry and elemental analysis were applied in order to verify the purity and chemical structure of **M2**. After **M2** purification using column chromatography, one spot only was noted on the TLC, indicating no side products were present with **M2**. A significant singlet peak at 1.32 ppm is observed on the ^{1}H NMR spectrum of **M2**, which can be ascribed to protons of methyl groups for pinacol boronic ester groups with the integration of twenty-four protons; this presents obvious evidence of the complete conversion of bromine atoms to pinacol boronic ester groups (**Figure**

2.4). In addition, the ^{1}H NMR spectrum of **M2** shows a predicted number of protons in both aromatic and aliphatic regions with full integration of forty protons. It can be seen from **Figure 2.4**, the doublet peak at 7.73 can be ascribed to *ortho* protons to pinacol boronic ester groups on the *p*-phenylene due to an electron-withdrawing effect of pinacol boronic ester groups. While the doublet peak at 6.88 can be related to *ortho* protons to the ether group on the *p*-phenylene because of a strongly electron-donating impact of ether groups. Additionally, the ^{1}H NMR spectrum of **M2** displayed the triplet peak at 3.99 ppm, which can be assigned to protons of the methylene group attached to the oxygen atom owing to the inductive effect of the oxygen atom.

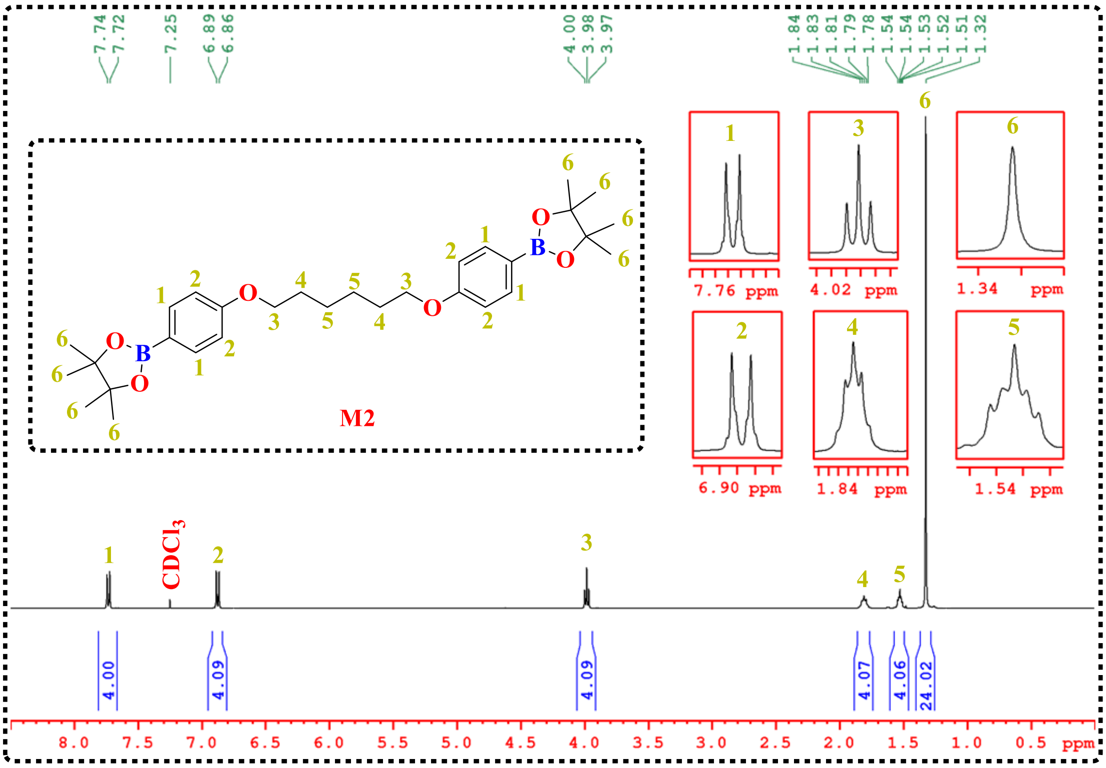

Figure 2.4: ^{1}H NMR spectrum of **M2** in $CDCl_3$.

The ^{13}C NMR spectrum of **M2** shows eight different carbon environments, which are in accordance with structure of **M2**, except the peak pertaining to the *ipso* carbon to the boron atom as it is not visible in the ^{13}C NMR spectrum because of broadening of quaternary carbon attached to quadrupolar boron nucleus (**Figure 2.5**). More interestingly, the ^{13}C NMR spectrum of **M2** exhibits new signals at 24.9 and 83.5 ppm, which can be attributed to primary methyl group carbons and quaternary carbons on the pinacol boronic ester groups; this offers a clear indication that the synthesis of **M2** was successful. Furthermore, a negative peak of **1** in the ^{13}C NMR spectrum of **M2** can be ascribed to *ipso* carbons to oxygen atoms on the *p*-phenylene due to the strong inductive effect of the oxygen atom. By looking at positive signals in the ^{13}C NMR spectrum of **M2**, a signal **8** is around double the height of the other two peaks, indicating that the peak **8** corresponds to methyl groups' carbons of the pinacol boronic ester groups, and signals **2** and **3** can be related to protonated carbons on *p*-phenylene. More precisely, the peak **3** in the ^{13}C NMR spectrum of **M2** is shifted to the shielded area in the aromatic region, meaning that this peak can be *ortho* carbons to the oxygen atom on *p*-phenylene due to the impact of the electron-donating ether group. Whilst a peak **2** in the ^{13}C NMR spectrum of **M2** is in the downfield area in the aromatic area, suggesting that this peak can be *ortho* carbons to the pinacol boronic ester groups on *p*-phenylene owing to the electron-withdrawing effect of the pinacol boronic ester group. Furthermore, the mass spectrometry of **M2** showed the main integer peaks at 521.3, 522.3, and 523.3 due to the presence of two boron isotopes ^{10}B and ^{11}B. Moreover, the elemental analysis determined the following results for $C_{30}H_{44}B_2O_6$: C, 69.10; H, 8.61, which concurs with its proposed formula. Therefore, all these abovementioned results of ^{1}H NMR spectroscopy, ^{13}C NMR spectroscopy, elemental analysis and mass spectrometry proved the formation of **M2**.

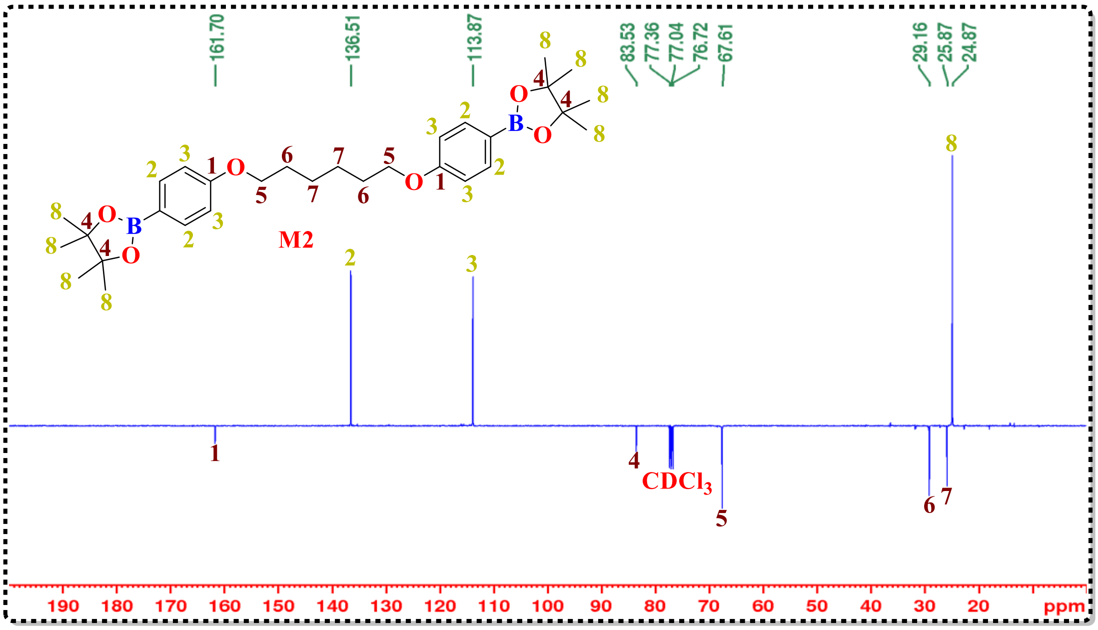

Figure 2.5: ^{13}C NMR spectrum of **M2** in $CDCl_3$.

2.2.3 Synthesis of TADF Emitter Monomer **M3**

A schematic representation of the synthetic route followed to produce **M3**, which was utilised as a TADF emitter, is shown in **scheme 2.9**. The purities of the compounds were verified using different techniques such as ^{1}H NMR spectroscopy, ^{13}C NMR spectroscopy, mass spectrometry, and elemental analysis.

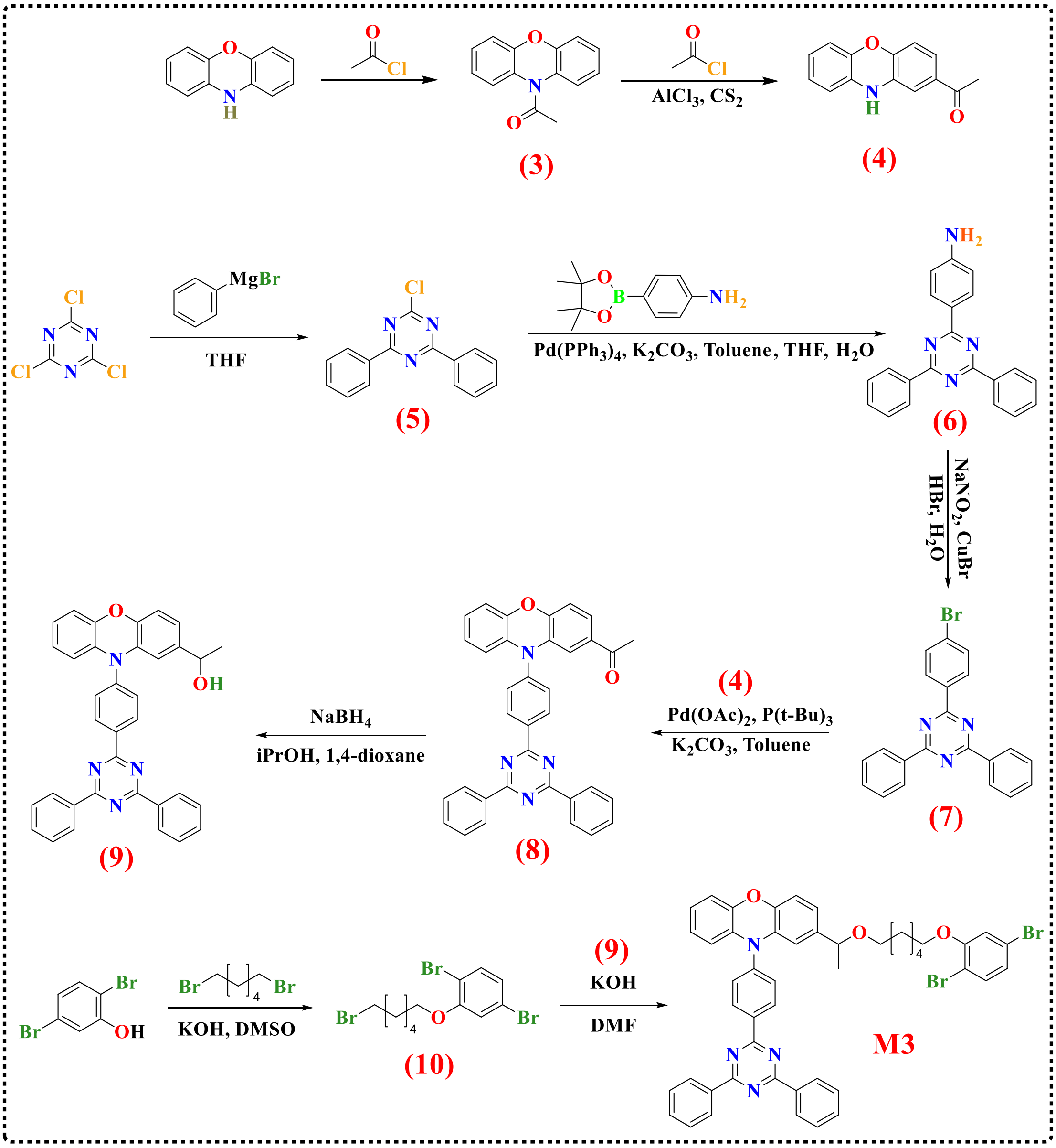

Scheme 2.9: Preparation of TADF emitter monomer **M3**.

2.2.3.1 Synthesis of 10-acetylphenoxazine (3)

10-Acetylphenoxazine **(3)** was synthesised in good yield using the procedure carried out by Vanderhaeghe *et al.*[32] The reaction between acetyl chloride and 10*H*-phenoxazine was conducted using triethylamine as a base in order to generate **(3)**, as illustrated in **scheme 2.10**. Following the entire purification process, compound **(3)** appeared as a white solid. The crude product was suitably extracted and washed five times using DCM and distilled water. The product underwent additional purification with the use of column chromatography utilising silica gel with petroleum ether as the stationary phase, together with petroleum ether: ethyl acetate in a 4:1 ratio as an eluent. An excellent yield (92%) of a pure white solid, i.e., compound **(3)**, was obtained.

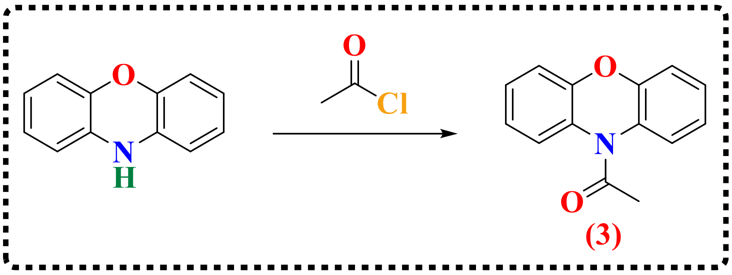

(3)

Scheme 2.10: Synthetic route of **(3)**.

The mechanism underlying the acylation reaction for 10*H*-phenoxazine with acid chloride is a type of nucleophilic addition-elimination reaction. This process comprises three main steps, as illustrated in **scheme 2.11**. Firstly, the nitrogen atom of the amino group on 10*H*-phenoxazine acts as a nucleophilic component, which attacks an acetyl chloride carbonyl carbon through the donation of a lone pair of electrons on the amine nitrogen of 10*H*-phenoxazine; this gives rise to the formation of a highly unstable ionic intermediate **(A)**. The following step involves two simultaneous stages, i.e., formation of the carbon-oxygen double bond and leaving the chlorine atom by taking one of the central carbon’s electrons as a chloride anion. The double bond of carbonyl is formed by transferring one of the lone pairs of electrons from the oxygen atom to the central carbon, leading to the generation of a second intermediate **(B)**. Finally, triethylamine is employed as a base in order to remove a proton from the intermediate **(B)**, resulting in the neutralisation of the molecule and generating a product **(3)** as a tertiary amide, and triethylammonium chloride as a salt.

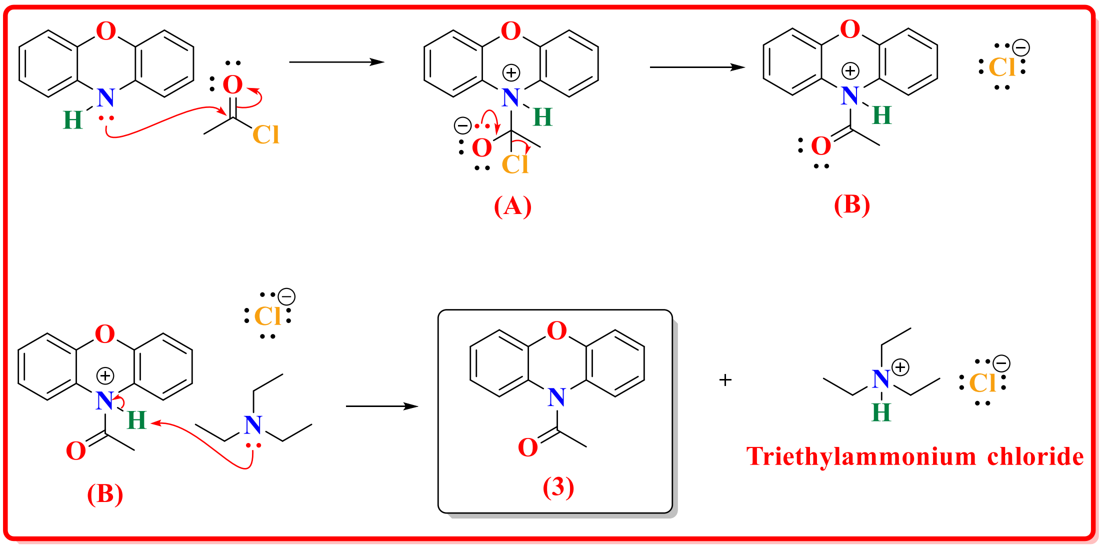

Scheme 2.11: The proposed mechanism of the formation of **(3)** using the acylation reaction.

The chemical structure and purity of compound **(3)** were verified using different techniques, including ^{1}H NMR spectroscopy, ^{13}C NMR spectroscopy, mass spectrometry and elemental analysis. The ^{1}H NMR spectrum of **(3)** exhibited only singlet peak at 2.35 ppm with the integration of three protons, which can be ascribed to methyl protons of the acetyl group. Furthermore, the ^{1}H NMR spectrum of **(3)** proved the entire disappearance of the broad singlet peak at 8.16 ppm for the amino proton, establishing the formation of product **(3)** as a tertiary amide. Additionally, the ^{1}H NMR spectrum of **(3)** showed a doublet of doublet resonance at 7.51 ppm with the integration of two protons, which can be attributable to two *ortho* aromatic protons to the amide group due to a through-space effect of carbonyl π bond of the amide group on the specified signal to be deshielded. Also, the ^{1}H NMR spectrum of **(3)** presented a triplet of doublet peak at 7.22 ppm, which can be attributed to two *para* protons to the amide group because there are two adjacent *ortho* protons and one *meta* proton to this determined proton, bringing about its coupling with neighbouring protons to produce the triplet of doublet peak. Interestingly, this triplet of doublet signal at the slightly upfield resonance of 7.22 ppm was mainly selected for *para* protons to the amide group rather than the adjacent proton relating to the *para* position to the ether group on account of the moderately electron-donating amide group that impacts the *para* position slightly. In addition, the total number of integrated protons in the ^{1}H NMR spectrum of

(3) was eleven, offering further evidence for the synthesis and presence of the tertiary amide group in the molecule **(3)**.

The ^{13}C NMR spectroscopy of **(3)** displayed eight different environments of carbon atoms, indicating the successful acylation reaction of **(3)**. More specifically, the ^{13}C NMR spectrum of the molecule **(3)** revealed two additional signals at 23.1 and 169.3 ppm, which can be ascribed to the primary carbon of methyl group and the carbonyl carbon of the product **(3)**, respectively. Besides, the main integer mass of 225.1 was obtained by mass spectrometry of **(3)**, which corresponds to the predicted structure of **(3)**. Thus, the desired configuration of the product **(3)** was confirmed by the results from ^{1}H NMR spectroscopy, ^{13}C NMR spectroscopy, and mass spectrometry. Comparison with the literature data revealed excellent agreement.[33]

2.2.3.2 Synthesis of 2-acetylphenoxazine (4)

Müller's procedure was successfully followed for preparing compound **(4)**.[34] The preparation of **(4)** was performed by reacting **(3)** with acetyl chloride in the presence of aluminium chloride as a catalyst, together with carbon disulphide as a solvent, under refluxing conditions as shown in **scheme 2.12**. The final product **(4)** was perfectly produced with an impressive yield of 90%; greenish yellow crystals were formed.

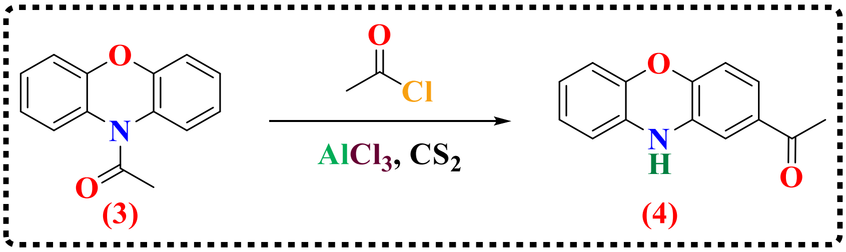

Scheme 2.12: Synthetic route of **(4)**.

The proposed mechanism of the prepared compound **(4)** is shown below. It is formed using a type of electrophilic aromatic substitution reaction, which involves three empirical phases of the Friedel-Crafts acylation reaction; product **(4)** is attained following the acylation of compound **(3)** (**scheme 2.13**). Firstly, a reaction occurs between acetyl chloride and a Lewis acid catalyst, such as aluminium chloride. Since the latter functions as an electron acceptor in the acylation reaction, the reaction generates a tetrachloroaluminate anion $[AlCl_4]^-$ and an acetyl cation as an acylium ion, which acts as a strong electrophilic constituent in the reaction. The reason for the formation of the acylium ion is that acetyl chloride is not sufficiently strong to act as an electrophilic moiety in the reaction. Secondly, the electrophilic carbocation part on the acylium ion is attracted to the π electrons system on the product **(3)**, attacking the acylium ion's electrophilic carbocation by a double bond from a benzene ring of the product **(3)**. This is selectively targeted by a strongly electron-donating group of an ether group on the product **(3)** rather than an amide group. Therefore, the ether group donates electron density into the ring through resonance, and then one of the lone pairs of electrons on the oxygen atom of the compound **(3)** is delocalised into the ring, giving rise to the *ortho* and *para* positions to the ether group to be more electron rich. The *ortho* position to the ether group is here disfavoured due to the highly steric hindrance effect. In this case, the aromaticity is broken to form a cation intermediate **(A)**. Thirdly, the proton attached to the product **(A)** at the *para* position to the ether group is eliminated by the tetrachloroaluminate anion to reform the carbon-carbon double bond in the aromatic moiety, leading to a formation of another intermediate **(B)**, an aluminium chloride catalyst, and hydrochloric acid. Next, a hydrolysis of an amide group for the intermediate **(B)** is performed by a hydronium ion in order to convert the amide group to an amino group. Lastly, the target product of **(4)** is gained after the hydrolysis process, as illustrated in **scheme 2.13**.

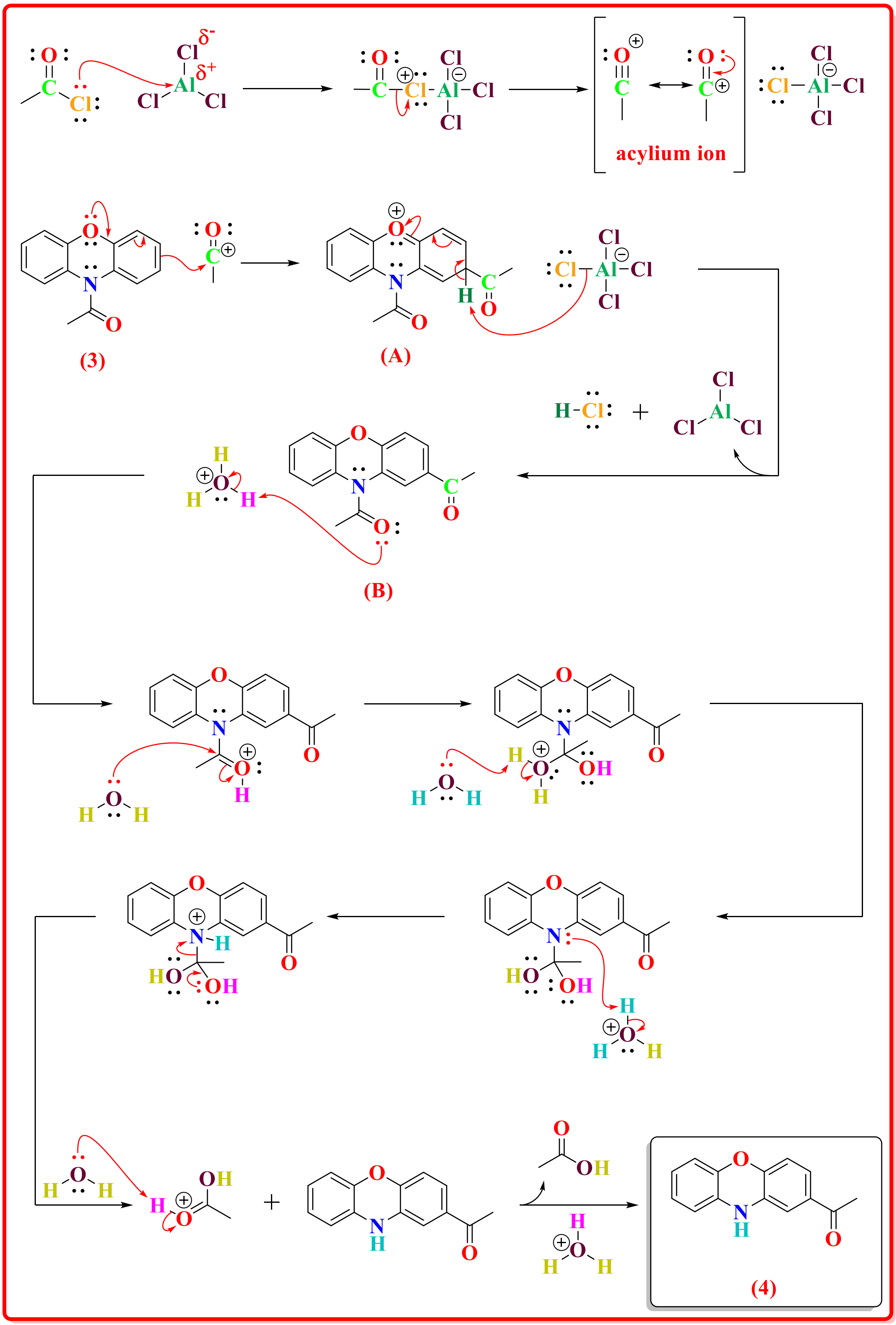

Scheme 2.13: The proposed mechanism of the formation of **(4)** using the Friedel-Crafts reaction.

The exact purity and chemical formula of **(4)** were analysed through different characterisation techniques, such as ^{1}H NMR spectroscopy, ^{13}C NMR spectroscopy, TLC, mass spectrometry and elemental analysis. A broad singlet peak at 8.42 ppm was observed in the ^{1}H NMR spectrum of **(4)**, which can be ascribed to the amino proton owing to the fast intermolecular exchange of amine proton, giving the first indication of converting the tertiary amide group to the amino group in the product **(4)**. In addition, the ^{1}H NMR spectrum of **(4)** exhibited only singlet peak in the aliphatic region at 2.44 ppm with the integration of three protons, which can be attributed to methyl protons of the acetyl group. Furthermore, the ^{1}H NMR spectrum of **(4)** showed an increase of signals' positions relative the starting material of **(3)** because of breaking a plane of symmetry for compound **(4)** by the acetyl group. Moreover, the ^{1}H NMR spectrum of **(4)** presented two doublet peaks at 6.96 and 6.69 ppm, which be assigned to the proton between the amino group and the acetyl group and the proton positioning *ortho* to the ether group and *meta* to the acetyl group, respectively, owing to their coupling constant. Also, the ^{1}H NMR spectrum of **(4)** displayed two triplet of doublet peaks at 6.76 and 6.59 ppm, which be selectively specified for the *para* proton to the ether group and the *para* proton to the amino group on the benzene ring that does not include the acetyl group, respectively, on account of strongly electron-donating effects of the ether and amino groups on the determined signals to be more shielded. All mentioned resonances in the ^{1}H NMR spectrum of **(4)** gave clear evidence of succeeding the acylation reaction of **(4)**.

The ^{13}C NMR spectrum of **(4)** displayed an evident shift towards a downfield region in the signal position of the carbonyl group carbon to be at 196.5 ppm compared to the molecule **(3)**, which offered evidence for the change in position of the carbonyl group for the molecule **(4)** to be attached to the aromatic region in the *para* position to the ether group. In addition, the ^{13}C NMR spectrum of the molecule **(4)** revealed a positive signal at 26.7 ppm, which can be ascribed to the primary carbon of the methyl group in the product **(4)**. Moreover, the mass spectrometry of **(4)** showed the main integer peak at 225.1, which concurred with the desired structure of molecule **(4)**. Therefore, all these abovementioned results of ^{1}H NMR spectroscopy, ^{13}C NMR spectroscopy, and mass spectrometry demonstrated the successful formation of **(4)**.

2.2.3.3 Synthesis of 2-chloro-4,6-diphenyl-1,3,5-triazine (5)

Synthesis of **(5)** was appropriately prepared as reported by Zhong *et al*.[35] The reaction carried out between cyanuric chloride and the Grignard reagent phenylmagnesium bromide in anhydrous tetrahydrofuran as a solvent, to produce molecule **(5)** as shown in **scheme 2.14**. A white solid compound **(5)** was obtained after purification of the crude product using column chromatography; the pure product yield was acceptable, i.e., approximately 61%.

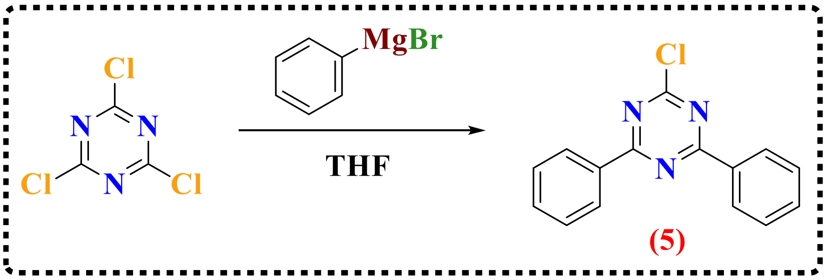

Scheme 2.14: Synthetic route of **(5)**.

The reaction mechanism of compound **(5)** is carried out in two stages, as illustrated in **scheme 2.15**. The initial stage involves the formation of a Grignard reagent through a free radical reaction, which comprises two main steps. The first step is a transfer of a single electron from magnesium to the carbon-bromine bond to generate phenyl radical and magnesium bromide radical (**$^{\bullet}$Mg-Br**). The second step is a recombination of phenyl radical and magnesium bromide radical, bringing about the Grignard reagent's formation, which acts as a strongly nucleophilic component because it contains a carbanion. Interestingly, a covalent bond between carbon and magnesium on the Grignard reagent is highly polarised towards carbon. As a result, there is a partial positive charge on the magnesium atom and a partial negative charge on the carbon atom, making the Grignard reagent strongly nucleophilic and basic.

In the second stage, a carbon atom bound to a chlorine atom (**C-Cl**) on cyanuric chloride is attacked by the phenyl group carbon, which contains a partial negative charge on the Grignard reagent, generating molecule **(A)** with magnesium bromide chloride. Finally, the whole process is repeated for another equivalent of the Grignard reagent with the resulting molecule **(A)** in order to form the desired molecule **(5)** as outlined in **scheme 2.15**.

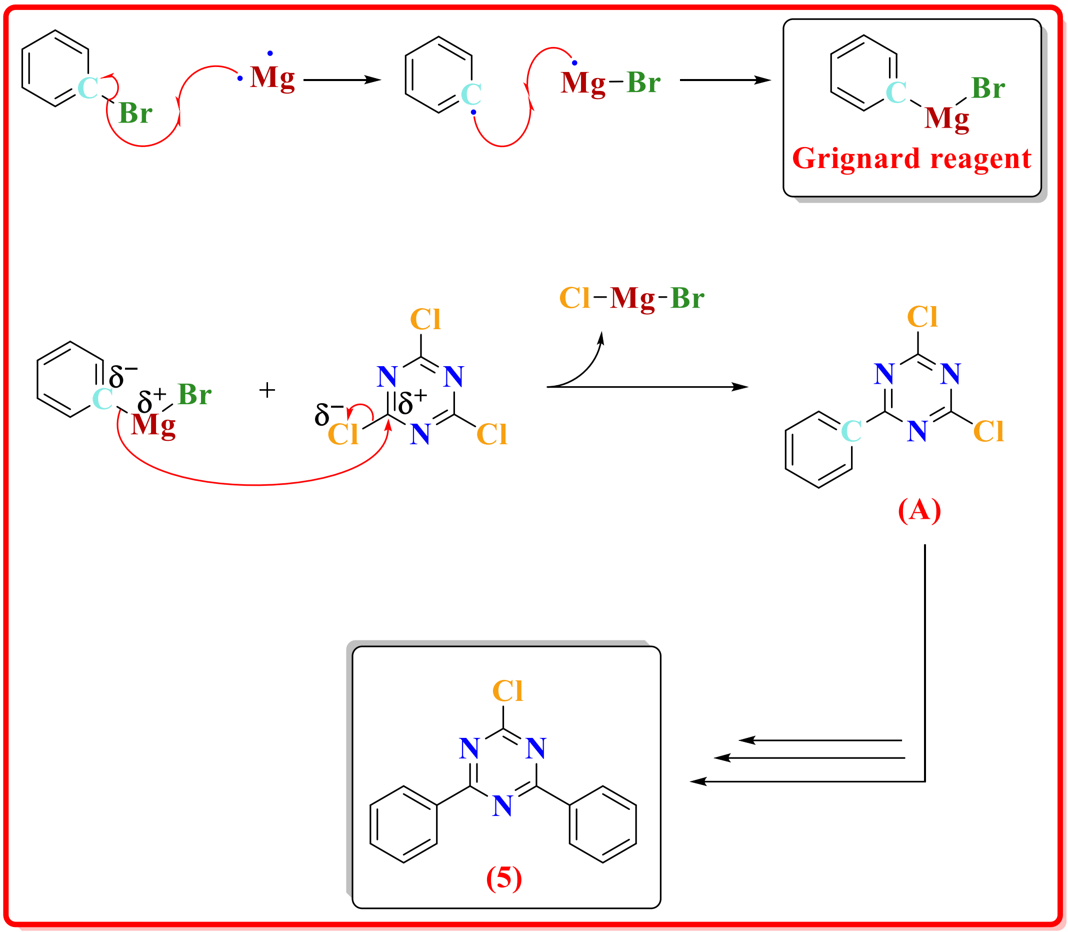

Scheme 2.15: The proposed mechanism of the formation of **(5)**.

Structure and purity of compound **(5)** were established using ^{1}H NMR spectroscopy, ^{13}C NMR spectroscopy, mass spectrometry and elemental analysis, and the acquired results were compared with the published literature. The ^{1}H NMR spectroscopy of **(5)** exhibited doublet of doublet, triplet of triplet, and triplet peaks in the aromatic region at 8.65, 7.65 and 7.57 ppm, respectively, which exactly matches the expected structural molecule of **(5)**. More specifically, the doublet of doublet peak at 8.65 ppm in the ^{1}H NMR spectrum of **(5)** can be ascribed to the four *ortho* protons to 1,3,5-triazine in diphenyl groups due to a strongly electron-withdrawing effect of 1,3,5-triazine ring on *ortho* locations to be more downfield. In addition, the triplet of triplet peak at 7.65 ppm in the ^{1}H NMR spectrum of **(5)** can be related to the two *para* protons to 1,3,5-triazine ring in diphenyl groups on account of the integration of two protons only and the electron-withdrawing group that affects the *para* location in terms of deshielding the peak. By process of elimination, the triplet signal at 7.57 ppm in the ^{1}H NMR spectrum of **(5)** can be attributable to the two *meta* protons to the 1,3,5-triazine ring in diphenyl groups. Furthermore, the total number of integrated protons in the ^{1}H NMR spectroscopy of **(5)** was ten; this integration analysis matched with the structure of product **(5)**. All the mentioned peaks with the integration analysis in the ^{1}H NMR spectroscopy of **(5)** proved the successful composition of molecule **(5)**.

The ^{13}C NMR spectrum of the molecule **(5)** displayed six different environments of carbon atoms in the aromatic area, offering further evidence for the the molecule **(5)**. More precisely, the ^{13}C NMR spectrum of the molecule **(5)** showed three negative peaks at 173.4, 172.2, and 134.4 ppm and three positive signals at 133.6, 129.4, and 128.8 ppm, indicating the apparent formation of product **(5)**. By comparing negative signals in the ^{13}C NMR spectrum of **(5)**, peaks at 173.4 and 172.2 ppm were more deshielded than the peak at 134.4 ppm, implying that peaks at 173.4 and 172.2 ppm can be related to quaternary carbons on 1,3,5-triazine ring due to the strong inductive effect of the 1,3,5-triazine ring. Therefore, the peak at 134.4 ppm can be assigned to two *ipso* carbons to the 1,3,5-triazine ring. More specifically, the peak at 172.2 ppm was around half-height of the peak at 173.4 ppm, suggesting that the peak at 172.2 ppm belongs to the *ipso* carbon to the chlorine atom on the 1,3,5-triazine ring since there is one *ipso* carbon to the chlorine atom relative to two other quaternary carbons. In comparison of positive signals in the ^{13}C NMR spectrum of **(5)**, the peak at 133.6 ppm is around half-height of the other two peaks at 129.4 and 128.8 ppm, referring that this peak at 133.6 ppm can be ascribed to two *para* carbons to 1,3,5-triazine ring on diphenyl groups because a number of *para* carbons on diphenyl groups to 1,3,5-triazine ring is less than *ortho* and *meta* carbons to 1,3,5-triazine ring on diphenyl groups. Also, the mass spectrometry of compound **(5)** showed two main integer masses at 267.1 and 269.1 in 3:1 ratio as expected due to the presence of two chlorine isotopes ^{35}Cl and ^{37}Cl, indicating the successful formation of **(5)**. Hence, the results mentioned above of ^{1}H NMR spectroscopy, ^{13}C NMR spectroscopy, and mass spectrometry indicated the successful formation of **(5)**.

2.2.3.4 Synthesis of 2-(4-aminophenyl)-4,6-diphenyl-1,3,5-triazine (6)

Modification procedure of **(6)** was suitably performed according to Tanaka *et al.*[36] As shown in **scheme 2.16**, **(5)** underwent reaction with 4-(4,4,5,5-tetrame-thyl-1,3,2-dioxaborolan-2-yl) aniline using tetrakis (triphenylphosphine) palladium (0) as a catalyst, THF/toluene as a co-solvent and potassium carbonate as a base in order to attain compound **(6)** as a brown solid, in a yield of 76%.

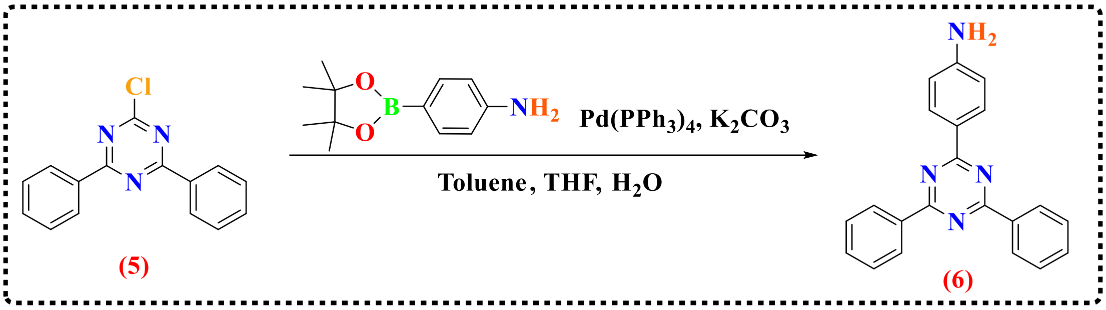

Scheme 2.16: Synthetic route of **(6)**.

The Suzuki mechanism was presented in Chapter 1 in more detail. The purity and structure of **(6)** were fully characterised by the ^{1}H NMR spectroscopy, ^{13}C NMR spectroscopy, mass spectrometry and elemental analysis. The ^{1}H NMR spectrum of the molecule **(6)** displayed a broad singlet peak at 6.15 ppm, which can be related to two protons of the amino group on account of the rapid intermolecular exchange of amine protons. Additionally, the total number of protons in the ^{1}H NMR spectroscopy of **(6)** were sixteen protons, offering further evidence for the synthesis the molecule **(6)**. Furthermore, the ^{1}H NMR spectroscopy of **(6)** showed two doublet peaks at 8.47 and 6.75 ppm, which can be attributed to two *ortho* protons and two *meta* protons to the amino group, respectively, on account of a strongly electron-donating effect of amino group on the specified peak at 6.75 ppm to be more upfield, and a strongly electron-withdrawing impact of 1,3,5-triazine ring on the determined peak at 8.47 ppm to be more deshielded. More precisely, the doublet peak at 8.47 ppm in the ^{1}H NMR spectrum of **(6)** can be ascribed to two *meta* protons to the amino group in the product **(6)** because it possesses the same *J* value to the coupling peak at 6.75 ppm, which is large about 8.5 Hz relative to other coupling constants. Moreover, the ^{1}H NMR spectrum of **(6)** displayed a doublet of doublet peak at 8.70 ppm, which can be attributed to the four *ortho* protons to 1,3,5-triazine in diphenyl groups due to the strongly electron-withdrawing effect of 1,3,5-triazine ring on *ortho* positions.

The ^{13}C NMR spectrum of the molecule **(6)** showed ten different environments of carbon atoms, indicating that the molecule **(6)** was successfully composed. More importantly, the appearance of the new four signals in the ^{13}C NMR spectrum of the molecule **(6)** relative to the ^{13}C NMR spectrum of the molecule **(5)**, including two negative and two positive peaks, offered a clear indication of the successful composition of the molecule **(6)**. More specifically, two negative signals at 154.4 and 122.1 ppm in the ^{13}C NMR spectrum of the molecule **(6)** can be related to the *ipso* and *para* positions of quaternary carbons to the amino group, respectively, due to the influence of the amino group on these positions. Additionally, two positive signals at 113.8 and 131.3 ppm in the ^{13}C NMR spectrum of the molecule **(6)** can be assigned to *ortho* and *meta* positions of carbons to the amino group, respectively, due to the strongly electron-donating amino effect on the *ortho* position at the peak of 113.8 ppm to be more shielded. Besides, the mass spectrometry of the compound **(6)** exhibited the main integer peak at 325.1 relating to the mass of the molecular ion [M^+] of **(6)**, which concurs with the expected mass of the molecule **(6)**. Therefore, all these abovementioned results of ^{1}H NMR spectroscopy, ^{13}C NMR spectroscopy, and mass spectrometry proved the formation of **(6)**.

2.2.3.5 Synthesis of 2-(4-bromophenyl)-4,6-diphenyl-1,3,5-triazine (7)

The preparation of **(7)** was conducted by reacting **(6)**, aqueous hydrobromic acid (47%) and aqueous sodium nitrite at 0 °C for one hour in order to generate 4-(4,6-diphenyl-1,3,5-triazin-2-yl) benzene diazonium bromide as a diazonium salt before adding copper(I) bromide as a source of electron transfer. Copper(I) bromide and HBr were added to the solution to produce a bromine radical, which reacted with 2,4,6-triphenyl-1,3,5-triazine radical as an aryl radical so as to obtain the desired molecule **(7)**. The yield of the target product **(7)** was acceptable as a white solid at around 67% according to the Tanaka procedure, as illustrated in **scheme 2.17**.[36]

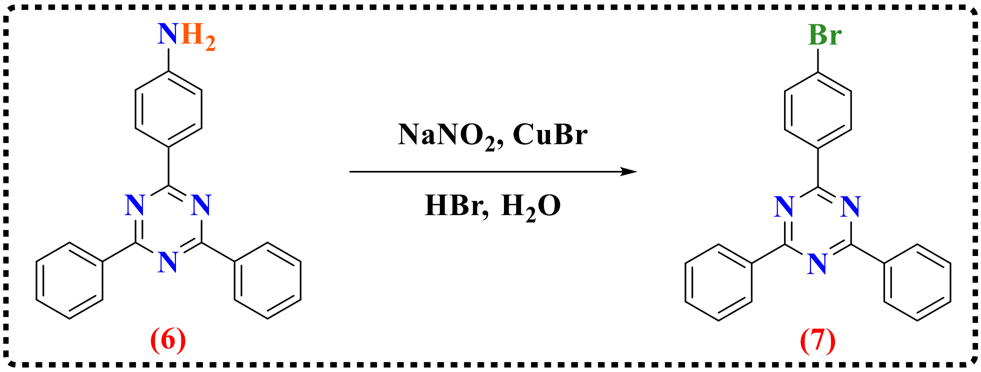

Scheme 2.17: Synthetic route of **(7)**.

The Sandmeyer mechanism for the product formation **(7)** follows a radical-nucleophilic aromatic substitution ($S_{RN}Ar$). Fundamentally, this mechanism comprises three main stages which give rise to the generation of the product **(7)**, as illustrated in **scheme 2.18**. The first stage involves the preparation of a nitrosonium ion through protonating nitrous acid, which is formed *in situ* by mixing hydrobromic acid with sodium nitrate, followed by losing a leaving group of water to obtain the nitrosonium ion. The second stage requires a formation of a diazonium ion via reacting the generated nitrosonium ion, which functions as a strongly electrophilic component due to the positive charge on it, with the product of **(6)** as a nucleophilic moiety. A lone pair of electrons on the amino group of the molecule **(6)** attacks the nitrosonium ion to produce an intermediate **(A)**. This is followed by the loss of proton from the amino group of the intermediate **(A)** by water, which leaves the electrons behind onto the nitrogen to form an *N*-nitrosamine intermediate **(B)**. Then, a proton transfer to the terminal oxygen atom of the *N*-nitrosamine intermediate **(B)** is achieved by a hydronium ion, generating a third intermediate **(C)**. Next, the proton on the nitrogen atom of the third intermediate **(C)** is lost by water to yield a fourth intermediate **(D)**, then a protonation process is carried out on the hydroxyl group of the fourth intermediate **(D)** by a hydronium ion to produce a fifth intermediate **(E)** containing a good leaving group of water. Subsequently, the fifth intermediate **(E)**'s water group is eliminated in order to form the diazonium ion. The third stage includes a single electron transfer (SET) process to the diazonium ion from copper(I) bromide catalyst so as to convert the diazonium ion to a neutral compound with the generation of Cu^+(II)Br species arising from the electron transfer from copper(I) bromide. Next, a homolytic cleavage process of the carbon-nitrogen bond for the neutral compound is carried out, leading to the production of 2,4,6-triphenyl-1,3,5-triazine radical with the loss of N_2 as gas bubbles. At last, copper (II) bromide, which is produced by the reaction between Cu^+(II)Br moiety and the bromide anion, couples with 2,4,6-triphenyl-1,3,5-triazine radical, bringing about the formation of a sigma bond between carbon and bromine in order to obtain the product **(7)** as well as the re-formation of the copper(I) bromide catalyst.

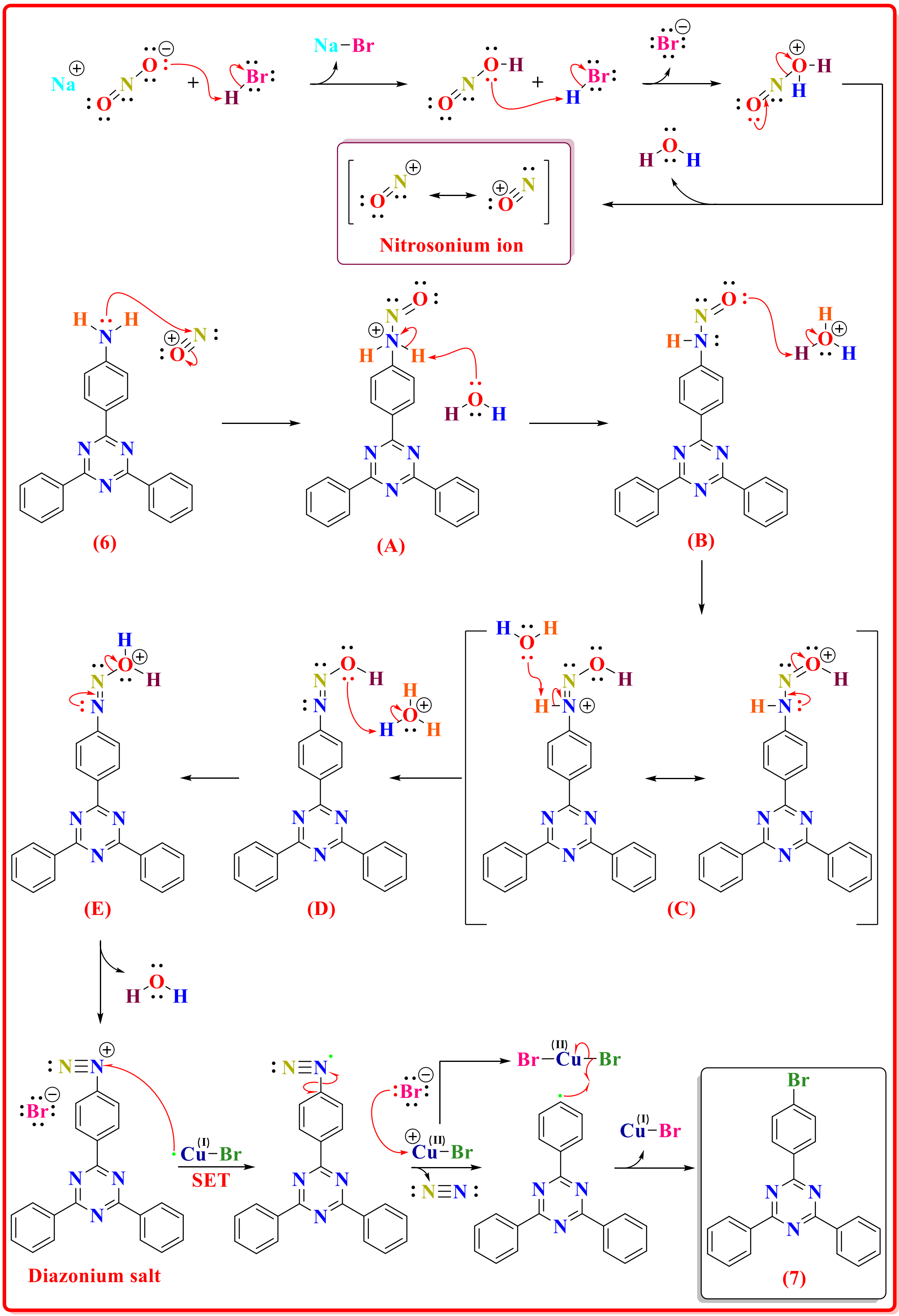

Scheme 2.18: The proposed mechanism of the formation of **(7)** using the Sandmeyer reaction.

After purifying the crude molecule **(7)** using column chromatography, its purity and structure were assessed by different analysis methods, i.e., ^{1}H NMR spectroscopy, ^{13}C NMR spectroscopy, elemental analysis and mass spectrometry. The ^{1}H NMR spectrum of the pure compound **(7)** showed a doublet of doublet, two doublet, and multiplet peaks at 8.76, 8.64, 7.71 and 7.67–7.55 ppm, respectively, which belong to fourteen aromatic protons, indicating that the product **(7)** had been successfully formed. In addition, a broad singlet peak at 6.15 ppm relating to the amino group protons of the compound **(6)** disappeared in the ^{1}H NMR spectrum of **(7)**, and thereby its absence represents obvious evidence of the reaction's success and formation of **(7)**. Furthermore, the doublet peak at 6.75 ppm in the ^{1}H NMR spectrum of **(6)**, which belongs to two *ortho* protons to the amino group, was deshielded to the position of 7.71 ppm in the product **(7)** owing to the substitution of the strongly electron-donating amino group for the bromine group that has an indictive effect. Hence, this gives evident proof of replacing the amino group with the bromine group. Also, doublet of doublet and doublet peaks at resonances of 8.76 and 8.64 ppm in the ^{1}H NMR spectrum of **(7)** can be ascribed to four *ortho* protons on diphenyl groups and two *ortho* protons on *p*-phenylene to 1,3,5-triazine ring, respectively, according to their *J* values, integrations, and spin-spin splitting. Chemical shifts for two signals positioning at 8.76 and 8.64 ppm in the ^{1}H NMR spectrum of **(7)** were more deshielded than other peaks because of the strongly electron-withdrawing effect of 1,3,5-triazine affected *ortho* protons.

The ^{13}C NMR spectrum of **(7)** displayed ten different environments of carbon atoms, indicating that the molecule **(7)** was successfully formed. More specifically, a negative signal at 154.4 ppm in the ^{13}C NMR spectrum of **(6)**, which can be attributed to the *ipso* carbon to the amino group, was shielded in the ^{13}C NMR spectrum of **(7)** to be at 127.5 ppm because of the conversion of the amino group to bromine atom. Moreover, a positive signal at 113.8 ppm in the ^{13}C NMR spectrum of **(6)**, which can be assigned to the *ortho* position of carbons to the amino group, was shifted towards a downfield region in the ^{13}C NMR spectrum of **(7)** to be at 131.9 ppm owing to the effect of bromine atom on *ortho* position to be relatively downfield. Also, the mass spectrometry of compound **(7)** exhibited two main integer masses at 388.1 and 390.1 in 1:1 ratio as expected due to the presence of two bromine isotopes ^{79}Br and ^{81}Br, proving the successful formation of **(7)**.

2.2.3.6 Synthesis of 1-(10-(4-(4,6-diphenyl-1,3,5-triazin-2-yl)phenyl)-10*H*-phenoxazin-2-yl)ethanone **(8)**

The synthesis of **(8)** was appropriately prepared according to the Buchwald-Hartwig amination reaction as described by Moon *et al*.[37] The reaction between **(4)** and **(7)** was perfectly performed in order to produce **(8)** in the presence of potassium carbonate as a base, palladium (II) acetate and tri-tert-butylphosphine as catalysts, and toluene as a solvent under refluxing conditions as depicted in **scheme 2.19**. Following purification of **(8)** using column chromatography, **(8)** was attained in a high yield of 61% in the form of a green powder.

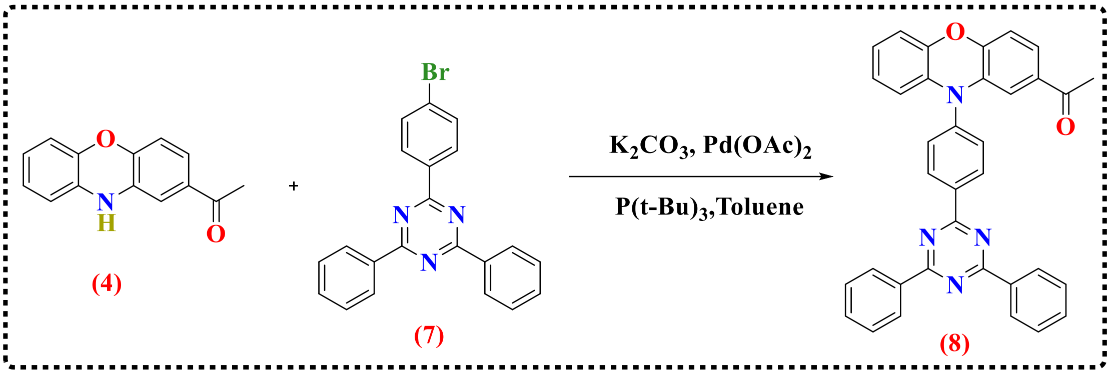

Scheme 2.19: Synthetic route of **(8)**.

The reaction mechanism of the Buchwald-Hartwig amination for synthesising the product **(8)** follows the catalytic cycle shown in **scheme 2.20**. This mechanism includes five fundamental steps. Firstly, an active catalyst is formed in the reaction by mixing palladium (II) acetate with tri-tert-butylphosphine so as to obtain bis(tri-tert-butylphosphine) palladium (0) which is referred to as **$Pd^0(L)_2$**, as illustrated in **scheme 2.20**. In the second step, the active catalyst is inserted into the product **(7)** between the bromine-carbon bond producing an arylpalladium (II) bromide complex; this step is called oxidative addition. Thirdly, coordination of the product **(4)** as a secondary amine with palladium is carried out through the substitution of a single ligand in order to generate a second complex in the presence of the secondary amine. In the fourth step, potassium carbonate is employed so as to abstract proton and bromine atoms from the second complex, resulting in the generation of a bond between palladium and nitrogen atoms to give the third complex. Finally, a reductive elimination step occurs so that the third complex can give rise to the formation of the product **(8)** and regain the active catalyst.

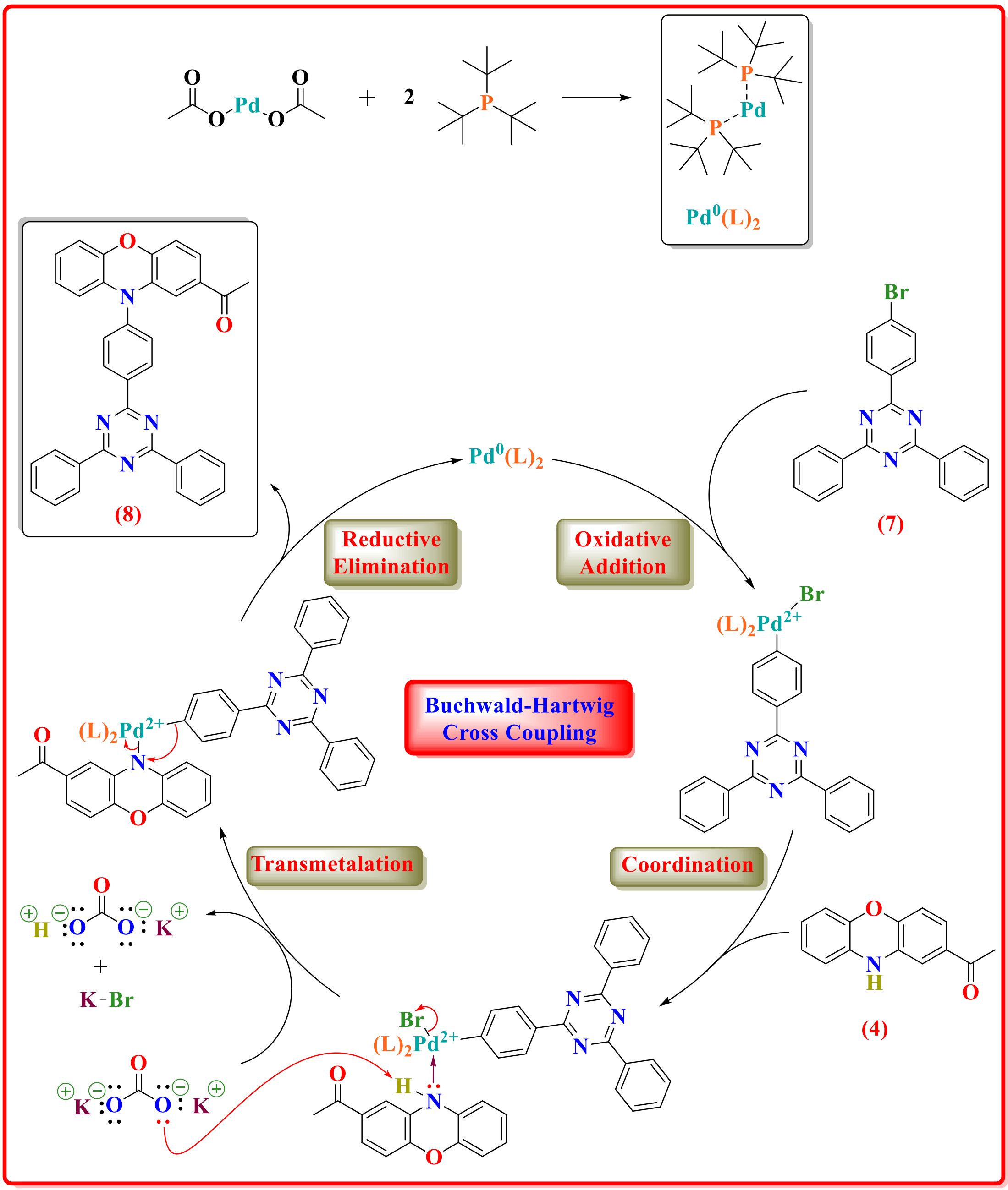

Scheme 2.20: The proposed mechanism of the formation of **(8)** using the Buchwald-Hartwig amination.

The chemical structure and purity of **(8)** were thoroughly analysed using ^{1}H NMR spectroscopy, ^{13}C NMR spectroscopy, elemental analysis, and mass spectrometry. The first obvious indication of successful composition of **(8)** was that the full number of integrated protons in the ^{1}H NMR spectrum of **(8)** was twenty-four protons, as expected for the molecule **(8)**. Additionally, the broad singlet peak at 8.42 ppm completely disappeared in the ^{1}H NMR spectrum of **(8)**, which belongs to the amino proton in the molecule **(4)**, reflecting the successful synthesis of the compound **(8)**. Besides, a singlet peak at 2.37 ppm with the integration of three protons was observed in the ^{1}H NMR spectrum of **(8)**, which can be ascribed to the methyl moiety protons in the acetyl group. Furthermore, the ^{1}H NMR spectrum of **(8)** showed a doublet of doublet peak at a resonance of 8.83 ppm, which can be related to four *ortho* protons to 1,3,5-triazine ring on diphenyl groups on account of a strongly electron-withdrawing impact of 1,3,5-triazine ring on the determined peak at 8.83 ppm to be more deshielded. Also, the ^{1}H NMR spectrum of **(8)** exhibited a doublet of doublet peak at 6.06 ppm, which can be ascribed to one of benzene rings' protons that does not include the acetyl group, particularly the *ortho* proton to the ether group due to a strongly electron-donating ether effect on the specified peak at 6.06 ppm to be more shielded.

The ^{13}C NMR spectrum of **(8)** exhibited different twenty-four environments of carbon atoms, which indicated the successful attachment of **(4)** to **(7)**. In addition, the ^{13}C NMR spectrum of **(8)** showed a negative peak at 196.3 ppm, which can be assigned to the carbonyl group carbon due to a strongly inductive influence of carbonyl group. Furthermore, the ^{13}C NMR spectrum of the molecule **(8)** displayed a positive signal at 26.2 ppm, which can be attributed to the primary carbon of the methyl group on the acetyl group. Moreover, two negative peaks at 171.9 and 170.8 ppm in the ^{13}C NMR spectrum of **(8)** were observed, which can be related to quaternary carbons on the 1,3,5-triazine ring because of the strong inductive effect of the 1,3,5-triazine ring. Besides, two positive signals at 129 and 128.7 ppm in the ^{13}C NMR spectrum of **(8)** were noted, which can be ascribed to *ortho* and *meta* positions of eight carbons to 1,3,5-triazine ring on diphenyl groups since these signals were the highest peaks relative to other peaks. Moreover, the mass spectrometry of **(8)** showed the main integer peak at 533.2, which represented the mass of the molecular ion, [M^{+}] of **(8)** as anticipated. Therefore, all these abovementioned results of ^{1}H NMR spectroscopy, ^{13}C NMR spectroscopy, and mass spectrometry proved the formation of **(8)**.

2.2.3.7 Synthesis of 1-(10-(4-(4,6-diphenyl-1,3,5-triazin-2-yl)phenyl)-10*H*-phenoxazin-2-yl)ethanol **(9)**

The reduction of molecule **(8)** was successfully performed in order to generate **(9)** using a modified version of the procedure by Kamogawa *et al.*[38] Product **(9)** was readily synthesised using a solution of sodium borohydride in ethanol as a reducing agent so as to generate a yellow powder of compound **(9)** with an acceptable yield of 69%. This yield 69% is lower than an expected result owing to the use of silica gel in purifying the compound **(9)**, which is acidic and sensitive towards basic triazine of compound **(9)**, leading to decreasing the yield. This reaction is illustrated in **scheme 2.21**.

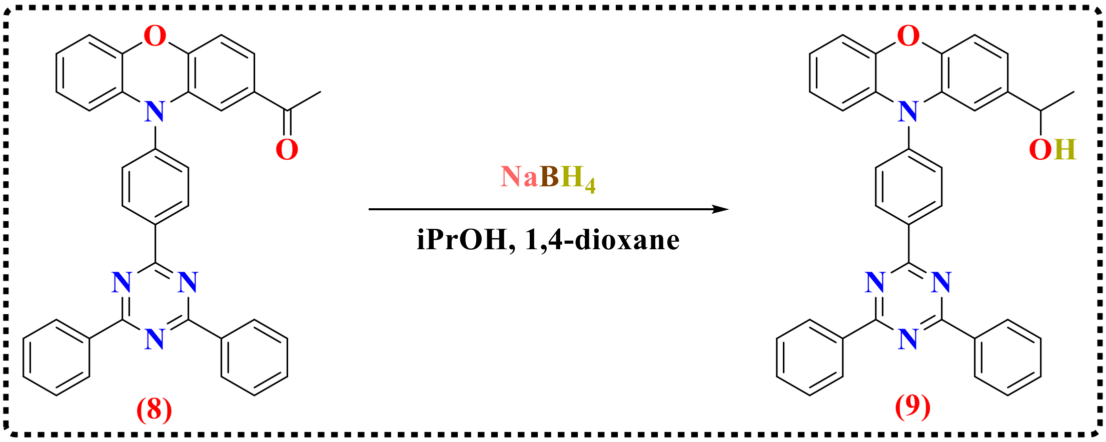

Scheme 2.21: Synthetic route of **(9)**.

The reduction reaction mechanism for the product generation **(9)**, which encompasses two core steps, is depicted simply in **scheme 2.22**. Firstly, the attack of a hydride anion of sodium borohydride, which functions as a nucleophilic portion, on a carbonyl carbon for the compound **(8)**, which acts as an electrophile, is easily carried out to form an intermediate **(A)** as an alkoxide anion as well as borane. In the next step, the protonation of the alkoxide anion **(A)** is readily performed by adding isopropanol solvent to the reaction so as to obtain the molecule **(9)** as a secondary alcohol.

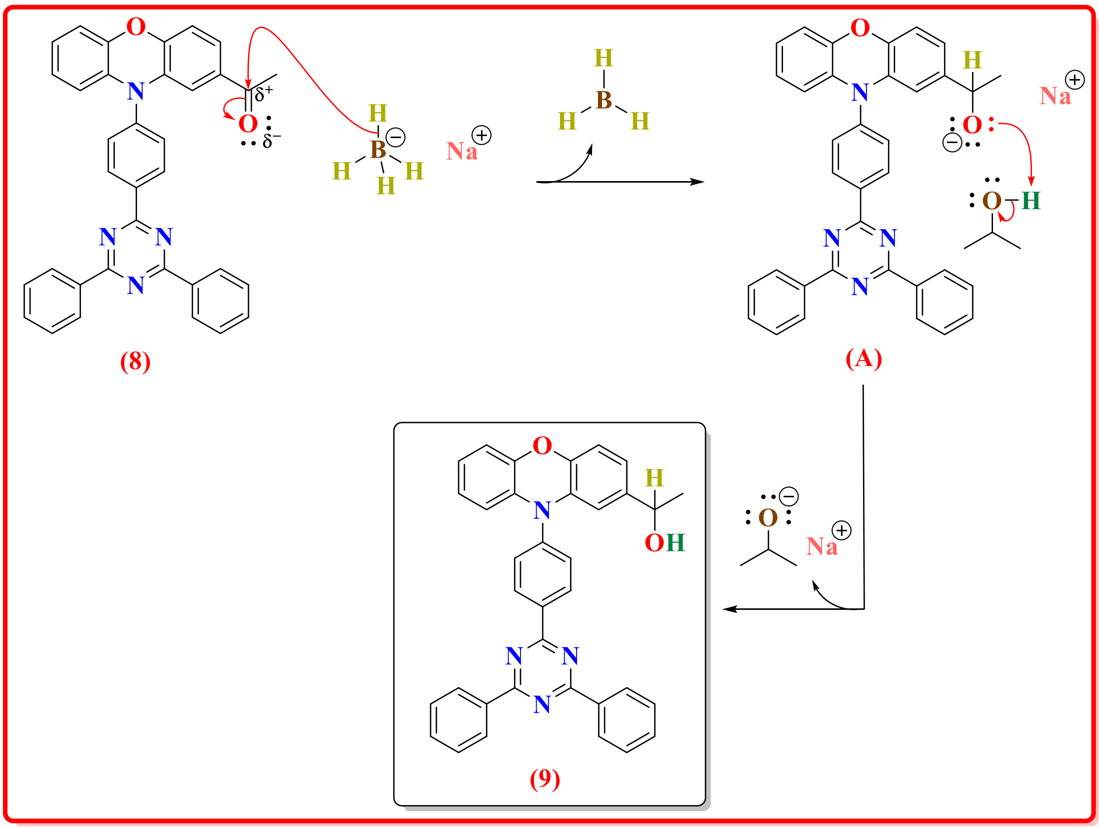

Scheme 2.22: The proposed mechanism of the formation of **(9)** using the reduction reaction.

A variety of analytical techniques, including ^{1}H NMR spectroscopy, ^{13}C NMR spectroscopy, mass spectrometry, and elemental analysis were utilised in order to verify the product's purity and chemical structure **(9)**. The ^{1}H NMR spectrum of the product **(9)** exhibited a broad singlet signal at 4.23 ppm, which can be attributable to the hydroxyl proton due to a rapid intermolecular exchange of alcoholic proton. Additionally, a quartet signal at 4.54 ppm in the ^{1}H NMR spectrum of the product **(9)** was observed with the integration of one proton, which can be ascribed to a proton of the methine group attached to the hydroxyl and the methyl groups due to a high electronegativity of adjacent oxygen atom that affect the determined signal to be more downfield. Therefore, these two peaks in the ^{1}H NMR spectrum of **(9)** were fundamental factors that proved success of the reduction reaction. Furthermore, the ^{1}H NMR spectrum of the product **(9)** displayed a doublet peak at 1.29 ppm with the integration of three protons, which can be attributed to methyl protons.

More importantly, a negative signal at 196.3 ppm in the ^{13}C NMR spectrum of **(8)**, which can be attributed to the carbonyl group carbon, was strongly shielded in the ^{13}C NMR spectrum of **(9)** to be at 69.9 ppm because of the conversion of the carbonyl group to alcoholic group. This negative signal in the ^{13}C NMR spectrum of **(9)** offered an obvious indication that the desired product **(9)** was successfully formed. Moreover, the mass spectrometry result for the compound **(9)** showed the main integer peak at 534.2, which matched with the expected mass. Therefore, all these abovementioned data of ^{1}H NMR spectroscopy, ^{13}C NMR spectroscopy, and mass spectrometry demonstrated the composition of **(9)**.

2.2.3.8 Synthesis of 1,4-dibromo-2-(6-bromohexyloxy) benzene (10)

The etherification reaction was carried out to produce **(10)** according to the procedure of Hsieh *et al.*[39] Molecule **(10)** was successfully synthesised by reacting 2,5-dibromophenol with 1,6-dibromohexane using potassium hydroxide as a base and DMSO as a solvent in order to form the product as white crystals with a high yield of 97%. The reaction is depicted in **scheme 2.23**.

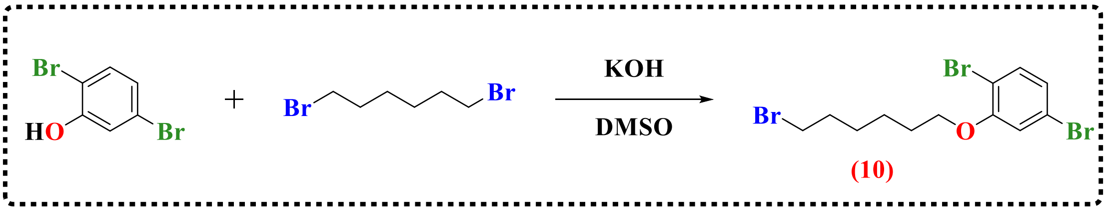

Scheme 2.23: Synthetic route of **(10)**.

Compound **(10)** was thoroughly analysed through different characterisation techniques, including ^{1}H NMR spectroscopy, ^{13}C NMR spectroscopy, TLC, mass spectrometry and elemental analysis. The first clear indication of successful composition of **(10)** was that the full number of integrated protons in the ^{1}H NMR spectrum of **(10)** was fifteen protons. In addition, the broad singlet signal at 5.63 ppm entirely disappeared in the ^{1}H NMR spectrum of **(10)**, which belongs to the hydroxyl proton in 2,5-dibromophenol, providing an indication that the etherification reaction was successful. Furthermore, the ^{1}H NMR spectrum of **(10)** showed two doublet peaks at 7.35 and 6.97 ppm, which can be attributed to *meta* and *ortho* protons to the ether group, respectively, according to their coupling constants. Moreover, the ^{1}H NMR spectrum of the product **(10)** displayed two triplet peaks at 3.97 and 3.40 ppm, which can be assigned to protons of methylene groups bound directly to the ether group and bromine atom, respectively, owing to high electronegativities of oxygen and bromine atoms. Hence, all of these mentioned signals in the ^{1}H NMR of **(10)** proved the success of the etherification reaction.

The ^{13}C NMR spectrum of **(10)** presented twelve different environments of carbon atoms in both aliphatic and aromatic areas, which were in accordance with the desired structural product **(10)**. Additionally, the ^{13}C NMR spectrum of the molecule **(10)** exhibited a negative signal at 156 ppm, which can be ascribed to *ipso* carbon to the ether group due to the strong inductive effect of the ether group. Moreover, the ^{13}C NMR spectrum of **(10)** exhibited a negative signal at 69.2 ppm, which can be assigned to the methylene group carbon attached directly to the oxygen atom because of a strong inductive impact of the oxygen atom on the specified signal to be more downfield. Also, four main integer signals at 412, 414, 416, and 418 in a 1:3:3:1 ratio were noted for the compound **(10)** by mass spectrometry technique, and these four signals were due to the fact that the bromine atom has two isotopes ^{79}Br and ^{81}Br. Hence, all these abovementioned results of ^{1}H NMR spectroscopy, ^{13}C NMR spectroscopy, and mass spectrometry indicated the formation of **(10)**.

2.2.3.9 Synthesis of 2-(1-((6-(2,5-dibromophenoxy) hexyl) oxy) ethyl)-10-(4-(4,6-diphenyl-1,3,5-triazin-2-yl) phenyl)-10*H*-phenoxazine M3

The preparation of the product **M3** was performed using the etherification synthesis as reported in Luo *et al.*[40] The reaction between **(9)** and **(10)** led to the formation of product **M3** using potassium hydroxide as a base and dimethylformamide as a solvent, as illustrated in **scheme 2.24**. Column chromatography was utilised to purify the crude product in order to obtain the desired end compound **M3**. The final product was a yellow powder produced in a reasonable yield of 75%.

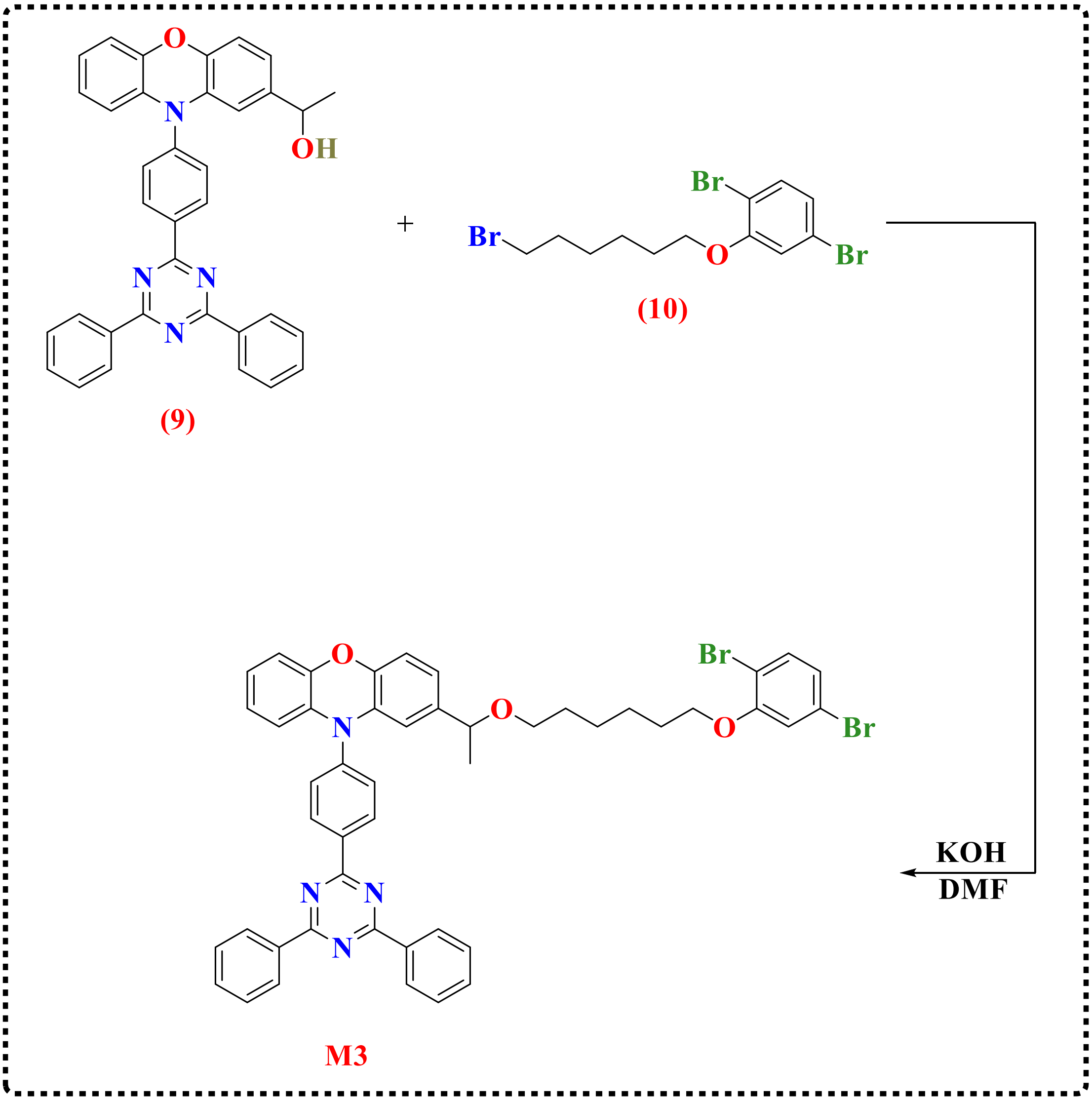

Scheme 2.24: Synthetic route of **M3**.

The purity and chemical structure of **M3** were thoroughly analysed using a range of analytical techniques, e.g., ^{1}H NMR spectroscopy, ^{13}C NMR spectroscopy, thin layer chromatography, elemental analysis, and mass spectrometry. After purifying the product **M3** using column chromatography, one spot was observed on the thin layer chromatography, which corresponds to compound **M3**. Based on the ^{1}H NMR spectroscopy data of the compound **M3**, the main factor that confirms the formation of the compound **M3** is the disappearance of the broad singlet peak for the hydroxyl proton at 4.23 ppm; this was evidenced for the final monomer, **M3**. As seen in **Figure 2.6**, the ^{1}H NMR spectrum of **M3** exhibits the correct number of integrated protons in different environments, which is forty protons as expected. In addition, the quartet peak at 4.54 ppm in the ^{1}H NMR spectrum of the product **(9)**, which can be attributed to the proton of the methine group attached to the hydroxyl and the methyl groups, is upfield to the position of 4.05 ppm in the ^{1}H NMR spectrum of the product **M3** due to the conversion of the adjacent group from the alcoholic moiety to the ether group, giving a clear indication that the product **M3** was successful formed. Furthermore, two triplet peaks at 3.80 and 3.20 ppm in the ^{1}H NMR spectrum of the product **M3** are observed, which can be pertaining to two positions **10** and **11**, respectively, based on their spin-spin splitting by neighbouring protons and their locations next to the electronegative atoms as shown in **Figure 2.6**. More specifically, the triplet signal at 3.80 ppm is more downfield than the triplet peak at 3.20 ppm because the adjacent phenol ether group possesses more electronegative than the aliphatic ether group. Moreover, the ^{1}H NMR spectrum of **M3** shows three peaks at positions **4**, **5**, and **6**, ascribing to three aromatic protons on 2,5-dibromophenol ether moiety, according to their integrations and spin-spin couplings. More interestingly, the doublet peak at the position **4** in the ^{1}H NMR spectrum of **M3** can be attributed to a *meta* proton to the ether group because it has a high coupling constant of about 8.5 Hz, compared to another doublet peak at **6** containing a small *J* value around 2.0 Hz, owing to its coupling with the *ortho* proton to this determined proton only. In addition, the ^{1}H NMR spectrum of **M3** exhibits doublet and doublet of doublet peaks at 9.01 and 8.79 ppm, which be ascribed two *ortho* protons on *p*-phenylene and four *ortho* protons on diphenyl groups to 1,3,5-triazine ring, respectively, due to a strongly inductive effect of 1,3,5-triazine ring on *ortho* protons to be more downfield. Besides, the multiplet peak at 6.07-6.02 ppm in the ^{1}H NMR spectrum of **M3** can be attributable to two *ortho* protons to the ether group on the phenoxazine moiety on account of a strongly electron-donating ether effect on *ortho* protons to be more upfield. Therefore, all abovementioned signals in the ^{1}H NMR spectrum of **M3** support obvious evidence that the molecule **M3** was successfully composed.

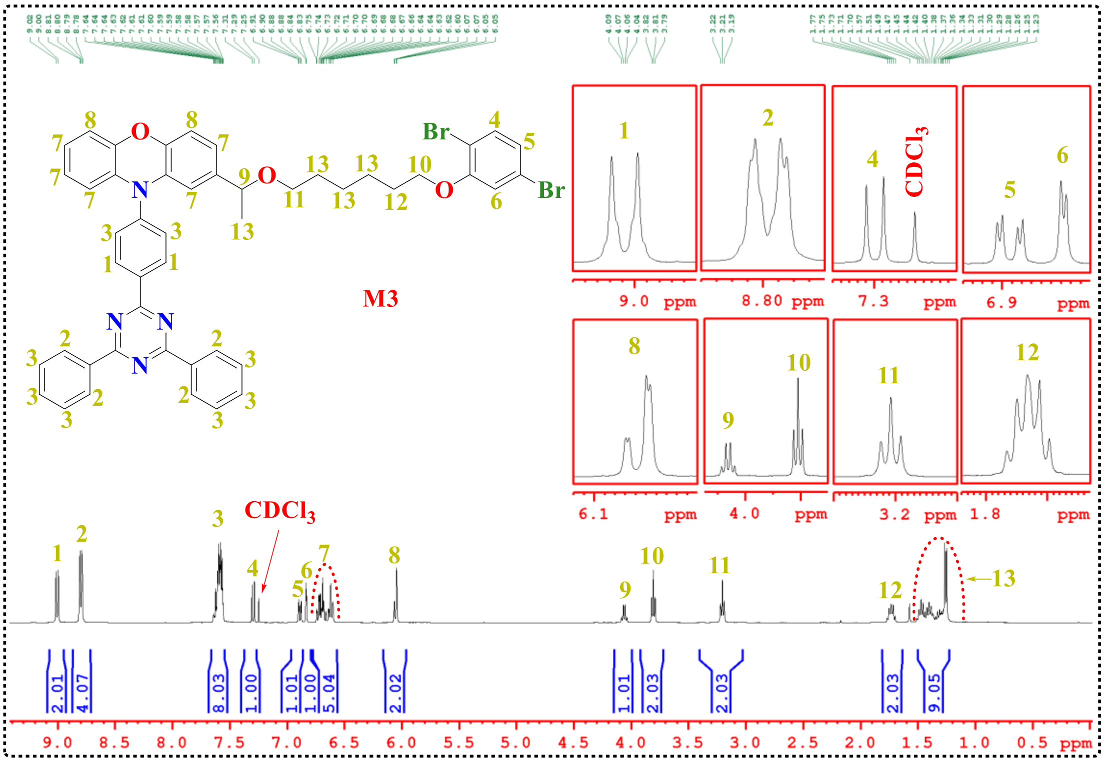

Figure 2.6: ^{1}H NMR spectrum of **M3** in CDCl3.

The ^{13}C NMR spectrum of product **M3** offers a significant increase in environments of carbon atoms, indicating the presence of **M3** (**Figure 2.7**). In particular, a positive signal at 69.9 ppm in the ^{13}C NMR spectrum of **(9)**, pertaining to the carbon of the methine group bound to the alcoholic group, is deshielded in the ^{13}C NMR spectrum of **M3** to the position of 77.3 ppm as a result of the conversion of the alcoholic group to the ether group. Furthermore, a negative signal at 33.8 ppm in the ^{13}C NMR spectrum of **(10)**, which can be attributed to the carbon of the methylene group in the aliphatic region bound to the bromine atom, is downfield in the ^{13}C NMR spectrum of **M3** to the position of **31** at 68.3 ppm because of a high electronegativity of the oxygen atom. Moreover, two negative peaks at 171.8 and 170.8 ppm in the ^{13}C NMR spectrum of **M3** are observed in **Figure 2.7**, which can be related to quaternary carbons on the 1,3,5-triazine ring due to the strong inductive effect of the 1,3,5-triazine ring on defined peaks to be more deshielded. Therefore, all mentioned peaks in the ^{13}C NMR spectrum of **M3** prove the successful composition of **M3**. Furthermore, three main integer peaks at 866.7, 868.7, and 870.7 in a 1:2:1 ratio were noted for the compound **M3** by mass spectrometry technique, and these three peaks were by the fact that the bromine atom has two isotopes ^{79}Br and ^{81}Br. Also, the elemental analysis determined the following results for $C_{47}H_{40}Br_2N_4O_3$: C, 65.08; H, 4.71; Br, 18.32; N, 6.37, which concurs with its proposed formula. Therefore, all these abovementioned results of ^{1}H NMR spectroscopy, ^{13}C NMR spectroscopy, elemental analysis and mass spectrometry demonstrated the successful formation of **M3**.

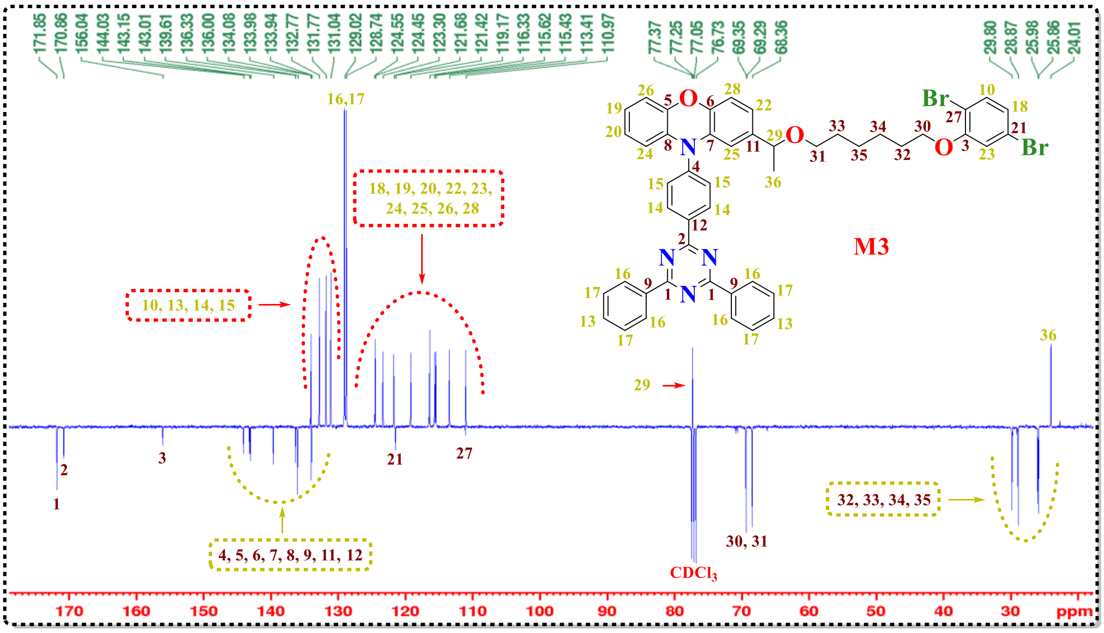

Figure 2.7: ^{13}C NMR spectrum of **M3** in $CDCl_3$.

2.2.4 Preparation of the Polymers

2.2.4.1 Synthesis and Characterisation of the Polymers

As depicted in **scheme 2.25**, the target TADF polymers were successfully prepared utilising a Suzuki polycondensation technique using monomers **M1**, **M2** and **M3**, which were combined with the respective feed molar ratios of 50: 50: 0 (**PmCP-DPOXH**), 45: 5: 5 (**PmCP-DPOXH-PxzTrz-5**), 40: 50: 10 (**PmCP-DPOXH-PxzTrz-10**) and 30: 50: 20 (**PmCP-DPOXH-PxzTrz-20**). The polymer, **PmCP-DPOXH**, which contained no TADF moiety, was generated for comparison with the other polymers.

These polymers were synthesised using the reactions between different ratios of **M1** and **M2**; specific proportions of **M3** were then added. Potassium carbonate was utilised as a base, palladium (II) acetate ($Pd(OAc)_2$) as a catalyst, and tri(o-tolyl) phosphine (($P(o\text{-}tol)_3$) as a ligand, in a minimum amount of anhydrous toluene; distilled degassed water was used for dissolution of the mineral base under refluxing conditions. The synthesised copolymers could be readily dissolved in common organic solvents, such as DCM, chloroform, toluene, THF and chlorobenzene. In order to complete polymer formation, reaction times of 72 hours were required.[41] Before stopping the reactions, bromobenzene and phenylboronic acid were added in order to end-cap the polymer chains, a process which enhanced polymer stability during the operation of OLED devices.[42,43] The elimination of any trace catalyst residue was performed by adding a small volume of ammonium hydroxide solution to all polymers following the dilution of the polymer solutions with DCM in order to wash them; soluble complexes of $Pd(NH_3)_4(OH)_2$ were generated, dissolved in the aqueous layer and eliminated this way. All the desired polymers were purified using a silica gel pad in order to remove any traces of catalyst. The desired polymers were subsequently collected as white to yellow solids, depending on the polymer TADF moiety content, by re-precipitation in methanol.

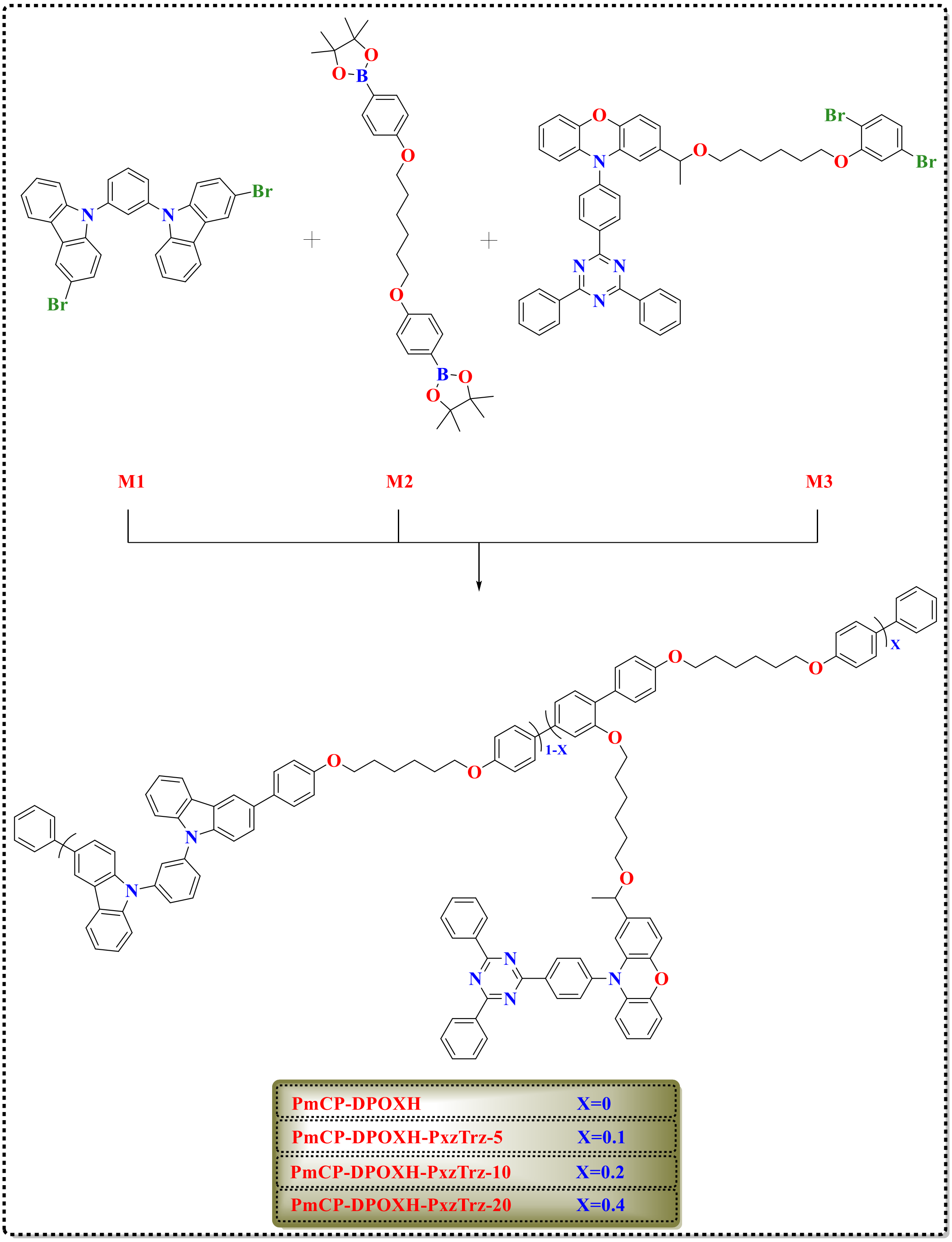

Scheme 2.25: Synthetic route of the **PmCP-DPOXH**, **PmCP-DPOXH-PxzTrz-5**, **PmCP-DPOXH-PxzTrz-10**, and **PmCP-DPOXH-PxzTrz-20**. Reagents and conditions: anhydrous toluene, K_2CO_3, $Pd(OAc)_2$, $P(o\text{-}tol)_3$, and 100°C.

The chemical structures of **PmCP-DPOXH**, together with the polymers grafted with the **PXZ-TRZ** TADF moiety located at the sidechain, i.e., **PmCP-DPOXH-PxzTrz-5**, **PmCP-DPOXH-PxzTrz-10**, and **PmCP-DPOXH-PxzTrz-20**, were fully verified using ^{1}H NMR spectroscopy. The ^{1}H NMR spectroscopy data for all polymers were in good agreement with the expected structures. The comparison of the results from **PmCP-DPOXH** and the polymers grafted with the TADF unit facilitated confirmation of the presence of **M3** in **PmCP-DPOXH-PxzTrz-5**, **PmCP-DPOXH-PxzTrz-10**, and **PmCP-DPOXH-PxzTrz-20**. Broad singlet peaks at 9.02, 8.79, 6.05, 3.80, and 3.20 ppm were observed, which can be attributed to **M3** protons, giving a clear indication of the successful incorporation of the **PXZ-TRZ** TADF moiety into the polymer backbones during polymerisation. The intensities of the abovementioned peaks within the ^{1}H NMR spectrum of TADF polymers were heightened with increasing **M3** feed molar ratios within the target TADF polymers. There are two characteristic proton peaks at 8.98 and 8.77 ppm related to TADF unit, which could be distinguished from those of **PmCP-DPOXH**. These two protons are relative to a proton signal at 3.98 ppm, which is ascribed to four protons of **M2**, to determine the actual ratio of TADF unit in TADF polymers. Hence, the actual contents of TADF moieties in the polymers were estimated from analysis of their ^{1}H NMR spectra to be 7.5%, 14%, and 27.5% for **PmCP-DPOXH-PxzTrz-5**, **PmCP-DPOXH-PxzTrz-10**, and **PmCP-DPOXH-PxzTrz-20**, respectively, which are comparable to the feed molar percent of **M3**. After gaining the actual ratio of each monomer from the ^{1}H NMR spectra of polymers, the degree of polymerisation (DP) of all desired polymers was calculated from the ^{1}H NMR spectra of polymers to be approximately in the range between 2-4.

Gel permeation chromatography (GPC) was successfully conducted in order to estimate the number-average molecular weight (Mn) and weight-average molecular weight (Mw) of all polymers formed, utilising THF as an eluent and polystyrene as the internal standard (**Table 2.1**). Mn values and polydispersity index (PDI) values for the copolymers, **PmCP-DPOXH**, **PmCP-DPOXH-PxzTrz-5**, **PmCP-DPOXH-PxzTrz-10**, and **PmCP-DPOXH-PxzTrz-20**, were determined to be in the ranges 5300–6800 Daltons (Da) and 1.25–1.36, respectively (**Table 2.1**). The relatively low molecular weights of all the synthesised polymers could be attributed to the result of the large steric effect of carbazole in the **mCP** moiety. The introduction of the π-interrupted structure of 1,6-diphenoxyhexane (**DPOXH**) to the polymer backbone enabled attainment of the low electronic delocalisation of the desired polymers.

Table 2.1: Physical properties of the TADF polymers (**PmCP-DPOXH**, **PmCP-DPOXH-PxzTrz-5**, **PmCP-DPOXH-PxzTrz-10**, and **PmCP-DPOXH-PxzTrz-20**).

Polymers	TADF in polymers (mol %)		DP(a)	Mn (Da)(b)	Mw (Da)(b)	PDI(b)
	Feed ratio	Actual ratio(a)				
PmCP-DPOXH	0	0	4	6800	8500	1.25
PmCP-DPOXH-PxzTrz-5	5	7.5	2	5700	7500	1.32
PmCP-DPOXH-PxzTrz-10	10	14	2	5300	7200	1.36
PmCP-DPOXH-PxzTrz-20	20	27.5	3	5400	7200	1.33

(a) Calculated from ^{1}H NMR spectra. **(b)** Determined by GPC in THF using polystyrene as the standard.

2.2.4.2 Optical Properties of Polymers

The photophysical properties for all the resulting polymers grafted with varying molar ratios of the TADF moieties, i.e., **PmCP-DPOXH-PxzTrz-5**, **PmCP-DPOXH-PxzTrz-10**, and **PmCP-DPOXH-PxzTrz-20**, together with the polymer without the TADF moiety, **PmCP-DPOXH**, and **PXZ-TRZ** (TADF), were investigated employing ultraviolet-visible (UV-vis) absorption spectroscopy (**Figure 2.8**) and photoluminescence (PL) (**Figure 2.9**) spectroscopy, respectively, both in diluted toluene solutions and as neat films. The optical gaps for **PmCP-DPOXH**, **PmCP-DPOXH-PxzTrz-5**, **PmCP-DPOXH-PxzTrz-10**, **PmCP-DPOXH-PxzTrz-20** and the TADF moiety were calculated through the onset of absorption in the neat film. **Table 2.2** presents a summary of the experimental values obtained for the optical properties of these compounds.

Table 2.2: Optical properties of the TADF polymers (**PmCP-DPOXH**, **PmCP-DPOXH-PxzTrz-5**, **PmCP-DPOXH-PxzTrz-10**, and **PmCP-DPOXH-PxzTrz-20**).

Polymer/ Compound	$\lambda_{abs}^{(a)}$ (nm)	$\lambda_{abs}^{(b)}$ (nm)	$\lambda_{em}^{(a)}$ (nm)	$\lambda_{em}^{(b)}$ (nm)	Optical E_g (eV)
PXZ-TRZ	**292/ 345/ 420**	**297/ 350/ 425**	**545**	**537**	**----**
PmCP-DPOXH	**304**	**311**	**401**	**404**	**3.20 ± 0.006$^{(c)}$**
PmCP-DPOXH-PxzTrz-5	**303**	**309**	**400/ 536**	**403/ 523**	**3.26 ± 0.004$^{(c)}$**
PmCP-DPOXH-PxzTrz-10	**301**	**310**	**400/ 538**	**526**	**3.27 ± 0.01$^{(c)}$**
PmCP-DPOXH-PxzTrz-20	**302**	**310**	**401/ 541**	**529**	**3.27 ± 0.006$^{(c)}$**

(a) Measured in toluene. **(b)** Measured in the neat film. **(c)** Range error at the peak of the absorbance curve of a different extinction coefficient.

Figure 2.8 depicts the UV-Vis absorption spectra of the target polymers, **PmCP-DPOXH**, **PmCP-DPOXH-PxzTrz-5**, **PmCP-DPOXH-PxzTrz-10**, and **PmCP-DPOXH-PxzTrz-20**, and the TADF moiety (**PXZ-TRZ**) in toluene solutions **(a)** and neat films **(b)**.

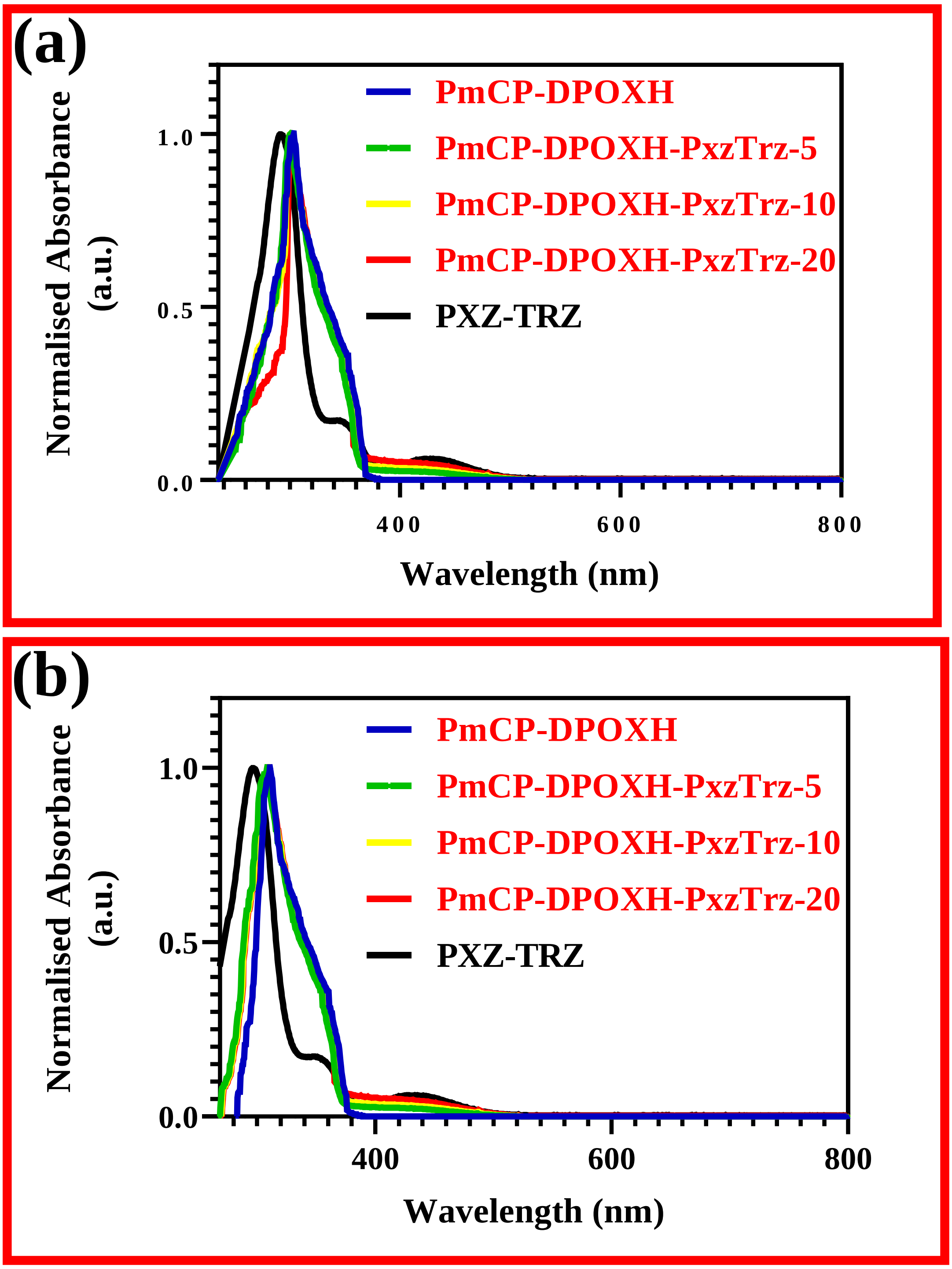

Figure 2.8: UV-vis spectra of **PXZ-TRZ** and green-emitting TADF polymers (**PmCP-DPOXH-PxzTrz-5**, **PmCP-DPOXH-PxzTrz-10**, and **PmCP-DPOXH-PxzTrz-20**), and **PmCP-DPOXH**, in **(a)** dilute toluene solutions (10^{-3} M) and **(b)** neat films.

PmCP-DPOXH the polymer without **PXZ-TRZ** TADF emitters shows a main absorption peak in toluene solutions (**Figure 2.8a**), at approximately 304 nm which can be ascribed to the π-π* transition from the backbone of the polymer. All other polymers i.e., **PmCP-DPOXH-PxzTrz-5**, **PmCP-DPOXH-PxzTrz-10**, and **PmCP-DPOXH-PxzTrz-20**, also show the same absorption peak at around the same energy (301-303 nm) indicating that this peak is also related to their polymeric backbone. Compared with **PXZ-TRZ**, the weak but noticeable broad absorption bands positioned in the range, 375-500 nm, in the absorption spectra of **PmCP-DPOXH-PxzTrz-5**, **PmCP-DPOXH-PxzTrz-10** and **PmCP-DPOXH-PxzTrz-20** can be ascribed to the ICT between the donor (phenoxazine) and the acceptor (triphenyltriazine) on their **PXZ-TRZ** substituents. By comparing **PmCP-DPOXH**, **PmCP-DPOXH-PxzTrz-5**, **PmCP-DPOXH-PxzTrz-10**, and **PmCP-DPOXH-PxzTrz-20** with **PXZ-TRZ**, it is evident that the absorption bands in the TADF-grafted polymers are almost identical at the same energy, proving that the contribution of the TADF unit to the target polymers' absorption spectra increases progressively with an increase in the loading content of the TADF moieties attached to the polymers. In the neat film (**Figure 2.8b**), the profiles of the absorption bands for **PmCP-DPOXH**, **PmCP-DPOXH-PxzTrz-5**, **PmCP-DPOXH-PxzTrz-10** and **PmCP-DPOXH-PxzTrz-20** are similar to those in toluene solution, whereas the curves show slight bathochromic shift absorption maxima of about 7 nm compared to their absorption in toluene solutions. This can be ascribed to a stronger intermolecular π-π interaction and a more planar structure in the thin films. The optical gaps (E_g), measured from the onset of the absorption spectrum in neat film, for **PmCP-DPOXH**, **PmCP-DPOXH-PxzTrz-5**, **PmCP-DPOXH-PxzTrz-10** and **PmCP-DPOXH-PxzTrz-20** are 3.20 eV, 3.26 eV, 3.27 eV, and 3.27 eV, respectively.

When the target TADF polymers, i.e., **PmCP-DPOXH-PxzTrz-5**, **PmCP-DPOXH-PxzTrz-10**, and **PmCP-DPOXH-PxzTrz-20**, are compared with both the TADF unit (**PXZ-TRZ**) and the polymer without the TADF unit (**PmCP-DPOXH**) in toluene solutions, dual emission peaks in the ranges 400 nm and 540 nm are observed in the PL profiles of **PmCP-DPOXH-PxzTrz-5**, **PmCP-DPOXH-PxzTrz-10** and **PmCP-DPOXH-PxzTrz-20**. These can be ascribed to emissions of both the polymeric backbone and the TADF moiety, respectively (**Figure 2.9a**). With rising proportions of TADF emitter (5% to 20%) in the polymers **PmCP-DPOXH-PxzTrz-5**, **PmCP-DPOXH-PxzTrz-10** and **PmCP-DPOXH-PxzTrz-20**, the emission peak's intensity at around 541 nm gradually increases, signifying more efficient transfer of energy from the polymeric backbone to the TADF unit. In the thin films (**Figure 2.9b**), with the exception of **PmCP-DPOXH-PxzTrz-5**, in the polymeric backbone's emission residue, an almost entire interchain and intrachain energy transfer from the polymeric backbone to the sidechain TADF moiety is clearly observed, giving rise to only a TADF emission peak and scarcely any residual emission from the main chain backbone for **PmCP-DPOXH-PxzTrz-10** and **PmCP-DPOXH-PxzTrz-20**. Remarkably, with the rising molar ratios of the TADF monomer, the PL emission peaks of the target TADF copolymers are gradually red-shifted from 523 nm, with respect to **PmCP-DPOXH-PxzTrz-5**, to 528 nm in relation to **PmCP-DPOXH-PxzTrz-20**. This results from existing aggregation, which demonstrates that the TADF moiety makes a significant contribution to the copolymers' emission profile. It is noteworthy that dual emission from both the backbone of the polymer and TADF is more pronounced in solutions than in films indicating better energy transfer in films and a total energy transfer in films with 10% **PXZ-TRZ** substituents.

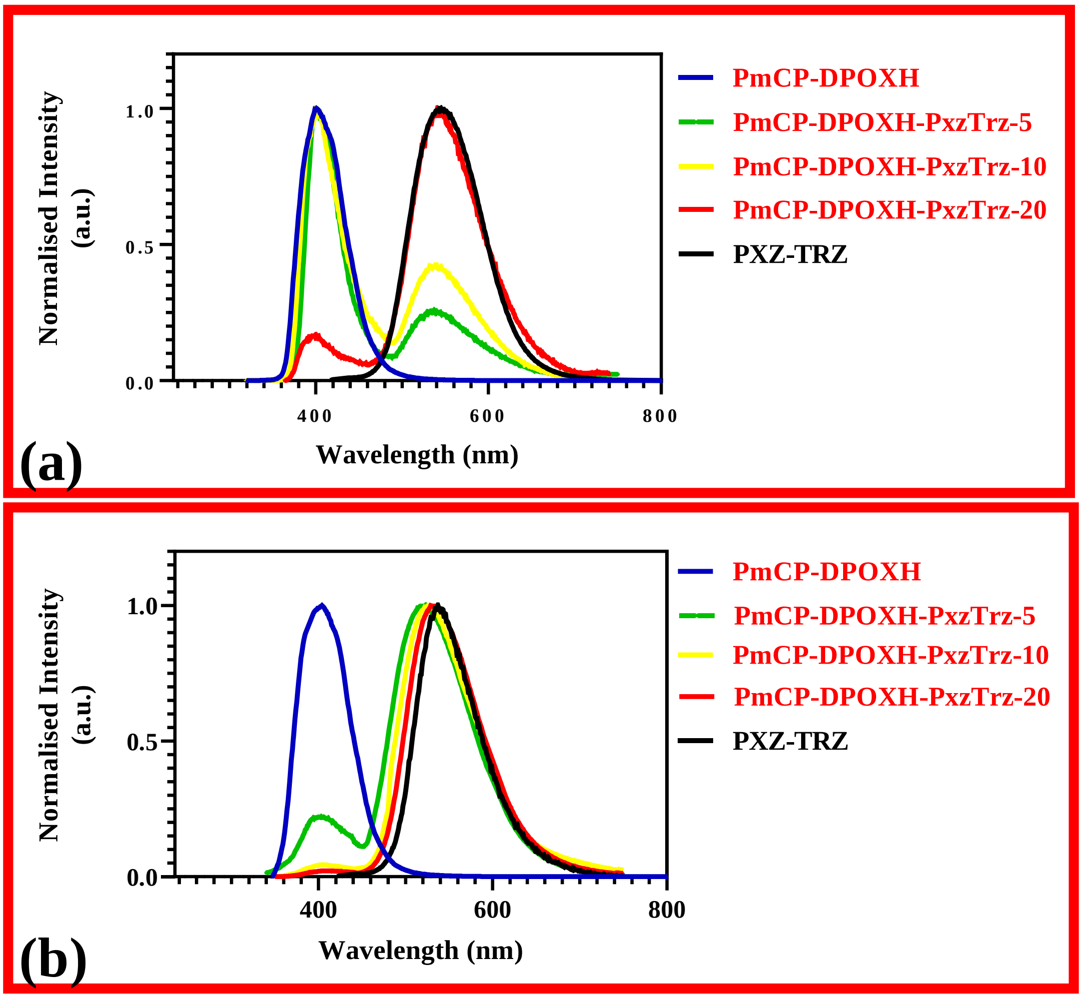

Figure 2.9: PL spectra of **PXZ-TRZ** and green-emitting TADF polymers (**PmCP-DPOXH-PxzTrz-5**, **PmCP-DPOXH-PxzTrz-10**, **PmCP-DPOXH-PxzTrz-20**), and **PmCP-DPOXH**, in **(a)** dilute toluene solutions (10^{-3} M) and **(b)** neat films.

2.2.4.3 Electrochemical Properties of Polymers

Cyclic voltammetry (CV) was conducted in order to examine the electrochemical properties of the green-emitting TADF polymers, **PmCP-DPOXH-PxzTrz-5**, **PmCP-DPOXH-PxzTrz-10**, and **PmCP-DPOXH-PxzTrz-20**, and **PmCP-DPOXH**. All CV studies were undertaken using drop-cast polymer films on platinum disc electrodes, employed as the working electrode, in tetra-n-butylammonium perchlorate dissolved in acetonitrile solution (0.1 M) as the electrolyte, together with silver nitrate (Ag/Ag^{+}) dissolved in acetonitrile solution (10^{-2} M) as a reference electrode, at a scan rate of 0.1 V s^{-1} under argon conditions.

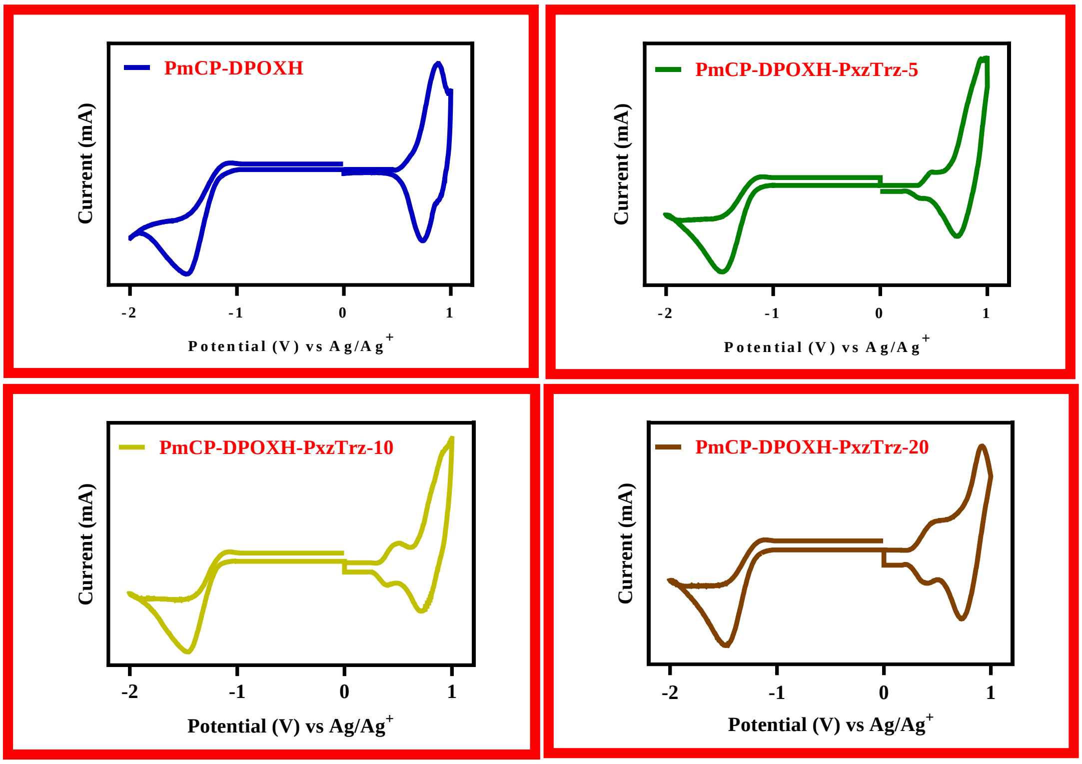

Figure 2.10: CV of **PmCP-DPOXH**, **PmCP-DPOXH-PxzTrz-5**, **PmCP-DPOXH-PxzTrz-10**, and **PmCP-DPOXH-PxzTrz-20**.

Comparison of the electrochemical properties of the TADF polymers, **PmCP-DPOXH-PxzTrz-5**, **PmCP-DPOXH-PxzTrz-10**, and **PmCP-DPOXH-PxzTrz-20**, with **PmCP-DPOXH** (**Figure 2.10**), revealed that **PmCP-DPOXH** shows a reversible anodic peak and an irreversible cathodic peak, which can be attributed to the mCP-based backbone. In contrast, **PmCP-DPOXH-PxzTrz-5**, **PmCP-DPOXH-PxzTrz-10**, and **PmCP-DPOXH-PxzTrz-20** display two anodic peaks and one irreversible cathodic peak at similar potentials. These results indicate that the green-emitting TADF polymers exhibit an additional reversible oxidation peak at the lower potential, which can be attributable to the electron-donating phenoxazine moiety of the TADF unit. Noticeably, with the increasing loading density of the TADF moiety in the TADF polymers from 5% to 20%, the intensity of the lower potential oxidation peak is gradually enhanced (**Figure 2.10)**.

Table 2.3: Electrochemical properties of **PmCP-DPOXH**, **PmCP-DPOXH-PxzTrz-5**, **PmCP-DPOXH-PxzTrz-10**, and **PmCP-DPOXH-PxzTrz-20**.

Polymers/ compound	HOMO (eV)	LUMO (eV)	HOMO-LUMO gap (eV)
PmCP-DPOXH	**-5.36**	**-3.55**	**1.81 ± 0.06**
PmCP-DPOXH-PxzTrz-5	**-5.09**	**-3.53**	**1.56 ± 0.02**
PmCP-DPOXH-PxzTrz-10	**-5.06**	**-3.53**	**1.53 ± 0.05**
PmCP-DPOXH-PxzTrz-20	**-4.99**	**-3.52**	**1.47 ± 0.09**

As can be seen from the data summarised in **Table 2.3**, the HOMO energy levels of the green-emitting TADF polymers, **PmCP-DPOXH-PxzTrz-5**, **PmCP-DPOXH-PxzTrz-10**, and **PmCP-DPOXH-PxzTrz-20**, were measured by their onset potential of oxidation peaks, which varied from -5.09 eV to -4.99 eV, appearing an increasing trend of the HOMO levels. **PmCP-DPOXH** exhibits the deepest HOMO level at -5.36 eV, owing to the absence of the TADF moiety. Thus, the increasing TADF moiety ratios exert a clear impact on the HOMO levels of the synthesised polymers.

Compared with the TADF polymers, **PmCP-DPOXH-PxzTrz-5**, **PmCP-DPOXH-PxzTrz-10** and **PmCP-DPOXH-PxzTrz-20**, the HOMO levels of the analogues, PTPA-mCP-PxzTrz-10, PTPA-mCP-PxzTrz-20, PTPA-mCP-PxzTrz-30, and PTPA-mCP-PxzTrz-40 are deeper, i.e., -5.97, -5.96, -5.97, and -5.94 eV, respectively.[44] Additionally, the HOMO energy levels of the TADF polymers (**PmCP-DPOXH-PxzTrz-5**, **PmCP-DPOXH-PxzTrz-10**, and **PmCP-DPOXH-PxzTrz-20**) are shallower relative to those PCz-mCP-PxzTrz-10, PCz-mCP-PxzTrz-20, PCz-mCP-PxzTrz-30, and PCz-mCP-PxzTrz-40 analogues which represent HOMO levels of -5.58, -5.55, -5.54 and -5.52 eV, respectively.[45] These differences in the HOMO levels can be attributed to various structures of the polymers.

However, the LUMO energy levels of **PmCP-DPOXH** and the green-emitting TADF polymers (**PmCP-DPOXH-PxzTrz-5**, **PmCP-DPOXH-PxzTrz-10**, and **PmCP-DPOXH-PxzTrz-20**) are determined by the onset potential of the reduction peaks, which lie within the range -3.55 eV to -3.52 eV. The LUMO levels of the TADF polymers are deeper than for the analogues, **PTPA-mCP-PxzTrz-10**, **PTPA-mCP-PxzTrz-20**, **PTPA-mCP-PxzTrz-30** and **PTPA-mCP-PxzTrz-40**, which exhibit LUMO levels of -2.93, -2.97, -3.03, and -3.01 eV, respectively.[44] Furthermore, the LUMO energy levels of the TADF polymers (**PmCP-DPOXH-PxzTrz-5**, **PmCP-DPOXH-PxzTrz-10**, and **PmCP-DPOXH-PxzTrz-20**) are deeper compared to those analogues **PCz-mCP-PxzTrz-10**, **PCz-mCP-PxzTrz-20**, **PCz-mCP-PxzTrz-30**, and **PCz-mCP-PxzTrz-40**, which represent LUMO levels of -2.96, -2.93, -2.94, and -2.93 eV, respectively.[45] The variation within the LUMO levels can be ascribed to the dissimilar polymer configurations.

Both HOMO and LUMO levels of the polymers are impacted by the TADF moiety tethered to the polymeric backbone containing the **mCP** unit. Noteworthily, the HOMO-LUMO gaps of the green-emitting TADF polymers, **PmCP-DPOXH-PxzTrz-5**, **PmCP-DPOXH-PxzTrz-10** and **PmCP-DPOXH-PxzTrz-20**, and **PmCP-DPOXH**, which were deduced by subtracting the LUMO values from the HOMO values, demonstrate a transparent decrease with increasing TADF unit loading, i.e., from 1.56 eV (**PmCP-DPOXH-PxzTrz-5**) to 1.47 eV (**PmCP-DPOXH-PxzTrz-20**). In contrast, **PmCP-DPOXH** shows the highest HOMO-LUMO gap of 1.81 eV owing to the absence of the TADF moiety in the polymer. With increasing proportions of TADF moiety in the polymers, the HOMO-LUMO gaps of polymers **PTPA-mCP-PxzTrz-X** and **PCz-mCP-PxzTrz-X** exhibit a similar effect with respect to the reduction in HOMO-LUMO gaps of polymers.[44,45] It can be concluded that the existence of the TADF moiety in the polymers has an evident effect on the HOMO-LUMO gap, which is reduced in relation to an increase in TADF unit ratio. Thus, the **PXZ-TRZ** tethered on the polymeric backbone-containing **mCP** host significantly affects the polymers' electrochemical behaviours, as illustrated in **Table 2.3**. More importantly, the optical gaps of the target polymers should be lower than HOMO-LUMO gaps since the electron and hole remain electrostatically bound to each other in the excited state. However, HOMO-LUMO gaps of target polymers were obtained lower than expected, which can be referred to the desired polymers were oxidised during the reduction process.

2.2.4.4 Thermal Properties of Polymers

The thermal stability of each polymer was assessed using thermogravimetric analysis (TGA), which was conducted in a deoxygenated atmosphere at a heating rate of 10 °C min^{-1}. The initial degradation temperatures of **PmCP-DPOXH**, **PmCP-DPOXH-PxzTrz-5**, **PmCP-DPOXH-PxzTrz-10**, and **PmCP-DPOXH-PxzTrz-20** occur at 281 °C, 290 °C, 297 °C and 301 °C, respectively, as summarised in **Table 2.4**.

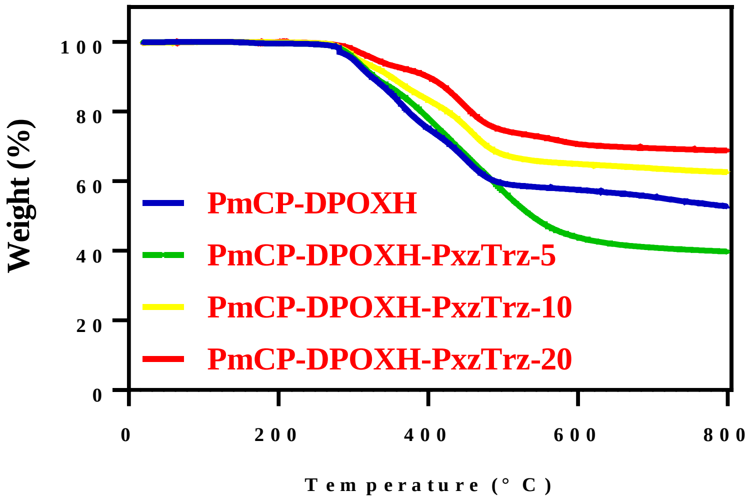

Figure 2.11: TGA of **PmCP-DPOXH**, **PmCP-DPOXH-PxzTrz-5**, **PmCP-DPOXH-PxzTrz-10**, and **PmCP-DPOXH-PxzTrz-20**.

As displayed in **Figure 2.11**, all polymers reveal excellent thermal stability with thermal decomposition temperatures (T_d) exceeding 280 °C. This high thermal stability of the target polymers therefore renders them suitable for application in solution-processable OLED devices with long-term stability.

PmCP-DPOXH-PxzTrz-5, **PmCP-DPOXH-PxzTrz-10**, and **PmCP-DPOXH-PxzTrz-20** show similar thermal properties compared to **PmCP-DPOXH** as they contain the same TADF units onto the side chain with different ratios. Interestingly, **PmCP-DPOXH** displays one decomposition phase at the temperature of 281 °C, which is the lowest onset of degradation temperature compared to TADF polymers, as **PmCP-DPOXH** contains the **mCP** host without further TADF moieties. Remarkably, **PmCP-DPOXH-PxzTrz-5**, **PmCP-DPOXH-PxzTrz-10**, and **PmCP-DPOXH-PxzTrz-20** exhibit thermal decomposition temperatures, which marks the onset of degradation temperatures, at 290 °C, 297 °C, and 301 °C, respectively. Noteworthily, the onset of degradation temperatures of **PmCP-DPOXH-PxzTrz-5**, **PmCP-DPOXH-PxzTrz-10**, and **PmCP-DPOXH-PxzTrz-20** increase gradually with rising proportions of TADF units. This fact can be attributed to increasing steric hindrance of these TADF polymers with rising TADF moiety ratios, which make them more rigid and stable. The rigidity of TADF polymers require more thermal energy to give rise to cleavage through combustion process.

Table 2.4: Thermal properties of **PmCP-DPOXH**, **PmCP-DPOXH-PxzTrz-5**, **PmCP-DPOXH-PxzTrz-10**, and **PmCP-DPOXH-PxzTrz-20**.

Polymers	**T_d (° C)**
PmCP-DPOXH	**281**
PmCP-DPOXH-PxzTrz-5	**290**
PmCP-DPOXH-PxzTrz-10	**297**
PmCP-DPOXH-PxzTrz-20	**301**

2.3 Conclusion

A surge in commercial interest in relation to the utilisation of OLEDs as next generation displays and lighting fields has fuelled the constant expansion of organic emissive materials. Over previous years, the primary organic emissive materials used in OLEDs have evolved swiftly, initially encompassing fluorescent substances, subsequently, phosphorescent heavy-metal complexes and finally, TADF materials. The latter's potential for converting-up triplet excitons into singlet excitons confers approximately 100% EUE without exploiting any heavy-metal components in the new generation of materials which include TADF characteristics. The development of cutting-edge OLEDs based on TADF materials has made significant progress in the last few years. Despite improvements in efficiency, the evaporated deposition technique required for their synthesis is reliant on sophisticated and expensive structures, and fine regulation, making it impractical for large-scale device production. Compared to other manufacturing approaches, a solution-process is simpler, less expensive, and a more readily controlled option for enabling large-scale production. However, most of the published TADF dopants are essentially small molecules which are incompatible with solution-processing. As a result, the evolution of solution-processable organic emissive materials exhibiting TADF characteristics is of critical relevance. Thus, focus was placed on an engineering strategy to design TADF-containing polymers in this work.

These polymers comprise two portions, i.e., a polymeric backbone, which functions as a host and the charge transport channel, and a sidechain of the polymeric backbone, which acts as a guest molecule with TADF properties, tethered to the polymer backbone. All the current TADF polymers were designed to be of the sidechain type, containing both partially conjugated and non-conjugated systems in the main chain backbone in order to achieve equilibrium; the usage of only a non-conjugated main chain system is potentially harmful to the properties of charge transfer or device performance.[15]

The resulting green emitting TADF polymers could easily be dissolved in common organic solvents, such as DCM, chloroform, toluene, THF and chlorobenzene.

The chemical structures of **PmCP-DPOXH**, together with the polymers grafted by a TADF moiety located at the sidechain, i.e., **PmCP-DPOXH-PxzTrz-5**, **PmCP-**

DPOXH-PxzTrz-10, and **PmCP-DPOXH-PxzTrz-20**, were fully verified by ^{1}H NMR spectroscopy. The ^{1}H NMR spectroscopy data for all polymers were in good agreement with the expected structures.

GPC analysis was successfully conducted in order to estimate the Mn and Mw values of all polymers. Mn and PDI values of the copolymers, **PmCP-DPOXH**, **PmCP-DPOXH-PxzTrz-5**, **PmCP-DPOXH-PxzTrz-10**, and **PmCP-DPOXH-PxzTrz-20**, were determined to be within the ranges 5300–6800 Daltons (Da) and 1.25–1.36, respectively. The relatively low molecular weight of the synthesised polymers could be a result of the large steric effect of carbazole in the **mCP** moiety. The introduction of the π-interrupted structure of 1,6-diphenoxyhexane (**DPOXH**) to the polymer backbone facilitated attainment of polymers with high bandgap backbone suitable for energy transfer to lower bandgap TADF substituents.

The UV-Vis absorption spectra of the target polymers, **PmCP-DPOXH**, **PmCP-DPOXH-PxzTrz-5**, **PmCP-DPOXH-PxzTrz-10**, and **PmCP-DPOXH-PxzTrz-20**, as well as the TADF moiety, **PXZ-TRZ,** were examined in both toluene solution and neat film. An intense absorption band, which peaked at approximately 304 nm, reflects the π-π* transition in the target polymers, indicating that this peak can be related to their polymeric backbone. Remarkably, the absorption peaks in these polymers were almost identical, proving that the contribution of the low loading content of the TADF unit to the target polymer absorption spectra was negligible.

The optical gaps (E_g) of **PmCP-DPOXH**, **PmCP-DPOXH-PxzTrz-5**, **PmCP-DPOXH-PxzTrz-10** and **PmCP-DPOXH-PxzTrz-20** were 3.20 eV, 3.26 eV, 3.27 eV and 3.27 eV, respectively. In toluene solution, dual emission peaks within the ranges 340-460 nm and 460-700 nm were observed in the PL profiles of **PmCP-DPOXH-PxzTrz-5**, **PmCP-DPOXH-PxzTrz-10**, and **PmCP-DPOXH-PxzTrz-20**. These represent the polymeric backbone and TADF moiety emissions, respectively. Remarkably, with the rising molar ratios of the TADF monomer, the PL emission peaks of the target TADF copolymers were gradually red-shifted, from 523 nm for **PmCP-DPOXH-PxzTrz-5**, to 528 nm for **PmCP-DPOXH-PxzTrz-20**, owing to existing aggregation, which demonstrates that the TADF moiety makes an obvious contribution to the copolymers’ emission profiles.

The HOMO levels of the green-emitting TADF polymers vary from -5.09 eV to -4.99 eV, appearing as a rising HOMO levels with incremental TADF moiety loading ratios. **PmCP-DPOXH** exhibits the deepest HOMO level of -5.36 eV owing to the absence of the TADF moiety in the polymer. The HOMO level data indicate the influence of the increasing ratios of TADF moiety on the synthesised polymers.

Thus, both HOMO and LUMO levels of the polymers are notably influenced by the TADF moiety tethered on the polymeric backbone-containing **mCP** unit. Notably, the HOMO-LUMO gaps of green-emitting TADF polymers, **PmCP-DPOXH-PxzTrz-5**, **PmCP-DPOXH-PxzTrz-10**, and **PmCP-DPOXH-PxzTrz-20**, as well as **PmCP-DPOXH,** decrease clearly with elevated TADF unit loading ratios from 1.56 eV (**PmCP-DPOXH-PxzTrz-5**) to 1.47 eV (**PmCP-DPOXH-PxzTrz-20**). It can be concluded that the existence of the TADF moiety in the polymers has an evident effect on the HOMO-LUMO gap; the latter diminishes with rising TADF unit proportions.

2.4 References

(1) Tao, Y.; Yuan, K.; Chen, T.; Xu, P.; Li, H.; Chen, R.; Zheng, C.; Zhang, L.; Huang, W. Thermally Activated Delayed Fluorescence Materials towards the Breakthrough of Organoelectronics. *Advanced Materials* **2014**, *26* (47), 7931–7958.

(2) Chi, Y.; Chou, P.-T. Transition-Metal Phosphors with Cyclometalating Ligands: Fundamentals and Applications. *Chemical Society Reviews* **2010**, *39* (2), 638–655.

(3) Zhu, M.; Yang, C. Blue Fluorescent Emitters: Design Tactics and Applications in Organic Light-Emitting Diodes. *Chemical Society Reviews* **2013**, *42* (12), 4963–4976.

(4) Itoh, T. Fluorescence and Phosphorescence from Higher Excited States of Organic Molecules. *Chemical Reviews* **2012**, *112* (8), 4541–4568.

(5) Dias, F. B.; Bourdakos, K. N.; Jankus, V. M.; KC, K.; KT, B. V. Santos, J. Bryce, MR and Monkman, AP,“Triplet Harvesting with 100% Efficiency by Way of Thermally Activated Delayed Fluorescence in Charge Transfer OLED Emitters,.” *Adv. Mater* **2013**, *25*, 3707–3714.

(6) Ishimatsu, R.; Matsunami, S.; Kasahara, T.; Mizuno, J.; Edura, T.; Adachi, C.; Nakano, K.; Imato, T. Electrogenerated Chemiluminescence of Donor–Acceptor Molecules with Thermally Activated Delayed Fluorescence. *Angewandte Chemie* **2014**, *126* (27), 7113–7116.

(7) Zhang, Q.; Li, B.; Huang, S.; Nomura, H.; Tanaka, H.; Adachi, C. Efficient Blue Organic Light-Emitting Diodes Employing Thermally Activated Delayed Fluorescence. *Nature Photonics* **2014**, *8* (4), 326–332.

(8) Uoyama, H.; Goushi, K.; Shizu, K.; Nomura, H.; Adachi, C. Highly Efficient Organic Light-Emitting Diodes from Delayed Fluorescence. *Nature* **2012**, *492* (7428), 234–238.

(9) Kim, B. S.; Lee, J. Y. Engineering of Mixed Host for High External Quantum Efficiency above 25% in Green Thermally Activated Delayed Fluorescence Device. *Advanced Functional Materials* **2014**, *24* (25), 3970–3977.

(10) Zhang, Q.; Kuwabara, H.; Potscavage Jr, W. J.; Huang, S.; Hatae, Y.; Shibata, T.; Adachi, C. Anthraquinone-Based Intramolecular Charge-Transfer Compounds: Computational Molecular Design, Thermally Activated Delayed Fluorescence, and Highly Efficient Red Electroluminescence. *Journal of the American Chemical Society* **2014**, *136* (52), 18070–18081.

(11) Albrecht, K.; Matsuoka, K.; Fujita, K.; Yamamoto, K. Carbazole Dendrimers as Solution-Processable Thermally Activated Delayed-Fluorescence Materials. *Angewandte Chemie International Edition* **2015**, *54* (19), 5677–5682.

(12) Cho, Y. J.; Jeon, S. K.; Chin, B. D.; Yu, E.; Lee, J. Y. The Design of Dual Emitting Cores for Green Thermally activated delayed fluorescence Materials. *Angewandte Chemie International Edition* **2015**, *54* (17), 5201–5204.

(13) Cho, Y. J.; Yook, K. S.; Lee, J. Y. High Efficiency in a Solution-processed Thermally Activated Delayed-fluorescence Device Using a Delayed-fluorescence Emitting Material with Improved Solubility. *Advanced Materials* **2014**, *26* (38), 6642–6646.

(14) Nikolaenko, A. E.; Cass, M.; Bourcet, F.; Mohamad, D.; Roberts, M. Thermally Activated Delayed Fluorescence in Polymers: A New Route toward Highly Efficient Solution Processable OLEDs. *Advanced Materials* **2015**, *27* (44), 7236–7240.

(15) Luo, J.; Xie, G.; Gong, S.; Chen, T.; Yang, C. Creating a Thermally Activated Delayed Fluorescence Channel in a Single Polymer System to Enhance Exciton Utilization Efficiency for Bluish-Green Electroluminescence. *Chemical Communications* **2016**, *52* (11), 2292–2295.

(16) Shao, S.; Ding, J.; Wang, L.; Jing, X.; Wang, F. Highly Efficient Blue Electrophosphorescent Polymers with Fluorinated Poly (Arylene Ether Phosphine Oxide) as Backbone. *Journal of the American Chemical Society* **2012**, *134* (37), 15189–15192.

(17) Gong, S.; Yang, C.; Qin, J. Efficient Phosphorescent Polymer Light-Emitting Diodes by Suppressing Triplet Energy Back Transfer. *Chemical Society Reviews* **2012**, *41* (14), 4797–4807.

(18) Segal, M.; Baldo, M. A.; Holmes, R. J.; Forrest, S. R.; Soos, Z. G. Excitonic Singlet-Triplet Ratios in Molecular and Polymeric Organic Materials. *Physical Review B* **2003**, *68* (7), 075211.

(19) Cao, Y.; Parker, I. D.; Yu, G.; Zhang, C.; Heeger, A. J. Improved Quantum Efficiency for Electroluminescence in Semiconducting Polymers. *Nature* **1999**, *397* (6718), 414–417.

(20) Wilson, J. S.; Dhoot, A. S.; Seeley, A.; Khan, M. S.; Köhler, A.; Friend, R. H. Spin-Dependent Exciton Formation in π-Conjugated Compounds. *Nature* **2001**, *413* (6858), 828–831.

(21) Reufer, M. J.; Walter, P. G.; Lagoudakis, A. B.; Hummel, J. S.; Kolb, H. G. R. U. Scherf, and JM Lupton. *Nat. Mater* **2005**, *4*, 340.

(22) Brunner, K.; van Dijken, A.; Börner, H.; Bastiaansen, J. J. A. M.; Kiggen, N. M. M.; Langeveld, B. M. W. Carbazole Compounds as Host Materials for Triplet Emitters in Organic Light-Emitting Diodes: Tuning the HOMO Level without Influencing the Triplet Energy in Small Molecules. *Journal of the American Chemical Society* **2004**, *126* (19), 6035–6042.

(23) Lee, J.; Shizu, K.; Tanaka, H.; Nomura, H.; Yasuda, T.; Adachi, C. Oxadiazole-and Triazole-Based Highly-Efficient Thermally Activated Delayed Fluorescence Emitters for Organic Light-Emitting Diodes. *Journal of Materials Chemistry C* **2013**, *1* (30), 4599–4604.

(24) Li, W.; Pan, Y.; Xiao, R.; Peng, Q.; Zhang, S.; Ma, D.; Li, F.; Shen, F.; Wang, Y.; Yang, B. Employing∼ 100% Excitons in OLEDs by Utilizing a Fluorescent Molecule with Hybridized Local and Charge-transfer Excited State. *Advanced Functional Materials* **2014**, *24* (11), 1609–1614.

(25) Peng, H.-Q.; Niu, L.-Y.; Chen, Y.-Z.; Wu, L.-Z.; Tung, C.-H.; Yang, Q.-Z. Biological Applications of Supramolecular Assemblies Designed for Excitation Energy Transfer. *Chemical Reviews* **2015**, *115* (15), 7502–7542.

(26) Xie, Z.; Chen, C.; Xu, S.; Li, J.; Zhang, Y.; Liu, S.; Xu, J.; Chi, Z. White-light Emission Strategy of a Single Organic Compound with Aggregation-induced Emission and Delayed Fluorescence Properties. *Angewandte Chemie* **2015**, *127* (24), 7287–7290.

(27) Xu, S.; Liu, T.; Mu, Y.; Wang, Y.; Chi, Z.; Lo, C.; Liu, S.; Zhang, Y.; Lien, A.; Xu, J. An Organic Molecule with Asymmetric Structure Exhibiting Aggregation-induced Emission, Delayed Fluorescence, and Mechanoluminescence. *Angewandte Chemie* **2015**, *127* (3), 888–892.

(28) Sun, K.; Xie, X.; Liu, Y.; Jiang, W.; Ban, X.; Huang, B.; Sun, Y. Thermally Cross-Linkable Thermally activated delayed fluorescence Materials for Efficient Blue Solution-Processed Organic Light-Emitting Diodes. *Journal of Materials Chemistry C* **2016**, *4* (38), 8973–8979.

(29) Jeon, S. O.; Lee, J. Y. Comparison of Symmetric and Asymmetric Bipolar Type High Triplet Energy Host Materials for Deep Blue Phosphorescent Organic Light-Emitting Diodes. *Journal of Materials Chemistry* **2012**, *22* (15), 7239–7244.

(30) Zhang, R.; Peterson, J. P.; Fischer, L. J.; Ellern, A.; Winter, A. H. Effect of Structure on the Spin–Spin Interactions of Tethered Dicyanomethyl Diradicals. *Journal of the American Chemical Society* **2018**, *140* (43), 14308–14313.

(31) Hermann, M.; Wassy, D.; Kratzert, D.; Esser, B. Dibenzo [a, e] Pentalenophanes: Bending a Non-Alternant Hydrocarbon. *Chemistry–A European Journal* **2018**, *24* (29), 7374–7387.

(32) Vanderhaeghe, H. Phenoxazines. I. Ring-Substituted Derivatives. *The Journal of Organic Chemistry* **1960**, *25* (5), 747–753.

(33) Anchan, K.; Puttappa, N. H.; Poongavanam, B.; Sarkar, S. K. Microwave Assisted Rapid Synthesis of Phenoxazines and Benzopyridoxazines. *Synthetic Communications* **2021**, *51* (4), 635–646.

(34) MÜLLER, P.; Buu-Hoi, N. P.; Rips, R. Preparation and Some Reactions of Phenoxazine and Phenoselenazine. *The Journal of Organic Chemistry* **1959**, *24* (1), 37–39.

(35) Zhong, H.; Xu, E.; Zeng, D.; Du, J.; Sun, J.; Ren, S.; Jiang, B.; Fang, Q. New Optoelectronic Materials Based on Bitriazines: Synthesis and Properties. *Organic Letters* **2008**, *10* (5), 709–712.

(36) Tanaka, H.; Shizu, K.; Miyazaki, H.; Adachi, C. Efficient Green Thermally Activated Delayed Fluorescence (TADF) from a Phenoxazine–Triphenyltriazine (PXZ–TRZ) Derivative. *Chemical Communications* **2012**, *48* (93), 11392–11394.

(37) Moon, Y. K.; Jang, H. J.; Hwang, S.; Kang, S.; Kim, S.; Oh, J.; Lee, S.; Kim, D.; Lee, J. Y.; You, Y. Modeling Electron-Transfer Degradation of Organic Light-Emitting Devices. *Advanced Materials* **2021**, *33* (12), 2003832.

(38) Kamogawa, H.; Todo, Y.; Nanasawa, M. Synthesis of Vinyl Polymers with Pendant Phenoxazinyl Group. *Journal of Polymer Science: Polymer Chemistry Edition* **1981**, *19* (10), 2571–2579.

(39) Hsieh, C.-H.; Chen, W.-C.; Yang, S.-H.; Chao, Y.-C.; Lee, H.-C.; Chiang, C.-L.; Lin, C.-Y. A Simple Route to Linear and Hyperbranched Polythiophenes Containing Diketopyrrolopyrrole Linking Groups with Improved Conversion Efficiency. *AIMS Materials Science* **2017**, *4* (4), 878–893.

(40) Luo, X.; Ma, X.; Lebreux, F.; Markó, I. E.; Lam, K. Electrochemical Methoxymethylation of Alcohols–a New, Green and Safe Approach for the Preparation of MOM Ethers and Other Acetals. *Chemical Communications* **2018**, *54* (71), 9969–9972.

(41) Suzuki, A. Organoboron Compounds in New Synthetic Reactions. *Pure and Applied Chemistry* **1985**, *57* (12), 1749–1758.

(42) Krebs, F. C.; Nyberg, R. B.; Jørgensen, M. Influence of Residual Catalyst on the Properties of Conjugated Polyphenylenevinylene Materials: Palladium Nanoparticles and Poor Electrical Performance. *Chemistry of Materials* **2004**, *16* (7), 1313–1318.

(43) Nielsen, K. T.; Bechgaard, K.; Krebs, F. C. Removal of Palladium Nanoparticles from Polymer Materials. *Macromolecules* **2005**, *38* (3), 658–659.

(44) Yao, Z.; Zong, W.; Wang, K.; Yuan, P.; Liu, Y.; Xu, S.; Cao, S. Triphenylamine-Carbazole Alternating Copolymers Bearing Thermally activated delayed fluorescence Emitting and Host Pendant Groups for Solution-Processable OLEDs. *Reactive and Functional Polymers* **2021**, *163*, 104898.

(45) Zong, W.; Qiu, W.; Yuan, P.; Wang, F.; Liu, Y.; Xu, S.; Su, S.-J.; Cao, S. Thermally Activated Delayed Fluorescence Polymers for High-Efficiency Solution-Processed Non-Doped OLEDs: Convenient Synthesis by Binding TADF Units and Host Units to the Pre-Synthesized Polycarbazole-Based Backbone via Click Reaction. *Polymer* **2022**, *240*, 124468.

Chapter 3: DPEPO-Based Polymers with Pendant TADF Emitters for use in Solution Processable OLEDs

Abstract

The Use of polymers with TADF properties with solution-processing properties is attracting great attention in the area of OLEDs. Nonetheless, up until now, there has been little examples of efficacious TADF polymers, critically limiting commercial objectives relating to their usage in display and lighting fields. Work in this chapter is concerned with development of green light emitting TADF polymers which display excellent solubility and good thermal stability. The **DPEPO** molecule is known as an excellent host material to TADF emitters in OLEDs as it has good electron transporting properties and a high triplet energy enabling its use as a host material to a number of emitters with different energies. The newly developed polymers described here consist of **DPEPO**-based polymers with varying loadings of the **PXZ-TRZ** green-emitting TADF molecule. The optical properties of the polymers are investigated using UV-vis spectroscopy and photoluminescence (PL) spectroscopy. The electrochemical and thermal properties of the polymers were undertaken using cyclic voltammetry (CV) and thermal gravimetric studies (TGA analyses) respectively. Remarkably, using PL spectroscopy, practically complete interchain and intrachain energy transfer from the polymeric backbone to the sidechain TADF moiety is observed, resulting in only a TADF emission peak with tail residual emission from the main chain backbone for **PDPEPO-DPOXH-PxzTrz-10** and **PDPEPO-DPOXH-PxzTrz-20**. Furthermore, the HOMO levels of TADF polymers, **PDPEPO-DPOXH-PxzTrz-X**, range from -5.11 eV to -5.00 eV, evidencing an increasing trend of the HOMO levels with rising TADF moiety loading ratios in polymers. It is noteworthy that the HOMO-LUMO gaps of the TADF polymers, **PDPEPO-DPOXH-PxzTrz-X**, reduced noticeably with incremental TADF unit loading, from 1.75 eV (**PDPEPO-DPOXH-PxzTrz-5**) to 1.62 eV (**PDPEPO-DPOXH-PxzTrz-20**). Moreover, high thermal stability for all polymers was observed with thermal decomposition temperatures higher than 310 °C, proving that these target polymers could be exploited in solution processable OLED devices with long-term stability.

3.1 Introduction

The noted evolution of OLEDs can be divided into three primary phases based on the different emission processes characterising the emitters, i.e., classic fluorescent and phosphorescent materials, respectively, and TADF emitters.[1,2] In contrast to formerly synthesised fluorescent or phosphorescent materials, TADF emitters have attracted considerable interest as they have the theoretical potential to attain 100% internal quantum efficiency without the need for noble metals, such as iridium or platinum.[3,4] In order to gain TADF characteristics, an adequately elevated spatial isolation between the HOMO and the LUMO states is required so as to establish a reduced ΔE_{ST} between the lowest excited triplet (T_1) and singlet (S_1) levels.[5,6] By taking advantage of the reduced ΔE_{ST}, the non-radiative triplet excitons can be easily up-converted into the radiative singlet states through RISC processes by means of thermal activation. This offers an appropriate method *via* which to fully exploit both the singlet and triplet excitons in OLEDs.

Up until this point, considerable progress has been achieved in the development of small molecule TADF materials; performances are comparable to those of phosphorescence OLEDs.[7–10] Although, standard *vacuum* deposition methods have been extensively utilised as popular and conventional techniques in industrial OLED applications, solution-processed OLED applications are more attractive owing to their potential for large-scale production, cheap cost, and roll-to-roll production processes.[11,12]

In spite of this, the performance of solution-processed OLEDs continues to lag significantly behind that of traditional *vacuum*-evaporation OLEDs. Consequently, this necessitates significant investments of time and resources in the development of the more recently available TADF materials in order to meet the needs of the solution-processed technology.[13–16]

Following the innovation of the sidechain design approach for the generation of highly efficient TADF polymers, Zhou *et al.* (2019) devised and synthesised a variety of green TADF copolymers, each of which contained different molar ratios of TADF moieties incorporated onto the sidechains (**Figure 3.1**).[17] Owing to the fact that the fully non-conjugated main chain backbone has an adverse effect on charge transport features and can give rise to poor device performance, the copolymer main chain backbone encompassed both a partially conjugated carbazole unit and a non-conjugated tetraphenyl silicon moiety so as to reach equilibrium. In addition, a sidechain, containing a conventional TADF moiety, 10,10′-(((2-(4-(9H-carbazol-9-yl) phenyl) pyrimidine−4,6-diyl) pyrimidine bis (4,1-phenylene) bis (10H-phenoxazine) (PXZ-Pm-MeOCz), was inserted in order to confer TADF features to the copolymers. Interestingly, in neat films, these TADF polymeric films all demonstrated elevated PLQYs. When the proportion of TADF moiety hanging on the sidechain was 6%, the PLQYs amounted to a maximum of 71%. The solution-processed polymer light emitting diodes (PLEDs), which were produced utilising these TADF polymers as the emissive layer, gave rise to a reasonably high performance, yielding a maximum EQE of 7.0%.[17]

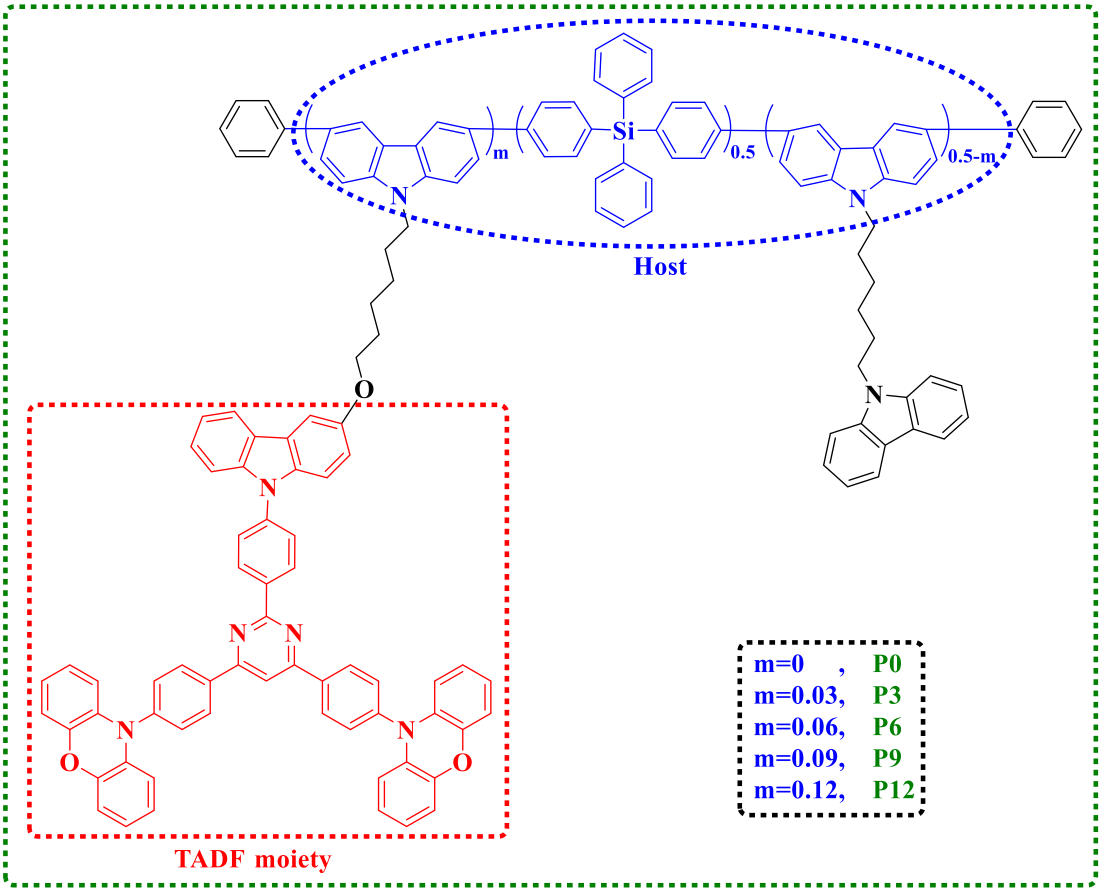

Figure 3.1: TADF polymers (**P0**, **P3**, **P6**, **P9**, and **P12**) synthesised by Zhou *et al.*[17]

3.2 Results and Discussion

PXZ-TRZ is well-recognised as an efficient green TADF light emitter in OLED devices. Acquisition of the active layers, so as to facilitate the emitter's application within devices, requires the evaporation of **PXZ-TRZ** on a substrate. In order to permit the usage of polymer-based TADF materials in solution-processed devices, a polymer sidechain engineering approach was employed by grafting a TADF group onto the polymer backbone sidechain. This engineering strategy requires two distinct types of functional sites within a single-polymer system, i.e., the polymer backbone, which serves as the host and the charge transport channel, and the grafted unit on the polymer sidechain, which enables additional functionalities. These green-emitting TADF polymers were appropriately designed by means of a sidechain engineering approach using a polymeric backbone, which contains a mixture of a non-conjugated main chain with a partially conjugated **DPEPO** moiety so as to reach an equilibrium. **DPEPO** was chosen as a polymer host as this compound possesses a high triplet level as well as excellent electron transport characteristics, thus preventing undesired TEBT from the TADF emitter to the host molecule.

1,6-Diphenoxyhexane (**DPOXH**) from **M2** was added into the polymer backbone in order to limit electronic delocalisation along the polymer backbone which uses the **DPEPO** host as repeat units. The role of the spacer, **M2**, helps to tune the polymer host's triplet energy levels (E_T).

PXZ-TRZ is grafted onto the polymer sidechains as this compound exhibits notable TADF properties and can be adjusted at the molecular level. **Scheme 3.1** demonstrates the synthesis of the polymer, **PDPEPO-DPOXH**, utilising the two monomers, **M4** and **M2,** in a molar ratio of 50:50. As illustrated, a typical Suzuki polycondensation of the monomers, **M4**, **M2** and **M3,** at feed molar ratios of 45:50:5, 40:50:10 and 30:50:20, respectively, was employed. These polymers were designated as **PDPEPO-DPOXH-PxzTrz-5**, **PDPEPO-DPOXH-PxzTrz-10**, and **PDPEPO-DPOXH-PxzTrz-20,** according to their respective **M3** feed ratios. Additionally, the polymer, **PDPEPO-DPOXH,** without **M3,** was prepared for the purpose of comparison against **PDPEPO-DPOXH-PxzTrz-5**, **PDPEPO-DPOXH-PxzTrz-10** and **PDPEPO-DPOXH-PxzTrz-20**.

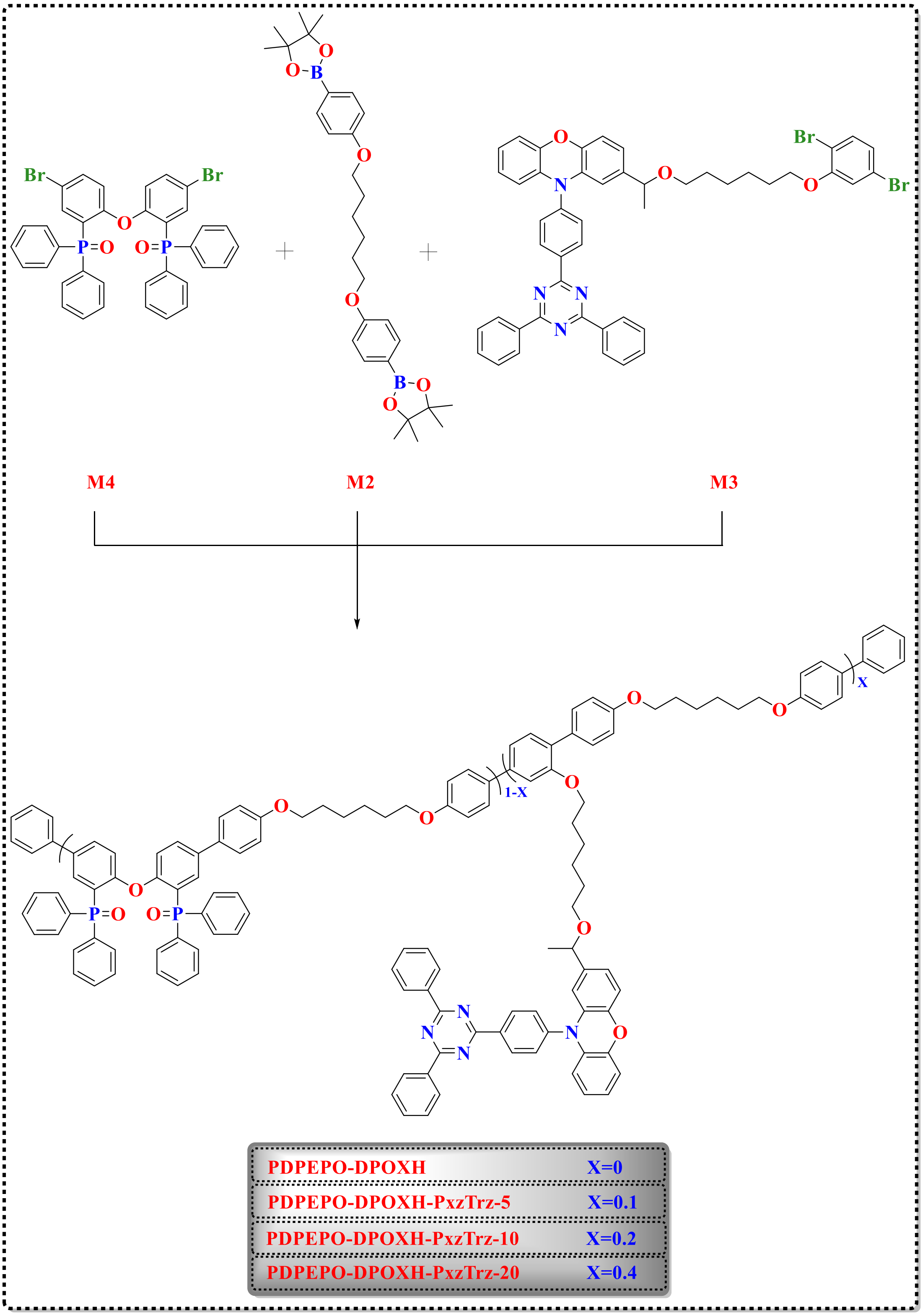

PDPEPO-DPOXH	X=0
PDPEPO-DPOXH-PxzTrz-5	X=0.1
PDPEPO-DPOXH-PxzTrz-10	X=0.2
PDPEPO-DPOXH-PxzTrz-20	X=0.4

Scheme 3.1: Synthetic route of the **PDPEPO-DPOXH**, **PDPEPO-DPOXH-PxzTrz-5**, **PDPEPO-DPOXH-PxzTrz-10**, and **PDPEPO-DPOXH-PxzTrz-20**. Reagents and conditions: anhydrous THF, K_2CO_3, $Pd(OAc)_2$, $P(o\text{-}tol)_3$, and 95 °C.

3.2.1 Synthesis of Host Monomer **M4**

3.2.1.1 Synthesis of bis[2-(diphenylphosphino)phenyl] ether oxide (**DPEPO**)

Bis[(2-diphenylphosphino)phenyl] ether, **DPEPhos,** was successfully oxidised using 30% hydrogen peroxide (H_2O_2) as an oxidising agent in DCM, at a temperature of 0 °C, in order to form **DPEPO** according to the modified procedure published by Miyata *et al.*[18] (**scheme 3.2**). The desired pure **DPEPO** molecule was obtained, following precipitation in hexane, as a white powder, with a yield of 99%.

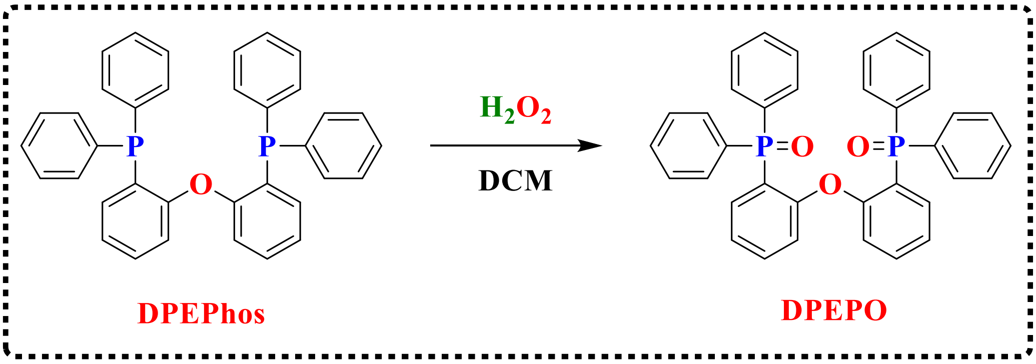

Scheme 3.2: Synthetic route of **DPEPO**.

Scheme 3.3 shows the oxidation reaction mechanism for the **DPEPhos** compound using hydrogen peroxide as an oxidising reagent. This oxidation mechanism shows the conversion of phosphine groups on **DPEPhos**, which has the (III) oxidation state, to phosphine oxide groups present in **DPEPO** with the oxidation state (V). A phosphorus atom of **DPEPhos** behaves as a nucleophile. It attacks one of the oxygen atoms on hydrogen peroxide, leading to the formation of phosphine oxide protonated on the oxygen atom as an intermediate **(A)**. The latter undergoes hydrogen abstraction by a hydroxide anion to produce an intermediate **(B)** as a tertiary phosphine oxide for one of the phosphine groups. A second phosphine group of the resulting compound **(B)** is subsequently oxidised to a tertiary phosphine oxide group, giving rise to the formation of the desired molecule of **DPEPO**.

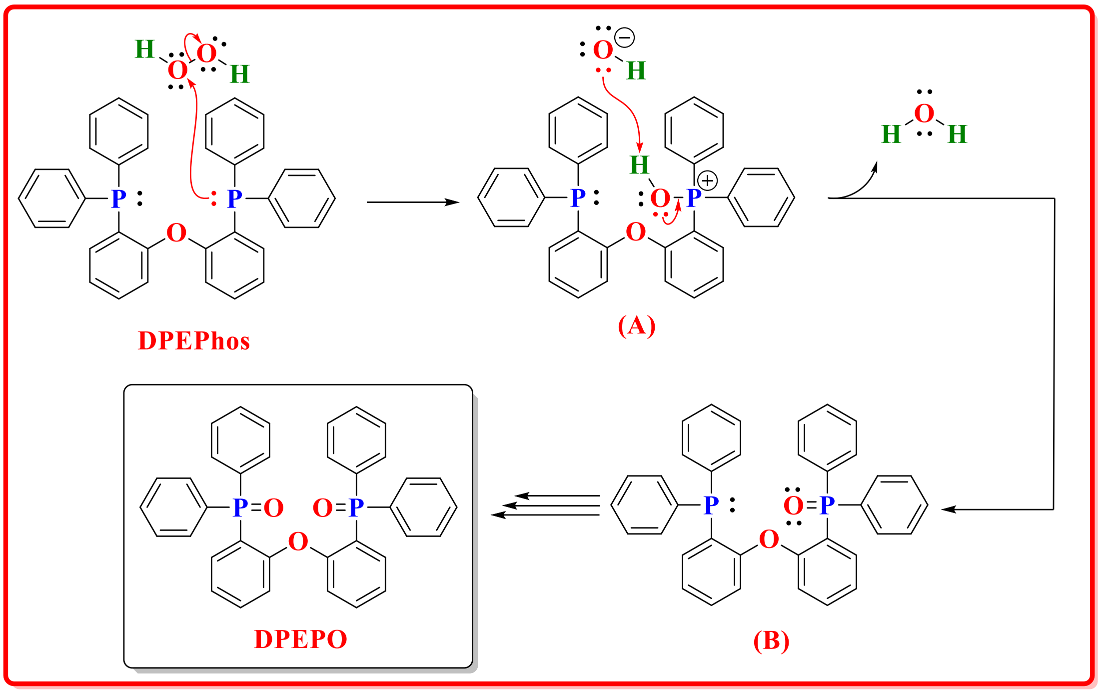

Scheme 3.3: The proposed mechanism of the formation of **DPEPO** using the oxidation reaction.

The structure and purity of **DPEPO** were demonstrated using several analytical methods, including ^{1}H NMR spectroscopy, ^{13}C NMR spectroscopy, ^{31}P NMR spectroscopy, mass spectrometry and elemental analysis. The critical fundamental analysis, which confirmed that the two phosphine groups had been completely converted to two phosphine oxide groups in the **DPEPO** compound, was ^{31}P NMR spectroscopy. When ^{31}P NMR spectroscopy data for **DPEPhos** and the product **DPEPO** were compared, a singlet peak at -16.6 ppm was observed in the former attributed to phosphine groups, while the latter was notably shifted to the downfield region to a position of 25.84 ppm due to moderately electron-withdrawing phosphine oxide groups. This indicated that the two phosphine moieties were fully converted to two phosphine oxide groups. The ^{1}H NMR spectrum of **DPEPO** showed the total number of integrated twenty-eight protons, matching with the chemical structure of **DPEPO**. Furthermore, the quartet peak for the two integrated protons at 6.01 ppm was observed in the ^{1}H NMR spectrum of **DPEPO**, which can be ascribed to two *ortho* protons to phosphine oxide groups on the diphenyl ether moiety due to a strong couple with the phosphorus atoms.[19] Additionally, the ^{1}H NMR spectrum of **DPEPO** displayed a triplet peak of 7.07 ppm, which can be assigned to *para* protons to the ether group on the diphenyl ether group because of an increase of electron density in the *para* position to the ether group impacted by the electron-donating ether group, resulting in shielding the specified signal. The ^{13}C NMR spectrum of **DPEPO** displayed ten different environments of carbon atoms between 158.8 to 120.1 ppm; these data are in agreement with the proposed formula of **DPEPO**. More precisely, three negative signals at 158.8, 124.6, and 123.5 ppm were observed in the ^{13}C NMR spectrum of **DPEPO**, which can be attributable to quaternary carbons. The peak at 158.8 ppm was more deshielded than the two peaks at 124.6 and 123.5 ppm, suggesting that this signal at 158.8 ppm can be related to *ipso* carbons to the oxygen atom on the diphenyl ether group due to the inductive effect of the oxygen atom. Moreover, the mass spectrometry data of **DPEPO** displayed the main integer peak at 570, which is in keeping with the expected mass of **DPEPO**. Therefore, the results mentioned above of ^{31}P NMR spectroscopy, ^{1}H NMR spectroscopy, ^{13}C NMR spectroscopy, and mass spectrometry indicated the formation of **DPEPO**.

3.2.1.2 Synthesis of 1-bromo-4-[4-bromo-2-(diphenylphosphinoyl)-phenoxy]-5-(diphenylphosphinoyl)-benzene M4

M4 was appropriately prepared by brominating **DPEPO** utilising two equivalents of *N*-bromosuccinimide (NBS) in the solvent, glacial acetic acid, in the presence of a small volume of the catalyst, sulphuric acid, in dark conditions, according to the procedure published by Han *et al.* (**scheme 3.4**).[20] Column chromatography was employed to purify the crude product, using ethyl acetate as an eluent, in order to generate the desired molecule of **M4** as a white solid in a yield of 61%.

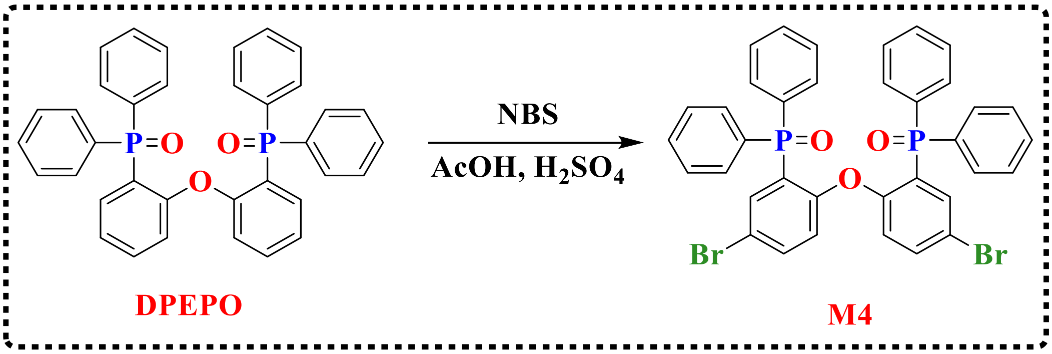

Scheme 3.4: Synthetic route of **M4**.

The mechanism of the bromination reaction for the product **DPEPO** follows an electrophilic aromatic substitution (EAS) and comprises four phases, as depicted in **scheme 3.5**. Firstly, the ether group on diphenyl ether of **DPEPO** donates electron density into the ring through resonance, and then one of lone pairs of electrons on the oxygen atom of **DPEPO** is delocalised into one of the rings, rendering the *ortho* and *para* positions to the ether group on diphenyl ether of **DPEPO** more electron rich. The *para* position to the ether group is here favoured to be more reactive due to the lesser steric hindrance effect compared to the *ortho* position, which is affected by highly steric hindrance. Thus, as the more electron rich position is a good nucleophile, an EAS reaction will be carried out on the *para* position more rapidly. In the second step, a *para* carbon to the ether group on diphenyl ether of **DPEPO** attacks the electrophilic bromine of the NBS reagent in order to afford a carbocation intermediate **(A)** with a succinimide anion. The positive charge is put on an oxygen atom of the intermediate **(A)** in order to achieve a complete octet for all atoms. Next, deprotonation of the carbocation **(A)** is performed by the succinimide anion, which works as a base to yield 4-bromo-2-(diphenylphosphinoyl)-1-[2-(diphenylphosphinoyl) phenoxy] benzene **(DPEPOBr)**. At last, the other *para* carbon to the ether group of the compound **DPEPOBr** is subsequently brominated, bringing about the formation of the desired molecule **M4**.

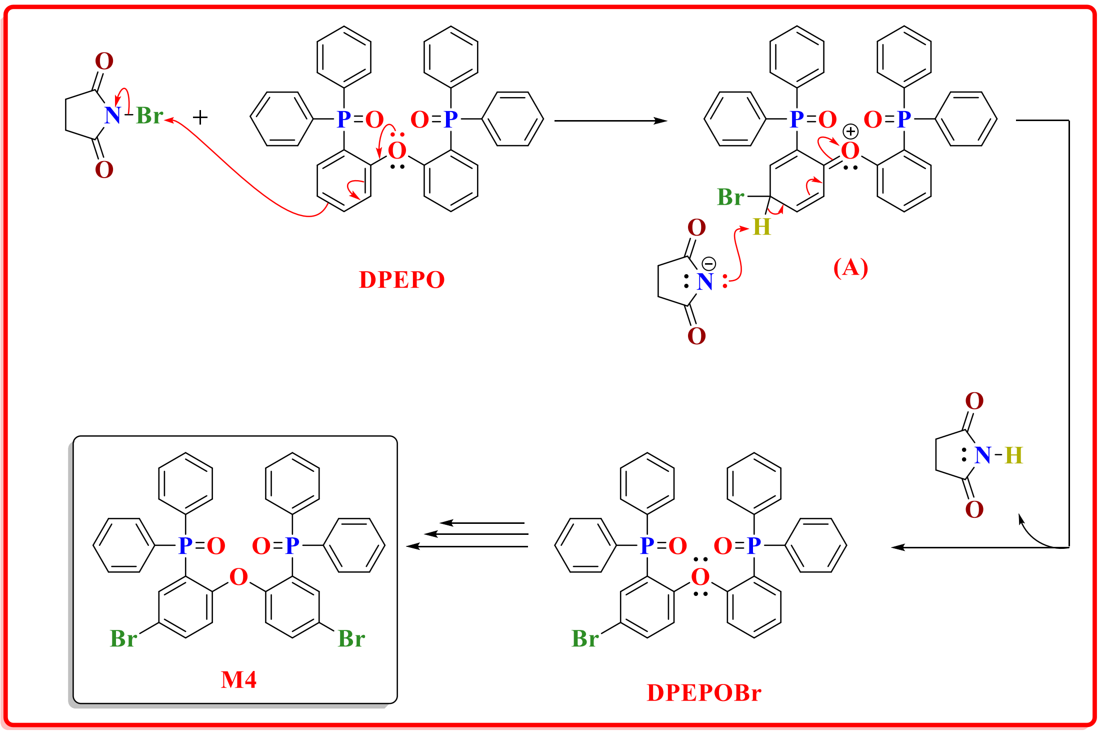

Scheme 3.5: The proposed mechanism of bromination of **M4**.

The purity and chemical structure of the **M4** was confirmed by employing TLC, ^{1}H NMR spectroscopy, ^{31}P NMR spectroscopy, ^{13}C NMR spectroscopy, elemental analysis and mass spectrometry. ^{31}P NMR spectroscopy data for **M4** confirmed the existence of phosphine oxide groups in the product. As shown in **Figure 3.2**, a singlet peak at 24.49 ppm in the ^{31}P NMR spectroscopy of **M4** is noticed, proving the presence of two phosphine oxide groups.

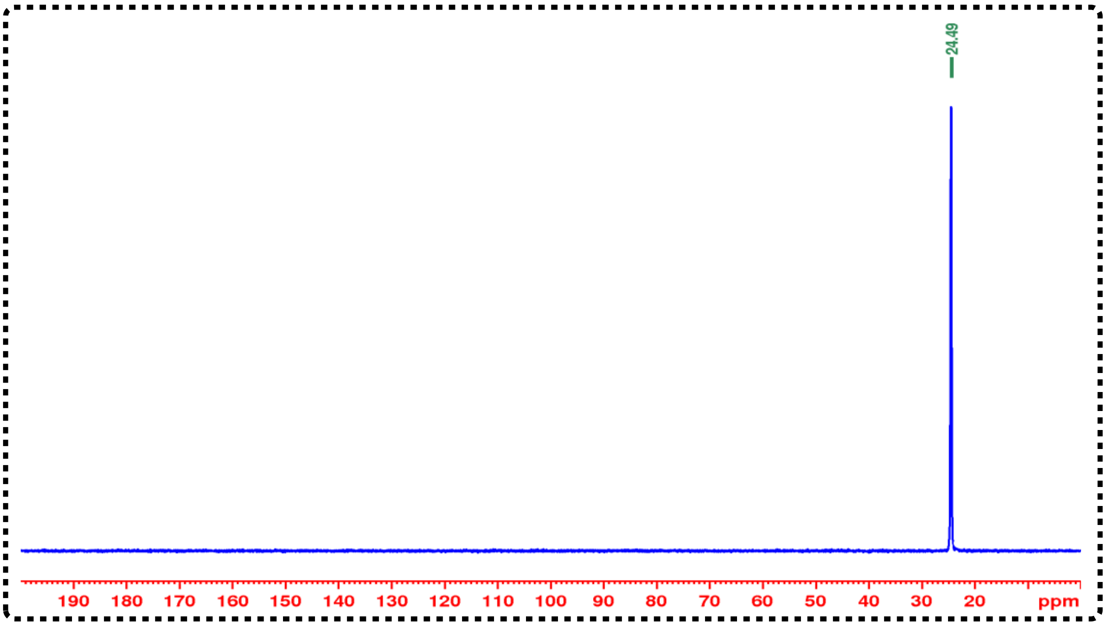

Figure 3.2: ^{31}P NMR spectrum of **M4** in CDCl$_3$.

The ^{1}H NMR spectrum of **M4** shows a doublet of doublet, four multiplets, and quartet peaks at 7.78, 7.70-7.54, 7.53-7.47, 7.45-7.31, 7.29-7.20 and 5.84 ppm, respectively, which are in accordance with the proposed results for **M4** (**Figure 3.3**). Comparison of **M4** and **DPEPO** ^{1}H NMR spectroscopy data revealed that the total number of integrated protons for **M4** decreased by two protons to become twenty-six protons, which indicated the substitution of two protons for two bromine atoms. More specifically, the triplet peak at 7.07 ppm for two integrated protons in the ^{1}H NMR spectrum of **DPEPO**, pertaining to two *para* protons to the ether group on the diphenyl ether, noticeably disappears in the ^{1}H NMR spectrum of **M4**, offering further evidence for the replacement of two protons with two bromine atoms in these positions. Furthermore, the ^{1}H NMR spectrum of **DPEPO** exhibits a doublet of doublet signal at 7.78 ppm, which can be ascribed to two *para* protons to phosphine oxide groups on the diphenyl ether moiety of **DPEPO** due to its spin-spin coupling with the *ortho* proton and the *meta* proton.

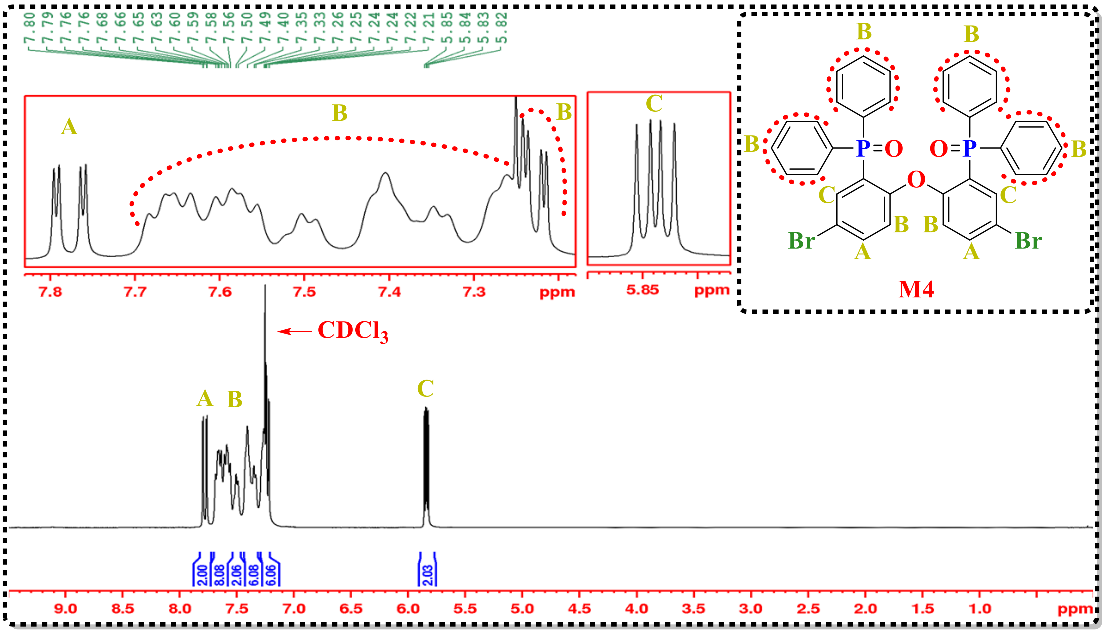

Figure 3.3: ^{1}H NMR spectrum of **M4** in $CDCl_3$.

The ^{13}C NMR spectrum of **M4** presents nine different environments of carbon atoms between 157.5 to 117.4 ppm, which correspond to the expected chemical structure of **M4**, as shown in **Figure 3.4**. Two negative signals are observed at 157.5 and 117.4 ppm in the ^{13}C NMR spectrum of **M4**, which can be ascribed to *ipso* carbons bound to the oxygen atom and bromine atoms on the diphenyl ether group, respectively, on account of the inductive effect of the ether group and the heavy atom effect of the bromine atom, respectively. Furthermore, the positive peak at 121.7 ppm in the ^{13}C NMR spectrum of **M4** is shifted to the shielded area, implying that this signal can be ascribed to *ortho* carbons to the oxygen atom on the diphenyl ether group due to the impact of electron-donating ether group. In addition, the mass spectrometry of **M4** displayed three main integer signals at 726, 728, and 730 in a 1:2:1 ratio as expected due to the presence of two bromine isotopes ^{79}Br and ^{81}Br. Moreover, the elemental analysis determined the following results for $C_{36}H_{26}Br_2O_3P_2$: C, 59.44; H, 3.69; Br, 21.86, which concurs with its proposed formula. Therefore, the results, as mentioned earlier, of ^{1}H NMR spectroscopy, ^{31}P NMR spectroscopy, ^{13}C NMR spectroscopy, elemental analysis and mass spectrometry proved the formation of **M4**.

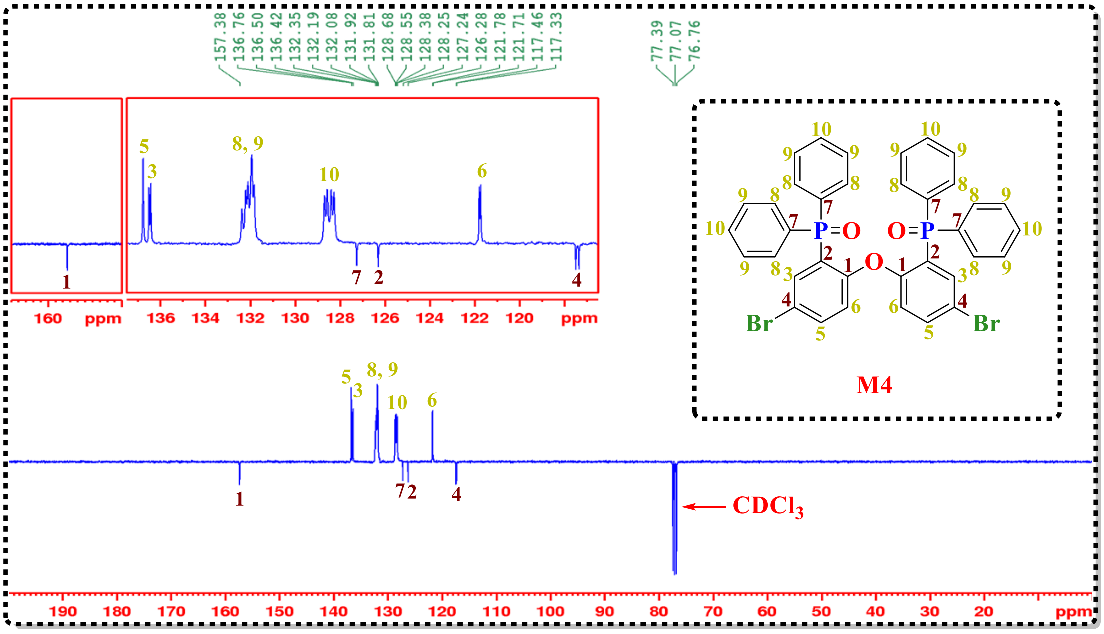

Figure 3.4: ^{13}C NMR spectrum of **M4** in CDCl3.

3.2.2 Preparation of Polymers

3.2.2.1 Synthesis and Characterisation of the Polymers

The target TADF polymers were suitably synthesised via Suzuki polycondensation of the following monomers, **M4**, **M2** and **M3**, with feed molar ratios of 50:50:0 (**PDPEPO-DPOXH**), 45:50:5 (**PDPEPO-DPOXH-PxzTrz-5**), 40:50:10 (**PDPEPO-DPOXH-PxzTrz-10**) and 30:50:20 (**PDPEPO-DPOXH-PxzTrz-20**), respectively, as illustrated in **Scheme 3.6**. The polymer, **PDPEPO-DPOXH**, with no TADF unit, was employed for comparison with the polymers that included the **PXZ-TRZ** TADF moiety. The polymerisations were successfully conducted via the reaction between **M4** and **M2**, with the presence of different percentages of **M3** in order to generate **PDPEPO-DPOXH-PxzTrz-5**, **PDPEPO-DPOXH-PxzTrz-10**, and **PDPEPO-DPOXH-PxzTrz-20**, respectively.

Potassium carbonate was employed as a base, together with the catalysts, palladium (II) acetate ($Pd(OAc)_2$) and tri(otolyl) phosphine (($P(o\text{-}tol)_3$), in a minimum amount of anhydrous THF with degassed distilled water. Polymerisation reactions took three days with refluxing at 95 °C.[21] An end-capping process was then conducted through the addition of bromobenzene and phenylboronic acid under refluxing conditions for 12 hours. The latter enhances the stability of the polymers during operation of OLED devices.[22,23] All the polymers were diluted in DCM and washed in ammonium hydroxide solution in order to eliminate any traces of catalyst by the formation of catalyst complexes dissolved in water. Further polymeric purification was performed using a silica gel pad so as to get rid of any catalyst residues. The desired polymers were re-precipitated in methanol; they formed white to yellow solids according to the amount of TADF moieties present. All polymers were tested for their solubility in various common solvents; complete dissolution in chloroform and toluene was observed.

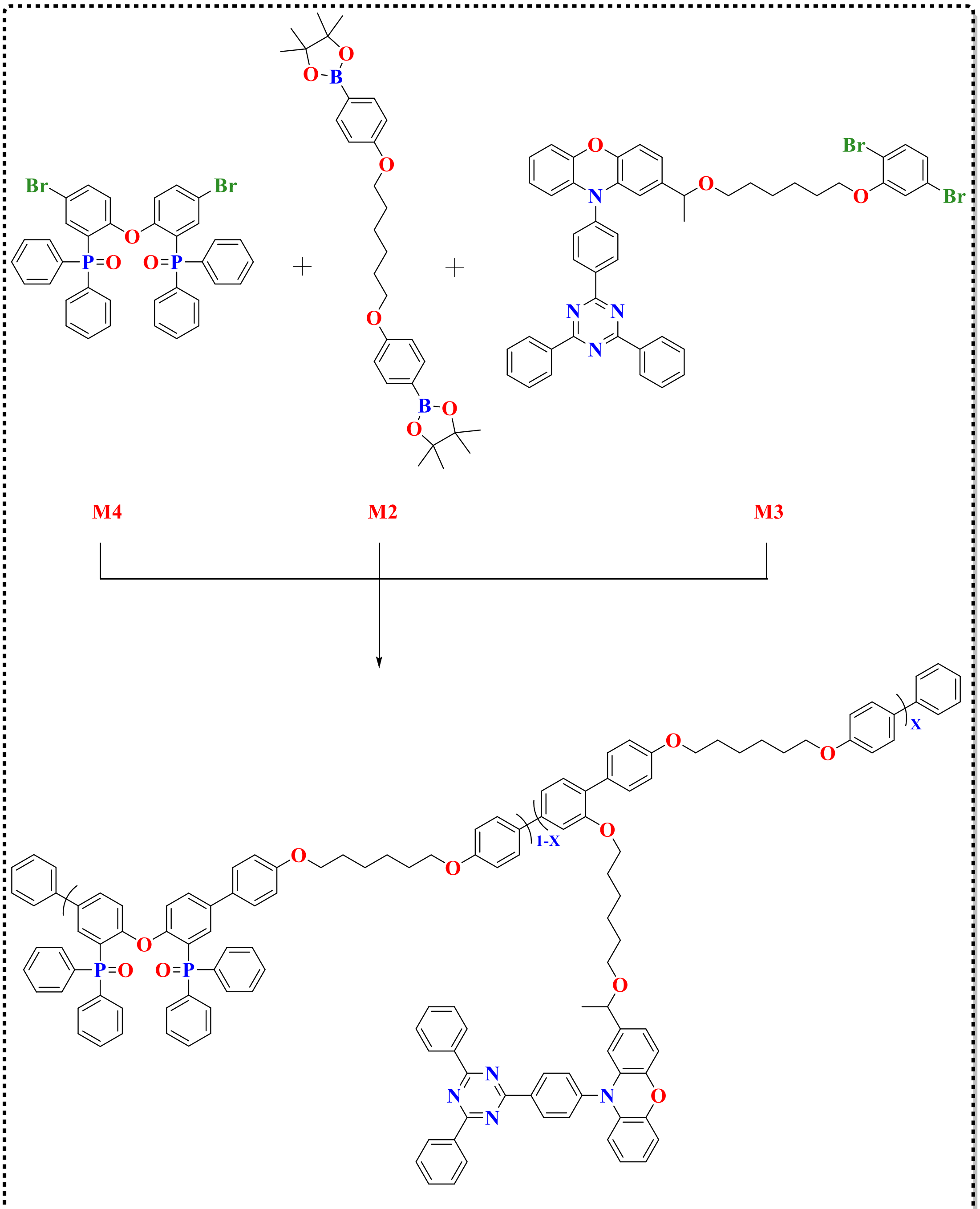

PDPEPO-DPOXH	X=0
PDPEPO-DPOXH-PxzTrz-5	X=0.1
PDPEPO-DPOXH-PxzTrz-10	X=0.2
PDPEPO-DPOXH-PxzTrz-20	X=0.4

Scheme 3.6: Synthetic route of the **PDPEPO-DPOXH**, **PDPEPO-DPOXH-PxzTrz-5**, **PDPEPO-DPOXH-PxzTrz-10**, and **PDPEPO-DPOXH-PxzTrz-20**. Reagents and conditions: anhydrous THF, K_2CO_3, $Pd(OAc)_2$, $P(o\text{-}tol)_3$, and 95 °C.

The chemical structures of **PDPEPO-DPOXH** and the polymers grafted by a TADF unit positioned on the sidechain, i.e., **PDPEPO-DPOXH-PxzTrz-5**, **PDPEPO-DPOXH-PxzTrz-10**, and **PDPEPO-DPOXH-PxzTrz-20**, were fully characterised using ^{31}P NMR spectroscopy and ^{1}H NMR spectroscopy. ^{31}P NMR spectroscopy and ^{1}H NMR spectroscopy data for all polymers corresponded to the expected structures. ^{31}P NMR spectroscopy was employed in order to verify the presence of phosphine oxide groups in the polymers. A singlet peak at the position of 25.89 ppm for all polymers was observed, demonstrating the presence of two phosphine oxide groups. When **PDPEPO-DPOXH** was compared with the three TADF polymers, ^{1}H NMR spectroscopy data confirmed the existence of **M3** in the TADF polymers; broad singlet peaks at 8.98, 8.77, 6.01, 3.80, and 3.20 ppm were noticed, which can be ascribed to TADF monomer protons and prove the successful presence of a TADF moiety into the polymer backbone during polymerisation. With respect to the different feed molar ratios of **M3** in the target polymers, the intensity of the abovementioned peaks in the ^{1}H NMR spectrum increases with rising **M3** feed molar ratios and the generation of the target TADF polymers, **PDPEPO-DPOXH-PxzTrz-5**, **PDPEPO-DPOXH-PxzTrz-10**, and **PDPEPO-DPOXH-PxzTrz-20**. There are two characteristic proton signals at 9.02 and 8.79 ppm originating from **PXZ-TRZ** unit, which could be distinguished from those of **PDPEPO-DPOXH**. These two protons are compared to a proton signal at 4.01 ppm, which is ascribed to four protons of **M2**, to determine the actual ratio of TADF unit in TADF polymers. Therefore, the actual contents of TADF units in the TADF polymers were estimated from analysis of their ^{1}H NMR spectra to be 6.5%, 12.5%, and 27% for **PDPEPO-DPOXH-PxzTrz-5**, **PDPEPO-DPOXH-PxzTrz-10** and **PDPEPO-DPOXH-PxzTrz-20**, respectively, which are consistent with the feed ratio of **M3**. After obtaining the actual content of each monomer from the ^{1}H NMR spectra of polymers, DP of all resultant polymers was estimated from the ^{1}H NMR spectra of polymers to be around in the range between 2-3.

GPC analysis was successfully performed in order to estimate the Mn and Mw of all the polymers generated, using polystyrene as the internal standard and THF as an eluent. The Mn and PDI of the copolymers, **PDPEPO-DPOXH**, **PDPEPO-DPOXH-PxzTrz-5**, **PDPEPO-DPOXH-PxzTrz-10** and **PDPEPO-DPOXH-PxzTrz-20** were found to be in the ranges, 4600–4900 Daltons (Da) and 1.22–1.35, respectively (**Table**

3.1). The relatively low molecular weight of all the formed polymers could be caused by the large steric hindrance of the **DPEPO** moiety promoting polymer rigidity.

Table 3.1: Physical properties of the TADF polymers (**PDPEPO-DPOXH**, **PDPEPO-DPOXH-PxzTrz-5**, **PDPEPO-DPOXH-PxzTrz-10**, and **PDPEPO-DPOXH-PxzTrz-20**).

Polymers	TADF in polymers (mol %)		DP$^{(a)}$	Mn (Da)$^{(b)}$	Mw (Da)$^{(b)}$	PDI$^{(b)}$
	Feed ratio	Actual ratio$^{(a)}$				
PDPEPO-DPOXH	0	0	3	4700	6100	1.30
PDPEPO-DPOXH-PxzTrz-5	5	6.5	2	4800	6100	1.27
PDPEPO-DPOXH-PxzTrz-10	10	12.5	3	4900	6600	1.35
PDPEPO-DPOXH-PxzTrz-20	20	27	2	4600	5600	1.22

(a) Calculated from ^{1}H NMR spectra. **(b)** Determined by GPC in THF using polystyrene as the standard.

3.2.2.2 Optical Properties of Polymers

Photophysical properties for all the resulting polymers incorporating a TADF moiety graft in different molar ratios, i.e., **PDPEPO-DPOXH-PxzTrz-5**, **PDPEPO-DPOXH-PxzTrz-10** and **PDPEPO-DPOXH-PxzTrz-20**, the polymer without the TADF moiety, **PDPEPO-DPOXH**, and **PXZ-TRZ** (TADF) were investigated using UV-vis absorption (**Figure 3.5**) and PL spectroscopy (**Figure 3.6**) in both diluted toluene solutions and in neat films. The optical gaps for **PDPEPO-DPOXH**, **PDPEPO-DPOXH-PxzTrz-5**, **PDPEPO-DPOXH-PxzTrz-10**, **PDPEPO-DPOXH-PxzTrz-20** and the TADF unit were calculated by recording the onset of absorption in the neat films. A summary of the experimental values attained is presented in **Table 3.2**.

Table 3.2: Optical properties of the TADF polymers (**PDPEPO-DPOXH**, **PDPEPO-DPOXH-PxzTrz-5**, **PDPEPO-DPOXH-PxzTrz-10**, and **PDPEPO-DPOXH-PxzTrz-20**).

Polymer/ Compound	λ_{abs} (a) (nm)	λ_{abs} (b) (nm)	λ_{em} (a) (nm)	λ_{em} (b) (nm)	Optical E_g (eV)
PXZ-TRZ	**292/ 345/ 420**	**297/ 350/ 425**	**545**	**537**	**----**
PDPEPO-DPOXH	**295**	**304**	**398**	**400**	**3.68 ± 0.02**(c)
PDPEPO-DPOXH-PxzTrz-5	**296**	**304**	**398/ 537**	**402/ 528**	**3.67 ± 0.01**(c)
PDPEPO-DPOXH-PxzTrz-10	**298**	**305**	**397/ 539**	**531**	**3.67 ± 0.008**(c)
PDPEPO-DPOXH-PxzTrz-20	**297**	**305**	**400/ 542**	**533**	**3.68 ± 0.01**(c)

(a) Measured in toluene. **(b)** Measured in the neat film. **(c)** Range error at the peak of the absorbance curve of a different extinction coefficient.

Figure 3.5 illustrates the UV-Vis absorption spectra of the target polymers **PDPEPO-DPOXH**, **PDPEPO-DPOXH-PxzTrz-5**, **PDPEPO-DPOXH-PxzTrz-10**, and **PDPEPO-DPOXH-PxzTrz-20**, and the TADF unit (**PXZ-TRZ**) in both toluene solutions **(a)** and neat films **(b)**.

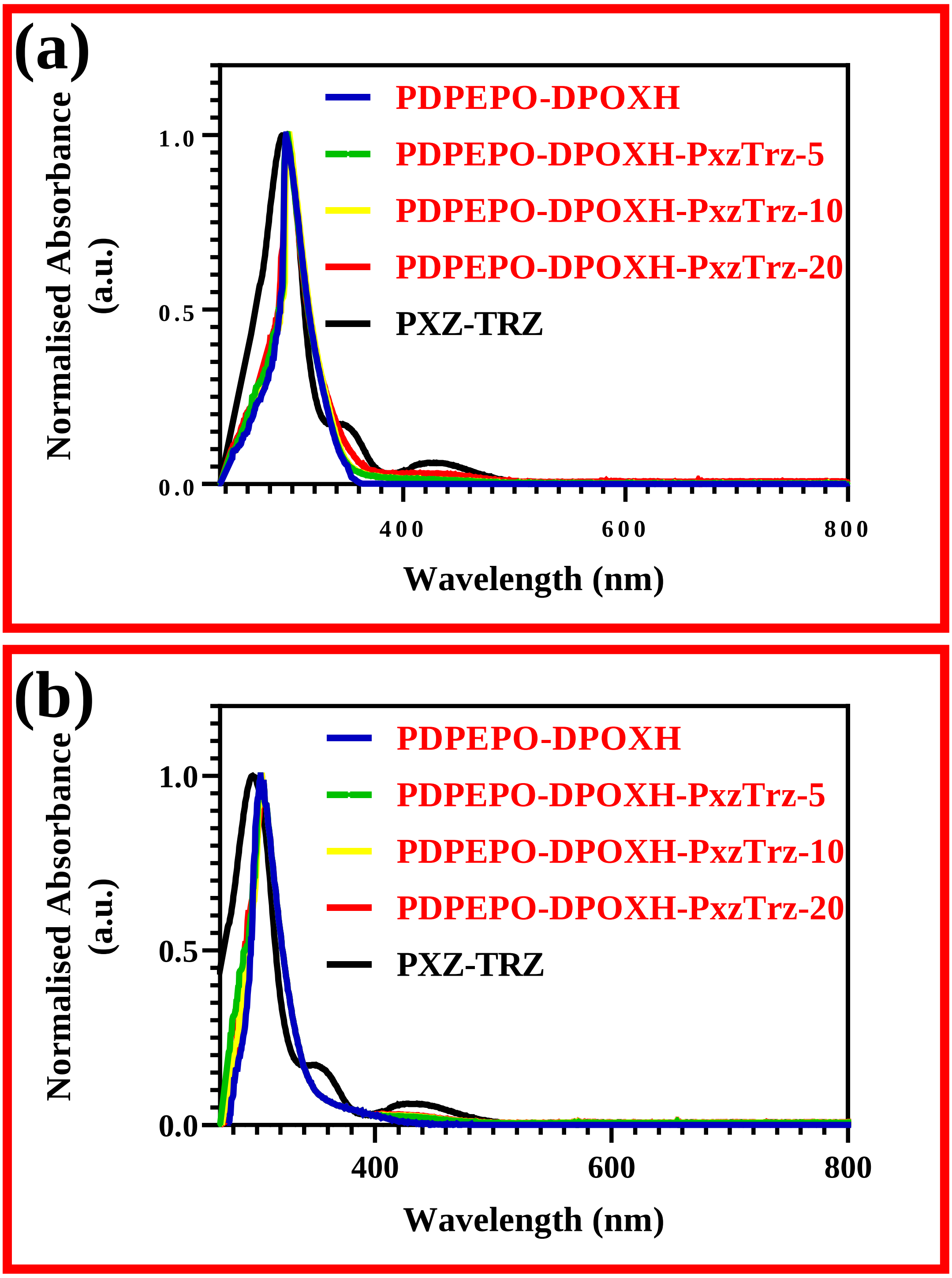

Figure 3.5: UV-vis spectra of **PXZ-TRZ** and green-emitting TADF polymers (**PDPEPO-DPOXH**, **PDPEPO-DPOXH-PxzTrz-5**, **PDPEPO-DPOXH-PxzTrz-10**, and **PDPEPO-DPOXH-PxzTrz-20**), in **(a)** dilute toluene solutions (10^{-3} M) and **(b)** neat films.

The comparison of the TADF polymers with **PDPEPO-DPOXH** in toluene solution (**Figure 3.5a**) revealed single obvious intense absorption bands positioned at 295, 296, 298 and 297 nm which represent the π-π* transition of the polymeric backbones of **PDPEPO-DPOXH**, **PDPEPO-DPOXH-PxzTrz-5**, **PDPEPO-DPOXH-PxzTrz-10**, and **PDPEPO-DPOXH-PxzTrz-20**, respectively. The TADF unit UV-vis spectral data exhibited a weak but perceptible wide absorption band peak in the range, 370-500 nm, in the absorption spectra of **PDPEPO-DPOXH-PxzTrz-5**, **PDPEPO-DPOXH-PxzTrz-10** and **PDPEPO-DPOXH-PxzTrz-20**, which can be ascribed to the ICT between the donor (**PXZ**) and the acceptor (**TRZ**) of the appended TADF dye.

The contribution of the TADF unit absorption to the target polymer absorption is negligible owing to the low TADF unit loading concentrations in the polymers. As can be clearly seen in the neat film (**Figure 3.5b**), the profiles of the absorption bands for **PDPEPO-DPOXH**, **PDPEPO-DPOXH-PxzTrz-5**, **PDPEPO-DPOXH-PxzTrz-10** and **PDPEPO-DPOXH-PxzTrz-20** are comparable to those in toluene solution, although the curves tend towards a bathochromic shift of the absorption maxima of approximately 8 nm related to their absorption in solution. This could be attributed to a stronger intermolecular π-π interaction and more planar structures than present in the toluene solutions.

It is worth noting that the optical gaps, (E_g), of **PDPEPO-DPOXH**, **PDPEPO-DPOXH-PxzTrz-5**, **PDPEPO-DPOXH-PxzTrz-10** and **PDPEPO-DPOXH-PxzTrz-20** are 3.68 eV, 3.67 eV, 3.67 eV and 3.68 eV, respectively; these are measured from the onset of the absorption spectra in neat film. The optical gaps, (E_g), of **PDPEPO-DPOXH**, **PDPEPO-DPOXH-PxzTrz-5**, **PDPEPO-DPOXH-PxzTrz-10** and **PDPEPO-DPOXH-PxzTrz-20** are somewhat wider than those of the analogous polymers generated in the work presented in Chapter 2, i.e., **PmCP-DPOXH**, **PmCP-DPOXH-PxzTrz-5**, **PmCP-DPOXH-PxzTrz-10** and **PmCP-DPOXH-PxzTrz-20**. It is speculated that the raised optical gaps of the current set polymers, based on **DPEPO**, are the result of the higher optical gap of the **DPEPO** units as compared to the **mCP** units which are used in the polymers in chapter 2.

By comparing the PL of the synthesised TADF polymers, **PDPEPO-DPOXH-PxzTrz-5**, **PDPEPO-DPOXH-PxzTrz-10** and **PDPEPO-DPOXH-PxzTrz-20** with both the TADF moiety, **PXZ-TRZ**, and the polymer without the TADF moiety, **PDPEPO-**

DPOXH, two different emission peaks at around 398 and 540 nm in toluene solutions are noticed in the PL curves for **PDPEPO-DPOXH-PxzTrz-5**, **PDPEPO-DPOXH-PxzTrz-10** and **PDPEPO-DPOXH-PxzTrz-20**, which can be ascribed to the emissions of the polymeric backbone and the TADF moiety, respectively (**Figure 3.6a**). With the rising TADF moiety loading density in **PDPEPO-DPOXH-PxzTrz-5**, **PDPEPO-DPOXH-PxzTrz-10**, and **PDPEPO-DPOXH-PxzTrz-20**, ranging from 5% to 20%, in toluene solutions, the intensity of the emission peak at ~540 nm enhances gradually, demonstrating the need for a more efficient energy transfer through the polymeric backbone to the TADF moiety. As can be observed in the thin film (**Figure 3.6b**), with the exception of **PDPEPO-DPOXH-PxzTrz-5** which displays a residual main chain backbone emission, practically complete interchain and intrachain energy transfer from the polymeric backbone to the sidechain TADF moiety is obtained, which is reflected by a single TADF emission peak with tail residual emission from the main chain backbone in **PDPEPO-DPOXH-PxzTrz-10** and **PDPEPO-DPOXH-PxzTrz-20**. Noticeably, with the increasing proportions of the TADF monomer, the positions of PL emission peaks for the target TADF copolymers exhibit a red-shift, from 528 nm for **PDPEPO-DPOXH-PxzTrz-5**, to 533 nm for **PDPEPO-DPOXH-PxzTrz-20**. This arises from aggregation, proving that the TADF moiety clearly contributes to the copolymers' emission profile. It is noteworthy that dual emission from both the backbone of the polymer and the TADF moiety is more pronounced in solutions than in films indicating better energy transfer in films and a total energy transfer in films with 10% **PXZ-TRZ** substituents.

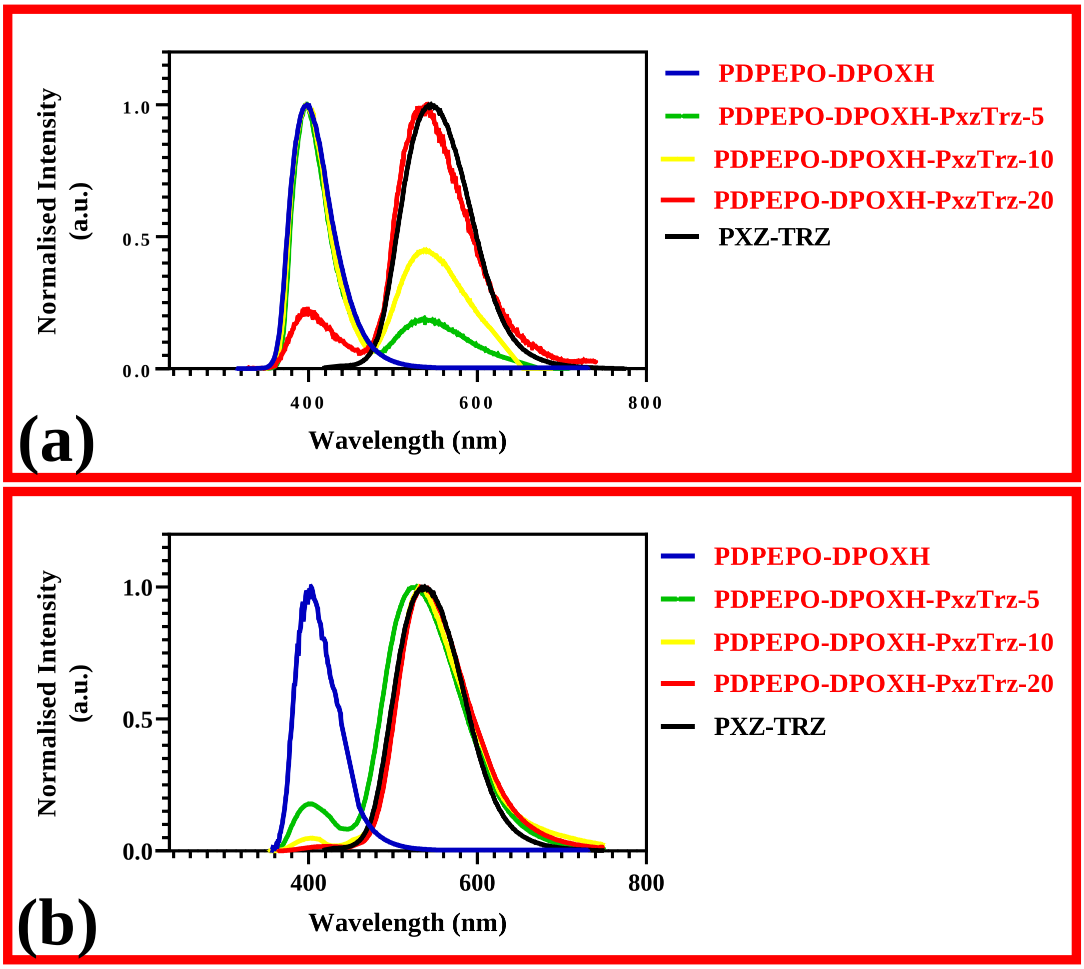

Figure 3.6: PL spectra of **PXZ-TRZ** and green-emitting TADF polymers (**PDPEPO-DPOXH**, **PDPEPO-DPOXH-PxzTrz-5**, **PDPEPO-DPOXH-PxzTrz-10**, and **PDPEPO-DPOXH-PxzTrz-20**), in **(a)** dilute toluene solutions (10^{-3} M) and **(b)** neat films.

3.2.2.3 Electrochemical Properties of Polymers

Cyclic voltammetry (CV) was conducted in order to examine the electrochemical properties of the green-light emitting TADF polymers, **PDPEPO-DPOXH-PxzTrz-5**, **PDPEPO-DPOXH-PxzTrz-10**, and **PDPEPO-DPOXH-PxzTrz-20**, and **PDPEPO-DPOXH**. All the CV measurements on these polymers were achieved using drop-cast polymer films on a platinum disc electrode. The latter was applied as the working electrode in tetra-n-butylammonium perchlorate dissolved in acetonitrile solution (0.1 M) as the electrolyte, together with silver nitrate (Ag/Ag^{+}) dissolved in acetonitrile solution (10^{-2} M) as a reference electrode, at a scan rate of 0.1 V s^{-1} under argon conditions.

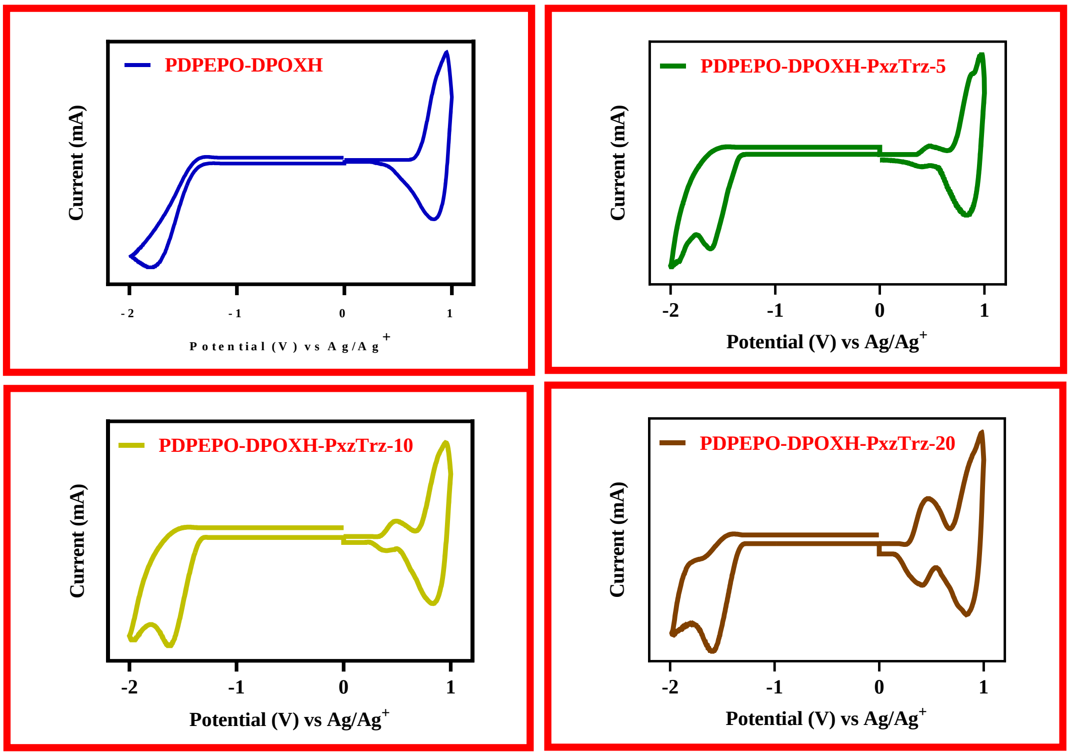

Figure 3.7: CV of **PDPEPO-DPOXH**, **PDPEPO-DPOXH-PxzTrz-5**, **PDPEPO-DPOXH-PxzTrz-10**, and **PDPEPO-DPOXH-PxzTrz-20**.

In comparison between the electrochemical behaviours of the TADF polymers (**PDPEPO-DPOXH-PxzTrz-5**, **PDPEPO-DPOXH-PxzTrz-10**, and **PDPEPO-DPOXH-PxzTrz-20**) with **PDPEPO-DPOXH** (**Figure 3.7**), **PDPEPO-DPOXH** exhibits a reversible anodic peak and an irreversible cathodic peak. However, all green-light emitting TADF polymers (**PDPEPO-DPOXH-PxzTrz-5**, **PDPEPO-DPOXH-PxzTrz-10**, and **PDPEPO-DPOXH-PxzTrz-20**) show two reversible oxidation waves and two irreversible reduction waves. These results for both anodic and cathodic peaks prove that green-light emitting TADF polymers display a further reversible oxidation peak at the lower potential, which can be ascribed to the electron-donating phenoxazine moiety of the TADF unit, together with an additional irreversible reduction peak at the lower potential, which can be ascribed to the electron-accepting triphenyltriazine of the TADF unit. Remarkably, with increasing proportions of TADF moiety in the TADF polymers (**PDPEPO-DPOXH-PxzTrz-5**, **PDPEPO-DPOXH-PxzTrz-10**, and

PDPEPO-DPOXH-PxzTrz-20) ranging from 5% to 20%, the intensity of the lower potential oxidation peak and the higher potential reduction peak increases gradually as illustrated in **Figure 3.7**.

Table 3.3: Electrochemical properties of **PDPEPO-DPOXH**, **PDPEPO-DPOXH-PxzTrz-5**, **PDPEPO-DPOXH-PxzTrz-10**, and **PDPEPO-DPOXH-PxzTrz-20**.

Polymer/ Compound	HOMO (eV)	LUMO (eV)	HOMO-LUMO gap (eV)
PDPEPO-DPOXH	-5.42	-3.31	2.11 ± 0.02
PDPEPO-DPOXH-PxzTrz-5	-5.11	-3.36	1.75 ± 0.1
PDPEPO-DPOXH-PxzTrz-10	-5.07	-3.37	1.70 ± 0.04
PDPEPO-DPOXH-PxzTrz-20	-5.00	-3.38	1.62 ± 0.08

As the data summarised in **Table 3.3**, the HOMO energy levels for the green-light emitting TADF polymers (**PDPEPO-DPOXH-PxzTrz-5**, **PDPEPO-DPOXH-PxzTrz-10**, and **PDPEPO-DPOXH-PxzTrz-20**), which were determined by their onset potential of the oxidation peaks, ranging from -5.11 eV to -5.00 eV, show an increasing trend of the HOMO levels. In contrast, **PDPEPO-DPOXH** has a lower HOMO level at -5.42 eV owing to the lack of TADF moiety in the polymer. These results demonstrate that high TADF moiety loading exerts an apparent effect on the target polymers. The HOMO levels of the TADF polymers, i.e., **PDPEPO-DPOXH-PxzTrz-5**, **PDPEPO-DPOXH-PxzTrz-10** and **PDPEPO-DPOXH-PxzTrz-20**, are similar to **P3**, **P6**, **P9** and **P12**, which have different ratios of the TADF unit loaded and exhibit values of -5.12, -5.12, -5.10 and -5.06 eV, respectively.[17] However, the HOMO energy levels of the TADF polymers, **PDPEPO-DPOXH-PxzTrz-5**, **PDPEPO-DPOXH-PxzTrz-10** and **PDPEPO-DPOXH-PxzTrz-20**, are shallower compared to those of the analogues, **PCz-mCP-PxzTrz-10**, **PCz-mCP-PxzTrz-20**, **PCz-mCP-PxzTrz-30** and **PCz-mCP-PxzTrz-40**, which exhibit values of -5.58, -5.55 -5.54, and -5.52 eV, respectively.[24] The variation in the HOMO levels of the polymers can be attributed to the different polymer structures. The HOMO levels of the TADF polymers, i.e., **PDPEPO-DPOXH-PxzTrz-5**, **PDPEPO-DPOXH-PxzTrz-10**, and **PDPEPO-DPOXH-PxzTrz-20**, are comparable to those of the analogous polymers, **PmCP-**

DPOXH-PxzTrz-5, **PmCP-DPOXH-PxzTrz-10** and **PmCP-DPOXH-PxzTrz-20**, which have values of -5.09, -5.06 and -4.99 eV, respectively, as mentioned in Chapter 2. This could be ascribed to the similar abilities of the stronger electron-donating phenoxazine units in the polymers. In addition, the slight disparity in the HOMO levels values for **PmCP-DPOXH-PxzTrz-X** and **PDPEPO-DPOXH-PxzTrz-X** can be attributed to the different polymeric backbone hosts.

In contrast, the LUMO energy levels of the green-emitting TADF polymers, **PDPEPO-DPOXH-PxzTrz-5**, **PDPEPO-DPOXH-PxzTrz-10**, and **PDPEPO-DPOXH-PxzTrz-20**, and **PDPEPO-DPOXH** were estimated by their onset potential of reduction peaks and differ in the range, -3.31 eV to -3.38 eV. The LUMO levels of the TADF polymers, **PDPEPO-DPOXH-PxzTrz-5**, **PDPEPO-DPOXH-PxzTrz-10** and **PDPEPO-DPOXH-PxzTrz-20**, are deeper than **P3**, **P6**, **P9** and **P12**, which exhibit values of -2.53, -2.53, -2.51 and -2.47 eV, respectively.[17] Moreover, the LUMO energy levels of the TADF polymers, **PDPEPO-DPOXH-PxzTrz-5**, **PDPEPO-DPOXH-PxzTrz-10** and **PDPEPO-DPOXH-PxzTrz-20,** are deeper than those for the analogues, **PCz-mCP-PxzTrz-10**, **PCz-mCP-PxzTrz-20**, **PCz-mCP-PxzTrz-30** and **PCz-mCP-PxzTrz-40,** which have values of -2.96, -2.93, -2.94 and -2.93 eV, respectively.[24] The LUMO levels of the former TADF polymers based on **DPEPO** are considerably shallower than those of the analogue polymers founded on **mCP**; **PmCP-DPOXH-PxzTrz-5**, **PmCP-DPOXH-PxzTrz-10** and **PmCP-DPOXH-PxzTrz-20** have LUMO levels of -3.53, -3.53 and -3.52 eV, respectively, as mentioned in Chapter 2. The obvious difference in the LUMO level values for **PmCP-DPOXH-PxzTrz-X** and **PDPEPO-DPOXH-PxzTrz-X** could be attributed to the various hosts in the polymeric backbone and the dissimilar polymer structures. The HOMO and LUMO levels of the polymers are impacted by the TADF moiety tethered on the polymeric backbone containing **DPEPO** host. It is worth mentioning that the HOMO-LUMO gaps of green-emitting TADF polymers, i.e., **PDPEPO-DPOXH-PxzTrz-5**, **PDPEPO-DPOXH-PxzTrz-10**, and **PDPEPO-DPOXH-PxzTrz-20**, and **PDPEPO-DPOXH**, which were inferred by subtracting the LUMO values from the HOMO values, reduced with the incremental rise of TADF unit loading from 1.75 eV for **PDPEPO-DPOXH-PxzTrz-5**, to 1.62 eV for **PDPEPO-DPOXH-PxzTrz-20**. However, **PDPEPO-DPOXH** exhibits the highest HOMO-LUMO gap of 2.11 eV owing to the lack of the TADF moiety in the polymer. With rising TADF moiety loading ratios, the HOMO-

LUMO gaps of the polymers, **PmCP-DPOXH-PxzTrz-X**, **PTPA-mCP-PxzTrz-X** and **PCz-mCP-PxzTrz-X,** show a similar effect with regard to minimising the polymers' HOMO-LUMO gaps as described in chapter 2.[24,25] It can be deduced that the presence of the TADF moiety in the polymers has an obvious impact on the HOMO-LUMO gap which is minimised by increasing the TADF unit. Thus, the **PXZ-TRZ** tethered on the polymeric backbone-containing **DPEPO** host notably controls the electrochemical behaviours of the polymers, as shown in **Table 3.3**. More interestingly, the optical gaps of the target polymers should be smaller than HOMO-LUMO gaps as the electron and hole remain electrostatically bound to each other in the excited state. However, HOMO-LUMO gaps of target polymers were obtained lower than anticipated, which can be ascribed to the TADF polymers were oxidised during the reduction process.

3.2.2.4 Thermal Properties of the Polymers

An investigation of all the polymers with respect to their thermal stability was conducted using TGA analysis in a deoxygenated atmosphere at a heating rate of 10 °C min^{-1}. The initial degradation temperatures of **PDPEPO-DPOXH**, **PDPEPO-DPOXH-PxzTrz-5**, **PDPEPO-DPOXH-PxzTrz-10**, and **PDPEPO-DPOXH-PxzTrz-20** take place at 312 °C, 316 °C, 322 °C and 325 °C, respectively, as summarised in **Table 3.4**.

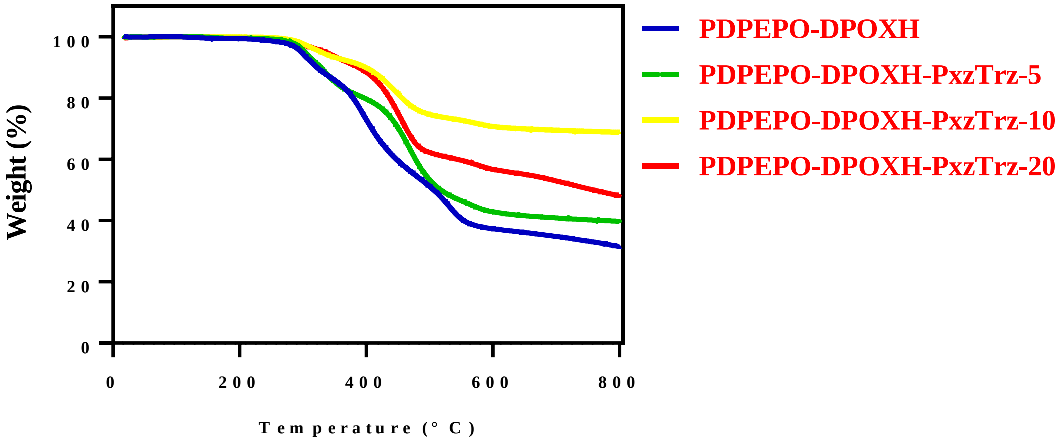

Figure 3.8: TGA of **PDPEPO-DPOXH**, **PDPEPO-DPOXH-PxzTrz-5**, **PDPEPO-DPOXH-PxzTrz-10**, and **PDPEPO-DPOXH-PxzTrz-20**.

As shown in **Figure 3.8**, a high thermal stability is observed for all polymers with thermal decomposition temperatures (T_d) higher than 310 °C, proving that these target polymers could be employed in solution processable OLED devices with long-term thermal stability.

PDPEPO-DPOXH-PxzTrz-5, **PDPEPO-DPOXH-PxzTrz-10**, and **PDPEPO-DPOXH-PxzTrz-20** exhibit comparable thermal properties compared to **PDPEPO-DPOXH** since they possess the same TADF moieties onto the side chain. Remarkably, **PDPEPO-DPOXH** displays one decomposition phase at the temperature of 312 °C, which is the lowest onset of degradation temperature compared to TADF polymers because **PDPEPO-DPOXH** comprises the **DPEPO** host without an addition of TADF moieties. In contrast, **PDPEPO-DPOXH-PxzTrz-5**, **PDPEPO-DPOXH-PxzTrz-10**, and **PDPEPO-DPOXH-PxzTrz-20** exhibit the onset of degradation temperatures at 316 °C, 322 °C, and 325 °C, respectively. It is interesting to note that the onset of degradation temperatures of **PDPEPO-DPOXH-PxzTrz-5**, **PDPEPO-DPOXH-PxzTrz-10**, and **PDPEPO-DPOXH-PxzTrz-20** rise incrementally with increasing molar ratios of TADF moiety. This could be ascribed to the large steric hindrance of these TADF polymers, which render them more rigid and stable. The rigidity of TADF polymers demand more thermal energy to lead to cleavage through degradation process.

Table 3.4: Thermal properties of **PDPEPO-DPOXH**, **PDPEPO-DPOXH-PxzTrz-5**, **PDPEPO-DPOXH-PxzTrz-10**, and **PDPEPO-DPOXH-PxzTrz-20**.

Polymers	**T_d (° C)**
PDPEPO-DPOXH	**312**
PDPEPO-DPOXH-PxzTrz-5	**316**
PDPEPO-DPOXH-PxzTrz-10	**322**
PDPEPO-DPOXH-PxzTrz-20	**325**

In comparison, **PmCP-DPOXH-PxzTrz-5**, **PmCP-DPOXH-PxzTrz-10**, and **PmCP-DPOXH-PxzTrz-20** show the same impact with respect to increasing the onset of degradation temperatures with rising loading ratios of TADF moiety in these polymers as mentioned in Chapter 2. Therefore, it can be concluded that the presence of TADF unit in the polymers affects thermal decomposition temperatures of polymers to be higher with increasing the TADF moiety. The thermal decomposition temperatures of the current set of **DPEPO** based TADF polymers are considerably higher than those of the analogue polymers founded on **mCP**. It is speculated that the raised thermal decomposition temperatures of the **DPEPO** based polymers are the result of rigidity of **DPEPO** host compared to the latter polymers, configured using **mCP**.

3.3 Conclusion

Although, standard *vacuum* deposition methods have been extensively utilised as popular and conventional techniques in industrial OLED applications, solution-processed OLED applications are more attractive owing to their potential for large-scale production, cheap cost, and roll-to-roll production processes; these characteristics do not apply to current *vacuum* deposition techniques. In spite of this, the performance of solution-processed OLEDs continues to lag significantly behind that of traditional *vacuum*-evaporation OLEDs. Consequently, this necessitates a significant investment of time and resources in the development of TADF materials which have recently become available so as to meet the requisites of solution-processed technology. The polymer design in the current research, based on the sidechain TADF polymeric materials, was therefore proposed. These polymers have two principal components, i.e., the polymer backbone, which behaves as the host and charge transporter channel, and the polymer backbone sidechain, which forms the guest molecule and includes a grafted TADF moiety in a predetermined ratio; the latter confers TADF characteristics on the polymer.[17]

The chemical structures of **PDPEPO-DPOXH** and the polymers grafted with a sidechain TADF unit, i.e., **PDPEPO-DPOXH-PxzTrz-5**, **PDPEPO-DPOXH-PxzTrz-10** and **PDPEPO-DPOXH-PxzTrz-20**, were fully characterised using ^{31}P NMR spectroscopy and ^{1}H NMR spectroscopy; the data corresponded to the polymers' expected structures. GPC analysis was performed in order to estimate Mn and Mw for the above polymers; Mn and PDI values were noted to be within the ranges, 4600–4900 Daltons (Da) and 1.22–1.35, respectively. The relatively low molecular weight of all polymers formed, i.e., **PDPEPO-DPOXH**, **PDPEPO-DPOXH-PxzTrz-5**, **PDPEPO-DPOXH-PxzTrz-10** and **PDPEPO-DPOXH-PxzTrz-20**, can be caused by the large steric hindrance of the **DPEPO** moiety. The introduction of the π-electron delocalisation interrupting unit 1,6-diphenoxyhexane (**DPOXH**) to the polymer backbone provides the polymer with similar photophysical characteristics to those of the **DPEPO** repeat units.

The UV-Vis absorption studies on the target polymers, i.e., **PDPEPO-DPOXH**, **PDPEPO-DPOXH-PxzTrz-5**, **PDPEPO-DPOXH-PxzTrz-10**, and **PDPEPO-DPOXH-PxzTrz-20**, and the TADF unit, **PXZ-TRZ,** were successfully undertaken in both toluene solutions and neat films. An obvious single intense absorption band positioned around 297 nm reflect the π-π* electronic transitions from the polymers' backbones for **PDPEPO-DPOXH**, **PDPEPO-DPOXH-PxzTrz-5**, **PDPEPO-DPOXH-PxzTrz-10**, and **PDPEPO-DPOXH-PxzTrz-20**, respectively. The absorption bands for these polymers were comparable, indicating that the contribution of the TADF unit to the target polymers' absorptions was only negligible owing to the low polymer TADF unit loading concentrations.

It is worth noting that the optical gaps, (E_g), of **PDPEPO-DPOXH**, **PDPEPO-DPOXH-PxzTrz-5**, **PDPEPO-DPOXH-PxzTrz-10** and **PDPEPO-DPOXH-PxzTrz-20** were 3.68 eV, 3.67 eV, 3.67 eV and 3.68 eV, respectively. Photoluminescence studies indicated that in toluene solutions, two distinctive emission peaks at approximately 398 and 540 nm were observed in the PL curves for **PDPEPO-DPOXH-PxzTrz-5**, **PDPEPO-DPOXH-PxzTrz-10** and **PDPEPO-DPOXH-PxzTrz-20**, which can be attributed to emissions from the polymeric backbone and TADF moieties, respectively. Noticeably, with increasing proportions of the TADF monomer grafted to these polymers, the positions of PL emission peaks for the target TADF copolymers exhibit a red-shift, i.e., from 528 nm for **PDPEPO-DPOXH-PxzTrz-5**, to 533 nm for **PDPEPO-DPOXH-PxzTrz-20** as a result of aggregation, proving that the TADF moiety clearly contributes to the copolymers' emission profile. Emission studies on thin films also indicated that apart from **PDPEPO-DPOXH-PxzTrz-5** which displays a residual main chain backbone emission, practically complete interchain and intrachain energy transfer from the polymeric backbone to the TADF moieties is observed, for polymers with 10% and 20% of grafted TADF units (**PDPEPO-DPOXH-PxzTrz-10** and **PDPEPO-DPOXH-PxzTrz-20)**.

The HOMO levels of the green light-emitting TADF polymers, i.e., **PDPEPO-DPOXH-PxzTrz-5**, **PDPEPO-DPOXH-PxzTrz-10** and **PDPEPO-DPOXH-PxzTrz-20**, range from -5.11 eV to -5.00 eV, demonstrating a rising trend of the HOMO levels with increasing TADF moiety proportions. The polymer, **PDPEPO-DPOXH,** exhibits a shallower HOMO level at -5.42 eV as it contains no TADF moiety. The polymer HOMO level data suggest that high TADF moiety loading produces an apparent effect on the target polymers. The polymer HOMO and LUMO levels are impacted by the TADF moiety tethered on the polymeric backbone containing **DPEPO** host.

Remarkably, the HOMO-LUMO gaps of the green-emitting TADF polymers obviously decrease with the incremental rise in TADF unit loading from 1.75 eV (**PDPEPO-DPOXH-PxzTrz-5**) to 1.62 eV (**PDPEPO-DPOXH-PxzTrz-20**). It can be deduced that the presence of the TADF moiety in the polymers has an obvious impact on the HOMO-LUMO gap, which is minimised by increasing the TADF unit.

3.4 References

(1) Xue, J.; Liang, Q.; Wang, R.; Hou, J.; Li, W.; Peng, Q.; Shuai, Z.; Qiao, J. Highly Efficient Thermally Activated Delayed Fluorescence via J-aggregates with Strong Intermolecular Charge Transfer. *Advanced Materials* **2019**, *31* (28), 1808242.

(2) Liu, Y.; Wang, Y.; Li, C.; Ren, Z.; Ma, D.; Yan, S. Efficient Thermally Activated Delayed Fluorescence Conjugated Polymeric Emitters with Tunable Nature of Excited States Regulated via Carbazole Derivatives for Solution-Processed OLEDs. *Macromolecules* **2018**, *51* (12), 4615–4623.

(3) Endo, A.; Sato, K.; Yoshimura, K.; Kai, T.; Kawada, A.; Miyazaki, H.; Adachi, C. Efficient Up-Conversion of Triplet Excitons into a Singlet State and Its Application for Organic Light Emitting Diodes. *Applied Physics Letters* **2011**, *98* (8), 42.

(4) Uoyama, H.; Goushi, K.; Shizu, K.; Nomura, H.; Adachi, C. Highly Efficient Organic Light-Emitting Diodes from Delayed Fluorescence. *Nature* **2012**, *492* (7428), 234–238.

(5) Wong, M. Y.; Zysman-Colman, E. Purely Organic Thermally Activated Delayed Fluorescence Materials for Organic Light-emitting Diodes. *Advanced Materials* **2017**, *29* (22), 1605444.

(6) Liu, Y.; Li, C.; Ren, Z.; Yan, S.; Bryce, M. R. All-Organic Thermally Activated Delayed Fluorescence Materials for Organic Light-Emitting Diodes. *Nature Reviews Materials* **2018**, *3* (4), 1–20.

(7) Lin, T. A.; Chatterjee, T.; Tsai, W. L.; Lee, W. K.; Wu, M. J.; Jiao, M.; Pan, K. C.; Yi, C. L.; Chung, C. L.; Wong, K. T. With 37% External Quantum Efficiency Using Thermally Activated Delayed Fluorescence from Spiroacridine-Triazine Hybrid. *Adv. Mater* **2016**, *28*, 6976–6983.

(8) Ahn, D. H.; Kim, S. W.; Lee, H.; Ko, I. J.; Karthik, D.; Lee, J. Y.; Kwon, J. H. Highly Efficient Blue Thermally Activated Delayed Fluorescence Emitters Based on Symmetrical and Rigid Oxygen-Bridged Boron Acceptors. *Nature Photonics* **2019**, *13* (8), 540–546.

(9) Wu, T.-L.; Huang, M.-J.; Lin, C.-C.; Huang, P.-Y.; Chou, T.-Y.; Chen-Cheng, R.-W.; Lin, H.-W.; Liu, R.-S.; Cheng, C.-H. Diboron Compound-Based Organic Light-Emitting Diodes with High Efficiency and Reduced Efficiency Roll-Off. *Nature Photonics* **2018**, *12* (4), 235–240.

(10) Zeng, W.; Lai, H.; Lee, W.; Jiao, M.; Shiu, Y.; Zhong, C.; Gong, S.; Zhou, T.; Xie, G.; Sarma, M. Achieving Nearly 30% External Quantum Efficiency for Orange–Red Organic Light Emitting Diodes by Employing Thermally Activated Delayed Fluorescence Emitters Composed of 1, 8-Naphthalimide-Acridine Hybrids. *Advanced Materials* **2018**, *30* (5), 1704961.

(11) Jou, J.-H.; Sahoo, S.; Dubey, D. K.; Yadav, R. A. K.; Swayamprabha, S. S.; Chavhan, S. D. Molecule-Based Monochromatic and Polychromatic OLEDs with Wet-Process Feasibility. *Journal of Materials Chemistry C* **2018**, *6* (43), 11492–11518.

(12) Eslamian, M. Inorganic and Organic Solution-Processed Thin Film Devices. *Nano-Micro Letters* **2017**, *9* (1), 1–23.

(13) Ban, X.; Zhu, A.; Zhang, T.; Tong, Z.; Jiang, W.; Sun, Y. Highly Efficient All-Solution-Processed Fluorescent Organic Light-Emitting Diodes Based on a Novel Self-Host Thermally Activated Delayed Fluorescence Emitter. *ACS Applied Materials & Interfaces* **2017**, *9* (26), 21900–21908.

(14) Ban, X.; Zhu, A.; Zhang, T.; Tong, Z.; Jiang, W.; Sun, Y. Design of Encapsulated Hosts and Guests for Highly Efficient Blue and Green Thermally Activated Delayed Fluorescence OLEDs Based on a Solution-Process. *Chemical Communications* **2017**, *53* (86), 11834–11837.

(15) Wada, Y.; Kubo, S.; Kaji, H. Adamantyl Substitution Strategy for Realizing Solution-Processable Thermally Stable Deep-Blue Thermally Activated Delayed Fluorescence Materials. *Advanced Materials* **2018**, *30* (8), 1705641.

(16) Cai, X.; Chen, D.; Gao, K.; Gan, L.; Yin, Q.; Qiao, Z.; Chen, Z.; Jiang, X.; Su, S. “Trade-Off” Hidden in Condensed State Solvation: Multiradiative Channels Design for Highly Efficient Solution-Processed Purely Organic Electroluminescence at High Brightness. *Advanced Functional Materials* **2018**, *28* (7), 1704927.

(17) Zhou, X.; Huang, M.; Zeng, X.; Chen, T.; Xie, G.; Yin, X.; Yang, C. Combining the Qualities of Carbazole and Tetraphenyl Silane in a Desirable Main Chain for Thermally Activated Delayed Fluorescence Polymers. *Polymer Chemistry* **2019**, *10* (30), 4201–4208.

(18) Miyata, K.; Nakagawa, T.; Kawakami, R.; Kita, Y.; Sugimoto, K.; Nakashima, T.; Harada, T.; Kawai, T.; Hasegawa, Y. Remarkable Luminescence Properties of Lanthanide Complexes with Asymmetric Dodecahedron Structures. *Chemistry–A European Journal* **2011**, *17* (2), 521–528.

(19) Xu, H.; Wang, L.-H.; Zhu, X.-H.; Yin, K.; Zhong, G.-Y.; Hou, X.-Y.; Huang, W. Application of Chelate Phosphine Oxide Ligand in EuIII Complex with Mezzo Triplet Energy Level, Highly Efficient Photoluminescent, and Electroluminescent Performances. *The Journal of Physical Chemistry B* **2006**, *110* (7), 3023–3029.

(20) Han, C.; Zhang, Z.; Xu, H.; Xie, G.; Li, J.; Zhao, Y.; Deng, Z.; Liu, S.; Yan, P. Convergent Modulation of Singlet and Triplet Excited States of Phosphine-Oxide Hosts through the Management of Molecular Structure and Functional-Group Linkages for Low-Voltage-Driven Electrophosphorescence. *Chemistry–A European Journal* **2013**, *19* (1), 141–154.

(21) Suzuki, A. Organoboron Compounds in New Synthetic Reactions. *Pure and Applied Chemistry* **1985**, *57* (12), 1749–1758.

(22) Krebs, F. C.; Nyberg, R. B.; Jørgensen, M. Influence of Residual Catalyst on the Properties of Conjugated Polyphenylenevinylene Materials: Palladium Nanoparticles and Poor Electrical Performance. *Chemistry of Materials* **2004**, *16* (7), 1313–1318.

(23) Nielsen, K. T.; Bechgaard, K.; Krebs, F. C. Removal of Palladium Nanoparticles from Polymer Materials. *Macromolecules* **2005**, *38* (3), 658–659.

(24) Zong, W.; Qiu, W.; Yuan, P.; Wang, F.; Liu, Y.; Xu, S.; Su, S.-J.; Cao, S. Thermally Activated Delayed Fluorescence Polymers for High-Efficiency Solution-Processed Non-Doped OLEDs: Convenient Synthesis by Binding TADF Units and Host Units to the Pre-Synthesized Polycarbazole-Based Backbone via Click Reaction. *Polymer* **2022**, *240*, 124468.

(25) Yao, Z.; Zong, W.; Wang, K.; Yuan, P.; Liu, Y.; Xu, S.; Cao, S. Triphenylamine-Carbazole Alternating Copolymers Bearing Thermally activated delayed fluorescence Emitting and Host Pendant Groups for Solution-Processable OLEDs. *Reactive and Functional Polymers* **2021**, *163*, 104898.

Chapter 4: Conclusions and Future Work

4.1 Conclusions

Accelerated growth in economic activities which exploit OLEDs as next generation displays and lighting sources has stimulated a rapid expansion of research activities in organic emissive materials. Recently, the evolution of mainly organic emissive materials in OLEDs has been expeditiously achieved, initially using fluorescent materials. These were followed by phosphorescent heavy-metal complexes and finally, by TADF materials. The power to upconvert triplet excitons into singlet excitons grants approximately 100% EUE without consuming any heavy-metal components in the new generation of materials with TADF characteristics. The development of cutting-edge OLEDs based on TADF materials has made significant strides in the last few years. Despite improvements in efficiency, their deposition through evaporation techniques demands sophisticated structures, elevated costs, and fine control, making this approach costly and impractical for large-scale device production. In contrast to other manufacturing techniques, solution-processing is a simpler, less expensive, and more readily controlled choice for enabling large-scale production. However, the majority of the published TADF dopants are small molecules which are incompatible with solution-processing. Consequently, the evolution of solution-processable organic emissive materials which include TADF characteristics is of critical relevance.

Molecular systems of donor-acceptor with strong CT character are vital to accomplish small ΔE_{ST} via separated HOMO and LUMO for TADF emission. The energy exchange of the D-A molecular system at the excited state of S_1 and T_1 is realised by HOMO and LUMO on donor and acceptor moieties, respectively. Hence, the slight overlap between HOMO and LUMO for achieving small ΔE_{ST} makes D-A molecular systems suitable candidates as TADF materials with an efficient RISC process. Most of the D-A type TADF materials were attained *via* intramolecular charge transfer state through separated HOMOs in donors and LUMOs in acceptors, interrupting the conjugation between donor and acceptor units, densely combining donors and acceptors, or linking donor and acceptor units by a steric hindrance. In the other method, TADF phenomena was realised by the intermolecular charge transfer between donor and acceptor moieties such as exciplexes. These two categories of D-A systems have the remarkable transition of electron from LUMO to HOMO on an acceptor and a donor, respectively, and thereby they own either strong intramolecular or intermolecular charge transfer states.

More interestingly, excited states of CT character for a specific material are experimentally proved by the solvatochromism noticed in their emission. The obvious spectral shift along with increasing solvent polarity is fundamentally on account of the excited state dipole of the TADF materials, originating from the redistribution of electronic density related to a CT state. Another important experiment to evidence that the DF is caused by a TADF mechanism is the temperature dependence of the DF. The integral of the DF will increase along with temperature increases in respect of TADF, and this will be noticed in time resolved data either in integrated DF or the form of decays. In addition, the variation of the DF integrated intensity with excitation dose is a fundamental factor to determine the intramolecular origin of the DF. As a result, TADF materials are recognised by the intramolecular origin of the DF relative to TTA. In the case of TADF materials, the TADF intensity varies linearly with excitation dose in the whole regime.

In chapter 2 of this work, we proposed a design-engineering strategy which encompassed target polymers containing two components, i.e., a polymeric backbone, which functions as a host and as a charge transporting channel, and a guest molecule, which encompasses TADF properties, tethered onto the polymer backbone sidechain. All the desired polymers, i.e., **PmCP-DPOXH-PxzTrz-5**, **PmCP-DPOXH-PxzTrz-10**, and **PmCP-DPOXH-PxzTrz-20**, in this study were designed to be of a sidechain type consisting of both partially conjugated and non-conjugated systems in the main chain backbone. This facilitated the attainment of polymers with non-conjugated main chain backbones which have the potential to positively impact charge transport properties and device performance. The target polymers, **PmCP-DPOXH-PxzTrz-5**, **PmCP-DPOXH-PxzTrz-10**, and **PmCP-DPOXH-PxzTrz-20** were designed to use the molecule, **mCP** repeat units, as host compounds since **mCP** possesses an outstanding high triplet energy level, (E_T) = 2.9 eV, which is sufficiently higher than the (E_T) of the TADF guest, such that the undesired TEBT from emitter guest to host is suppressed. Additionally, the **mCP**-containing main chain functions as the charge transport channel to the polymer sidechain, as well as suppressing the TADF moieties from concentration quenching and enhancing hole transport performance. Furthermore, 1,6-diphenoxyhexane (**DPOXH**) in **M2** was introduced into the polymer backbone as a spacer because the **mCP** host suffers from a large steric hindrance. **PXZ-TRZ** is characterised by having TADF properties, such as a reduced ΔE_{ST}. It also includes two moieties, i.e., **PXZ**, as a donor, and **TRZ**, as an acceptor, resulting in the generation of a charge-transfer structure. As a result, **PXZ-TRZ** was utilised in the production of green-light emitting TADF polymers as a green TADF guest and selected as a suitable polymer sidechain moiety. The resulting green-light emitting TADF polymers could easily be dissolved in common organic solvents, such as DCM, chloroform, toluene, THF and chlorobenzene. The chemical structures of **PmCP-DPOXH** and the polymers grafted by a green TADF moiety located at the sidechain, i.e., **PmCP-DPOXH-PxzTrz-5**, **PmCP-DPOXH-PxzTrz-10**, and **PmCP-DPOXH-PxzTrz-20**, were fully characterised by ^{1}H NMR spectroscopy; the data were in good agreement with the expected structures. GPC analysis was conducted in order to estimate Mn and PDI values for all the polymers, i.e., **PmCP-DPOXH**, **PmCP-DPOXH-PxzTrz-5**, **PmCP-DPOXH-PxzTrz-10**, and **PmCP-DPOXH-PxzTrz-20**. These number average molecular weights were determined to be within the ranges, 5300–6800 Da and polydispersities between 1.25 to 1.36. Relatively low molecular weights were obtained for the above TADF polymers. This could be attributed to the high steric hindrance of the carbazole moiety in **mCP**. The UV-Vis absorption spectra of the target polymers, i.e., **PmCP-DPOXH**, **PmCP-DPOXH-PxzTrz-5**, **PmCP-DPOXH-PxzTrz-10**, and **PmCP-DPOXH-PxzTrz-20**, were investigated in both dilute toluene solutions and neat films. An intense absorption peak positioned at approximately 303 nm for all these polymers could be assigned to the polymers' π-π^* electronic transition, proving that these bands can be ascribed to the polymeric backbones. It was evident that the absorption peaks in **PmCP-DPOXH**, **PmCP-DPOXH-PxzTrz-5**, **PmCP-DPOXH-PxzTrz-10**, and **PmCP-DPOXH-PxzTrz-20** were almost identical; it was therefore concluded that **PXZ-TRZ** made a negligible contribution to target polymer absorptions as a result of low **PXZ-TRZ** loading. The optical gaps, (E_g), for **PmCP-DPOXH**, **PmCP-DPOXH-PxzTrz-5**, **PmCP-DPOXH-PxzTrz-10**, and **PmCP-DPOXH-PxzTrz-20** were 3.20 eV, 3.26 eV, 3.27 eV, and 3.27 eV, respectively. Photoluminescence studies on toluene solutions of the polymers with **PXZ-TRZ** substituents i.e., **PmCP-DPOXH-PxzTrz-5**, **PmCP-DPOXH-PxzTrz-10**, and **PmCP-DPOXH-PxzTrz-20** showed dual emission peaks within the ranges, 400 nm and 540 nm, which can be attributable to the emissions of the polymeric backbones and **PXZ-TRZ**, respectively. Upon increasing molar ratios of the TADF unit, the PL emission peaks of the TADF polymers exhibited a gradual redshift from 523 nm for

PmCP-DPOXH-PxzTrz-5, to 528 nm for **PmCP-DPOXH-PxzTrz-20**, as a result of some aggregation. This proved that the TADF moiety contributes obviously to the polymers' emission profile. In the thin films, with the exception of **PmCP-DPOXH-PxzTrz-5**, in the polymeric backbone's emission residue, an almost entire interchain and intrachain energy transfer from the polymeric backbone to the sidechain TADF moiety is clearly observed, giving rise to only a TADF emission peak and scarcely any residual emission from the main chain backbone for **PmCP-DPOXH-PxzTrz-10** and **PmCP-DPOXH-PxzTrz-20**. These target polymers (**PmCP-DPOXH-PxzTrz-5**, **PmCP-DPOXH-PxzTrz-10**, and **PmCP-DPOXH-PxzTrz-20**) were considered ideal candidates for solution-processable OLEDs. CV analysis demonstrated the HOMO levels of the green-emitting TADF polymers, i.e., **PmCP-DPOXH-PxzTrz-5**, **PmCP-DPOXH-PxzTrz-10**, and **PmCP-DPOXH-PxzTrz-20**, which varied from -5.09 eV to -4.99 eV, evidencing a rising HOMO level trend with increasing TADF moiety loading ratios. In contrast, **PmCP-DPOXH** exhibited the deepest HOMO level at -5.36 eV owing to the lack of TADF moiety in the polymer. The HOMO level data therefore demonstrated that rising proportions of the TADF moiety have an obvious impact on the polymers. The polymer HOMO and LUMO levels were significantly influenced by the TADF moiety tethered on the polymeric backbone-containing **mCP** unit. Notably, the HOMO-LUMO gaps of the green light emitting TADF polymers decreased clearly with increasing TADF unit loading, from 1.56 eV (**PmCP-DPOXH-PxzTrz-5**) to 1.47 eV (**PmCP-DPOXH-PxzTrz-20**). It can be concluded that the existence of the TADF moiety in the polymers has an evident effect on the HOMO-LUMO gap which becomes lower with an increase in the TADF unit.

In chapter 3 of this work, we presented the preparation and characterisation of **DPEPO**-based polymers with TADF properties for OLED applications. **PDPEPO-DPOXH-PxzTrz-5**, **PDPEPO-DPOXH-PxzTrz-10**, and **PDPEPO-DPOXH-PxzTrz-20** were designed based on the sidechain type of TADF polymers involving the presence of two structural components, i.e., a polymer backbone, functioning as a polymer host and charge transporting channel, as well as a TADF unit on a sidechain linked to the polymer skeleton, which operates as a guest molecule. This sidechain was grafted by a TADF moiety in predetermined ratios in order to endow the polymers with TADF properties. The **DPEPO** molecule was employed in our design as a repeat unit in the polymeric backbone host compounds as this molecule has a high triplet energy level,

E_T = 3.0 eV, which is considered sufficiently higher than E_T of a number of TADF guests. It is capable to prevent undesired TEBT from the TADF emitter to the host molecule and to boost electron transport performance and has been widely used as a host material to TADF molecules in efficient OLEDs manufactured through evaporation of small molecules. **PXZ-TRZ** was exploited in the TADF polymer configurations as a green light-emitting TADF guest and selected as a convenient polymer sidechain unit in order to attain excellent TADF features, such as the small ΔE_{ST}. Furthermore, **PXZ-TRZ** possesses two units, i.e., PXZ, as a donor, and TRZ, as an acceptor, causing the formation of a charge-transfer structure, **PXZ-TRZ,** which was therefore exploited in generating the target TADF polymers, **PDPEPO-DPOXH-PxzTrz-5**, **PDPEPO-DPOXH-PxzTrz-10**, and **PDPEPO-DPOXH-PxzTrz-20**. The chemical structures and purity of **PDPEPO-DPOXH** and the polymers grafted by a TADF moiety located on the sidechain, **PDPEPO-DPOXH-PxzTrz-5**, **PDPEPO-DPOXH-PxzTrz-10**, and **PDPEPO-DPOXH-PxzTrz-20**, were completely characterised by ^{31}P NMR spectroscopy and ^{1}H NMR spectroscopy. The results obtained confirmed the predicted structures for all the target polymers. GPC analysis was carried out so as to obtain the Mn and PDI of the above synthesised polymers; the Mn values were within the ranges, 4600–4900 Da and polydispersities between 1.22 and 1.35. The low molecular weight of all the polymers generated could be due to the large steric hindrance of the **DPEPO** moiety, promoting polymer rigidity. Furthermore, introduction of the 1,6-diphenoxyhexane (**DPOXH**) repeat units to the polymeric backbones enabled the control of the optical gaps of the final polymers as they limited electronic delocalisation. The UV-Vis absorption spectra of the above target polymers were examined in both toluene solutions and as thin films. Single clear intense absorption band peaks around 296 nm could be observed for all 4 polymers, attributable for the π-π* transitions of the polymeric backbones. The absorption peaks of all the polymers were similar, giving a clear indication that the TADF units offered only a negligible contribution to the polymer's absorption spectra presumably owing to the low molar absorptivity of **PXZ-TRZ** units compared to those of the polymers' backbones as well as loading concentrations. The optical gaps, E_g of **PDPEPO-DPOXH**, **PDPEPO-DPOXH-PxzTrz-5**, **PDPEPO-DPOXH-PxzTrz-10** and **PDPEPO-DPOXH-PxzTrz-20** were 3.68 eV, 3.67 eV, 3.67 eV and 3.68 eV, respectively. Emission spectra in toluene solutions, show two distinctive emission bands at approximately 398 and 540 nm for **PDPEPO-DPOXH-PxzTrz-5**, **PDPEPO-DPOXH-PxzTrz-10**, and **PDPEPO-DPOXH-PxzTrz-20**, attributable to polymeric backbone and TADF moiety emissions, respectively. Polymers with greater proportions of TADF units exhibited a red-shift of the emission band from the TADF substituents from 528 nm for (**PDPEPO-DPOXH-PxzTrz-5**) to 533 nm for (**PDPEPO-DPOXH-PxzTrz-20**) owing to the aggregation. This demonstrated that the TADF moiety contributes clearly to the polymers' emission profile. These target TADF polymers, i.e., **PDPEPO-DPOXH-PxzTrz-5**, **PDPEPO-DPOXH-PxzTrz-10**, and **PDPEPO-DPOXH-PxzTrz-20**, were selected as perfect candidates for solution-processing OLEDs. Cyclic voltammetry (CV) analysis showed the HOMO levels for the green-light emitting TADF polymers, **PDPEPO-DPOXH-PxzTrz-5**, **PDPEPO-DPOXH-PxzTrz-10**, and **PDPEPO-DPOXH-PxzTrz-20**, to be within the range, -5.11 eV to -5.00 eV, indicating an increasing HOMO level trend with rising TADF moiety proportions. In contrast, **PDPEPO-DPOXH** showed a deeper HOMO level of -5.42 eV owing to the lack of TADF moiety in the polymer. Consequently, the polymer HOMO level data demonstrated the apparent influence of the high TADF moiety loading on the target polymers. The polymer HOMO and LUMO levels were impacted by the TADF moiety tethered on the polymeric backbone containing **DPEPO** host. The HOMO-LUMO gaps of the above green light emitting TADF polymers were obviously decreased with the incremental rise in TADF unit loading from 1.75 eV (**PDPEPO-DPOXH-PxzTrz-5**) to 1.62 eV (**PDPEPO-DPOXH-PxzTrz-20**). It can be deduced that the presence of the polymer TADF moiety has an obvious impact on the HOMO-LUMO gap which is minimised by increasing the TADF unit.

4.2 Future Work

The **mCP**-based TADF polymers (**PmCP-DPOXH-PxzTrz-5**, **PmCP-DPOXH-PxzTrz-10**, and **PmCP-DPOXH-PxzTrz-20**) as well as the **DPEPO**-based TADF polymers (**PDPEPO-DPOXH-PxzTrz-5**, **PDPEPO-DPOXH-PxzTrz-10**, and **PDPEPO-DPOXH-PxzTrz-20**) were prepared successfully in this work. The corresponding polymers **PmCP-DPOXH** and **PDPEPO-DPOXH** which have the same backbone of the respective two classes of polymers but with no TADF functional groups were also successfully prepared for comparison purposes. The two classes of TADF polymers were subjected to a range of analytical techniques including NMR, UV-vis and PL spectroscopy, CV analysis and TGA studies. Both sets of TADF polymers displayed partial or full energy transfer from the host backbone of these polymers to the TADF dye attached to polymer chains depending on the percentage of dye functionalisation and whether these polymers are in solution or in the solid state.

The two sets of polymers are designed for use in OLED devices; however, a number of studies are required to further investigate their potential use in devices. Measurement of the triplet energy of the two polymers is therefore important in order to assess whether the **mCP** and **DPEPO**-based polymers have the same triplet energy as **mCP** and **DPEPO** molecules. These measurements could be undertaken upon running time-resolved photoluminescence experiments at low temperatures on **PmCP-DPOXH** and **PDPEPO-DPOXH**. Measurements on the emission lifetime of the two sets of TADF polymers are also important to demonstrate their TADF properties. The electroluminescent properties of the above six TADF polymers should also be analysed in cooperation with the Department of Physics at the University of Sheffield. Future work could include additional analyses and comparison of the properties of these TADF polymers in OLED devices using blends of the polymers without TADF emitters **PmCP-DPOXH** and **PDPEPO-DPOXH** with equivalent amounts the free TADF dye **PXZ-TRZ**. This approach would indicate the value of covalent attachment of TADF dyes to polymer backbones rather than using the blends which could lead to phase separation issues.

Chapter 5: Experimental Section

5.1 Reagents and Solvents

All chemicals and reagents were purchased from commercial suppliers and utilised as received unless otherwise stated. A certain of reactions were synthesised under an inert argon atmosphere and carried out using anhydrous solvents which were gained from Grubbs solvent purification system at the University of Sheffield, specifically from the Chemistry Department.

5.2 Instrumentation

5.2.1 Nuclear Magnetic Resonance Spectroscopy (NMR)

All analysis of ^{1}H, ^{13}C NMR and ^{31}P spectra were run out on Bruker Avance 250 (250 MHz), Avance AV 3HD 400 (400 MHz) or DRX-500 (500 MHz) NMR spectrometer using deuterochloroform solution ($CDCl_3$) or dimethyl sulfoxide-d_6 (DMSO-d_6) as a solvent which purchased from Sigma-Aldrich and used as received at 22 °C. In NMR, chemical shifts (δ) are analysed by parts per million (ppm), coupling constants (J) are measured by Hertz (Hz) and tetramethylsilane (TMS) was utilised for calibrating chemical shifts which are related to the internal standard. The NMR splitting types mentioned are indicated as the following abbreviations: s, d, t, dd, m and qt are assigned as a singlet, doublet, triplet, doublet of doublet multiplet, and quartet, respectively.

5.2.2 Mass Spectrometry (MS)

Mass spectrometry for products was analysed by Perkin Elmer Turbomass provided with autosampler and autosystem XL Gas Chromatography. Mass spectra were carried out by both the electron ionisation (EI) and chemical ionisation (CI) methods.

5.2.3 Elemental Analysis (EA)

Elemental analyses of carbon, hydrogen, and phosphorus were operated by the Perkin Elmer 2400 series II analyser, while the Schöniger oxygen flask combustion process was performed for anions analysis such as halides. The weights of the chemical compounds taken were approximately 7 mg for the CHP analysis, whilst 10-15 mg for the anion analysis.

5.2.4 Analytical Gel Permeation Chromatography (GPC)

The record of GPC data was suitably gained by means of the instrument containing Erma ERC-7512 RI Detector, GILSON Model 234 Autoinjector, MILLIPORE Waters Lambda-Max Model 481 LC Spectrometer, and a Waters 410 Differential Refractometer. The calibration of GPC system was conducted by a series of polystyrene narrow standards (Polymer Laboratories). Molecular weights and the PDI for all target polymers were estimated by dissolving the polymer in HPLC grade THF (1 mg mL^{-1}), which was utilised as an eluent at 40 °C at a flow rate of 1 mL min^{-1}. The synthesised polymers were spiked by toluene solution as a reference.

5.2.5 UV-visible (UV-vis) Absorption Spectroscopy

All the measurements of UV-vis absorption spectra were obtained by SPECORD S600 UV/visible Spectrophotometer at ambient temperature. The measurement of the target polymers absorptions was carried out in dilute anhydrous toluene solutions utilising blank quartz cuvettes containing toluene solution as a reference and then running quartz glass cuvettes including the target sample in dilution at (10^{-3} M) (light path length= 1 cm). On the other hand, the results of desired polymers absorptions in solid state were acquired by coating the target polymer on quartz substrates after dissolving it in a volatile solvent such as DCM (1 mg in 1 mL) and blank quartz substrate was employed as a reference. All the data of desired polymers absorptions in solid state was gained after evaporating the solvents from the film in the air and then left the coated films in the *vacuum* oven overnight.

5.2.6 Photoluminescence Spectroscopy (PL)

The measurements of PL spectra were gained by means of the Hitachi F-4500 Fluorescence Spectrophotometer fitted with Hamamatsu Photonics R928F Photomultiplier Tube (PMT). The determinations of the emissions for all target polymers were performed employing a Quartz Glass Fluorescence Cuvette (light path length = 1 cm). All results of PL emissions for all target polymers were obtained in dilute anhydrous toluene solutions (10^{-3} M) at room temperature. With respect of polymers emissions measurements on the thin films, samples of polymers were prepared by dissolving 1 mg of polymer in 1 mL of DCM and then drop casting it onto quartz substrate, which were left to dry in 15 minutes in the air.

5.2.7 Cyclic Voltammetry (CV)

To measure CV of the target polymers, a Model 263A Potentiostat/ Galvanostat-Princeton Applied Research was exploited to obtain CV curves. All measurements of desired polymers were conducted in a supporting electrolyte solution of tetrabutylammonium perchlorate (Bu_4NClO_4) dissolved in anhydrous acetonitrile (0.1 M). The system set-up required the use of three main electrodes: a platinum disc as a working electrode, a silver wire immersed in silver nitrate solution (0.01 M) in anhydrous acetonitrile (Ag/Ag^+) as a reference electrode, and a platinum wire as a counter (auxiliary) electrode. All the mentioned three electrodes were immersed in the prepared supporting electrolyte during carrying out CV on the samples. Based on IUPAC's recommendations, ferrocene (Fc/Fc+) was employed as a reference redox system. The preparation of all polymer's thin films was perfectly obtained by dissolving 1 mg of the target polymer in 1 mL of DCM and then drop casting onto the platinum disk of working electrode, which was left it to dry in the air for 10 minutes. Before conducting the cathodic sweep, the supporting electrolyte with the three electrodes were bubbled using an argon gas for at least 10 minutes.

5.2.8 Thermogravimetric Analysis (TGA)

The collections of TGA curves were acquired by means of the Perkin Elmer Pyris 1 Thermogravimetric Analyser at a scan rate of 10 °C $minute^{-1}$ under an inert nitrogen atmosphere. The weights of used target polymers were about 8 mg, and the platinum pans were consumed as the sample holder.

5.3 Preparation of Monomers

5.3.1 Synthesis of 3-bromo-9*H*-carbazole (1)[1]

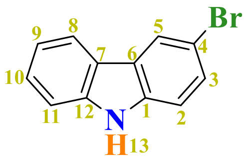

(1)

A solution of NBS (2.68 g, 15.06 mmol) in anhydrous DMF (15 mL) was added dropwise to a stirred solution of 9H-carbazole (2.5 g, 14.95 mmol) in anhydrous DMF at room temperature. The period of dropwise addition lasted 10 minute to complete. After the addition was carried out, the mixture was left under stirring for 24 h. Next, the solution was quenched by 100 mL of distilled water and extracted with DCM (3 × 50 mL). The organic phase was dried using anhydrous $MgSO_4$ and evaporated *in vacuo*. The desired product was purified by silica gel column chromatography using petroleum ether: ethyl acetate in ratios of (1:1) as an eluent to obtain a colourless solid **(1)** (3.39 g, 92%).

^{1}H NMR (400 MHz, $CDCl_3$) δ (ppm): 8.19 (d, *J* = 2.0 Hz, 1H, H**5**), 8.08 (bs, 1H, H**13**), 8.04 (d, *J* = 8.0 Hz, 1H, H**8**), 7.55 (dd, *J* = 8.0 Hz, *J* = 2.0 Hz, 1H, H**3**) 7.50-7.40 (m, 2H, H**10**, H**11**), 7.35 (d, *J* = 8.0 Hz, 1H, H**2**), 7.30 (td, *J* = 8.0 Hz, *J* = 2.0 Hz, 1H, H**9**).

^{13}C NMR (DEPTQ, 100 MHz, $CDCl_3$) δ (ppm): 139.8 (C**12**, -ve), 138.1 (C**1**, -ve), 128.5 (C**3**, +ve), 126.6 (C**10**, +ve), 125.2 (C**6**, -ve), 123.1 (C**5**, +ve), 122.4 (C**7**, -ve), 120.5 (C**8**, +ve), 119.9 (C**9**, +ve), 112.3 (C**4**, -ve), 112 (C**2**, +ve), 110.8 (C**11**, +ve).

EA (%) Calculated for $C_{12}H_8BrN$: C, 58.56; H, 3.28; Br, 32.47; N, 5.69 %. **Found:** C, 58.68; H, 3.39; Br, 32.31; N, 5.57 %.

EI-MS (*m/z*): 245, 247 ($[M^+]$, $[M^++2]$).

5.3.2 Synthesis of 1,3-bis(3-bromo-9*H*-carbazole-9-yl)benzene **M1**[2]

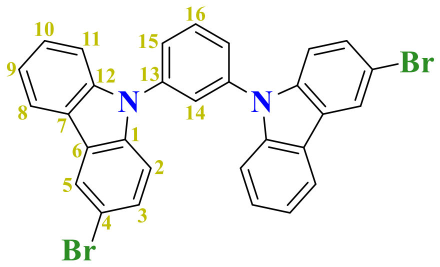

M1

(1) (1.64 g, 6.65 mmol), 1,3-diiodobenzene (1.00 g, 3.025 mmol), potassium carbonate (3.35 g, 24.225 mmol), Cu powder (770 mg, 12.1 mmol) and dibenzo 18-crown-6 (160 mg, 0.605 mmol) were dissolved in 10 mL anhydrous 1,2-dichlorobenzene (ODCB) under argon atmosphere. The reaction mixture was left under stirring for 12 h at 180 °C. Upon completion, the mixture was quenched with 100 mL of deionised water and extracted (3 × 50 mL). The organic phase was dried over anhydrous $MgSO_4$ and evaporated *in vacuo* to afford the crude product, which was loaded on column chromatography using petroleum ether: ethyl acetate in ratio of (22:1) as an eluent. The target white powdery product **M1** was gained (1.54 g, 90%).

^{1}H NMR (400 MHz, $CDCl_3$) δ (ppm): 8.25 (d, *J* = 2.0 Hz, 2H, H**5**), 8.09 (d, *J* = 8.0 Hz, 2H, H**8**), 7.85 (t, *J* = 8.0 Hz, 1H, H**16**), 7.73 (t, *J* = 2.0 Hz, 1H, H**14**), 7.67 (dd, *J* = 8.0 Hz, *J* = 2.0 Hz, 2H, H**15**), 7.53-7.44 (m, 6H, H**3**, H**10**, H**11**), 7.37 (d, *J* = 8.0 Hz, 2H, H**2**), 7.32 (td, *J* = 8.0 Hz, *J* = 2.0 Hz, 2H, H**9**).

^{13}C NMR (DEPTQ, 100 MHz, $CDCl_3$) δ (ppm): 140.9 (C**12**, -ve), 139.3 (C**1**, -ve), 139.1 (C**13**, -ve), 131.5 (C**16**, +ve), 128.9 (C**3**, +ve), 127 (C**10**, +ve), 126.1 (C**15**, +ve), 125.4 (C**6**, -ve), 125.2 (C**14**, +ve), 123.3 (C**5**, +ve), 122.6 (C**7**, -ve), 120.8 (C**8**, +ve), 120.7 (C**9**, +ve), 113.2 (C**4**, -ve), 111.1 (C**2**, +ve), 109.9 (C**11**, +ve).

EA (%) Calculated for $C_{30}H_{18}Br_2N_2$: C, 63.63; H, 3.20; Br, 28.22; N, 4.95 %. **Found:** C, 63.75; H, 3.33; Br, 28.01; N, 4.79 %.

EI-MS (*m/z*): 564.8, 566.8, 568.8 ([M^+], [M^++2], [M^++4]).

5.3.3 Synthesis of 1,6-bis(4-bromophenoxy)hexane (2)[3]

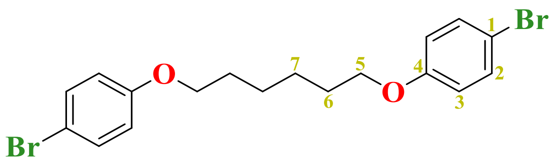

(2)

4-Bromophenole (289 mg, 1.67 mmol) 1,6-dibromohexane (128 µL, 0.83 mmol), and potassium carbonate (690 mg, 5 mmol) were dissolved in anhydrous acetone (5 mL). The reaction mixture was left under refluxing for 24 h. After cooling to ambient temperature, acetone solvent was eliminated under reduced pressure, and the residue was quenched with 100 mL of distilled water and extracted with 100 mL of DCM three times. The organic layer was dried over anhydrous $MgSO_4$. The solvent was removed by rotary evaporation. The crude product was successfully recrystallised by ethanol to obtain (2) a white solid (273 mg, 77%).

^{1}H NMR (400 MHz, $CDCl_3$) δ (ppm): 7.35 (d, *J* = 9.0 Hz, 4H, H2), 6.75 (d, *J* = 9.0 Hz, 4H, H3), 3.92 (t, *J* = 7.0 Hz, 4H, H5), 1.83-1.76 (m, 4H, H6), 1.55-1.44 (m, 4H, H7).

^{13}C NMR (DEPTQ, 100 MHz, $CDCl_3$) δ (ppm): 158.3 (C4, -ve), 132.3 (C2, +ve), 116.3 (C3, +ve), 112.7 (C1, -ve), 68.2 (C5, -ve), 29.1 (C6, -ve), 25.8 (C7, -ve).

EA (%) Calculated for $C_{18}H_{20}Br_2O_2$: C, 50.49; H, 4.71; Br, 37.32 %. **Found:** C, 50.61; H, 4.84; Br, 37.21 %.

EI-MS (*m/z*): 426, 428, 430 ([M^+], [M^++2], [M^++4]).

5.3.4 Synthesis of 1,6-bis(4-(4,4,5,5-tetramethyl-1,3,2-dioxaborolan-2-yl)phenoxy)hexane **M2**[4]

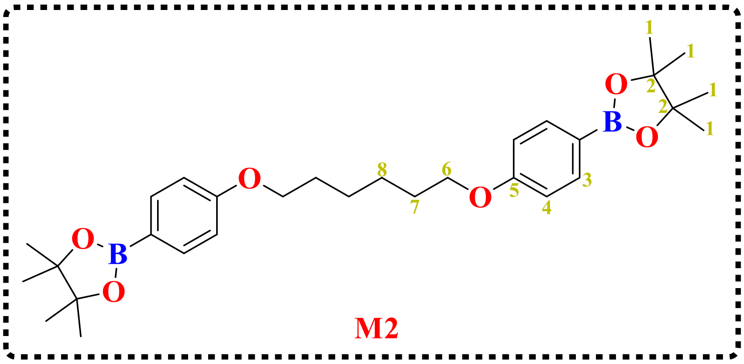

M2

In a two-neck bottom round flask, **(2)** (1.07 g, 2.5 mmol) was dissolved in (25 mL) anhydrous THF and cooled to −78 °C. A solution of *n*-BuLi (2.5 M in hexanes, 2.10 mL, 5.27 mmol) was slowly added, and the reaction mixture was left under stirring at −78 °C for 1 hour. 2-Isopropoxy-4,4,5,5-tetramethyl-1,3,2-dioxaborolane (*i*-PrOBpin) (1.13 mL, 1.03 g, 5.57 mmol) was slowly added, and the reaction was left under stirring at −78 °C for an hour. The reaction mixture was then warmed to room temperature and left for overnight. Upon completion, the reaction mixture was quenched with saturated aqueous ammonium chloride solution (150 mL) and extracted with DCM (3 × 100 mL). The organic phase was dried over $MgSO_4$, and the solvent was removed under reduced pressure. The crude product was purified by column chromatography using petroleum ether: ethyl acetate: methanol in ratio of (100:2.5:1) to afford the desired product **M2** as a colourless solid (1.17 g, 2.23 mmol, 89%).

^{1}H NMR (400 MHz, $CDCl_3$) δ (ppm): 7.73 (d, *J* = 9.0 Hz, 4H, H**3**), 6.88 (d, *J* = 9.0 Hz, 4H, H**4**), 3.99 (t, *J* = 7.0 Hz, 4H, H**6**), 1.86-1.77 (m, 4H, H**7**), 1.59-1.49 (m, 4H, H**8**), 1.32 (s, 24H, H**1**).

^{13}C NMR (DEPTQ, 100 MHz, $CDCl_3$) δ (ppm): 161.7 (C**5**, -ve), 136.5 (C**3**, +ve), 113.9 (C**4**, +ve), 83.5 (C**2**, -ve), 67.6 (C**6**, -ve), 29.2 (C**7**, -ve), 25.9 (C**8**, -ve), 24.9 (C**1**, +ve).

EA (%) Calculated for $C_{30}H_{44}B_2O_6$: C, 68.99; H, 8.49 %. **Found:** C, 69.10; H, 8.61 %.

EI-MS (*m/z*): 521.3, 522.3, 523.3 ([M$^+$], [M$^+$+], [M$^+$+2]).

5.3.5 Synthesis of 10-acetylphenoxazine (3)[5]

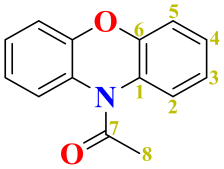

(3)

Under argon atmosphere, acetyl chloride (600 mg, 545 µL, 7.64 mmol) diluted in anhydrous DCM (3.75 mL) was slowly added to a pre-cooled solution of 10*H*-phenoxazine (1.00 g, 5.46 mmol) and triethylamine (830 mg, 1.15 mL, 8.20 mmol) in anhydrous DCM (8.75 mL) at 0 °C. The reaction mixture was left under stirring at room temperature for 3 hours. Next, the resulting mixture was quenched with an aqueous hydrochloric acid solution (50 mL, 125 mM), and the aqueous portion was extracted by DCM (3 × 50 mL). The organic phase was collected, dried over $MgSO_4$, and subsequently evaporated *in vacuo*. The pure compound **(3)** was gained by column chromatography (1 ethyl acetate / 5 petroleum ether) (1.13 g, 92%).

^{1}H NMR (400 MHz, $CDCl_3$) δ (ppm): 7.51 (dd, *J* = 8.0 Hz, *J* = 2.0 Hz, 2H, H2), 7.22 (td, *J* = 8.0 Hz, *J* = 2.0 Hz, 2H, H4), 7.18-7.12 (m, 4H, H3, H5), 2.35 (s, 3H, H8).

^{13}C NMR (DEPTQ, 100 MHz, $CDCl_3$) δ (ppm): 169.3 (C7, -ve), 151.1 (C6, -ve), 129.5 (C1, -ve), 126.9 (C2, +ve), 125.2 (C4, +ve), 123.4 (C3, +ve), 116.9 (C5, +ve), 23.1 (C8, +ve).

EA (%) Calculated for $C_{14}H_{11}NO_2$: C, 74.65; H, 4.92; N, 6.22 %. **Found:** C, 74.78; H, 5.02; N, 6.09 %.

EI-MS (*m/z*): 225.1 $[M^+]$.

5.3.6 Synthesis of 2-acetylphenoxazine (4)[6]

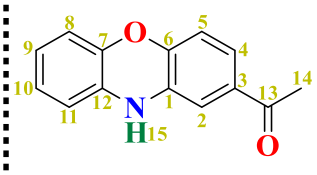

(4)

(3) (5.63 g, 25 mmol) pre-dissolved completely in 100 mL of carbon disulphide was added dropwise to powdered aluminium chloride (10 g, 75 mmol) under refluxing for an hour. After leaving the reaction to cool at room temperature, acetyl chloride (2.93 g, 38 mmol) was slowly added to the reaction mixture. Then, the reaction mixture was stirred under refluxing for another 2.5 hours. Next, the solvent was decanted after giving it 30 minutes to cool. The decomposition of the gummy residue was performed by crushed ice and 100 mL of concentrated hydrochloric acid. Later, the crude was filtered, washed, suspended on a mixture of glacial acetic acid and hydrochloric acid in ratio of (4:1), and refluxed again for 30 minutes. The precipitate was filtered, washed with deionised water, and dried using high *vacuum*. The precipitate was dissolved in ethyl acetate, then washed, and extracted with ethyl acetate (62.5 mL) three times. The organic layer was dried over $MgSO_4$ and evaporated *in vacuo* to gain the desired product (4) as greenish yellow crystals 5.05 g in a high yield (90%).

^{1}H NMR (400 MHz, DMSO-d$_6$) δ (ppm): 8.42 (bs, 1H, H15), 7.25 (dd, *J* = 8.0 Hz, *J* = 2.0 Hz, 1H, H4), 6.96 (d, *J* = 2.0 Hz, 1H, H2), 6.76 (td, *J* = 8.0 Hz, *J* = 2.0 Hz, 1H, H10), 6.69 (d, *J* = 8.0 Hz, 1H, H5), 6.64 (dd, *J* = 8.0 Hz, *J* = 2.0 Hz, 1H, H8), 6.59 (td, *J* = 8.0 Hz, *J* = 2.0 Hz, 1H, H9), 6.45 (dd, *J* = 8.0 Hz, *J* = 2.0 Hz, 1H, H11), 2.44 (s, 3H, H14).

^{13}C NMR (DEPTQ, 100 MHz, DMSO-d$_6$) δ (ppm): 196.5 (C13, -ve), 147.5 (C6, -ve), 142.6 (C7, -ve), 133.5 (C12, -ve), 133 (C1, -ve), 132.1 (C3, -ve), 125 (C4, +ve), 122.9 (C2, +ve), 121.1 (C5, +ve), 115.8 (C10, +ve), 115.3 (C8, +ve), 113.9 (C9, +ve), 112.4 (C11, +ve), 26.7 (C14, +ve).

EA (%) Calculated for $C_{14}H_{11}NO_2$: C, 74.65; H, 4.92; N, 6.22 %. **Found:** C, 74.73; H, 4.98; N, 6.10%.

EI-MS (*m/z*): 225.1 [M^+].

5.3.7 Synthesis of 2-chloro-4,6-diphenyl-1,3,5-triazine (5)[7]

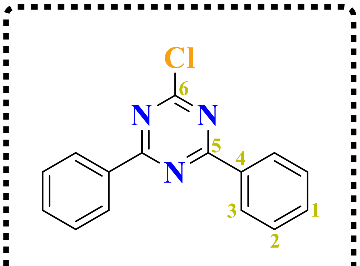

(5)

To iodine-activated magnesium (72.5 mg, 3 mmol) suspended on anhydrous THF (2.5 mL), was slowly added a solution of bromobenzene (393 mg, 2.5 mmol) in anhydrous THF (2.5 mL) over 20 minutes. In the condition of a delayed beginning to the reaction, brief heating was performed. Upon completion of addition, the reaction mixture was left for 2 more hours under refluxing. After leaving the reaction to cool at 0-10 °C, the Grignard solution was slowly added to a solution of cyanuric chloride (152.5 mg, 0.825 mmol) in anhydrous THF (1.25 mL). After completing the addition, the reaction mixture was stirred and left overnight at 50 °C. After that, the reaction mixture was cooled to reach to room temperature and then poured to a 12% aqueous solution of hydrochloric acid (12.5 mL). Then, the solvent was evaporated using a rotary evaporator, and the residue was extracted with toluene (3 × 25 mL). The organic layer was collected, washed three times with water, dried over anhydrous $MgSO_4$, and concentrated. The product crude was purified by flash column chromatography on silica gel using (petroleum ether/toluene 5:1) as an eluent to obtain **(5)** as a white solid (135 mg, 61%).

^{1}H NMR (400 MHz, $CDCl_3$) δ (ppm): 8.65 (dd, *J* = 7.5 Hz, *J* = 1.5 Hz, 4H, H**3**), 7.65 (tt, *J* = 7.5 Hz, *J* = 1.5 Hz, 2H, H**1**), 7.57 (t, *J* = 7.5 Hz, 4H, H**2**).

^{13}C NMR (DEPTQ, 100 MHz, $CDCl_3$) δ (ppm): 173.4 (C**5**, -ve), 172.2 (C**6**, -ve), 134.4 (C**4**, -ve), 133.6 (C**1**, +ve), 129.4 (C**3**, +ve), 128.8 (C**2**, +ve).

EA (%) Calculated for $C_{15}H_{10}ClN_3$: C, 67.30; H, 3.77; Cl, 13.24; N, 15.70 %. **Found:** C, 67.43; H, 3.98; Cl, 13.19; N, 15.61 %.

EI-MS (*m/z*): 267.1, 269.1 ([M^+], [M^++2].

5.3.8 Synthesis of 2-(4-aminophenyl)-4,6-diphenyl-1,3,5-triazine **(6)**[8]

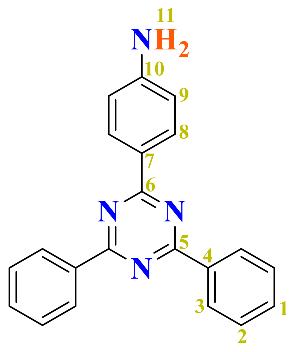

(6)

To a solution of **(5)** (1.34 g, 5 mmol), 4-(4,4,5,5-tetrame-thyl1,3,2-dioxaborolan-2-yl) aniline (1.21 g, 5.5 mmol) and tetrakis(triphenylphosphine)palladium(0) (290 mg, 0.25 mmol) in 25 mL of anhydrous THF, was slowly added potassium carbonate (1.38 g, 10 mmol) dissolved in 25 mL of deionised water under stirring. Next, the reaction mixture was refluxed under stirring for 50 hours. The cooled mixture was quenched with brine and extracted with ethyl acetate (50 mL) three times. The combined organic layers were dried over $MgSO_4$ and concentrated using a rotary evaporator. Subsequently, 25 mL of chloroform was added to the crude to obtain the brown precipitate. This precipitate generated was combined by filtration process, washed by 50 mL of chloroform, dried through the high *vacuum* pump and then the *vacuum* oven. The pure product **(6)** was yielded as a white solid (1.23 g, 76%).

^{1}H NMR (400 MHz, DMSO-d$_6$) δ (ppm): 8.70 (dd, *J* = 7.5 Hz, *J* = 1.5 Hz, 4H, H**3**), 8.47 (d, *J* = 8.5 Hz, 2H, H**8**), 7.71-7.61 (m, 6H, H**1**, H**2**), 6.75 (d, *J* = 8.5 Hz, 2H, H**9**), 6.15 (bs, 2H, H**11**).

^{13}C NMR (DEPTQ, 100 MHz, DMSO-d$_6$) δ (ppm): 171.3 (C**6**, -ve), 170.7 (C**5**, -ve), 154.4 (C**10**, -ve), 136.4 (C**4**, -ve), 133.1 (C**1**, +ve), 131.3 (C**8**, +ve), 129.3 (C**3**, +ve), 128.9 (C**2**, +ve), 122.1 (C**7**, -ve), 113.8 (C**9**, +ve).

EA (%) Calculated for $C_{21}H_{16}N_4$: C, 77.76; H, 4.97; N, 17.27 %. **Found:** C, 77.91; H, 5.09; N, 17.18 %.

EI-MS (*m/z*): 325.1 [M^+].

5.3.9 Synthesis of 2-(4-bromophenyl)-4,6-diphenyl-1,3,5-triazine (7)[8]

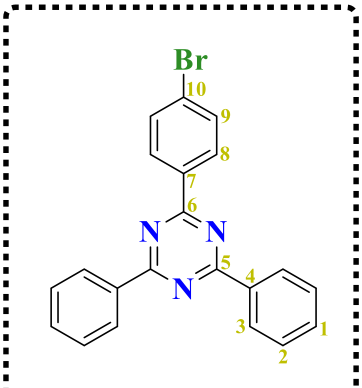

(7)

A mixture of (6) (1.11 g, 3.43 mmol) and hydrobromic acid (5 ml, 47%) was stirred and cooled at 0 °C for 30 minutes. Sodium nitrite (236.7 mg) dissolved in 5 mL of deionised water was cooled at 0 °C for 30 minutes, and then slowly added to the above solution. The resulting mixture was stirred in the cooled condition for 90 minutes. Subsequently, a mixture of copper(I) bromide (295 mg, 2.06 mmol) and 2 mL of hydrobromic acid was slowly added and stirred for 45 minutes at room temperature. The reaction mixture was then refluxed and left under stirring for 18 hours. Then, the reaction mixture was cooled at 0 °C to add sodium hydrogen carbonate to the resulting mixture for the neutralisation process. Next, 150 mL of chloroform was added to it, the organic layer was combined, and the aqueous layer was extracted with 50 mL of DCM three times. The collected organic layers were washed with brine, dried over $MgSO_4$, and concentrated using a rotary evaporator. The desired product was afforded by purifying the crude through column chromatography using chloroform/ petroleum ether in the ratio of (1:4) as an eluent to obtain (7) as a white solid in the yield of 67% (892 mg, 67%).

^{1}H NMR (400 MHz, $CDCl_3$) δ (ppm): 8.76 (dd, *J* = 7.5 Hz, *J* = 1.5 Hz, 4H, H3), 8.64 (d, *J* = 8.5 Hz, 2H, H8), 7.71 (d, *J* = 8.5 Hz, 2H, H9), 7.67-7.55 (m, 6H, H1, H2).

^{13}C NMR (DEPTQ, 100 MHz, $CDCl_3$) δ (ppm): 171.7 (C5, -ve), 170.8 (C6, -ve), 136 (C4, -ve), 135.2 (C7, -ve), 132,6 (C1, +ve), 131.9 (C9, +ve), 130.5 (C8, +ve), 129 (C3, +ve), 128.7 (C2, +ve), 127.5 (C10, -ve).

EA (%) Calculated for $C_{21}H_{14}BrN_3$: C, 64.96; H, 3.63; Br, 20.58; N, 10.82 %. **Found:** C, 65.09; H, 3.77; Br, 20.44; N, 10.69 %.

EI-MS (*m/z*): 388.1, 390.1 ($[M^+]$, $[M^++2]$).

5.3.10 Synthesis of 1-(10-(4-(4,6-diphenyl-1,3,5-triazin-2-yl)phenyl)-10*H*-phenoxazin-2-yl)ethanone **(8)**[9]

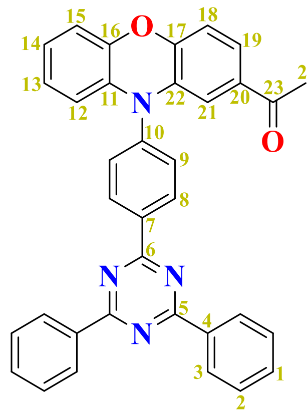

(8)

(4) (390 mg, 2.13 mmol), **(7)** (823 mg, 2.13 mmol), and potassium carbonate (1.34 g, 9.65 mmol) were dissolved in toluene (30 mL) in a 100 mL flask equipped with a magnetic stir bar under argon atmosphere. Palladium (II) acetate (21.68 mg, 0.0965 mmol) and tri-tert-butylphosphine (71.75 g, 0.355 mmol) pre-dissolved in toluene (5 mL) were added dropwise to a stirred reaction mixture under argon atmosphere. The solution was refluxed under stirring at 118 °C for 80 hours under argon atmosphere. The reaction mixture was cooled to reach to ambient temperature, resulting in the formation of greenish brown precipitates, which were then filtered and washed thoroughly with 250 mL of deionised water. Finally, the desired product was obtained by purifying it using silica gel column chromatography with the eluent DCM: petroleum ether = 1:2 (v/v) to afford **(8)** as a yellow powder (693 mg, 61%).

^{1}H NMR (400 MHz, $CDCl_3$) δ (ppm): 9.04 (d, *J* = 8.5 Hz, 2H, H8), 8.83 (dd, *J* = 7.5 Hz, *J* = 1.5 Hz, 4H, H3), 7.70-7.56 (m, 8H, H1, H2, H9), 7.33 (dd, *J* = 8.0 Hz, *J* = 2.0 Hz, 1H, H19), 6.79-6-65 (m, 5H, H12, H13, H14, H18, H21), 6.06 (dd, *J* = 8.0 Hz, *J* = 2.0 Hz, 1H, H15), 2.37 (s, 3H, H24).

^{13}C NMR (DEPTQ, 100 MHz, $CDCl_3$) δ (ppm): 196.3 (C23, -ve), 171.9 (C5, -ve), 170.8 (C6, -ve), 148.2 (C10, -ve), 143.3 (C17, -ve), 142.1 (C16, -ve), 136.8 (C11, -ve), 136 (C4, -ve), 134.1 (C22, -ve), 133.4 (C7, -ve), 133 (C20, -ve), 132.7 (C1, +ve), 132 (C8, +ve), 130.8 (C9, +ve), 129 (C3, +ve), 128.7 (C2, +ve), 124.1 (C19, +ve), 123.6

(C**14**, +ve), 122 (C**13**, +ve), 115.8 (C**21**, +ve), 115.3 (C**12**, +ve), 113.6 (C**15**, +ve), 112.4 (C**18**, +ve), 26.2 (C**24**, +ve).

EA (%) Calculated for $C_{35}H_{24}N_4O_2$: C, 78.93; H, 4.54; N, 10.52 %. **Found:** C, 79.08; H, 5.09; N, 10.40 %.

EI-MS (*m/z*): 533.2 [M^+].

5.3.11 Synthesis of 1-(10-(4-(4,6-diphenyl-1,3,5-triazin-2-yl)phenyl)-10*H*-phenoxazin-2-yl)ethanol **(9)**[10]

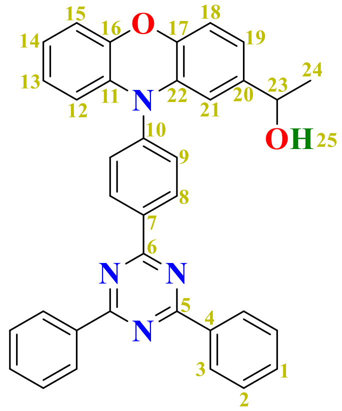

(9)

Sodium borohydride (187.5 mg, 4.7 mmol) almost dissolved in 5 mL of isopropanol was slowly added to a solution of **(8)** (700 mg, 1.313 mmol) in 20 mL of 1,4-dioxane. The reaction mixture was left under stirring for 120 minutes. Next, the reaction mixture was heated for 45 minutes. After cooling the reaction mixture to room temperature, the excess hydride was clearly decomposed with a concentrated hydrochloric acid. After concentrating the mixture *in vacuo* and adding distilled water to it, the crude product was obtained. Then, the crude was recrystallised in a mixed solvent (toluene-petroleum ether) to gain the target product **(9)** as yellow solid (484 mg, 69%).

^{1}H NMR (400 MHz, $CDCl_3$) δ (ppm): 8.99 (d, *J* = 8.5 Hz, 2H, H**8**), 8.80 (dd, *J* = 7.5 Hz, *J* = 1.5 Hz, 4H, H**3**), 7.67-7.53 (m, 8H, H**1**, H**2**, H**9**), 6.74-6-65 (m, 4H, H**12**, H**14**, H**19**, H**21**), 6.61 (td, *J* = 8.0 Hz, *J* = 2.0 Hz, 1H, H**13**), 6.07-6.00 (m, 2H, H**15**, H**18**), 4.54 (q, *J* = 6.5 Hz, 1H, H**23**), 4.23 (bs, 1H, H**25**), 1.29 (d, *J* = 6.5 Hz, 3H, H**24**).

^{13}C NMR (DEPTQ, 100 MHz, $CDCl_3$) δ (ppm): 171.9 (C**5**, -ve), 170.9 (C**6**, -ve), 144 (C**10**, -ve), 143.3 (C**16**, -ve), 142.8 (C**17**, -ve), 141.2 (C**22**, -ve), 136.5 (C**11**, -ve), 136

(C4, -ve), 133.9 (C20, -ve), 133.8 (C7, -ve), 132.8 (C1, +ve), 131.8 (C8, +ve), 131 (C9, +ve), 129 (C3, +ve), 128.8 (C2, +ve), 123.4 (C14, +ve), 121.7 (C13, +ve), 118.3 (C19, +ve), 115.6 (C12, +ve), 115.5 (C21, +ve), 113.4 (C15, +ve), ,110.6 (C18, +ve), 69.9 (C23, +ve), 24.9 (C24, +ve).

EA (%) Calculated for $C_{35}H_{26}N_4O_2$: C, 78.63; H, 4.90; N, 10.48 %. **Found:** C, 78.74; H, 5.01; N, 10.36 %.

EI-MS (*m/z*): 534.2 $[M^+]$.

5.3.12 Synthesis of 1,4-dibromo-2-(6-bromohexyloxy)benzene **(10)**[11]

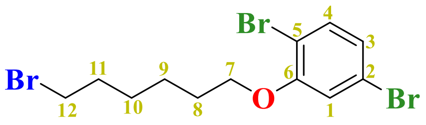

(10)

A mixture of 2,5-dibromophenol (150 mg, 0.6 mmol), 1,6-dibromohexane (0.2 mL, 291 mg, 1.2 mmol), and potassium hydroxide (135 mg, 2.4 mmol) was dissolved in DMSO (5 mL) under stirring at room temperature for 12 hours. The reaction mixture was then extracted with 100 mL of DCM and 150 mL of deionised water three times. The organic layer was collected and dried over anhydrous $MgSO_4$. The crude product was concentrated using a rotary evaporator and purified using column chromatography (silica gel, using petroleum ether: DCM = 10/1 in volume ratio as the eluent) to afford **(10)** as a white solid (241 mg, 97%).

^{1}H NMR (400 MHz, $CDCl_3$) δ (ppm): 7.35 (d, *J* = 8.5 Hz, 1H, H4), 6.97 (d, *J* = 2.0 Hz, 1H, H1), 6.92 (dd, *J* = 8.5 Hz, *J* = 2.0 Hz, 1H, H3), 3.97 (t, *J* = 6.5 Hz, 2H, H7), 3.40 (t, *J* = 6.5 Hz, 2H, H12), 1.93-1.77 (m, 4H, H8, H11), 1.57-1.44 (m, 4H, H9, H10).

^{13}C NMR (DEPTQ, 100 MHz, $CDCl_3$) δ (ppm): 156 (C6, -ve), 134.1 (C4, +ve), 124.6 (C1, +ve), 121.5 (C2, -ve), 116.4 (C3, +ve), 111.1 (C5, -ve), 69.2 (C7, -ve), 33.8 (C12, -ve), 32.7 (C8, -ve), 28.8 (C11, -ve), 27.8 (C9, -ve), 25.2 (C10, -ve).

EA (%) Calculated for $C_{12}H_{15}Br_3O$: C, 34.73; H, 3.64; Br, 57.77 %. **Found:** C, 34.81; H, 3.70; Br, 57.69 %.

EI-MS (*m/z*): 4.12, 414, 416, 418 ($[M^+]$, $[M^++2]$, $[M^++4]$, $[M^++6]$).

5.3.13 Synthesis of 2-(1-((6-(2,5-dibromophenoxy)hexyl)oxy)ethyl)-10-(4-(4,6-diphenyl-1,3,5-triazin-2-yl)phenyl)-10*H*-phenoxazine M3[12]

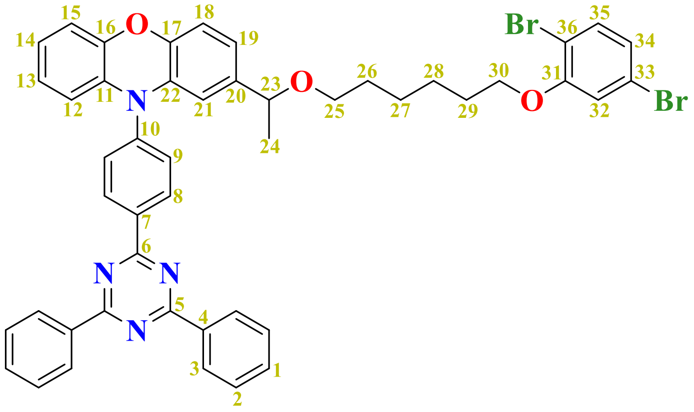

M3

(9) (550 mg, 1.03 mmol) and potassium hydroxide powder (580 mg, 10.29 mmol) were dissolved in anhydrous DMF (5 mL) in argon atmosphere. The reaction mixture was left under stirring for 3 hours and then added slowly into **(10)** (640 mg, 1.54 mmol) in a two-neck round bottom flask (100 mL). The solution was left under stirring overnight and then quenched with deionised water (150 mL) and extracted with DCM three times. The collected organic layer was dried over anhydrous MgSO$_4$ and concentrated using a rotary evaporator. The crude was purified by column chromatography using (eluent: DCM/petroleum ether 1/1) to afford M3 as a yellow powder (671 mg, 75%).

^{1}H NMR (400 MHz, CDCl$_3$) δ (ppm): 9.01 (d, *J* = 8.5 Hz, 2H, H8), 8.79 (dd, *J* = 7.5 Hz, *J* = 1.5 Hz, 4H, H3), 7.66-7.54 (m, 8H, H1, H2, H9), 7.30 (d, *J* = 8.5 Hz, 1H, H35), 6.89 (dd, *J* = 8.5 Hz, *J* = 2.0 Hz, 1H, H34), 6.83 (d, *J* = 2.0 Hz, 1H, H32), 6.75-6-58 (m, 5H, H12, H13, H14, H19, H21), 6.07-6.02 (m, 2H, H15, H18), 4.05 (q, *J* = 6.5 Hz, 1H, H23), 3.80 (t, *J* = 6.5 Hz, 2H, H30), 3.20 (t, *J* = 6.5 Hz, 2H, H25), 1.78-1.68 (m, 2H, H29), 1.48-1.22 (m, 9H, H24, H26, H27, H28).

^{13}C NMR (DEPTQ, 100 MHz, CDCl$_3$) δ (ppm): 171.8 (C5, -ve), 170.8 (C6, -ve), 156 (C31, -ve), 144 (C10, -ve), 143.1 (C16, -ve), 143 (C17, -ve), 139.6 (C22, -ve), 136.3 (C11, -ve), 136 (C4, -ve), 134.1 (C35, +ve), 134 (C20, -ve), 133.9 (C7, -ve), 132.7 (C1, +ve), 131.7 (C8, +ve), 131 (C9, +ve), 129 (C3, +ve), 128.7 (C2, +ve), 124.5 (C34, +ve), 124.4 (C14, +ve), 123.3 (C13, +ve), 121.7 (C33, -ve), 121.4 (C19, +ve), 119.1 (C32,

+ve), 116.3 (C12, +ve), 115.6 (C21, +ve), 115.4 (C15, +ve), 113.4 (C36, -ve), 110.9 (C18, +ve), 77.3 (C23, +ve), 69.2 (C30, -ve), 68.3 (C25, -ve), 29.8 (C29, -ve), 28.9 (C26, -ve), 26 (C28, -ve), 25.9 (C27, -ve), 24 (C24, +ve).

EA (%) Calculated for $C_{47}H_{40}Br_2N_4O_3$: C, 64.99; H, 4.64; Br, 18.40; N, 6.45 %. **Found:** C, 65.08; H, 4.71; Br, 18.32; N, 6.37 %.

EI-MS (*m/z*): 866.7, 868.7, 870.7 ([M^+], [M^++2], [M^++4]).

5.3.14 Synthesis of bis[2-(diphenylphosphino)phenyl] ether oxide (DPEPO)[13]

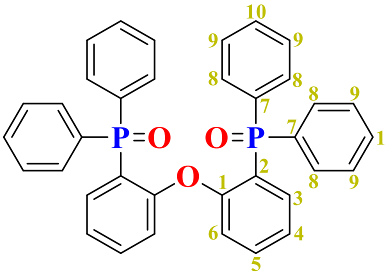

DPEPO

In 250 mL round bottom flask, a solution of **DPEPhos** (2.5 g, 4.64 mmol) was completely dissolved in 50 mL of DCM (50 mL) at cooled temperature using an ice bath. Then, an aqueous solution of 30% hydrogen peroxide (30%, 11.5 mL, 93 mmol) was added to the reaction mixture after the solution was stirred for an additional 20 minutes at 0 °C. After this addition, the reaction mixture was left under stirring at 0 °C for 4 hours. Next, the reaction mixture was quenched with distilled water (50 mL) and extracted three times with DCM (90 mL). The combined organic phase was dried over anhydrous $MgSO_4$, which was removed by filtration, and the solvent was evaporated using a rotary evaporator to produce a white residue. Reprecipitation of the crude from *n*-hexane (50 mL) was performed to provide the pure product **DPEPO** as a white powder (2.61 g, 99%).

^{1}H NMR (400 MHz, $CDCl_3$) δ (ppm): 7.76–7.52 (m, 10H, H6, H8), 7.50–7.18 (m, 12H, H9, H10), 7.15 (t, *J* = 7.5 Hz, 2H, H5), 7.07 (t, *J* = 7.5 Hz, 2H, H4), 6.01 (q, *J* = 8.0 Hz, *J* = 5.5 Hz, 2H, H3).

^{13}C NMR (DEPTQ, 100 MHz, CDCl$_3$) δ (ppm): 158.8 (d, J = 3.0 Hz, C**1**, -ve), 134.1 (d, J = 7.0 Hz, C**3**, +ve), 133.8 (d, J = 1.5 Hz, C**5**, +ve), 132.4-131.7 (m, C**8**, +ve), 131.4 (s, C**4**, +ve), 128.8-127.7 (m, C**10**, +ve), 124.6 (s, C**7**, -ve), 123.8 (d, J = 11.0 Hz, C**9**, +ve), 123.5 (s, C**2**, -ve), 120.1 (d, J = 6.5 Hz, C**6**, +ve).

^{31}P NMR (162 MHz, CDCl$_3$) δ (ppm): 25.84 (2P).

EA (%) Calculated for $C_{36}H_{28}O_3P_2$: C, 75.78; H, 4.95 %. **Found:** C, 75.86; H, 5.01 %.

EI-MS (*m/z*): 570 [M$^+$].

5.3.15 Synthesis of 1-bromo-4-[4-bromo-2-(diphenylphosphinoyl)-phenoxy]-5-(diphenylphosphinoyl)-benzene M4[14]

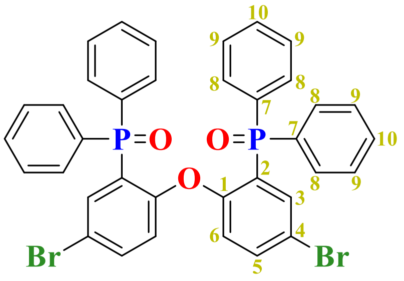

M4

To a stirred solution of **DPEPO** (1.14 g, 2 mmol) in sulfuric acid (2 mL) and glacial acetic acid (6 mL), was added NBS (720 mg, 4 mmol) in portions at room temperature. After addition, the reaction mixture was left under stirring for 8 hours. Upon completion, distilled water was added to quench the reaction and the aqueous layer was extracted with DCM (3 x 100 mL). The organic layers were combined, dried over $MgSO_4$ and then the solvent concentrated in vacuo. The crude was purified by column chromatography (1:14, petroleum ether: ethyl acetate) to afford a pure product of **M4** as a white powder (886 mg, 61% yield).

^{1}H NMR (400 MHz, CDCl$_3$) δ (ppm): 7.78 (dd, J = 12.5 Hz, J = 2.0 Hz, 2H, H**5**), 7.70-7.54 (m, 8H, H**8**), 7.53-7.18 (m, 14H, H**6**, H**9**), 5.84 (q, J = 8.0 Hz, J = 5.5 Hz, 2H, H**3**).

^{13}C NMR (DEPTQ, 100 MHz, CDCl$_3$) δ (ppm): 157.5 (d, *J* = 3.0 Hz, C**1**, -ve), 136.8 (s, C**5**, +ve), 136.5 (d, *J* = 13.0 Hz, C**3**, +ve), 132.5-131.4 (m, C**8**, C**9**, +ve), 128.9-127.8 (m, C**10**, +ve), 127.2 (s, C**7**, -ve), 126.3 (s, C**2**, -ve), 121.7 (d, *J* = 6.5 Hz, C**6**, +ve), 117.4 (d, *J* = 13.0 Hz, C**4**, -ve).

^{31}P NMR (162 MHz, CDCl$_3$) δ (ppm): 24.49 (2P).

EA (%) Calculated for $C_{36}H_{26}Br_2O_3P_2$: C, 59.37; H, 3.60; Br, 21.94 %. **Found:** C, 59.44; H, 3.69; Br, 21.86 %**.**

EI-MS (*m/z*): 726, 728, 730 ([M$^+$], [M$^+$+2], [M$^+$+4]).

5.4 General Procedure to Synthesise Polymers[15]

All polymers were synthesised according to the following procedure of palladium (0) catalysed Suzuki polycondensation. Under argon atmosphere, certain molar ratios of **M1**, **M2**, **M3**, **M4**, tri(o-tolyl)-phosphine, and palladium (II) acetate were dissolved in the smallest amount of toluene under stirring. To the reaction mixture, was added a saturated solution of potassium carbonate, which was saturated by argon for 3 hours to make it anhydrous. Then, the reaction mixture was refluxed under stirring at 110 °C for 72 hours. Followed by cooling down the reaction mixture to ambient temperature, then bromobenzene (10 eq. of **M2**) was added to the solution under argon atmosphere. Next, the mixture was gradually heated to reach to 110 °C for 24 hours after degassing the solution. Subsequently, the reaction mixture was cooled again to room temperature and phenylboronic acid (10 eq. of **M2**) dissolved in toluene was added to the reaction mixture under argon atmosphere. Then, the reaction mixture was degassed three times and refluxed at 110°C for 24 hours under argon atmosphere. After cooling the mixture to room temperature, the reaction mixture was dissolved in DCM (150 mL) and ammonium hydroxide solution 33% in water, 75 mL was added to the solution and left overnight under stirring to get rid of a catalyst. The mixture was extracted with DCM 100 mL three times and washed with deionised water. The combined organic layer was concentrated to approximately 10 mL and poured into methanol (200 mL) to form a polymer as a precipitate in different colour depending on TADF monomer amount.

PmCP-DPOXH: **M1** (100 mg, 0.177 mmol), **M2** (93 mg, 0.177 mmol), tri(o-tolyl)phosphine (11 mg, 0.036 mmol), Pd(OAc)$_2$ (4 mg, 0.0177 mmol), and the saturated solution of K_2CO_3 (3 mL) were utilised to obtain a white solid.

^{1}H NMR (400 MHz, CDCl$_3$) δ (ppm): 8.32 (d, *J* = 8.0 Hz, 2H), 8.18 (bs, 2H), 7.87-7.23 (m, 18H), 7.03-6.90 (m, 4H), 4.01 (bs, 4H), 1.84 (bs, 4H), 1.54 (s, 4H).

GPC: Toluene fraction, Mn = 6800 g mol^{-1}, Mw = 8500 g mol^{-1}, PDI = 1.25.

PmCP-DPOXH-PxzTrz-5: **M1** (97.6 mg, 0.172 mmol), **M2** (100 mg, 0.192 mmol), **M3** (16.6 mg, 0.0192 mmol), tri(o-tolyl)phosphine (12 mg, 0.0394 mmol), Pd(OAc)$_2$ (5 mg, 0.0192 mmol), and the saturated solution of K_2CO_3 (3 mL) were utilised to obtain a yellow-green solid.

^{1}H NMR (400 MHz, $CDCl_3$) δ (ppm): 9.02 (bs, 0.15H), 8.79 (bs, 0.3H), 8.36-8.08 (m, 1.73H), 7.95-7.23 (m, 23.98H), 7.19-6.9 (m, 4.4H), 6.05 (bs, 0.15H), 4.01 (bs, 4H), 3.80 (bs, 0.15H), 3.20 (bs, 0.14H), 1.84-22 (m, 8.75H).

GPC: Toluene fraction, Mn = 5700 g mol^{-1}, Mw = 7500 g mol^{-1}, PDI = 1.32.

PmCP-DPOXH-PxzTrz-10: **M1** (86.7 mg, 0.153 mmol), **M2** (100 mg, 0.192 mmol), **M3** (33.3 mg, 0.0384 mmol), tri(o-tolyl)phosphine (12 mg, 0.0394 mmol), $Pd(OAc)_2$ (5 mg, 0.0192 mmol), and the saturated solution of K_2CO_3 (3 mL) were utilised to obtain a yellow-green solid.

^{1}H NMR (400 MHz, $CDCl_3$) δ (ppm): 9.02 (bs, 0.28H), 8.79 (bs, 0.56H), 8.36-8.08 (m, 1.53H), 7.95-7.23 (m, 22.8H), 7.19-6.9 (m, 4.77H), 6.05 (bs, 0.27H), 4.01 (bs, 4H), 3.80 (bs, 0.25H), 3.20 (bs, 0.26H), 1.84-22 (m, 9.24H).

GPC: Toluene fraction, Mn = 5300 g mol^{-1}, Mw = 7200 g mol^{-1}, PDI = 1.36.

PmCP-DPOXH-PxzTrz-20: **M1** (65.1 mg, 0.115 mmol), **M2** (100 mg, 0.192 mmol), **M3** (66.5 mg, 0.0768 mmol), tri(o-tolyl)phosphine (12 mg, 0.0394 mmol), $Pd(OAc)_2$ (5 mg, 0.0192 mmol), and the saturated solution of K_2CO_3 (3 mL) were utilised to obtain a yellow-green solid.

^{1}H NMR (400 MHz, $CDCl_3$) δ (ppm): 9.02 (bs, 0.59H), 8.79 (bs, 1.1H), 8.36-8.08 (m, 1.1H), 7.95-7.23 (m, 18.6H), 7.19-6.9 (m, 5.4H), 6.05 (bs, 0.53H), 4.01 (bs, 4H), 3.80 (bs, 0.57H), 3.20 (bs, 0.51H), 1.84-22 (m, 10.4H).

GPC: Toluene fraction, Mn = 5400 g mol^{-1}, Mw = 7200 g mol^{-1}, PDI = 1.33.

PDPEPO-DPOXH: **M4** (100 mg, 0.14 mmol), **M2** (72 mg, 0.14 mmol), tri(o-tolyl) phosphine (8.4 mg, 0.0275 mmol), $Pd(OAc)_2$ (3.1 mg, 0.014 mmol), and the saturated solution of K_2CO_3 (3 mL) were utilised to obtain a white solid.

^{1}H NMR (400 MHz, $CDCl_3$) δ (ppm): 7.95 (bs, 2H), 7.75-7.03 (m, 26H), 6.95-6.85 (m, 4H), 6.01 (bs, 2H), 3.98 (bs, 4H), 1.82 (s, 4H), 1.62 (s, 4H).

^{31}P NMR (162 MHz, $CDCl_3$) δ (ppm): 25.89 (2P).

GPC: Toluene fraction, Mn = 4700 g mol^{-1}, Mw = 6100 g mol^{-1}, PDI = 1.30.

PDPEPO-DPOXH-PxzTrz-5: **M4** (125.1 mg, 0.172 mmol), **M2** (100 mg, 0.192 mmol), **M3** (16.6 mg, 0.0192 mmol), tri(o-tolyl)phosphine (12 mg, 0.0394 mmol), $Pd(OAc)_2$ (5 mg, 0.0192 mmol), and the saturated solution of K_2CO_3 (3 mL) were utilised to obtain a yellow-green solid.

^{1}H NMR (400 MHz, $CDCl_3$) δ (ppm): 8.98 (bs, 0.13H), 8.77 (bs, 0.26H), 7.92 (bs, 1.83H), 7.87-7.03 (m, 29.72H), 6.95-6.87 (m, 4.1H), 6.79-6-55 (m, 0.29H), 6.01 (bs, 1.93H), 3.98 (s, 4H), 3.80 (bs, 0.14H), 3.20 (bs, 0.13H), 1.82 (s, 3.99H), 1.58 (s, 4.36H), 1.24 (bs, 0.49H).

^{31}P NMR (162 MHz, $CDCl_3$) δ (ppm): 25.85 (2P).

GPC: Toluene fraction, Mn = 4800 g mol^{-1}, Mw = 6100 g mol^{-1}, PDI = 1.27.

PDPEPO-DPOXH-PxzTrz-10: **M4** (111.2 mg, 0.153 mmol), **M2** (100 mg, 0.192 mmol), **M3** (33.3 mg, 0.0384 mmol), tri(o-tolyl)phosphine (12 mg, 0.0394 mmol), $Pd(OAc)_2$ (5 mg, 0.0192 mmol), and the saturated solution of K_2CO_3 (3 mL) were utilised to obtain a yellow-green solid.

^{1}H NMR (400 MHz, $CDCl_3$) δ (ppm): 8.98 (bs, 0.24H), 8.77 (bs, 0.5H), 7.92 (bs, 1.54H), 7.87-7.03 (m, 27.25H), 6.95-6.87 (m, 4.1H), 6.79-6-55 (m, 0.61H), 6.01 (bs, 1.84H), 3.98 (s, 4H), 3.80 (bs, 0.26H), 3.20 (bs, 0.24H), 1.82 (s, 3.93H), 1.58 (s, 3.91H), 1.24 (bs, 0.98H).

^{31}P NMR (162 MHz, $CDCl_3$) δ (ppm): 25.85 (2P).

GPC: Toluene fraction, Mn = 4900 g mol^{-1}, Mw = 6600 g mol^{-1}, PDI = 1.35.

PDPEPO-DPOXH-PxzTrz-20: **M4** (83.4 mg, 0.115 mmol), **M2** (100 mg, 0.192 mmol), **M3** (66.5 mg, 0.0768 mmol), tri(o-tolyl)phosphine (12 mg, 0.0394 mmol),

$Pd(OAc)_2$ (5 mg, 0.0192 mmol), and the saturated solution of K_2CO_3 (3 mL) were utilised to obtain a yellow-green solid.

^{1}H NMR (400 MHz, $CDCl_3$) δ (ppm): 8.98 (bs, 0.54H), 8.77 (bs, 1.09H), 7.92 (bs, 1.17H), 7.87-7.03 (m, 24.05 H), 6.95-6.87 (m, 4.23H), 6.79-6-55 (m, 1.1H), 6.01 (bs, 1.55H), 3.98 (s, 4H), 3.80 (bs, 0.46H), 3.20 (bs, 0.44H), 1.82 (s, 3.8H), 1.58 (s, 3.88H), 1.24 (bs, 1.88H).

^{31}P NMR (162 MHz, $CDCl_3$) δ (ppm): 25.85 (2P).

GPC: Toluene fraction, Mn = 4600 g mol^{-1}, Mw = 5600 g mol^{-1}, PDI = 1.22.

5.5 References

(1) Sun, K.; Xie, X.; Liu, Y.; Jiang, W.; Ban, X.; Huang, B.; Sun, Y. Thermally Cross-Linkable Thermally activated delayed fluorescence Materials for Efficient Blue Solution-Processed Organic Light-Emitting Diodes. *Journal of Materials Chemistry C* **2016**, *4* (38), 8973–8979.

(2) Jeon, S. O.; Lee, J. Y. Comparison of Symmetric and Asymmetric Bipolar Type High Triplet Energy Host Materials for Deep Blue Phosphorescent Organic Light-Emitting Diodes. *Journal of Materials Chemistry* **2012**, *22* (15), 7239–7244.

(3) Zhang, R.; Peterson, J. P.; Fischer, L. J.; Ellern, A.; Winter, A. H. Effect of Structure on the Spin–Spin Interactions of Tethered Dicyanomethyl Diradicals. *Journal of the American Chemical Society* **2018**, *140* (43), 14308–14313.

(4) Hermann, M.; Wassy, D.; Kratzert, D.; Esser, B. Dibenzo [a, e] Pentalenophanes: Bending a Non-Alternant Hydrocarbon. *Chemistry–A European Journal* **2018**, *24* (29), 7374–7387.

(5) Vanderhaeghe, H. Phenoxazines. I. Ring-Substituted Derivatives. *The Journal of Organic Chemistry* **1960**, *25* (5), 747–753.

(6) MÜLLER, P.; Buu-Hoi, N. P.; Rips, R. Preparation and Some Reactions of Phenoxazine and Phenoselenazine. *The Journal of Organic Chemistry* **1959**, *24* (1), 37–39.

(7) Zhong, H.; Xu, E.; Zeng, D.; Du, J.; Sun, J.; Ren, S.; Jiang, B.; Fang, Q. New Optoelectronic Materials Based on Bitriazines: Synthesis and Properties. *Organic Letters* **2008**, *10* (5), 709–712.

(8) Tanaka, H.; Shizu, K.; Miyazaki, H.; Adachi, C. Efficient Green Thermally Activated Delayed Fluorescence (TADF) from a Phenoxazine–Triphenyltriazine (PXZ–TRZ) Derivative. *Chemical Communications* **2012**, *48* (93), 11392–11394.

(9) Moon, Y. K.; Jang, H. J.; Hwang, S.; Kang, S.; Kim, S.; Oh, J.; Lee, S.; Kim, D.; Lee, J. Y.; You, Y. Modeling Electron-Transfer Degradation of Organic Light-Emitting Devices. *Advanced Materials* **2021**, *33* (12), 2003832.

(10) Kamogawa, H.; Todo, Y.; Nanasawa, M. Synthesis of Vinyl Polymers with Pendant Phenoxazinyl Group. *Journal of Polymer Science: Polymer Chemistry Edition* **1981**, *19* (10), 2571–2579.

(11) Hsieh, C.-H.; Chen, W.-C.; Yang, S.-H.; Chao, Y.-C.; Lee, H.-C.; Chiang, C.-L.; Lin, C.-Y. A Simple Route to Linear and Hyperbranched Polythiophenes Containing Diketopyrrolopyrrole Linking Groups with Improved Conversion Efficiency. *AIMS Materials Science* **2017**, *4* (4), 878–893.

(12) Luo, X.; Ma, X.; Lebreux, F.; Markó, I. E.; Lam, K. Electrochemical Methoxymethylation of Alcohols–a New, Green and Safe Approach for the Preparation of MOM Ethers and Other Acetals. *Chemical Communications* **2018**, *54* (71), 9969–9972.

(13) Miyata, K.; Nakagawa, T.; Kawakami, R.; Kita, Y.; Sugimoto, K.; Nakashima, T.; Harada, T.; Kawai, T.; Hasegawa, Y. Remarkable Luminescence Properties of Lanthanide Complexes with Asymmetric Dodecahedron Structures. *Chemistry–A European Journal* **2011**, *17* (2), 521–528.

(14) Han, C.; Zhang, Z.; Xu, H.; Xie, G.; Li, J.; Zhao, Y.; Deng, Z.; Liu, S.; Yan, P. Convergent Modulation of Singlet and Triplet Excited States of Phosphine-Oxide Hosts through the Management of Molecular Structure and Functional-Group Linkages for Low-Voltage-Driven Electrophosphorescence. *Chemistry–A European Journal* **2013**, *19* (1), 141–154.

(15) Miyaura, N.; Suzuki, A. Palladium-Catalyzed Cross-Coupling Reactions of Organoboron Compounds. *Chemical Reviews* **1995**, *95* (7), 2457–2483.

Chapter 6: Supplementary Information

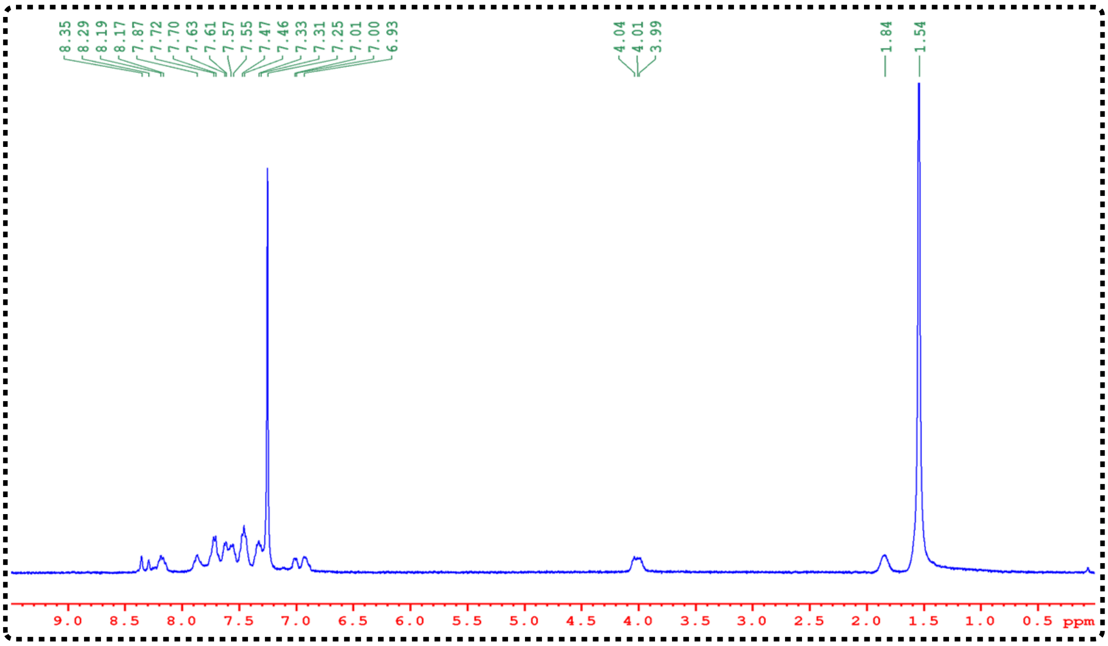

Figure 6.1: ^{1}H NMR Spectrum of **PmCP-DPOXH** in $CDCl_3$.

Figure 6.2: ^{1}H NMR Spectrum of **PmCP-DPOXH-PxzTrz-5** in $CDCl_3$.

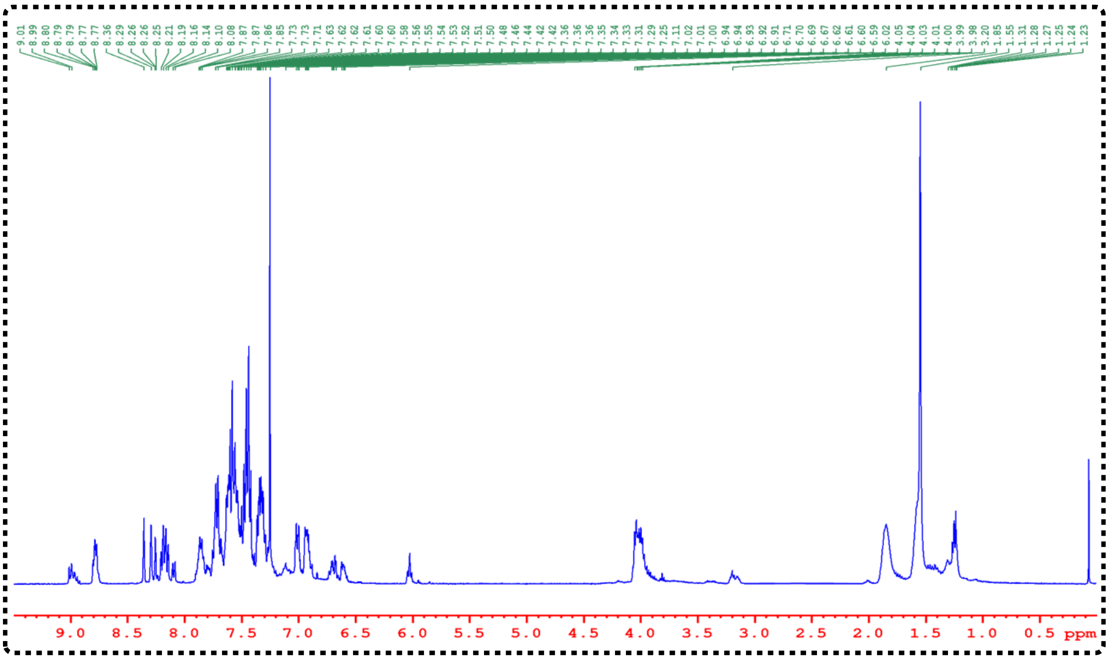

Figure 6.3: ^{1}H NMR Spectrum of **PmCP-DPOXH-PxzTrz-10** in $CDCl_3$.

Figure 6.4: ^{1}H NMR Spectrum of **PmCP-DPOXH-PxzTrz-20** in $CDCl_3$.

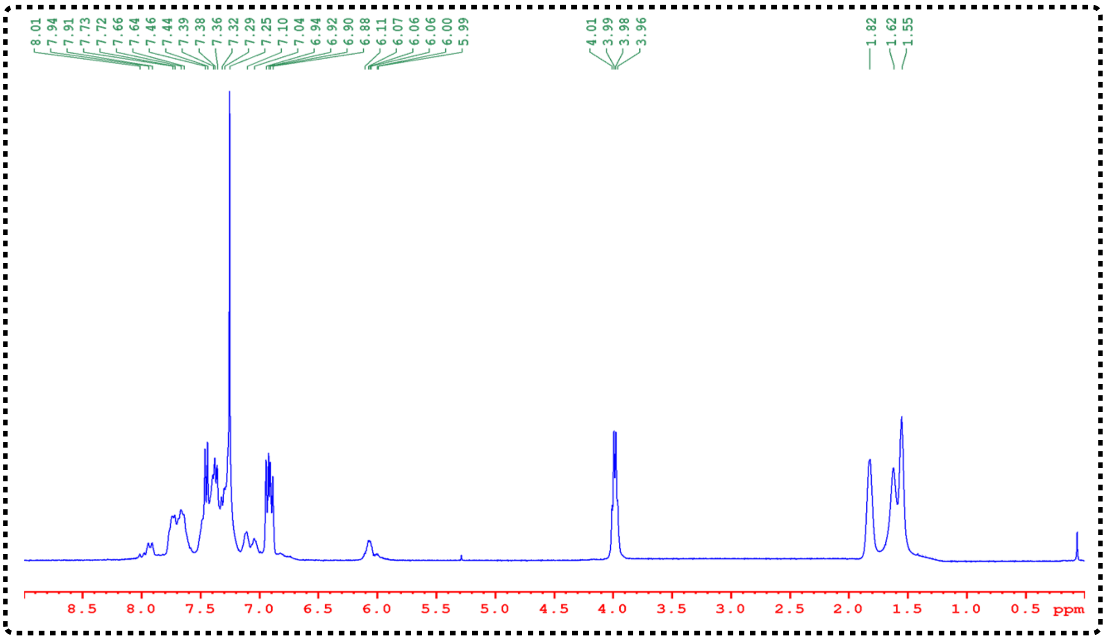

Figure 6.5: ^{1}H NMR Spectrum of **PDPEPO-DPOXH** in $CDCl_3$.

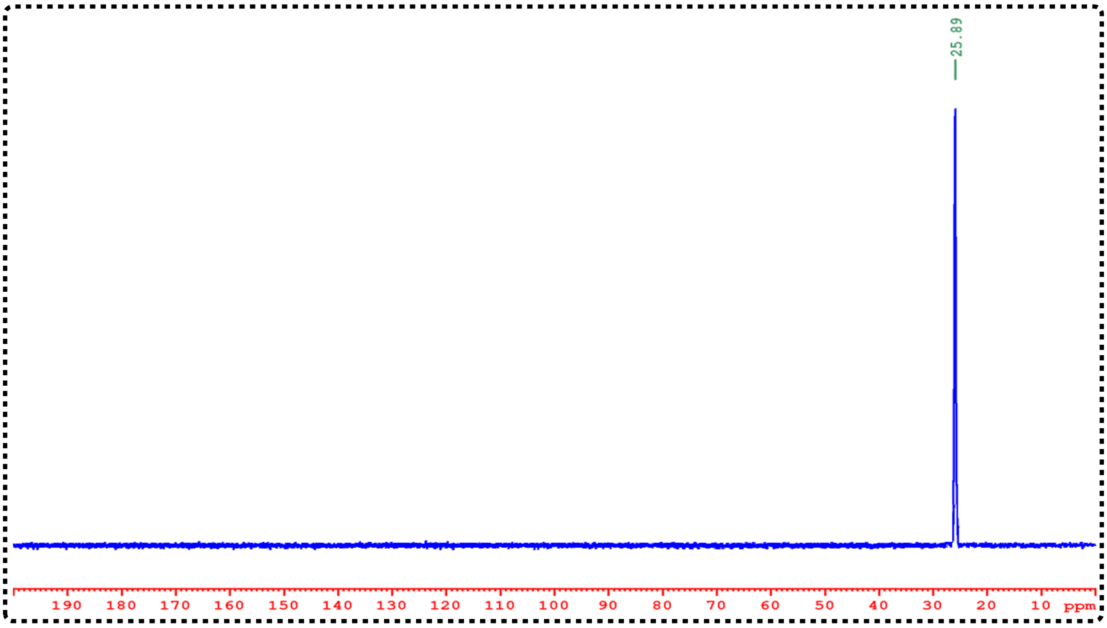

Figure 6.6: ^{31}P NMR Spectrum of **PDPEPO-DPOXH** in $CDCl_3$.

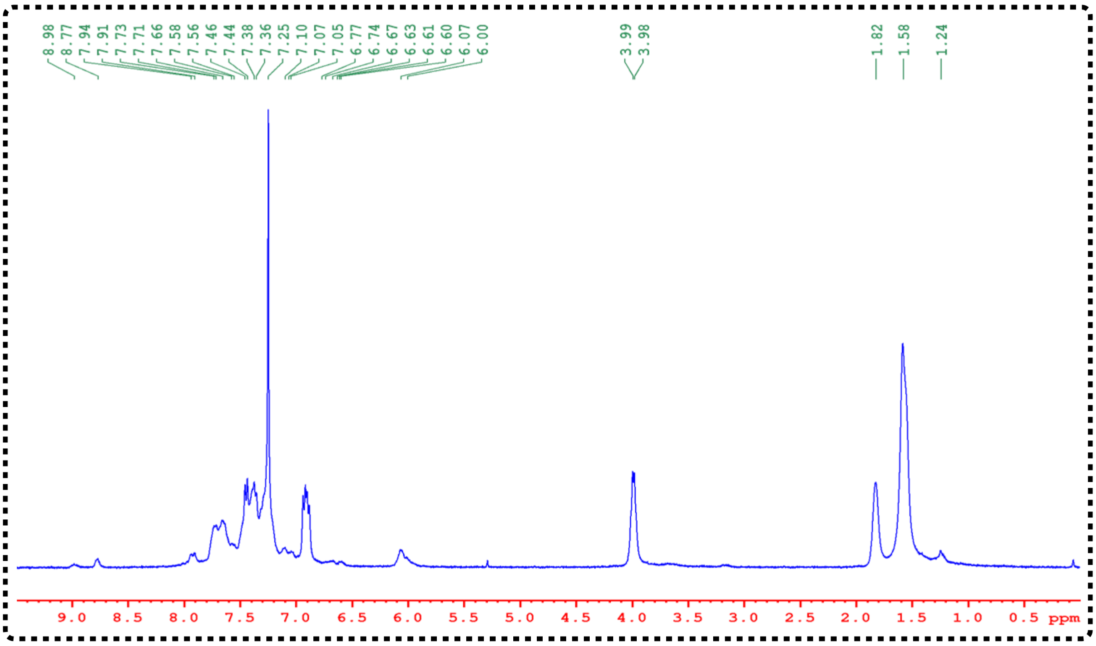

Figure 6.7: ^{1}H NMR Spectrum of **PDPEPO-DPOXH-PxzTrz-5** in $CDCl_3$.

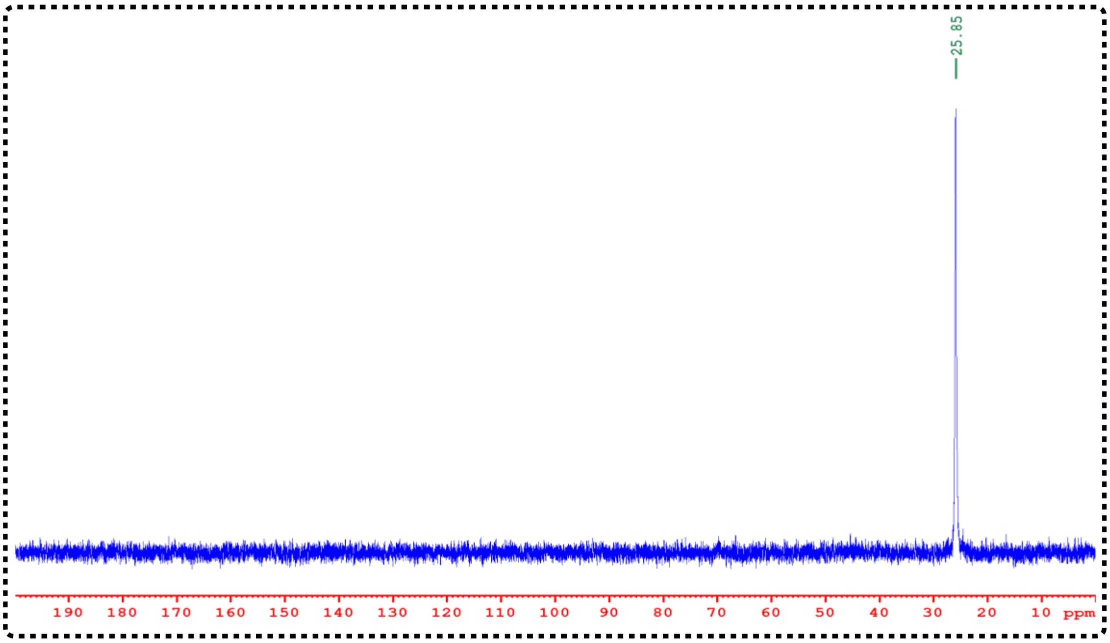

Figure 6.8: ^{31}P NMR Spectrum of **PDPEPO-DPOXH-PxzTrz-5** in $CDCl_3$.

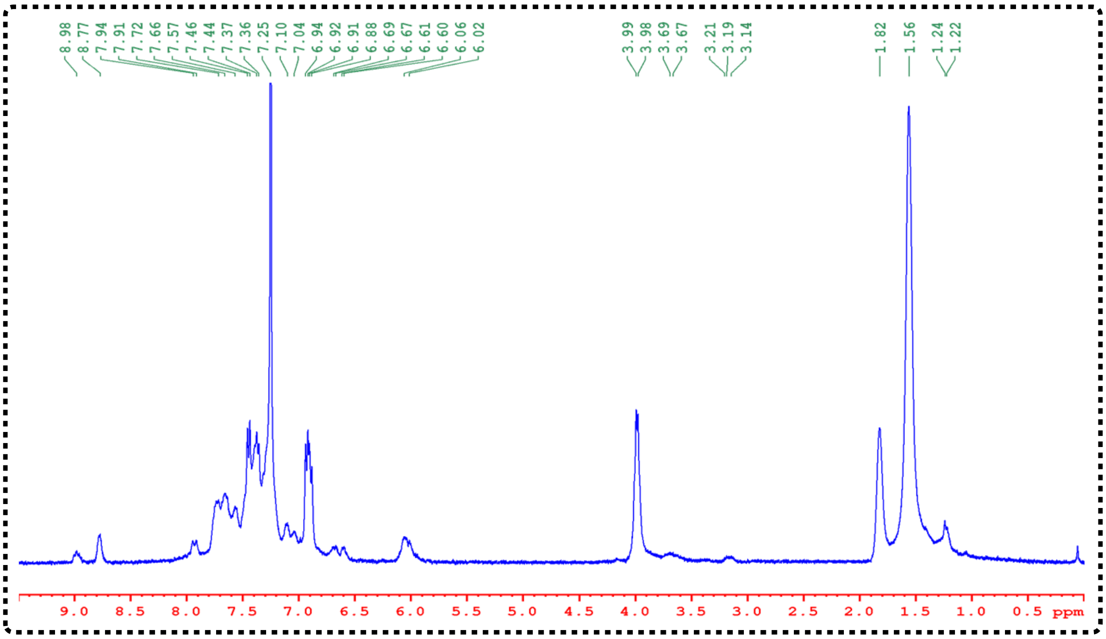

Figure 6.9: ^{1}H NMR Spectrum of **PDPEPO-DPOXH-PxzTrz-10** in $CDCl_3$.

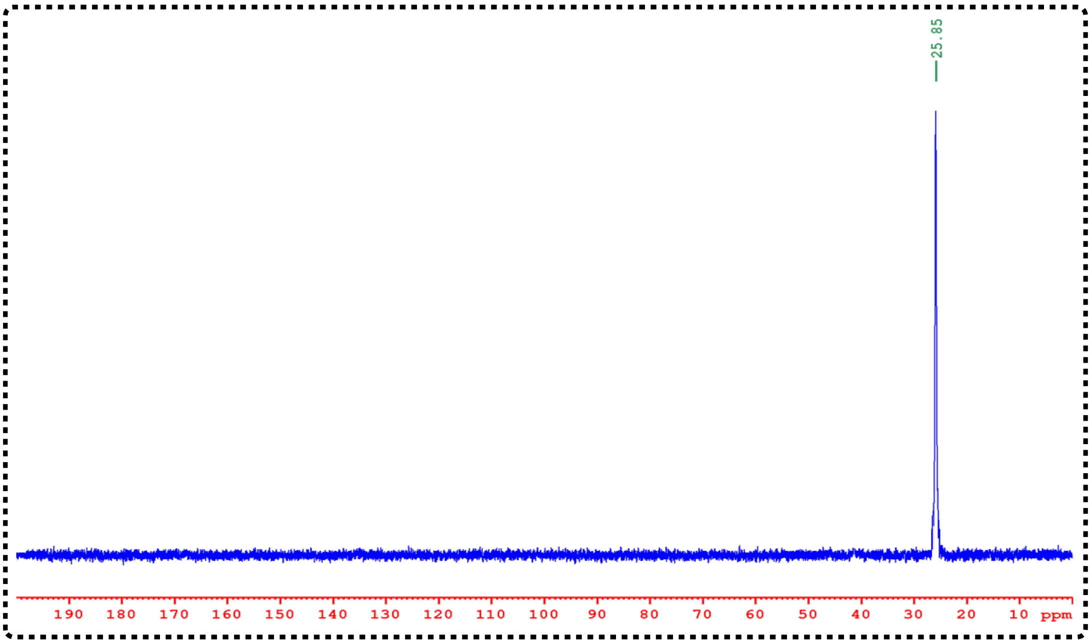

Figure 6.10: ^{31}P NMR Spectrum of **PDPEPO-DPOXH-PxzTrz-10** in $CDCl_3$.

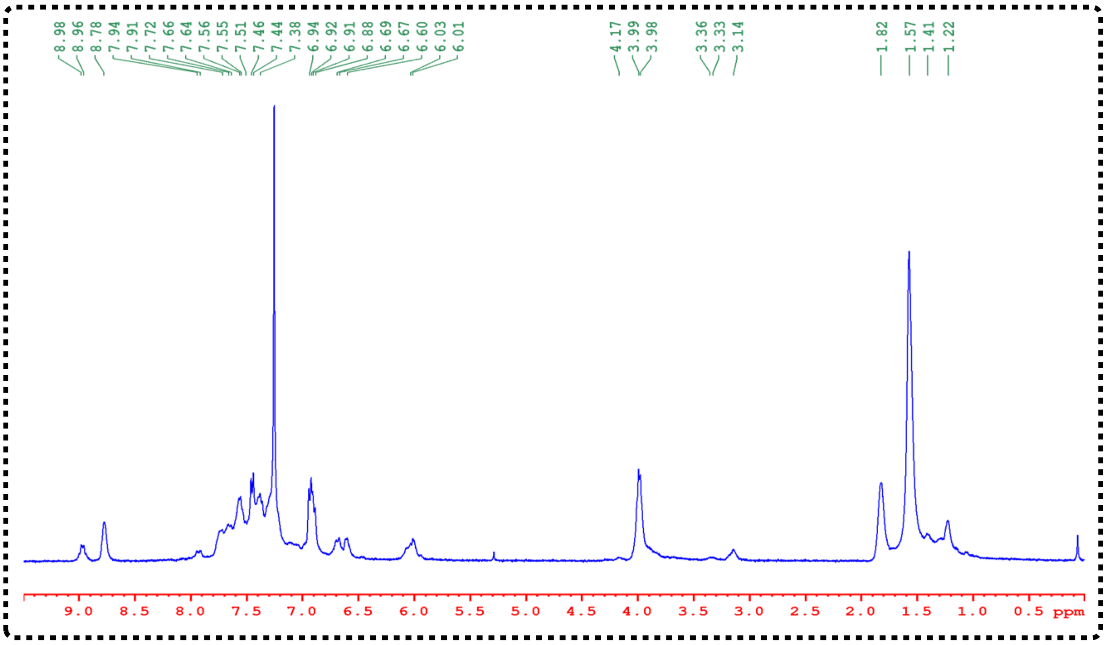

Figure 6.11: ^{1}H NMR Spectrum of **PDPEPO-DPOXH-PxzTrz-20** in $CDCl_3$.

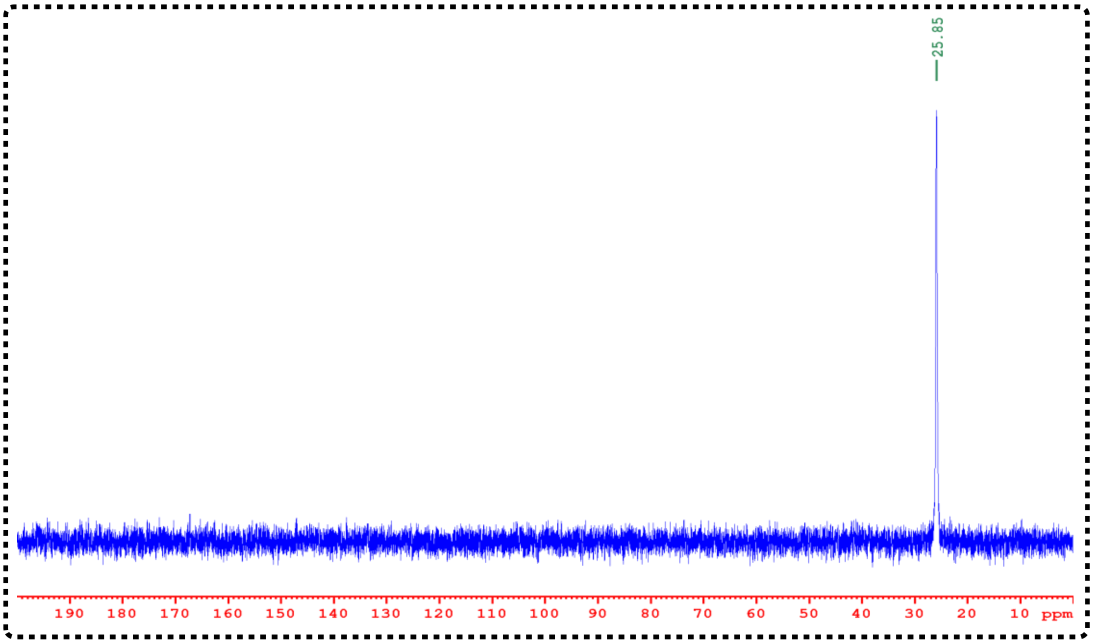

Figure 6.12: ^{31}P NMR Spectrum of **PDPEPO-DPOXH-PxzTrz-20** in $CDCl_3$.